

Univerza
v Ljubljani
Fakulteta
za gradbeništvo in
geodezijo



PODIPLOMSKI ŠTUDIJ
GEODEZIJE
DOKTORSKI ŠTUDIJ

Kandidat:

ROK VEZOČNIK, univ. dipl. inž. geod.

**ANALIZA TEHNOLOGIJE TERESTRIČNEGA
LASERSKEGA SKENIRANJA ZA SPREMLJANJE
DEFORMACIJ NA OBJEKTIH**

Doktorska disertacija štev.: 218

**ANALYSIS OF TERRESTRIAL LASER SCANNING
TECHNOLOGY FOR STRUCTURAL DEFORMATION
MONITORING**

Doctoral thesis No.: 218

Temo doktorske disertacije je odobrila Komisija za doktorski študij na 24. redni seji
10. septembra 2009. Za mentorja je bil imenovan izr. prof. dr. Tomaž Ambrožič, za
somentorja pa prof. dr. Norbert Pfeifer. Odobreno je pisanje disertacije v angleškem jeziku.

Ljubljana, 22. november 2011



Komisijo za oceno ustreznosti teme doktorske disertacije v sestavi

- doc. dr. Tomaž Ambrožič,
- prof. dr. Norbert Pfeifer, Tehnična univerza na Dunaju,
- izr. prof. dr. Bojan Stopar,
- izr. prof. dr. Dušan Kogoj,

je imenoval Senat Fakultete za gradbeništvo in geodezijo na 26. redni seji dne 25. marca 2009.

Komisijo za oceno doktorske disertacije v sestavi

- izr. prof. dr. Dušan Kogoj,
- doc. dr. Mojca Kosmatin Fras,
- zn. sod. dr. Tatjana Veljanovski, ZRC SAZU,

je imenoval Senat Fakultete za gradbeništvo in geodezijo na 22. redni seji dne 22. junija 2011.

Komisijo za zagovor doktorske disertacije v sestavi

- prof.dr. Matjaž Mikoš, dekan UL FGG, predsednik,
- izr. prof. dr. Tomaž Ambrožič,
- prof. dr. Norbert Pfeifer, Tehnična univerza na Dunaju,
- izr. prof. dr. Dušan Kogoj,
- doc. dr. Mojca Kosmatin Fras,
- zn. sod. dr. Tatjana Veljanovski, ZRC SAZU,

je imenoval Senat Fakultete za gradbeništvo in geodezijo na 24. redni seji dne 26. oktobra 2011.

Univerza
v Ljubljani
*Fakulteta
za gradbeništvo
in geodezijo*



IZJAVA O AVTORSTVU

Podpisani ROK VEZOČNIK, univ. dipl. inž. geod., izjavljam, da sem avtor doktorske disertacije z naslovom: »**ANALIZA TEHNOLOGIJE TERESTRIČNEGA LASERSKEGA SKENIRANJA ZA SPREMLJANJE DEFORMACIJ NA OBJEKTIH**«.

Izjavljam, da je elektronska različica v vsem enaka tiskani različici.

Izjavljam, da dovoljujem objavo elektronske različice v repozitoriju UL FGG.

Ljubljana, 22. november 2011

.....
(podpis)

ERRATA

Stran <i>Page</i>	Vrstica <i>Line</i>	Namesto <i>Instead of</i>	Naj bo <i>There should be</i>
----------------------	------------------------	------------------------------	----------------------------------

BIBLIOGRAFSKO-DOCUMENTACIJSKA STRAN IN IZVLEČEK

UDK:	528.3+528.53:528.7/.8(043.3)
Avtor:	Rok Vezočnik
Mentor:	izr. prof. dr. Tomaž Ambrožič
Somentor:	prof. dr. Norbert Pfeifer
Naslov:	Analiza tehnologije terestričnega laserskega skeniranja za spremljanje deformacij na objektih
Tip dokumenta:	doktorska naloga
Obseg in oprema:	224 str., 55 sl., 12 pregl., 26 en.
Ključne besede:	terestrično lasersko skeniranje, precizna klasična terestrična izmera, GNSS, analiza deformacij, dolgoročna geodetska spremljava

Izvleček:

Spremljanje premikov in deformacij antropogenih prostorskih struktur in objektov predstavlja eno izmed najbolj zahtevnih področij v geodeziji. Poleg merskih tehnologij, ki se tradicionalno uporabljajo za izvedbo takšnih nalog, predstavlja terestrično lasersko skeniranje dodatno možnost ploskovnega načina analiziranja objektnih površin. Glavni cilj doktorske naloge je v zagotovitvi odgovorov o možnostih uporabe terestričnega laserskega skeniranja za dolgoročno spremeljanje premikov in deformacij ter o načinu izvedbe takšne oblike spremeljave na poljubnih objektih. Poleg tega bo v okviru naloge ovrednotena hipoteza, da lahko s pomočjo te tehnologije daljinskega zaznavanja k analizi deformacij pristopimo v območju milimetrov. Za rešitev problema stabilnega referenčnega sistema, ki pogojuje visoko kakovostno analiziranje morebitnih sprememb položajev oblakov točk, je skeniranje treba povezati z ostalimi geodetskimi tehnikami, tj. zelo natančno statično izmero GNSS in precizno klasično terestrično izmero. Naloga predlaga metodologijo takšnega zelo natančnega načina spremeljanja, ki je bila preizkušena v okviru dveh testov v naravi. Poleg teh dveh testov so bili za potrebe naloge zasnovani tudi testi za preverjanje kakovosti uporabljenih merskih opreme (tarč laserskega skeniranja) in odzivnosti skenerja na lastnosti površinskega materiala.

BIBLIOGRAPHIC-DOCUMENTALISTIC INFORMATION AND ABSTRACT

UDC:	528.3+528.53:528.7/.8(043.3)
Author:	Rok Vezočnik
Supervisor:	Assoc. Prof. Tomaž Ambrožič, Ph.D.
Co-Advisor:	Prof. Norbert Pfeifer, Ph.D.
Title:	Analysis of terrestrial laser scanning technology for structural deformation monitoring
Dokument type:	Doctoral Dissertation
Notes:	224 p., 55 fig., 12 tab., 26 eq.
Keywords:	terrestrial laser scanning, precise classical terrestrial surveying, GNSS, deformation analysis, long-term monitoring

Abstract:

Monitoring displacements and deformations of anthropogenic spatial structures and objects represents one of the most intricate areas in geodetic surveying. Besides the measurement technologies that have been traditionally used for such tasks, terrestrial laser scanning represents another possibility employing the surface-wise deformation inspection of the objects' surfaces. The main aim of the thesis is to try to provide answers whether terrestrial laser scanning can be used for monitoring displacements and deformations in a long-term perspective and how this could be achieved for any arbitrary surface. Furthermore, the hypothesis will be challenged with the statement that the deformation inspection can be performed in the millimeter domain with this remote sensing measurement technology. In order to solve the problem of a stable reference system and to assure the high quality of possible position changes of point clouds, scanning is integrated with two complementary surveying techniques, i.e., high quality static GNSS positioning and precise classical terrestrial surveying. The methodology of such high precision monitoring approach is proposed in the thesis and was tested in two case study outdoor experiments. Besides these two outdoor experiments, also indoor tests were designed to evaluate the quality of the surveying equipment (laser scanning targets) as well as the response of the scanner to the surface material.

ZAHVALA (Acknowledgments)



Science never solves a problem without creating ten more.
Znanost nikoli ne reši problema ne da bi ustvarila deset novih.
George Bernard Shaw

Doktorska disertacija je v prvi vrsti rezultat aktivnega in uspešnega sodelovanja med akademsko ter podjetniško sfero na področju geodezije. Raziskovalno delo je financiralo Ministrstvo za visoko šolstvo, znanost in tehnologijo RS v okviru programa usposabljanja mladih raziskovalcev iz gospodarstva. Spodbujanje prenosa znanja v prakso je izrednega pomena ne samo za napredovanje posameznih znanstvenih panog, ampak družbe nasploh. Hvala!

Izredna zahvala gre izr. prof. dr. Tomažu Ambrožiču, mentorju, ki bi si ga želel vsak kandidat. Sodelovanje z njim je bilo tako strokovno kot tudi prijateljsko, vedno v luči nenehne pripravljenosti na nove izzive. Tomaž je hkrati edini, ki me je spremjal in mi pomagal pri izvedbi vseh testnih meritev, ne glede na uro in kraj. Spodbujal me je na vsakem koraku in mi bil vedno na razpolago za nešteta vprašanja. Tomaž, vse kar lahko rečem je SUPER HVALA in upam, da naju bo sodelovanje na tak ali drugačen način povezovalo še dolgo časa.

Rad bi se zahvalil tudi celotnemu kolektivu Oddelka za geodezijo na Fakulteti za gradbeništvo in geodezijo v Ljubljani (FGG), saj so mi zagotovili pisarno, kjer sem lahko v miru in v spodbudnem ter prijetnem okolju pisal disertacijo. Za nasvete bi se posebej rad zahvalil izr. prof. dr. Dušanu Kogoju, prof. dr. Bojanu Stoparju ter mag. Oskarju Sterletu, ki mi je bil vedno na razpolago za konstruktivno debato. Oskarju bi se hkrati zahvalil za pomoč pri obdelavi meritev in za uporabo njegovih programov. Hvala vsem!

Lepo bi se zahvalil tudi asist. dr. Juretu Klopčiču s Katedre za mehaniko tal z laboratorijem na FGG za skrbno in natančno pripravo testnih vzorcev. Hvala tudi za organizacijo dobave vsega potrebnega

materiala.

Many thanks also to Prof. Norbert Pfeifer from Vienna University of Technology, Institute of Photogrammetry and Remote Sensing for supervising the entire research process. His advice, propositions and comments were always very valuable and helped me guide my work in the right direction whenever stumbling on a problem. Furthermore, I wish to thank him for allowing me to stay and work at the Institute of Photogrammetry and Remote Sensing in Vienna as well as providing a very friendly and cooperative atmosphere during all my visits. The presentations I held in the Institute's Seminarraum were a great experience for me in terms of possibilities to discuss my research work in a wider circle of experts. I must say I have learned a lot not only from Norbert but also from other Institute members, such as Assist. Prof. Helmut Kager, Camillo Ressl, Christian Briese and my two good friends Alexander Haring and Milutin Milenković. I must thank Alexander for performing the ICP analysis on my datasets and Milutin for taking me under the roof whenever needed. Thank you all, again. Hopefully, we will stay in contact also in the future whether in the academic or private sphere.

Lepo bi se rad zahvalil tudi podjetju DFG CONSULTING, d.o.o., z direktorjem mag. Tomažem Gvozdanovičem na čelu. Mažotove dobre in unikatne ideje so bile vedno dobrodošle, še posebej pri reševanju konkretnih praktičnih problemov. Hvala tudi za razumevanje in odobritev mojih izostankov od tekočega dela, brez katerih bi bila izvedba raziskovalnega dela nemogoča. Posebej bi se zahvalil tudi sodelavcu mag. Domnu Smoletu, saj je v času moje odsotnosti na svoja ramena prevzel številne dodatne obveznosti ter mi hkrati pomagal pri izvedbi testnih meritev. Zahvala gre tudi vsem ostalim zaposlenim v podjetju, ki so tako ali drugače prispevali k uresničitvi tega obsežno zastavljenega cilja.

Lepo bi se zahvalil še podjetju Geoplín plinovodi d.o.o. in Družbi za avtoceste v Republiki Sloveniji (DARS d.d.) za dovoljenje uporabe rezultatov testnih meritev v nalogi.

Barbari in Dušanu gre zahvala za lektoriranje, ki sta ga kljub ostalim obveznostim in kratkemu roku brezpogojno sprejela. Hvala obema!

Ogromna zahvala gre seveda tudi Tanji in staršema za vse spodbude, odrekanja in podporo skozi vsa moja učna leta. Brez njih bi mi težko uspelo. Hvala vam za razumevanje!

TABLE OF CONTENTS

1	INTRODUCTION	1
1.1	Motivation	1
1.2	Research aims	2
1.3	Related work	3
1.4	Structure of the thesis	4
2	METHODS	7
2.1	General workflow	7
2.2	Reference frame	7
2.3	Geodetic network formation	8
2.4	Target scanning and extraction	9
2.4.1	Flat targets	10
2.5	Positioning of scan data within the reference frame	14
2.6	Object scanning	19
2.6.1	Physical limitations	19
2.6.2	Scanning geometry	21
2.7	Modelling the object shape	22
2.7.1	Planarity based segmentation	23
2.7.2	Model validity and parameter estimation	24
2.8	Deformation models	25
2.8.1	Model 1: Truncated direction	25
2.8.2	Model 2: Representative points	27
3	EXPERIMENTAL RESULTS	29
3.1	Target calibration tests	29
3.1.1	Mechanical imperfections	30
3.1.2	Range error modelling	33
3.2	Surface material response	48
3.3	Outdoor test 1: Pipeline	54
3.3.1	The test field and its characteristics	54
3.3.2	Field work	56
3.3.3	Results	59
3.3.3.1	GNSS	60
3.3.3.2	Classical terrestrial method	61
3.3.3.3	Terrestrial laser scanning	63
3.4	Outdoor test 2: Supporting wall	69
3.4.1	The test field and its characteristics	69

3.4.2	Field work	72
3.4.3	Results	75
3.4.3.1	Classical terrestrial method	75
3.4.3.2	Terrestrial Laser Scanning	77
4	ANALYSIS AND DISCUSSION	83
4.1	Outdoor test 1	83
4.1.1	The datum stability	83
4.1.2	Determination of representative points	84
4.1.3	Displacement evaluation	85
4.2	Outdoor test 2	87
4.3	The indoor test evaluation	92
5	CONCLUSIONS	95
5.1	Outlook	97
6	SUMMARY	99
7	REFERENCES	103

LIST OF FIGURES

Figure 1: Point-wise and surface-wise object inspection	2
Figure 2: TLS targets	10
Figure 3: Examples of model fitting	13
Figure 4: TLS measurement positioning diagram	14
Figure 5: Time and amplitude estimation	20
Figure 6: Impacts on point density	21
Figure 7: Anthropogenic structures captured by TLS	22
Figure 8: Segmentation results	24
Figure 9: Segment-wise displacement inspection	26
Figure 10: Testing target construction defects	30
Figure 11: Mounting offset results	32
Figure 12: Range error test setup	33
Figure 13: The area of point cloud selected for the distance estimation	34
Figure 14: Standard deviations of distance measurements	35
Figure 15: Slope distance levelling	36
Figure 16: Range error and average amplitude as a function of the distance for T1, T2	37
Figure 17: Range error and average amplitude as a function of the distance for T3, T4	38
Figure 18: Range error as a function of the amplitude for T1 and T2	40
Figure 19: Range error as a function of the amplitude for T3 and T4	41
Figure 20: Residual pattern for T1	44
Figure 21: Residual pattern for T2	45
Figure 22: Residual pattern for T3	46
Figure 23: Residual pattern for T4	47
Figure 24: Close-up images of the tested samples	48
Figure 25: Surface roughness variations	50
Figure 26: The plate holder and the measuring clock	50
Figure 27: Displacement results	52
Figure 28: Multiples under 0° incidence angle	53
Figure 29: Deviations from the clock's readings at various reduction levels	54
Figure 30: Orthophoto image of the test field	55
Figure 31: Pillars used for monitoring the movements of the underground pipeline	56
Figure 32: The geodetic network designed near the object of the study	58
Figure 33: Scanner positions with respect to the observation pillars	59
Figure 34: Locations of permanent GNSS stations	60
Figure 35: Cylinder parameters	64
Figure 36: Example of the spatial distribution of residuals	65
Figure 37: Residual pattern grids for 4212	66

Figure 38: Station configuration and ICP results	67
Figure 39: The standard deviations of the cylinder parameters after subsampling	69
Figure 40: Sectors selected for monitoring excavation effects	70
Figure 41: Objects of interest and stabilized pillars in sector 1	71
Figure 42: The geodetic network designed near the objects of the interest	73
Figure 43: Scanner stations in the two measurement campaigns	74
Figure 44: Profile irregularities	77
Figure 45: The overview of the absolute orientation accuracy	79
Figure 46: The overlapping areas on the wall and the road surface	81
Figure 47: Modelling of the wall using planar model	81
Figure 48: Graphical results of reference pillar displacements	84
Figure 49: Identical points for the determination of displacements	85
Figure 50: Pillar displacements	86
Figure 51: Histogram of the patch displacements from the truncated direction model	88
Figure 52: Histogram of the wall's displacements calculated in model 2	89
Figure 53: The directions of the displacement vectors for the wall's representative points	90
Figure 54: The magnitude of displacements of the roads surface	91
Figure 55: The road tracks' sinking pattern in the form of a grid	92

LIST OF TABLES

Table 1: Circular flat target characteristics	11
Table 2: Results of the targets' sensitivity to rotation	31
Table 3: Estimated values of parameters of the range error functions and a posteriori values	43
Table 4: Sample properties	49
Table 5: Outdoor test 1: atmospheric parameters of the two surveying campaigns	57
Table 6: GNSS campaign characteristics	59
Table 7: Estimated coordinates of reference pillars	61
Table 8: Results of the adjustment using minimum datum parameters	63
Table 9: Adjustment results estimated from four station configurations	67
Table 10: Outdoor test 2: atmospheric parameters of the two surveying campaigns	72
Table 11: Results of the adjustment using minimum datum parameters	76
Table 12: The quality of the absolute orientation process	80

1 INTRODUCTION

1.1 Motivation

Monitoring displacements and deformations of anthropogenic spatial structures and objects represents one of the most intricate areas in geodetic surveying. The knowledge about types, characteristics and scales of structural deformations is essential when defining their nature and for the consequent verification of potential permanent damage possibilities or eventual destruction of structures. In traditional surveying, different deformation analysis approaches have evolved (e.g.: Delft, Fredericton, Hannover, Karlsruhe, München, see Chrzanowski, 2006). All these methods are aimed at ensuring a safe operation and usage of these structures. The second relevant aspect is closely connected with the cost-effective construction and management. The expenses of conceivable restoration may go beyond the bounds; therefore, the causes for the occurrence of deformations should be discovered and prevented on time by means of carefully designed geodetic monitoring strategies.

In recent years, terrestrial laser scanning (TLS) has become increasingly used in different engineering surveying applications, including the field of displacement and deformation monitoring (see section 1.3). Despite the growing number of presented solutions, the millimeter domain in displacement detection is still an open area of investigation. The ability to perform a rapid and dense measurement of huge amounts of object points is a tempting advantage of TLS in comparison to other sensor technologies and point-wise monitoring approaches, where deformation evaluation is limited to a few discrete and well signalized points (Figure 1 on page 2). In contrast to the lower precision of individual sampled points which may preclude their use in high precision monitoring tasks, the effective detection of deformations on the entire object covering is possible by proper modelling of the object's surfaces exploiting the high data redundancy. TLS is a remote sensing measurement technology; therefore, the direct object accessibility is not required and the influence of installation of control points or other sensor compositions onto the observed object is minimized. In the process of long-term displacement and deformation determination and analysis, the quality and stability of the chosen reference system, i.e., geodetic datum, plays a vital role. The geodetic datum is realized on the basis of geodetic points which should be stabilized on geologically stable ground if deformation parameters (translations, rotations and other structural distortions, defined on the basis of the comparison of 3D surface models from TLS data) are not to be subdued by their movements. Therefore the connection of the TLS and other geodetic surveying technologies becomes inevitable. By integrating TLS with these surveying techniques into a multi-sensor composition, the weaknesses of individual measurement methods involved can be overcome, while their intrinsic advantages could be used for a complete expression of deformations on the entire surface of the structures in question.

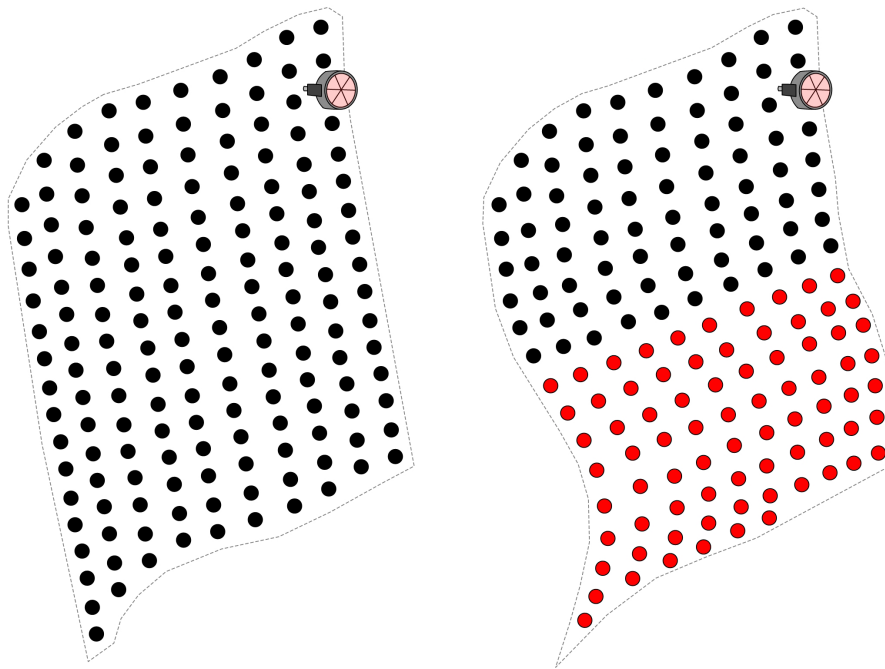


Figure 1: Point-wise and surface-wise object inspection. The amount of information on the change of object's condition is significantly smaller in the case of the first observation approach. Dots indicate the dense TLS sampling pattern with those reflecting deformations colored in red.

1.2 Research aims

The primary objective of the thesis is to challenge the hypothesis which states that **the millimeter precision in displacements and deformation monitoring can be achieved in the long-term perspective for objects and not only for few signalized (i.e., marked) points**, which is a typical approach when using the point-wise surveying techniques. The thesis will be focused primarily on the analysis of the time-of-flight (TOF) TLS since this distance measurement principle is on the one hand most common and suitable due to its wide range of operation but on the other hand the least accurate, posing an additional constraint during the process of testing the hypothesis. Concerning the objects of interest, only those with a well-defined and solid surface are considered appropriate for such tasks.

Within this research framework, the thesis is aimed at presenting an overall and effective methodological workflow for spatio-temporal change inspection incorporating complementary measurement technologies. These are employed in order to design and control the quality and stability of the frame for the evaluation of TLS surface model displacements and deformations. To be able to approach the evaluation in the millimeter domain the existing approaches first had to be examined in detail and finally refined or upgraded to meet such high end precision demands. Based on the extensive experimental tests, which were conducted to put the workflow under close analysis, the thesis will not only examine the hypothesis but try to provide answers to the following questions:

- what are the vital parts of the workflow;
- where are the limits of nowadays TOF systems;
- can TLS be considered accurate enough to stand side by side with geodetic measurement techniques that provide millimeter size displacements.

1.3 Related work

The interest for potential feasibility of TLS in precise engineering metrology has motivated the establishment of a special Task Force within the FIG organization (6.1.5. Terrestrial laser scanning for deformation monitoring), which indicates the relevance of implementation of this non-contact technique in the field of geodetic surveying (Tsakiri et al, 2006). The Task Force 6.1.5. collaborates with the ISPRS Working Group V/3 Terrestrial laser scanning on different research topics as well as on the exchange of ideas, methodology and practical experiences with research and applied projects. Each organization has a slightly different perspective on the TLS deformation analysis, since the first one originates directly from the geodetic background, whereas the second one from photogrammetry and remote sensing. Interdisciplinary cooperation of these two areas of metrology is vital when discussing the possibilities of employment of TLS technology for structural deformation monitoring. Most of the so-far conducted research agrees on the conclusion that the large redundancy in observations provided by TLS may potentially allow the detection of deformations well below the nominal individual point quality.

Since its introduction to deformation monitoring, TLS has been used in different applications and load test studies, ranging from indoor to outdoor experiments and research projects. The objects of studies include dams, tunnels, bridges, viaducts, towers and other buildings in general. Each author basically presents one's own approach to deformation evaluation, making it difficult to estimate which may be more effective and complete. This is one of the reasons that a general displacement and deformation workflow is needed and will be presented in the thesis.

One of the early outdoor projects by Alba et al (2006) presents the results of feasibility of monitoring deformations of large concrete dams by terrestrial laser scanning. Two approaches were presented for the analysis of surface displacements, including the shortest distance between the consecutive point clouds (one being a surface model) and, additionally, displacements computed by comparing two regular grids of the dam face. In this study it has been concluded that the stability of the reference frame is of great importance in order to separate the displacements from the noise produced by errors within the georeferencing process.

One interesting approach for structural monitoring of large dams by TLS is described in Gonzales-Aguilera et al (2008), where the Radial Basis Function was used for the parameterization of the dam surface. Moreover, the accuracy control of the georeferencing phase was performed by incorporating re-Weighted Extended Orthogonal Procrustes analysis.

In Van Gosliga et al (2006) it is described how artificial deformations of a cylindrical tunnel wall

were detected using a statistical adjusting and testing procedure (i.e., the Delft method). In this paper, the scanned surface was approximated with a cylindrical model, and the point-wise deformation analysis was performed by comparing surface patches.

Scanning of a bridge exposed to a controlled load testing is presented in Lovas et al (2009). The results are compared with high precision inductive transducers installed on the construction. The authors conclude that TLS is recommended as a supplementary method in load tests and displacement measurements, providing useful additional information, but cannot completely replace the traditional point-wise techniques.

Another load test study involving a Swiss viaduct was described by Zogg et al (2008) where the authors used a phase shift scanner. The study concluded that TLS can generally be used to detect deformations in the millimeter domain but the complementary surveying techniques (precise levelling in the case of this study) are indispensable in order to assess the accuracy and quality of TLS measurements and to confirm the final results.

Besides these case studies, many authors have applied TLS for the detection of deformations in the controlled environments or experiments with simulated values of displacements, e.g., Park et al (2007) or Gordon et al (2007). In this way, the actual displacements and the measurement noise can be distinguished more easily, also because the effects of meteorological conditions can be neglected. Furthermore, the quality and stability of the reference frame is also not particularly addressed in any of these studies (it is assumed to be stable) mainly due to the fact that complementary surveying technologies must be implemented in the measurement setup in order to tackle the problem of datum correctly, which is what the thesis tries to do by introducing the proposed methodological workflow.

1.4 Structure of the thesis

The thesis is structured according to the standard form of many scientific papers, the so-called IM-RAD format (**I**ntroduction, **M**ethods, **R**esults And **D**iscussion).

Chapter 1: Introduction

This first introduction chapter is meant to outline the motivation for the research and expose the working hypothesis which is evaluated based on the experimental results. The section on related work is added in order to examine the status of research, present the work done by other authors and finally to indicate the placement of the thesis's contents within the research community.

Chapter 2: Methods

Following the introduction, Chapter 2 describes the methodological steps. These steps represents the basic theoretical frame for the design of the experimental setups, the results of which will eventually be used to evaluate the working hypothesis. Chapter 2 begins by first presenting the general workflow of the deformation inspection approach which can be treated as a sort of abstract of the

entire chapter. Next, the individual parts of the workflow are described in more detail, starting with the reference frame and geodetic network formation. Afterwards, the focus is shifted to the laser scanning targets, needed for the relative/absolute orientation of the point clouds which is presented in the subsequent section. The chapter then presents the object's scanning and modelling process and concludes with the description of the two deformation models that were designed to conduct the final spatio-temporal change inspection. Conceptually, the contents of this chapter covers four separate topics:

- the formation of the reference frame;
- the positioning of the TLS point clouds;
- the object scanning and modelling;
- the presentation of the deformation models.

Chapter 3: Experimental results

In this chapter, the experiments are described involving three indoor and two outdoor tests. The first three were designed for the calibration purposes testing the most vital steps of the methodology, i.e., the quality of the targets and the evaluation of systematic errors as well as the surface material response to the incident laser light. The results of these three tests had to be taken under consideration during the two outdoor experiments where the methodology was employed on a full scale involving varying and limited field conditions and different objects (the pipeline and the supporting wall). The sections describing the outdoor experiments end with the computation of the input quantities for the deformation models.

Chapter 4: Analysis and discussion

In this chapter, the results of applying the deformation models for the objects of the two outdoor test are presented and discussed. The chapter ends with a short indoor test evaluation.

Chapter 5: Conclusions

The final chapter concludes with the evaluation of the working hypothesis and exposes the directions of the future research.

Chapter 7: References

The list of references used in the thesis.

2 METHODS

2.1 General workflow

In general, the workflow of the proposed deformation evaluation approach can be divided into the following seven steps:

1. a network of reference points should be established;
2. a geodetic network should be designed near the object of the study;
3. targets should be scanned and extracted to assure the connection to the reference frame;
4. the reference frame connection should be done by a proper transformation estimation;
5. TLS should be performed by taking good care of the object coverage;
6. the object shape must be modelled with appropriate surfaces;
7. the surface models can finally be compared in different deformation models.

Apart from this coarse workflow, the calibration of the instruments involved as well as the accompanying measuring equipment must be taken under consideration. However, as described in Lichten (2009) and Dorninger et al (2008), the investigation of the temporal stability of scanner systematic errors still remains somewhat open for discussion. Finally, the field work has to be performed with the utmost precision and care whereas special emphasis should be put on establishing the same surveying conditions in all measurement campaigns and following the same data processing algorithms. The surveying conditions do not include meteorological parameters since they cannot be controlled. The presented measurement approach enables a complete and effective control over the individual segments involved as well as the error propagation process. In the rest of this chapter, the steps of the workflow will be described in more detail.

2.2 Reference frame

In order to control the quality and stability of the reference frame, the GNSS observations represent one powerful tool since they are currently the only time-continuous geometric geodetic observation technology that provides absolute positions in a well-defined geocentric reference system. It is limited to open terrain areas where the interruption of satellite signals can be prevented. For high precision tasks, the planning and processing strategy of GNSS observations should be based on recommendations for high precision coordinate estimation found in, e.g., IGS processing strategy (IGS, 2009), EUREF guidelines for EPN Analysis Centres (EPN, 2009), or high precision geodynamic research (Bergeot et al, 2009; Caporali et al, 2009). The purpose of GNSS observations is

therefore the realization of a stable reference frame for further terrestrial observations in all measurement campaigns.

Another possibility of controlling the reference frame is to use precise classical terrestrial method; however, in this case the reference points must be checked for their quality and stability according to one of the methods mentioned in Chrzanowski (2006), with further consideration of field work recommendations from section 2.3. If classical terrestrial method is used in this step, it is important that there are enough reliable orientation points in the line of sight.

In general, this part of the workflow is one of most elusive ones to be performed in the long-term perspective, depending particularly on the site characteristics. The establishment of a stable reference frame with sufficient accuracy is absolutely essential and has to be done prior to scanning the objects under inspection. If possible, the reference points have to be located on geologically stable ground and stabilized by a firm construction (concrete pillars) allowing forced centering of instruments and reflectors to avoid the occurrence of centering errors.

2.3 Geodetic network formation

The reference frame is linked with the TLS measurements (i.e., point clouds) on the basis of the reference points forming the geodetic network. Therefore, this network must include the reference points, scanner target positions and control points as well. The control points can be utilized for comparison with the TLS results or may also support the determination of the representative points described in section 2.8.2.

It is important to design a high quality network with appropriate configuration near the object of the study to be used for an accurate absolute orientation of adjacent point clouds. In high precision surveying, this task is commonly a domain of precise classical terrestrial method. For the estimation of high precision coordinates of network points in a least squares adjustment (LSA), the classical terrestrial measurements are usually performed in several sets of angles, measuring horizontal and vertical angles and slope distances. Many precise electronic tacheometers provide the ATR (Automatic Target Recognition) functionality which can be used to minimize the observer-related errors and to speed up the measurement process. This way a high measurement redundancy can be achieved in order to assure the quality and stability of coordinate estimation. However, if ATR is applied, the standard deviations of raw measurements have to be examined to exclude the presence of gross errors which may occur due to the automatic measurement process (e.g., in the case when two reflectors are located almost in line).

Moreover, the measured slope distances have to be corrected properly for all errors which may systematically affect the measured quantities. The purpose of these corrections is to estimate the unknown coordinates of network points only on the basis of measurements affected by random errors. In order to perform these corrections, the atmospheric conditions have to be taken into account. A detailed description of slope distance corrections can be found in the literature, e.g., in Joeckel

(1989) or Kogoj (2005).

Finally, to estimate the positions of network points with high precision, precise reflectors with known submillimeter additive constants have to be employed during the measurement process. By doing so, the coordinate precision can reach up to few tenths of a millimeter for typical network sizes big enough to be designed in the vicinity of most (even larger) structures under inspection. This high coordinate estimation may not be achieved when performing the classical terrestrial observations directly on the scanner targets. Therefore, the position of a target in the geodetic network should be determined indirectly by estimating the position of a prism center in the first stage and applying the mounting offset between both reflectors in the next one. Levelling the reflectors will reduce this offset to a vertical component only, which can also be estimated with submillimeter accuracy. Hence, the precision level of coordinate estimation based on classical terrestrial measurements will provide a well-defined and qualitative frame for target based point cloud positioning, a level challenging to achieve when estimating the position of targets with the TLS.

2.4 Target scanning and extraction

When considering the suitability of a particular target type for high precision positioning tasks, there are three basic conditions that need to be accounted for:

- targets must have stable and rigid mechanical design;
- their size and shape should correspond to the maximum distance from the scanner, thus minimizing systematic errors due to the increase in laser spot size and assuring a high density sampling of their surface;
- they have to be well-defined to enable the extraction and modelling from the TLS measurements.

With respect to these rather self-evident requirements, the number of appropriate and commercially available target types can quickly be reduced to merely few. Besides the conditions mentioned, the quality of end results of the target extraction and modelling process at each scanner station, i.e., estimated positions of target centers, may be further influenced especially by systematic errors coming from both the scanner and target surface material response. Experimental results, such as those presented in the paper by Pesci and Teza (2008), have revealed the presence of large systematic range errors when scanning retroreflective target surfaces. Following their conclusions, it becomes evident that in most cases a precise target based positioning can be only achieved after modelling the systematic errors based on carefully designed calibration tests, such as those presented in section 3.1. However, exceptions may be found with certain manufacturers offering special target scanning modes or adjusting the laser pulse power to a particular target type, hence they minimize the range errors significantly. Eventually, part of systematic errors arising from the instantaneous atmospheric conditions should always be taken under consideration if necessary.

Among the appropriate target types, flat and spherical targets are particularly widely used in geodetic engineering applications where higher accuracy is needed (Figure 2). An advantage of spherical

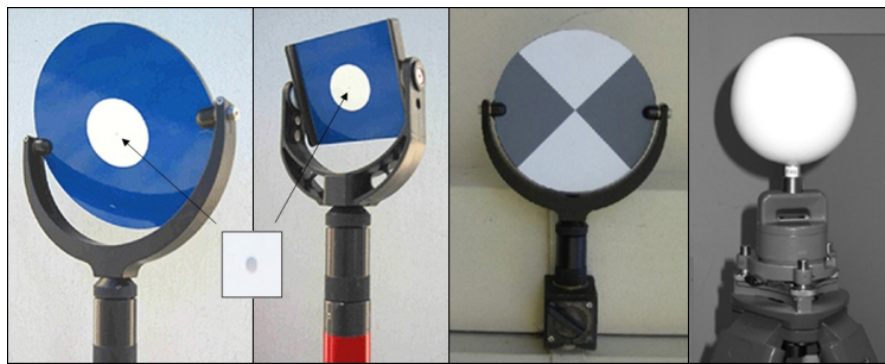


Figure 2: TLS targets. The first three from left are flat targets provided by Leica Geosystems (2011). The spherical target representing the alternative type is provided by Laserscanning Europe (2011).

targets is on the one hand their independance of accurate center determination from the incidence angle of the beam, provided that there are no systematic deviations of shape involved. On the other side, only a small fraction of their surface is usually useful for the computation of the center point, especially when placed up to 100 m away from the scanner where the laser spot diameter may increase to few centimeters. In this case the points closer to the sphere's edges should be weighted according to the incidence angle appropriately or should be possiblly even excluded from the computation. Furthermore, the precision of the best-fitting sphere center coordinates may be influenced by very noisy laser beam returns resulting in biases of up to 5 mm as found by Kersten et al (2004). Finally, the manufacturing of spherical targets with very low systematic errors in shape (below the order of millimeters if possible) can be very expensive and their handling difficult if their size becomes too big.

For the reasons stated and for meeting the above three conditions to the highest degree, flat target type was selected for extraction and modelling. This target type was also studied in detail during the calibration tests and finally used in the two outdoor experiments (see Chapter 3).

2.4.1 Flat targets

Contrary to spheres, flat target center extraction algorithms all take into account also the radiometric information of the returning pulses that most scanners store beside polar coordinates. The signal strength at the receiver, referred to as amplitude (A), provides vital information on the position of the center within the target plane. The model for the center estimation is target dependent since targets can have different configurations of high and low reflectivity regions. With two degrees of freedom for rotation, these targets have to be oriented towards the scanner at every new instrument station. In the thesis, the leftmost flat target in Figure 2 has been chosen for modelling, described in the rest of

this section. Table 1 gives their dimensions and scattering characteristics. According to Reshetuyk

Table 1: Circular flat target characteristics. R_A is the coefficient of retroreflection as defined by Austin and Schultz (2006). Blue and silver materials are a spherical type of retroreflectors.

Material Type	Diameter [mm]	R_A	Note
Blue	152.4	10	Material used for street sign backgrounds.
White	50.8	/	No retroreflective properties.
Silver	2	75	Material used for street sign letters.

(2009) most center computation algorithms involving flat targets are based on the assumption that the maximum amplitude will be recorded in the target center. For the one, used in the thesis, this fact is even embedded in the target design with the high reflectivity silver spot in the middle of the target surrounded by the low reflective white background. Following this approach, the coordinates of the target center are simply determined as the amplitude weighted mean $x_c = \sum_{i=1}^n A_i \cdot x_i / \sum_{i=1}^n A_i$. Here $x_c \in \mathbb{R}^3$ are the coordinates of the target center, $x_i \in \mathbb{R}^3$ are the coordinates of the i -th laser point, and A_i their corresponding amplitudes. Depending on the implementation, this weighted mean can be computed from all points falling onto the target or just a subset consisting of points with the highest amplitude values.

A closer inspection reveals that there are some drawbacks when estimating the target center based on the amplitude weighted mean approach because of the small size of the silver spot. The estimation may become very unstable or even impossible if the target distance starts to exceed 40 m, since this 2 mm spot is getting invisible in its center due to the increase in the laser spot diameter. In practice, short target distance is inversely proportional with the number of geodetic network points causing more time and resources to be used for the positioning of point clouds when larger objects are involved in the monitoring process. Furthermore, even at distances lower than 40 m the silver dot's diameter is much smaller than the usual laser spot size, resulting in the possible systematic shifts of the center coordinates depending particularly on the irregularities in the scanning pattern and how the returning echoes, reflected from both high and low reflectivity regions, are processed at the receiver side.

In order to overcome these limitations and to extend the operational distance beyond the range of the silver spot's "visibility" an *ad hoc* center estimation model can be considered and was designed for the purpose of the thesis. This approach aims at modelling the transition zone between the retroreflective blue and non-retroreflective white material to estimate the position of the center within the target plane. Compared to the size of the silver spot, the diameter of the zone is much bigger, which makes it possible to extend the maximum target distance significantly, even beyond 100 m. The final target center determination is therefore split into two steps, with the first being the target plane estimation followed by the estimation of the center position within this plane. To be able to estimate the target plane in the first step, additional two stages should be performed beforehand:

- extraction of the target measurements from the background;

- estimation of the initial target center position.

Automatic extraction of the target points from the background can be achieved on the basis of the amplitude histogram analysis and the retroreflective character of the target surface (blue material type). Once only target measurements are left, the initial center coordinates in the range image (consisting of polar TLS measurements φ_i , θ_i and D_i) can be obtained by simple cross correlation matching approach (Schenk, 1999) employing a generic target model. The initial center coordinates are in most cases a good enough approximation to select the appropriate subset of points $T_i = (x_i, y_i, z_i)^T$ which are to be used for the least squares adjustment of the estimated position and orientation of the target plane. Choosing the points within a certain homogeneous region of the target is important to avoid the edges and transitions between different material types as the laser spot gets bigger and could be reflected from more than one surface at the same time. In the least squares adjustment, the position of the estimated target plane is determined by the centroid of points $T_c = \frac{1}{n} (\sum_{i=1}^n x_i, \sum_{i=1}^n y_i, \sum_{i=1}^n z_i)^T$ and the orientation by the normal vector $\vec{n} = (n_x, n_y, n_z)^T$ corresponding to the smallest eigenvalue of the normal matrix $N = \sum_{i=1}^n T'_i \cdot T_i'^T$ where $T'_i = T_i - T_c$. In this way, the orthogonal distances of points from the estimated plane are minimized with the error vector $v_i = \vec{n} \cdot (T_i - T_c)$ providing the information on the quality of the adjustment. Before moving to the second step, the target plane coordinate system finally needs to be established and the target points transformed into the orthogonal view to compensate deviations in orthogonality (i.e., orientation of the target plane towards the scanner).

In the second step, the position of the center within the pre-determined target plane has to be estimated in the second LSA procedure whereby inevitably taking into account also the detected signal amplitudes in order to avoid singularity. When constructing the mathematical model for this step, it is desirable for the model to be defined by a small number of parameters and still being sufficiently adaptable to the growing laser spot diameter. The model proposed herein that is able to account for these requirements has the form:

$$f(x_p, y_p) = A = \frac{1}{1 + \left(a \cdot \sqrt{(x_p - x_0)^2 + (y_p - y_0)^2} \right)^b} \quad (1)$$

where x_p and y_p are the planar coordinates of points. The unknowns x_0 and y_0 represent the estimated planar coordinates of the position of the center and a and b the unknowns determining the shape of the model function. This model function can exploit the fact that the amplitude increases from the white to the blue material type resulting in a *bowl-like* shape that can be seen in Figure 3. The model from equation 1 may be seen as an extension of the weight function that was first proposed by Kraus and Pfeifer (1998) but has been used here for a completely different purpose. The unknowns (x_0, y_0, a, b) have to be computed iteratively with the initial values coming from the image matching and known radius of the white material type. Clearly the function is symmetric with respect to the target plane normal, hence the points have to be transformed into the orthogonal

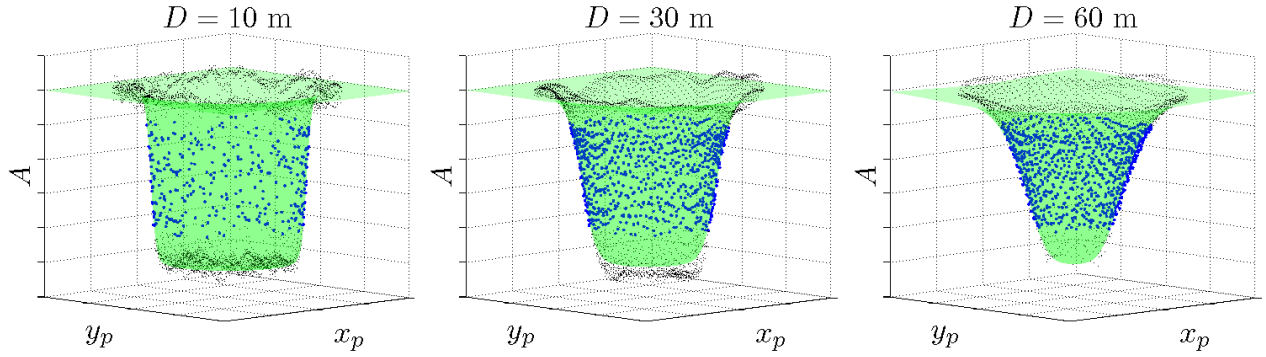


Figure 3: Examples of model fitting. The blurring of the transition zone between the blue and white material type is due to the increasing laser spot diameter as the distance (D) increases. The amplitude values are normalized between [0,1].

projection in the first place to avoid skewness of the transition zone. In conclusion, the estimation of the center within the target plane should be done on the basis of only those points which are lying close to the edge between the white and blue material where the amplitude drops. They are the most relevant in this step therefore the center estimation process needs to be confined to a chosen amplitude interval. In Figure 3 these points are shown in blue with the amplitude interval ranging from 0.2 to 0.8.

If the center point is estimated according to equation 1, the error vector is unitless since the vertical distances of points from the model function are those that are minimized in the LSA. This fact may be problematic when estimating the stochastic properties of model parameters x_0 and y_0 which are in metric units. An alternative option is to minimize the horizontal distances of points instead, which requires equation 1 to be rearranged:

$$\sqrt{(x_p - x_0)^2 + (y_p - y_0)^2} - \sqrt[b]{\frac{\frac{1}{A} - 1}{a}} = 0 \quad (2)$$

Again, in equation 2 the same unknowns are estimated as before, this time resulting in the error vector which is easier to interpret for being in metric units. The choice of the minimization function (equation 1 or equation 2) is expected to have very little effect on the estimated values of model parameters, a fact proved by the experimental results. The two step nature of this particular center extraction algorithm reveals an important implication. The precision measures (standard deviations) of coordinates in the target plane x_0 and y_0 can be up to ten times higher than the standard deviation of the plane fitting in the first step due to the noise produced by the rangefinder. As the laser spot gets bigger, more and more points find their way into the transition zone provided that the point density does not change with distance (see Figure 3). Consequently, from the point of view of the target design it is important that the white circular material type is as round as possible and no eccentricity is present. The latter condition must hold even when estimating the target center

according to the initially presented approach (amplitude weighted mean). Only then will the center estimation process be free of biases.

2.5 Positioning of scan data within the reference frame

After the establishment of geodetic network by means of precise classical terrestrial method and extraction of target centers at each scanner station, the transformation parameters can be estimated to be able to position the point clouds of objects under inspection within the reference frame. Provided the high accuracy of extracted target centers (from the high density point clouds of individual targets) can be assured, this point based positioning approach is to be preferred to other positioning methods (e.g., feature based or iterative closest point, see Vosselman and Mass, 2010) for it offers the possibility to derive the exact and direct correspondences between the extracted target centers and network points (Figure 4). Not using the targets in many deformation monitoring applications,

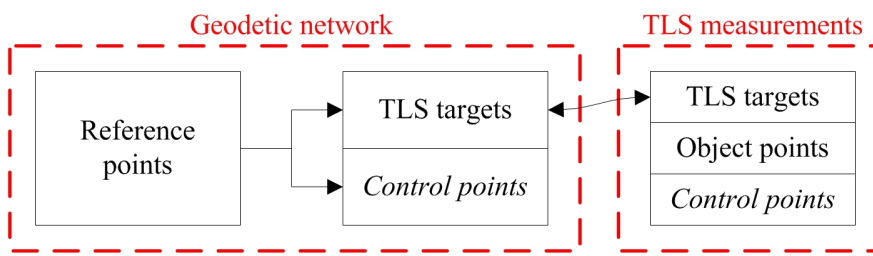


Figure 4: TLS measurement positioning diagram. Targets represent the link between point clouds and the reference frame. Control points can be used for displacement comparison or may support the determination of representative points, described in section 2.8.2.

the derivation of correspondences from multi-temporal scan data, whether point or feature based, may be hard to derive with sufficient accuracy as well as decide which objects (or parts of objects) in the scene have remained unaffected if these are to be treated as a reference. Since precise positioning of point clouds within the reference frame is one of very important steps especially when approaching the deformation evaluation in the millimeter domain, the use of targets may become unavoidable.

Another popular method, though inferior to target based positioning is the so-called *direct georeferencing* described in detail by Reshetyuk (2009). The method is based on stationing the scanner over a known point, levelling and orientating it to at least one other point with known coordinates in the reference frame. Conceptually this is how measurements are positioned in the traditional surveying. However, for the precise positioning of point clouds direct georeferencing is less appropriate because it introduces additional instrumental errors, such as centering and levelling errors which may be much larger compared to precise tacheometers even with scanners that use inclination sensors which are typically not accurate enough.

Focusing now on the target based approach, two sets of points denoted herein by $X_i, Y_i \in \Re^3$ and

referring to the identical physical entity but different coordinate system can be connected by estimating the spatial 7-parametric Helmert transformation in a LSA, minimizing the sum of squares of coordinate differences:

$$\sum_{i=1}^n \|v_i\|^2 = \sum_{i=1}^n \|Y_i - sR(X_i) - t\|^2 \quad (3)$$

where R is the rotation matrix, t the translation vector and s the scale factor. These unknowns can be estimated on the basis of three or more point pairs. If this is done in the scanner-to-scanner station relation, the process is called *relative orientation*. In case one set of points has its position in the pre-defined reference frame it is called *absolute* or *exterior orientation*.

Translation

To minimize the sum of squares of errors in equation 3 it is useful to first refer all points X_i and Y_i to their centroids $X_c = \frac{1}{n} \sum_{i=1}^n X_i$ and $Y_c = \frac{1}{n} \sum_{i=1}^n Y_i$:

$$X'_i = X_i - X_c \quad Y'_i = Y_i - Y_c \quad (4)$$

Now equation 3 can be rewritten using equation 4 to produce:

$$\sum_{i=1}^n \|Y'_i - sR(X'_i) - t'\|^2$$

or:

$$\sum_{i=1}^n \|Y'_i - sR(X'_i)\|^2 - 2t' \cdot \sum_{i=1}^n [Y'_i - sR(X'_i)] + n \|t'\|^2 \quad (5)$$

where $t' = t - Y_c + sR(X_c)$. By examining equation 5, it becomes evident that the sum in the second term is zero since the points are referred to their centroids (note that $\sum_{i=1}^n X'_i = 0$ and $\sum_{i=1}^n Y'_i = 0$). Moreover, the first term does not depend on t' and the last cannot be negative. Hence, the sum in equation 5 is minimized when $t' = 0$, so the estimated translation vector represents only the difference of the first and the scaled and rotated second centroid:

$$t = Y_c - sR(X_c) \quad (6)$$

According to Horn (1987), estimating the translation by using all points is to be preferred to one where only one or few selected points are used provided that all are comparable in precision and accuracy. Before the translation vector could be obtained, the scale and the rotation have to be estimated.

Estimating the scale

After the introduction of centroids and finding the translation vector, the total error to be minimized following equation 5 becomes:

$$\sum_{i=1}^n \left\| Y'_i - sR(X'_i) \right\|^2 \quad (7)$$

Expanding equation 7 and taking into account the fact that rotation is a linear transformation preserving lengths, i.e., $\|R(X'_i)\|^2 = \|X'_i\|^2$, we get:

$$\sum_{i=1}^n \left\| Y'_i \right\|^2 - 2s \sum_{i=1}^n Y'_i \cdot R(X'_i) + s^2 \sum_{i=1}^n \left\| X'_i \right\|^2 \quad (8)$$

or in short:

$$s^2 S_X - 2sD + S_Y \quad (9)$$

where $S_X = \sum_{i=1}^n \|X'_i\|^2$, $S_Y = \sum_{i=1}^n \|Y'_i\|^2$ and $D = \sum_{i=1}^n Y'_i \cdot R(X'_i)$. Completing the square in s in equation 9 leads to:

$$\left(s\sqrt{S_X} - \frac{D}{\sqrt{S_X}} \right)^2 + \frac{(S_Y S_X - D^2)}{S_X} \quad (10)$$

With respect to the scale, this is obviously minimized when the term in the brackets is zero, that is $s = \frac{D}{S_X}$ or:

$$s = \frac{\sum_{i=1}^n Y'_i \cdot R(X'_i)}{\sum_{i=1}^n \|X'_i\|^2} \quad (11)$$

In general this asymmetrical scale factor from equation 11 is direction dependent. If the transformation is done in the inverse direction, that is $X_i = \tilde{s}\tilde{R}(Y_i) + \tilde{t}$, it is not likely to expect that $\tilde{s} = \frac{1}{s}$, $\tilde{t} = -\frac{1}{s}R^{-1}(t)$ and $\tilde{R} = R^{-1}$. Instead we get:

$$\tilde{s} = \frac{\sum_{i=1}^n X'_i \cdot \tilde{R}(Y'_i)}{\sum_{i=1}^n \|Y'_i\|^2} \quad (12)$$

Again, referring to Horn (1987), one of the two scale factors from equations 11 and 12 may be more appropriate when the coordinates in one of the two systems are known with much greater precision than those in the other. This may be taken under consideration in the case of the absolute orientation with the well-defined and very precise classical terrestrial coordinate estimation. On the other hand, if the quality of coordinate estimation in both point sets is similar, using symmetry in scale is more reasonable (e.g., relative orientation). In this case equation 7 has to be slightly modified:

$$\sum_{i=1}^n \left\| \frac{1}{\sqrt{s}} Y'_i - \sqrt{s}R(X'_i) \right\|^2 \quad (13)$$

Finally, a similar rearrangement of equation 13 to that of equation 7 shows that the minimization with respect to the scale s (only this time symmetric) results in:

$$s = \sqrt{\frac{\sum_{i=1}^n \|Y'_i\|^2}{\sum_{i=1}^n \|X'_i\|^2}} \quad (14)$$

The advantage of this symmetrical case is that the scale can be determined without the need to estimate the rotation beforehand. However, in each case the estimation of rotation is independent of the choice of scale and the remaining error is minimized when D is as large as possible.

Finding the rotation using unit quaternions

Compared to the more familiar matrices, the representation of rotations with Hamilton's unit quaternions has a number of advantages. For example, it is much simpler to enforce the constraint that a quaternion has a unit magnitude than it is to ensure that a rotation matrix is orthonormal (Horn, 1987). Furthermore, quaternions are simple to compose, they are numerically more stable and avoid the problem of gimbal lock. A unit quaternion representing a rotation by angle θ around an axis $\vec{u} = (u_x, u_y, u_z)^T$, where $\|\vec{u}\| = 1$ is:

$$\dot{q} = \cos\left(\frac{\theta}{2}\right) + \sin\left(\frac{\theta}{2}\right)(iu_x + ju_y + ku_z) = \cos\left(\frac{\theta}{2}\right) + \sin\left(\frac{\theta}{2}\right)\vec{u} \quad (15)$$

In the quaternion notation, a point in space can be represented by a pure imaginary quaternion $\dot{r} = 0 + \vec{r}$ and its position after rotation using equation 15 in the form:

$$\dot{r}' = \dot{q}\dot{r}\dot{q}^* = \left[\cos\left(\frac{\theta}{2}\right) + \sin\left(\frac{\theta}{2}\right)\vec{u} \right] \vec{r} \left[\cos\left(\frac{\theta}{2}\right) - \sin\left(\frac{\theta}{2}\right)\vec{u} \right] \quad (16)$$

where \dot{q}^* is the conjugate of a quaternion obtained by negating the imaginary part in \dot{q} . Expanding equation 16 leads to the Rodrigues' rotation formula which is exactly what a rotation using angle-axis representation is.

Returning back to the problem of estimating the rotation, knowing that D has to be as large as possible in order to achieve the final minimization in equations 7 or 13, a unit quaternion maximizing:

$$\sum_{i=1}^n (\dot{q}\dot{r}_{X'_i}\dot{q}^*) \cdot \dot{r}_{Y'_i} \quad (17)$$

has to be found. Instead of X'_i and Y'_i , in equation 17 the quaternion notation is used, i.e., $\dot{r}_{X'_i}$ and $\dot{r}_{Y'_i}$. Based on the laws of quaternion arithmetic, Horn (1987) has proved that solving equation 17 is about finding the eigenvector corresponding to the most positive eigenvalue of a symmetrical $4 \times$

4 matrix:

$$N = \begin{bmatrix} S_{xx} + S_{yy} + S_{zz} & S_{yz} - S_{zy} & S_{zx} - S_{xz} & S_{xy} - S_{yx} \\ S_{yz} - S_{zy} & S_{xx} - S_{yy} - S_{zz} & S_{xy} + S_{yx} & S_{zx} + S_{xz} \\ S_{zx} - S_{xz} & S_{xy} + S_{yx} & -S_{xx} + S_{yy} - S_{zz} & S_{yz} + S_{zy} \\ S_{xy} - S_{yx} & S_{zx} + S_{xz} & S_{yz} + S_{zy} & -S_{xx} - S_{yy} + S_{zz} \end{bmatrix} \quad (18)$$

where $S_{xx} = \sum_{i=1}^n x'_{X_i} x'_{Y_i}$, $S_{xy} = \sum_{i=1}^n x'_{X_i} y'_{Y_i}$ and so on are sums of products of coordinate components in both systems that have been reduced to their centroids beforehand. The sought-after eigenvector is the unit quaternion $\dot{q} = q_0 + q_x + q_y + q_z$ representing the estimated rotation. Once this quaternion is determined, the computation of the corresponding 3 x 3 rotation matrix is straightforward:

$$R = \begin{bmatrix} q_0^2 + q_x^2 - q_y^2 - q_z^2 & 2(q_x q_y - q_0 q_z) & 2(q_x q_z + q_0 q_y) \\ 2(q_x q_y + q_0 q_z) & q_0^2 - q_x^2 + q_y^2 - q_z^2 & 2(q_y q_z - q_0 q_x) \\ 2(q_x q_z - q_0 q_y) & 2(q_y q_z + q_0 q_x) & q_0^2 - q_x^2 - q_y^2 + q_z^2 \end{bmatrix} \quad (19)$$

For the above presented approach of estimating the transformation no approximate values are needed. The unknowns are determined in a one-step procedure incorporating all the points X_i and Y_i and providing the best rigid body transformation between two coordinate systems given coordinates of a set of points are not collinear. The robustness of this method is an important advantage compared to the one where rotation is estimated using orthonormal matrices (Horn, 1988). If needed weights can also be introduced in the process to account for the inhomogeneous precision of X_i and Y_i (see Horn, 1988).

After estimating the transformation parameters these have to be applied to the point clouds that are the result of scanning the object under inspection. Besides the error vector (equation 3) or the a posteriori standard deviation σ_{AO} (σ_{RO})¹ providing one measure of the quality of transformation the overlapping areas should be examined to see if points acquired at different scanner stations coincide to a required degree. The transformed point locations will be influenced not only by the quality of coordinate estimation coming from both classical terrestrial and scanner measurements but also on the configuration of targets at each scanner station. Moreover, target and object distance from the scanner should be comparable otherwise small discrepancies between point sets X_i and Y_i after applying the transformation may produce large point cloud offsets at the object side. Prior to taking measurements in the field, the study of effects of a particular network configuration on the transformed point locations is possible, for example by using simulations during which each point is assigned a randomly generated noise. The results of such simulations may provide information on sensitivity of the transformed point locations with respect to all influencing factors.

¹AO – absolute orientation, RO – relative orientation

2.6 Object scanning

Scanning can be considered a geodetic technique that does not enable any measurement redundancy at the level of individual points due to its fully automated measurement process. This somewhat limits the use of its direct measurements (polar or cartesian coordinates) in the evaluation of displacements and deformations since their variance-covariance matrices are difficult to estimate (having only instrumental standard deviations at disposal). On the other hand, the measurement redundancy is significantly large if surfaces are considered indirect observables, making them a more convenient tool for possible change detection. Like in any measurement process, the quality of these observables is regulated by measurement errors, which have systematically been described by authors such as Reshetnyuk (2009). In TOF (pulsed) TLS, the observables are particularly influenced by distance related errors which are the outcome of physical limitations of reflectorless measurement process. To understand their effect, these limitations will be described in the next subsection. In addition, the quality of observables also depends on the scanning geometry, which will be discussed separately in the second subsection.

2.6.1 Physical limitations

The physical limitations of pulsed laser ranging are determined by a modified radar range equation that may be found in slightly different expressions in the literature with most of them derived from the work of Jelalian (1992). Wagner (2007) presented his version in the following form:

$$P_r = \frac{P_0 \cdot d_a^2}{(2D)^2} \cdot \rho \cdot \cos(\alpha) \cdot \eta_{ATM} \cdot \eta_{SYS} \quad (20)$$

with P_0 being the transmitted and P_r the detected (received) laser pulse power at distance D . d_a represents the receiver aperture diameter, ρ the reflectivity coefficient and α the incidence angle². The atmospheric and system transmission factors, η_{ATM} and η_{SYS} account for the losses of the pulse propagation through the atmosphere and the transmitter-receiver optics. The $1/D^2$ decay of P_r can only be expected if the whole area of the laser spot is reflected from the object's surface, otherwise higher orders of D have to be considered. Moreover, as demonstrated by, e.g., Riegl and Bernhard (1974), this power-distance dependency is further influenced by the configuration of laser emitter and receiver. Finally, in equation 20 it is assumed that the reflected laser light intensity (i.e., power density) decreases according to the Lambertian law, $I(\alpha) = I_0 \cos(\alpha)$, which only applies for an ideal diffuse reflection (scatterer) with the intensity being direction independent. Despite the fact that most anthropogenic surfaces can be considered rough for typical laser light wavelengths of commercial scanners (with λ in visible or near IR domain), this theoretical reflection model is more

²The incidence angle is the angle between the direction of the incoming laser beam and the surface normal.

likely to be replaced by more complex ones, e.g., Minnaert or Henyey-Greenstein found in Rees (2001).

If small scale displacements and deformations are to be estimated with sufficient precision it is important for the scanning to be performed with considerations based on equation 20 in the first place. The received optical power P_r is processed (discretized in the case of fully digital systems) inside the receiver and the pulse travel time and amplitude estimated. A simple demonstration of this process is shown in Figure 5 where the latter two parameters were estimated on the basis of LSA using a Gaussian pulse model. Clearly, the object distance along with the receiver's and

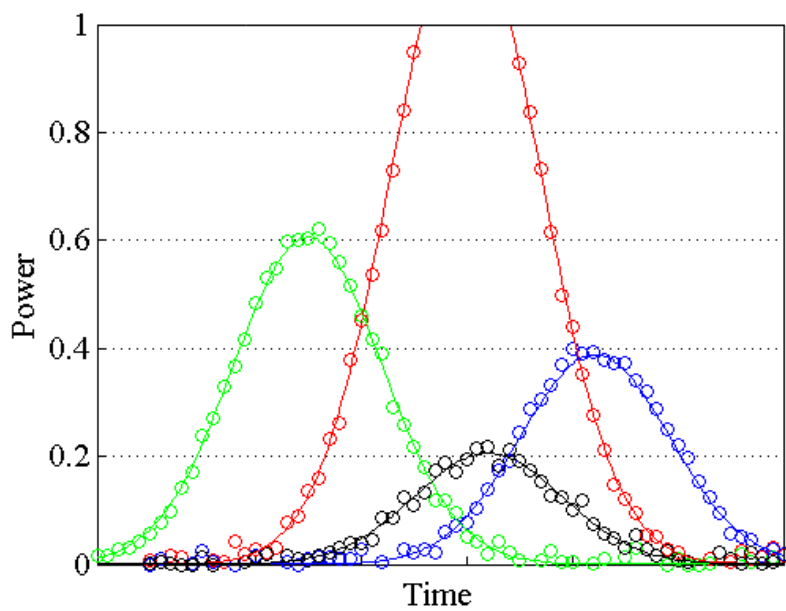


Figure 5: Time and amplitude estimation. In TOF systems a pulse is never a true Dirac delta function, that is why using a Gaussian model has proved to be more realistic and widely utilized (Wagner et al, 2006). The dots represent the discrete waveform with the interval $[0,1]$ corresponding to the dynamic range of the receiver.

signal processing unit's characteristics become important factors that not only affect the quality of estimating the observables (surfaces) but also limit the use of this technology when the object's reflectivity is too low or the loss of energy due to propagation through the atmosphere or device itself is large enough. Moreover, the incidence angle and the light scattering properties of materials (depending on the color, chemical composition, surface roughness, etc.) also determine the amount and direction of energy distribution on the object side resulting in further limitations in quality and reliability of distance estimation. Some of the systematic distance errors, such as atmospheric corrections, can be applied in a similar way as in the case of classical terrestrial measurements and must always be considered if their effects become significant. As for the errors which are regulated by surface material properties, their effects on the distance precision and the level of the instrument's detectivity can be tested experimentally (see section 3.2).

All the interrelated functional parameters make the quality of surface estimation more influenced

by distance than angular systematic errors. Even if pulses are not transmitted at perfectly equal angular intervals, the irregularities in the resulting range image are only device dependent and do not alter the amount of detail being captured. Hence, the dense sampling pattern that nowadays systems are able to provide with small angular increments between consecutive laser pulses can be used for precise surface estimation despite the ever-present sampling irregularities. This means that apart from understanding the physical limitations of reflectorless laser ranging given by equation 20, it is also relevant to consider how the scanner is stationed with respect to the object in order to assure the sufficient object coverage, i.e., point density.

2.6.2 Scanning geometry

If point density is to be sufficient, not only the predefined scan parameters (angular resolution) but also the scanning geometry, i.e., the incidence angle and distance to the object should be examined (Figure 6). The selection of these parameters has a direct influence on the quality of the point clouds

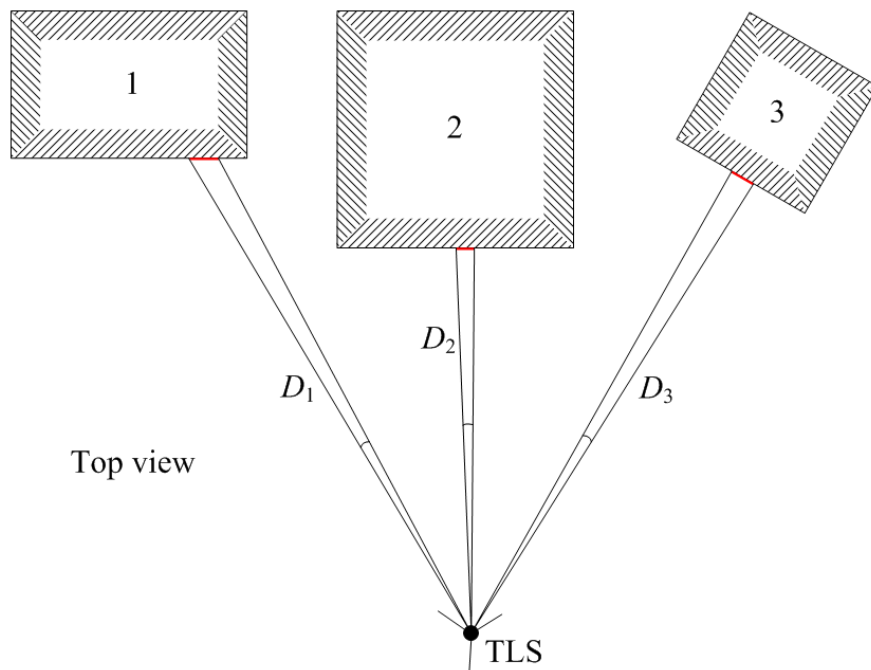


Figure 6: Impacts on point density. Although $D_1 \approx D_3$ the larger incidence angles at object 1 lead to wider spacing between individual points.

with the aim of assuring a comparatively homogeneous distribution of points on the whole object's surface. The rate in which density is decreasing can be quite fast in the case of scanning larger objects from a close distance, for example roads, tunnels or long walls. Particularly in these short proximities, Soudarissanane et al (2008) have concluded that by simply moving the scanner for two meters the point cloud quality can be improved by around 25 %. The effects of the object surface orientation on the quality of the measurements have also been studied in, e.g., Soudarissanane et al (2007).

Moreover, the object coverage also depends on the selection of instrument (scanner) stations since it is usually not possible to capture the entire structure from one station only due to occlusions made by the surface features or other obstacles in the line of sight. The remaining gaps are to be filled by points coming from adjacent stations after the individual point clouds have been positioned in one common reference coordinate system. In the areas where the neighboring point clouds overlap, the higher point density can provide information on the quality of the absolute (relative) orientation of scan data which is closely connected with the proper configuration of scanner targets in the geodetic network. The size and complexity of the object determine the number of scanner stations needed to produce the final object image with small variations in range and incidence angle between individual points. Some of today's high-end scanners are able to perform the acquisition process using angular increments lower than 1 arcsec, thus assuring millimeter point spacing in both directions through their full range of operation (Leica, 2011). Such high sampling capabilities lead to large local data redundancies and to a significant reduction of field work in general.

2.7 Modelling the object shape

The intrinsic character of TLS can be thoroughly exploited in the phase of reconstructing the object shape, the process typically referred to as modelling. Surface models can therefore be treated as abstract mathematical constructs imitating the actual object's geometry. The high data redundancy available may lead to a much higher precision of the estimated model parameters compared to the relatively low precision of the single point coordinates, a characteristic which became one of the trademarks of TLS. Compared to more arbitrary shapes of natural structures with possible high complexity in detail, the man-made objects are in general much simpler in this respect but with a well-defined and solid surface. To be able to approach the problem of estimating the displacements and deformations in the millimeter domain only these type of structures are suitable and can be used for further examination (Figure 7). There are a number of ways in which surfaces of anthropogenic

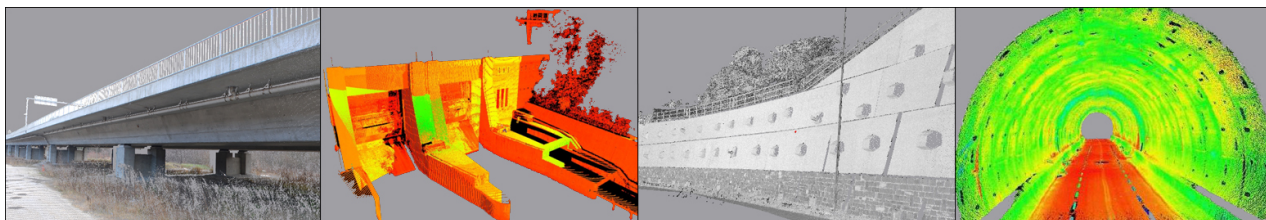


Figure 7: Anthropogenic structures captured by TLS and shown in the form of point clouds.

structures can be represented, ranging from geometric primitives, such as planes, cylinders, cones or spheres, to more complex ones, such as parametric patches and NURBS (Non Uniform Rational Basis Spline), which may be more convenient in the case of more complex objects with more surface features. The selection of the appropriate mathematical descriptor very much depends on the object

itself; however, the object model should resemble the actual shape to a required degree. In many cases the man-made objects can be modelled with geometric primitives only, whereby taking into account that the resemblance between the actual and modelled shape should not get violated. Before deciding what model to use, the points not belonging to the object in question have to be filtered out. The same process should also be applied to detect the presence of the so called mixed pixels (Reshetnyuk, 2009). These points are the outcome of a systematic effect of laser spot being split near the edges and reflected from several objects which are less than half the pulse width apart. For a 5 ns pulse this distance has to be larger than 0.75 m if a correct position is to be determined.

2.7.1 Planarity based segmentation

To have more control over the quality of modelling and to include all specific object features it is sometimes useful to split the original point clouds of larger objects with no single model description into smaller segments according to coordinate axes. The size of the segment may depend on the point density and the type of a descriptor. The smaller the size of the patch, the more likely the shape could be approximated by simplest primitives such as planes (or eventually tangential planes). Using a linear model is beneficial for its simplicity and if proved to be unacceptable in the initial patch size, this can be subdivided into smaller ones. A huge redundancy of points which is typically at disposal makes it possible to reduce the size of the patch to few centimeters if needed.

Another convenient way to find the planar regions in the point cloud is to employ segmentation algorithms described in detail by Hoover et al (1996) and tested particularly with airborne laser scanning data for the detection and modelling of various structures (e.g., Rottensteiner, 2003). All segmentation approaches are aimed at subdividing the unstructured point clouds into separate regions using different geometric criteria. Assuming planar regions exist, the process starts by choosing one of the points to represent a seed for which a normal vector (reference direction) is estimated on the basis of neighboring points. If any other point belongs to this seed plane it has to lie close enough and its normal vector has to coincide with the seed's to a preset angular threshold. Each time a new point is added to the plane, the reference direction is recalculated using all plane points. To avoid under segmentation the resulting region has to contain a big enough number of points. The results of this segmentation approach are shown in Figure 8. Compared to the way of simply splitting the original point cloud into equal segments, the surface growing segmentation algorithm from Figure 8 provides the possibility of controlling the planarity of points already during the classification process by choosing the appropriate input parameters. The parameters are a function of the instrumental errors (distance precision and accuracy), the point density and the boundary of what is tolerated as being flat enough. The surface growing algorithm is also able to detect and avoid the presence of mixed pixels or other points considered outliers and therefore do not belong to any planar region.

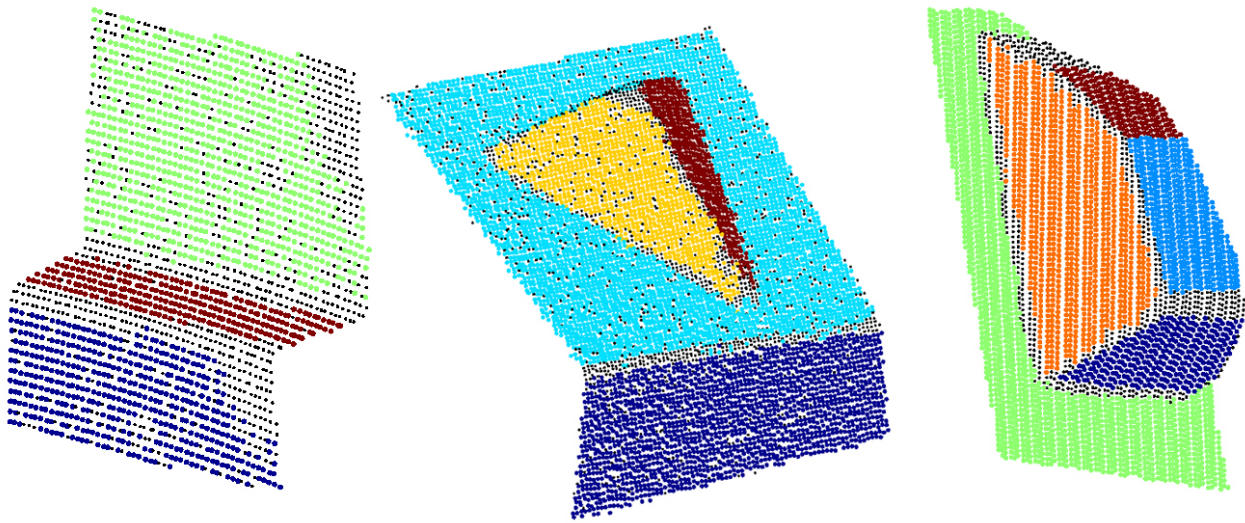


Figure 8: Segmentation results. Black points represent outliers, edges and mixed pixels and therefore do not belong to any planar region.

2.7.2 Model validity and parameter estimation

Before deformations and displacements can finally be evaluated, the validity of the model has to be tested for any underlying systematic errors in the shape description. The modelling adjustment results, i.e., the error vector (residuals) contain the discrepancies between the actual and the idealized object shape. A close study of the spatial distribution of residuals is necessary to estimate these biases. In some cases the residual pattern analysis can be approached within model related coordinate systems (such as cylinders or planes) with the examination not only based on visual inspection but also employing numerical statistics, e.g., autocorrelation (Chatfield, 1995). One important aspect to be considered when analyzing the residual pattern of scan data captured at consecutive time intervals is that they can reveal if the object has been subjected to deformations. If not, the residual patterns have to remain unchanged.

During the adjustment process a proper stochastic model has to be chosen in order to estimate the variance-covariance matrices Σ_{xx} of model parameters in the right way. The incorrect stochastic properties of observations usually have little effect on the estimated parameters but can alter their precision measures significantly. In the computation of Σ_{xx} , the a priori (reference) variance σ_0^2 is typically replaced by the a posteriori value $\hat{\sigma}_0^2$ since the first is not well known and the second being estimated from the available high redundant scan data. In the process of modelling, if needed, the individual points can also be assigned weights according to the distance ($p_{D_i} = 1/D_i^2$) and the incidence angle ($p_{\alpha_i} = \cos(\alpha_i)$), assuming Lambertian reflection model. However, splitting the model into small sized segments using local model descriptors as described in section 2.7.1 offers the possibility to apply equal weighting to all segment points due to little change in distance and incidence angle.

Another phenomenon closely connected to the determination of realistic precision measures of model parameter estimates is that the high data redundancy involved in the adjustment process may result in precision values being overestimated. As mentioned in Van Gosliga et al (2006), the high redundancy of the data may lead to a much higher precision of the estimated parameters compared to the relatively low precision of the single point coordinates. This being a well known characteristic of TLS, it is necessary to check how realistic these precision measures actually are if we want to draw conclusion on deformations on their basis. In order to obtain a more reliable precision measures, the LSA can be repeated in consecutive steps at each using a large number of random point subsamples equal in size whereby increasing the number of points from one step to the next. When dealing only with random errors, this empirical approach not only indicates at which boundary the precision values start settling down but also at what sample number the correlation between point becomes so high that the individual parameter estimates do not change any more.

2.8 Deformation models

In point-wise geodetic surveying it is before the acquisition process that the choice on where to place the representative points has to be made in order to control the position and integrity of the structure in question. From the TLS point of view, it is only after the point-to-surface transformation that the decision has to be made on how the evaluation should be performed. In general, when analyzing multi-temporal TLS models, the extensiveness of geometric description of variations in the object's condition is very much limited by the amount of surface detail. Hence, it is not always possible to approach the displacements and deformation inspection in the same way as in the case of point-wise geodetic monitoring with signalized points inherently enabling the determination of movements in all three coordinate directions. In an extreme imaginary case, for example if scanning a flat wall, any changes within this plane will be undetected by the device. Though rare, in such cases, the only option is to fix some control points onto the surface. More likely, when lacking surface features, it may be possible to extract some information on the magnitude and direction of displacements of individual surface segments. Provided enough features exist, the surface model can ultimately be reduced to some single specific (representative) points on the object surface and their position tracked with respect to time. The latter two cases, i.e., deformation inspection models, are discussed in more detail in the rest of this section.

2.8.1 Model 1: Truncated direction

The word *truncated* refers to the inability of this inspection model to describe the direction of displacements of individual surface segments in all coordinate system directions regardless of the type of system being chosen (cartesian or object dependent, such as cylindrical which is widely used

when modelling the surface of tunnels from the TLS data). This disadvantage is a direct consequence of the absence of any distinct object features preventing the surface models to be reduced to some identical points in all measurement campaigns. Consequently, the tracking of model segments is only possible along the predetermined normal vector directions (tracking directions), as shown in Figure 9. In Figure 9, the magnitude of displacements of individual surface segments is presented as

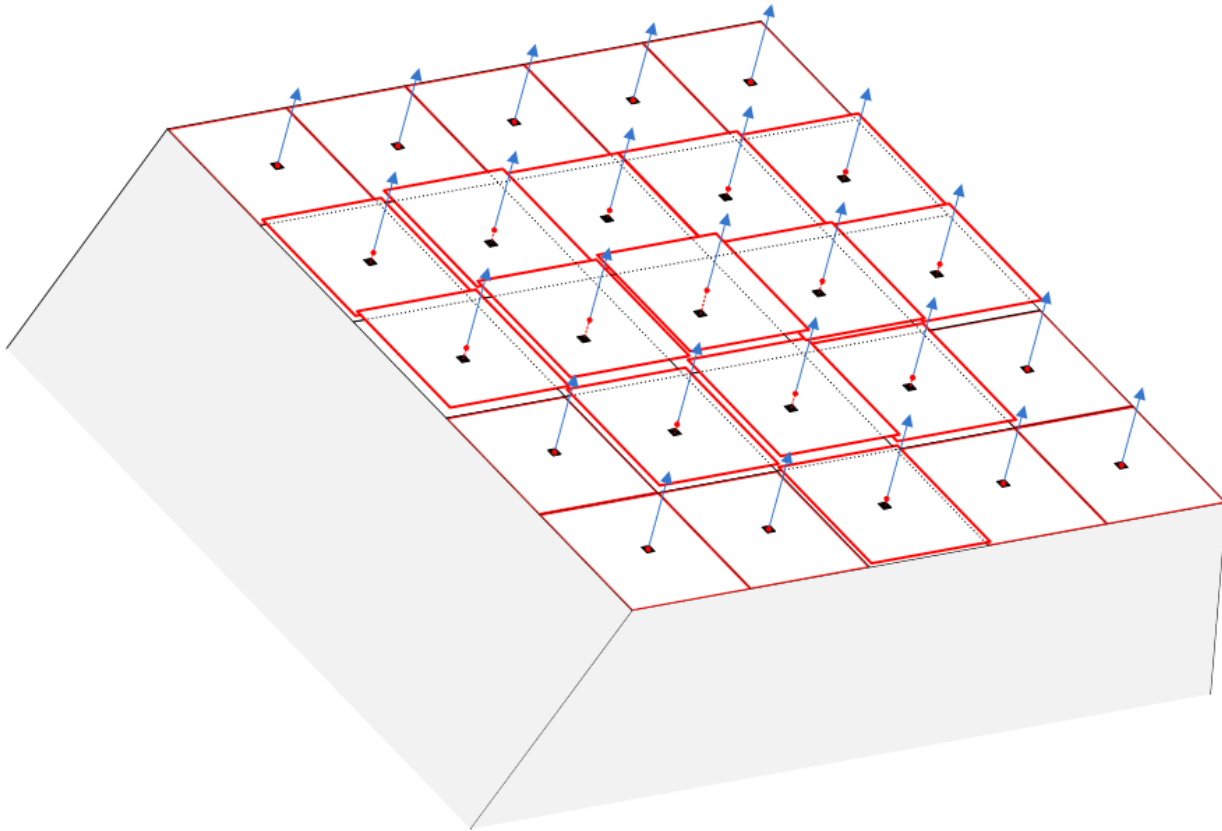


Figure 9: Segment-wise displacement inspection. The direction of movements is determined by the initial segment normal vectors.

the distance between the initial segment position (black dots) and the points where lines composed by the initial normal vector directions intersect with segments coming from any successive epoch. Such an approach also provides the ground for studying how the normals of successive segments diverge from the initial one and indicates how the deformation is progressing.

To apply this inspection model, the first requirement is that the point clouds are already split and modelled by segments as described in section 2.7.1 in order to have normal vectors available. The more surface segments of different orientation the structure contains, the larger the number of displacement tracking directions. The overall description of the object status (position and integrity) and its changes should be composed by analyzing the vector fields consisting of all tracking directions available, especially since the effects of forces acting onto the structure may be transmitted to various number of tracking directions with different magnitude depending on their nature. In

certain cases the direction of forces may coincide with the tracking directions to a high degree, such as when monitoring water pressure effects behind hydro plant dams or bridges being exposed to the force of gravity or heavy loads. If so, despite its limitations this inspection model can be successful in answering how the structure reacted at the presence of forces whether internal or external in origin.

Another advantage of this model worth noticing is the high number of model segments compared to the number of representative points which can typically be extracted from the surface models of anthropogenic structures and objects. Hence, the truncated direction model should be seen as a surface-wise inspection model enabling a near continuous study of displacements and deformations of the surface in question. Therefore, even when representative points are at disposal, it is advisable to evaluate the spatio-temporal changes of surface models according to this approach in order to confirm the consistency of results of both inspection models.

2.8.2 Model 2: Representative points

Compared to the truncated direction model, the reduction of surface models to single specific points leads to a point-wise displacement analysis which can provide full (3D) geometric information on the object's condition and its changes without the need to install any control points or other sensor compositions onto the object's surface. The determination of *identical* representative points in all measurement campaigns is of great importance in order to treat their displacements correctly (i.e., referring to the same point at all times). Again the definition of these points is problem dependent; still some guidelines can be drawn as to where and how they should be extracted.

Regarding the location of their extraction, if the object's shape has been deformed, the representative points must be determined on the surface itself with the extraction process resulting in exact point solutions. In such deformable cases when the number of points is low, the results of this inspection model may have to be combined with those coming from model 1. Contrary to that, if the object's shape has remained unchanged and it has only changed its position, the object may be presented by some specific points on its surface whereby their number depends on the size of the object. In special cases when monitoring objects with well-defined geometry, which have not changed their form, we may choose the representative points which do not necessarily lie on the surface of the object (e.g., object axis); an example that will be described in section 3.3.

During the process of extraction of representative points, these can be obtained by intersecting different kinds of surface model descriptors, such as planes or lines which have been modelled beforehand and have their parameters estimated on the basis of redundant observations. Referring to Figure 8 on page 24 for demonstration, the representative points can be determined in the intersection of three adjacent planes. Furthermore, if identical representative points are to be extracted on a line (axis), this cannot be done straightforward because of the line's direction vector having a slightly different position in each measurement epoch depending on point configuration. The only

way to overcome the problem is by intersecting the line by another model descriptor (plane, line, etc.) or by projecting a point with known position onto the line. In the case of outdoor test 1 the projection was only possible by using one of the network's control points since no other single point could be extracted from the surface model. In addition, with models containing structured lines (breaklines), these can be also included in the evaluation process following the same steps as presented above. Finally, in the presence of certain surface features, e.g., spheres or hemispheres, the models can directly be reduced to single points without the need of any adjacent model descriptors. After obtaining the points, one common and simple approach for the determination of displacements is to use the rule of thumb (Savšek-Safić, 2006). In this case, the point has moved, if the displacement vector is bigger than the positional standard deviation of end points increased by a factor of 3 or 5. Three sigmas are sometimes taken as the limit value to what can be regarded as the random error of the determined position. Therefore, any larger deviation from the estimated position is usually considered a blunder or an actual displacement. Regardless of the model selected for the displacement and deformation analysis, careful error propagation steps have to be performed alongside in order to make the final conclusions reliable enough.

3 EXPERIMENTAL RESULTS

According to the methodology presented in Chapter 2, the proposed workflow (section 2.1) was tested in the two outdoor experiments described herein (see section 3.3 and 3.4). The characteristics of the two outdoor experiments are in many ways quite different with respect to:

- the terrain features and ground stability;
- the size of the object under inspection;
- the object's accessibility;
- the limitations of the geodetic network formation;
- the complexity of displacement and deformation evaluation process.

Comparing test 1 and 2 based on these factors, test 2 most certainly appears to be more challenging for TLS when deciding whether to accept or reject the working hypothesis with enough confidence. During the two outdoor tests two different scanners were used, namely the Leica scanner in test 1 and the Riegl scanner in test 2 both belonging to a similar instrument quality class. The fact that the first scanner was used with the targets coming from the same manufacturer has resulted in a significant reduction of systematic range errors due to the possibility of scanning the target surface with a specially designed acquisition mode. By using this mode the target centers are estimated with the amplitude weighted mean algorithm built into the scanner's software for data processing. On the other hand, the range error behavior had to be tested and modelled prior to test 2 in order to reveal how the second scanner will comply to the same targets (see subsection 3.1.2). Consequently, the scanner-target "compatibility" poses an additional factor to the ones listed above that needed to be analyzed for the purpose of test 2 alone. Finally in test 2, objects of different material composition and surface roughness were involved which meant tests on the scanner's detectivity level had to be performed to determine its sensitivity to small scale displacements and deformations (see subsection 3.2).

3.1 Target calibration tests

Target calibration scheme consist of two subsequent tests: the test to determine the target's mechanical imperfections and the test to estimate the possible range errors. Altogether four targets of the same type (leftmost target in Figure 2) have been examined for they were later used in the outdoor tests. The targets' properties are summarized in Table 1. The results of calibration should provide the optimal frame of their operation in which the systematic errors are minimized so that the estimation of the transformation is to be unbiased.

3.1.1 Mechanical imperfections

The purpose of this simple test is twofold. First of all, it is important to know how the target's center point is affected by the rotation particularly because it is oriented towards the scanner at each instrument station. Ideally, the position of the center should not change when the target is rotated in any of the two directions (horizontal or vertical). However, the mechanical imperfections distort this ideal case and information is needed on how the orientation has to be done to minimize these errors. Concerning the second aspect of the test, the mounting offset between the target and the prism has to be examined to make sure it corresponds to the one obtained from the technical specifications of both reflectors. The results of this test are scanner independent.

To answer the questions an indoor measurement setup was designed, shown in Figure 10 (left image). Two pillars stationed approximately 3 m apart were used for fixing the measuring instrument

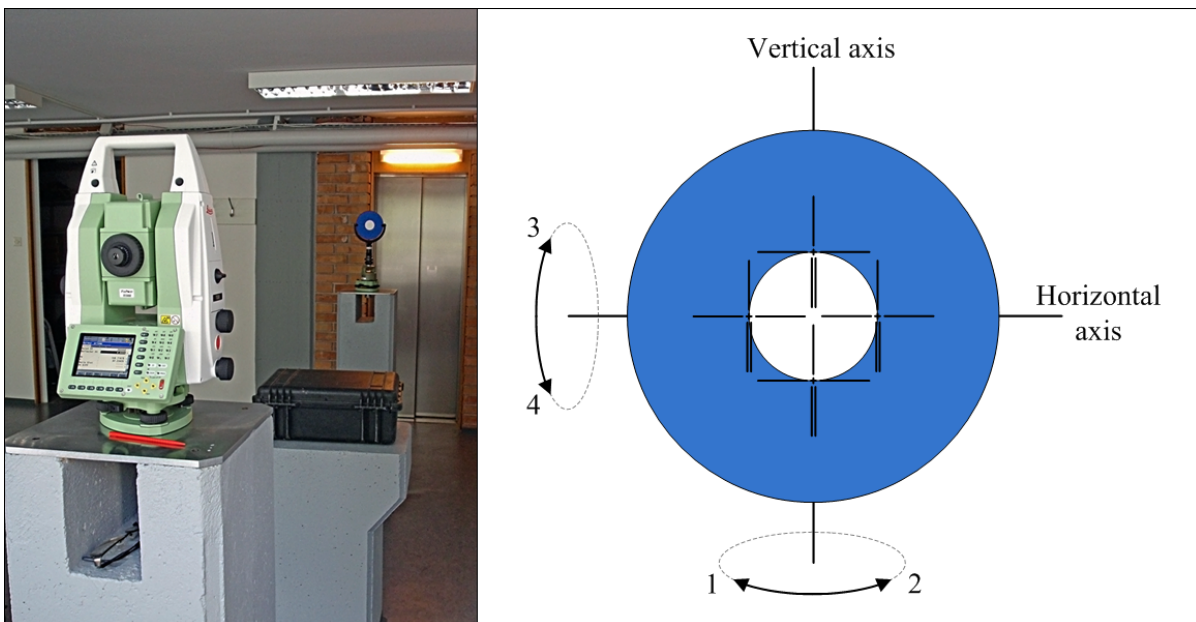


Figure 10: Testing target construction defects. The numbers in the right image represent the directions in which each target was rotated, i.e., first left-right, then up-down.

on one side and the target on the other. Both tribrachs were levelled with precise tubular levels beforehand. The instrument Leica TS30 with an angular precision of $0.5''$ and distance precision of $0.6 \text{ mm} + 1 \text{ ppm}$ was chosen for the task. In each direction 1, 2, 3, and 4 (Figure 10, right image) the target was rotated by an incremental step of 10° up to the angle of 40° , resulting in 17 target positions including the position where both rotations were 0° . Furthermore, in every position the target center was calculated in two stages. In the first stage, the horizontal and the vertical angle of the center point were computed from the four readings of the telescope's crosshair as shown in Figure 10. The left-right readings were used to calculate the horizontal angle and the up-down readings to determine the vertical angle. In the second stage, the distance to the center was measured by placing the crosshair to the center of the small (2 mm) silver spot in the middle of the target. This

two stage approach has proved to be freer of ambiguity and more accurate than the one where the silver dot is used to determine all three coordinate components. Even if the distance in the second stage is measured along the direction which does not perfectly coincide with the one computed from stage one, the difference in the distance is negligible because the latter direction never leaves the silver spot. The presented measurement sequence was repeated for all four targets. Finally, the Leica reflector GHP1P with an additive constant below 0.1 mm was measured to be able to determine the mounting offset. All measurements to determine the horizontal and the vertical angle of the target centers in the first stage were performed with no redundancy for they were carried out manually. In the second stage, five measurements were registered each time to estimate the distance to the target center. Concerning prism measurements, the ATR functionality was used again to perform five consecutive repetitions of all measured quantities, i.e., both angles and the distance.

The results of the test reveal that all distances were estimated with the precision which was always below 0.2 mm. These slope distances were finally transformed to horizontal distances which were used for comparison. As for the angular measurements to the prism, these were estimated with a standard deviation of 0.1" and 0.3", which represents an insignificant level of dispersion at the distance of 3 m. In Table 2 the results of this test are shown with respect to the targets' sensitivity to rotation. On average the positions of the target centers are the most prone to errors in the *forward-*

Table 2: Results of the targets' sensitivity to rotation. Δ_1 , Δ_2 , Δ_3 are the spans in which the centers are moving with Δ_1 representing the *left-right*, Δ_2 the *forward-backward* and the Δ_3 the *up-down* direction as seen from the observation point.

Target	Δ_1 [mm]	Δ_2 [mm]	Δ_3 [mm]
T1	1.2	0.8	0.2
T2	0.2	0.6	0.2
T3	0.7	0.9	0.2
T4	0.3	1.3	0.1

backward direction and the least in the *up-down* direction. With the exception of T1 (Δ_1) and T4 (Δ_2) all spans are confined to a 1 mm range but in the submillimeter domain the targets' sensitivity obviously is slightly different. A closer inspection indicates no strong correlation exists between the incidence angle and the size of the error in any direction Δ_i at this small deviation level. On the other hand, the results reveal that the rotation of the target around its vertical axis contributes more to the error in the *forward-backward* direction than the rotation around its horizontal axis. Consequently, the values of Δ_2 in Table 2 are basically the outcome of rotation around the first axis and are even lower with respect to the horizontal axis. At this point a final conclusion is that it is hard to say what the spans would be like if the observations were carried out by rotating each target around its vertical axis in a full circle. Based on the results from Table 2, some values of Δ_1 and Δ_2 would probably go beyond 1 mm compared to Δ_3 , which tends to be 3 to 4 times lower and quite stable within the observed $80^\circ \times 80^\circ$ spherical window. However, such a measurement scheme cannot be done from one instrument station only and was not considered within the thesis.

Focusing now on the analysis of the mounting offset, the technical specifications of both reflectors show that the target center should be 114.5 mm (± 0.7 mm) above the prism center, hence the offset should be limited to a vertical direction only. However, the results presented in Table 2 already indicated that particularly in the submillimeter domain the offset could not be constrained to this direction only. This fact can eventually be seen in Figure 11 where the positions of the target centers are illustrated with respect to the position of the prism center whereby taking into account the vertical offset of 114.5 mm. Based on Figure 11, the confirmation of the first impression about the

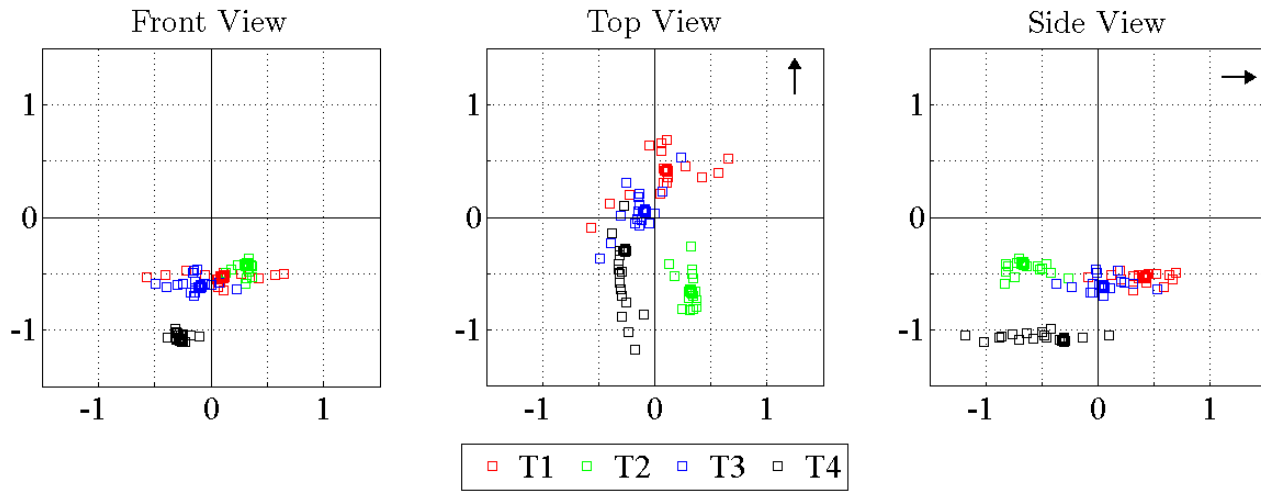


Figure 11: Mounting offset results. The views show the positions of the centers as seen from the observation point. The direction to the observation point is indicated by the arrows in the middle and right image for more clarity. The highlighted brackets represent the positions where both rotations are zero. All values on the axes are in [mm].

targets' construction inequalities becomes firmly noticeable. Centers are clustered in a systematic pattern around the origin. In terms of the mounting offset, the centers for T1, T2 and T3 are about 0.5 mm lower but within the specified tolerance threshold. The same cannot be said about T4 with its centers arranged approximately around the value of 113.5 mm, i.e., 1 mm lower than specified. At least for T4 this vertical eccentricity error should be considered every time the target is used especially because it seems to change very little. Therefore, the offset for T4 is the least accurate in the vertical direction, whereas all the others are nearly the same.

Concerning the eccentricity errors in the other two spatial directions, it is important how the spans Δ_1 and Δ_2 of each target are positioned with respect to the origin. For example, a 2 mm span would be split in half if positioned centrally. This fact can be observed for T1 with its Δ_1 being confined to a ± 1 mm boundary. The graphs reveal that the most precise is T2 but almost the least accurate. T1 and T3 are similar in precision but T3 tends to be more accurate. As for T4, its centers are the most disperse with some falling more than 1 mm from the origin. These largest deviations are obtained when the target is rotated around its vertical axis to the right side (direction 2 in Figure 10). Such an outcome for T4 supports the assumption that if the centers were observed in a full

circle around the vertical axis, the deviations for this target would probably be at least of this level if not a little more. On the other hand, the results for T1, T2 and T3 within this $80^\circ \times 80^\circ$ spherical window suggest more strongly that the full circle observations would still produce centers fenced by the ± 1 mm boundary. Finally, when examining the results, it also becomes clear that applying any kind of modelling routines to eliminate such horizontal eccentricity errors would be hard for no firm patterns to appear at this deviation level. Therefore, no reason exists that extending observations to a full circle would ultimately contribute to the modelling efficiency of this type of errors. It seems some of their effect can only be minimized through the transformation process if at all (see equation 3). Due to the manual observation process and the small deviation level, the increase in the reliability of the results could eventually be obtained by repeating the test at the same or perhaps different instrument-target distances.

3.1.2 Range error modelling

As indicated at the beginning of this chapter, the behavior of the Riegl scanner with respect to the Leica flat targets was examined in an indoor test to reveal the presence of possible systematic range errors which should be applied right after the process of estimating the target centers in test 2 where this scanner was employed. The length of the facility where the indoor test took place was close to 70 m; therefore the range error could only be tested within that window. Inside the 70 m perimeter, altogether 43 tripods were stationed every 1.5 m, starting from 3 m to 66 m (Figure 12). The tripods



Figure 12: Range error test setup.

were placed almost in line and levelled with precise tubular levels. At every station each of the four targets was scanned in a consecutive sequence and under two incidence angles, first 0° and then 20° . The 20° angle was realized by rotating the target only around the vertical axis to see how the

error would behave in a non-perpendicular position with less energy returning back to the receiver. Furthermore, experience had showed that the 20° angle corresponds to the upper boundary of manual target orientation which can be assured if the field work is done with care. The Riegl VZ-400 scanner acquired 344 scans in total each time producing a 1 mm raster on the target surface hence resulting in about 20 000 points per scan. For the extraction of the target centers, the proposed two step algorithm (see section 2.4.1) was used. All target planes in the first step of the algorithm were estimated from corresponding subsets of points shown in Figure 13 (green colored points). The

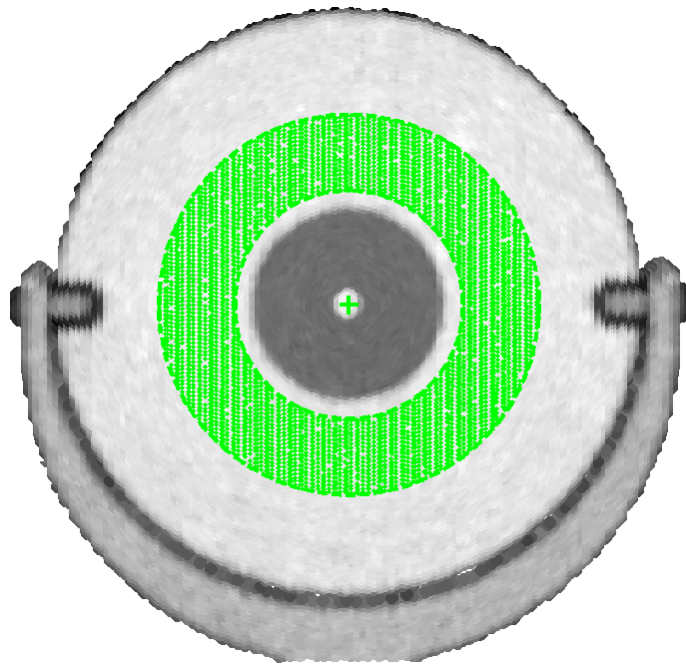


Figure 13: The area of the point cloud selected for the distance estimation. The points are color-coded by amplitude. The marker represents the initial center calculated by cross correlation.

decision for this particular center extraction algorithm was motivated by the fact that in test 2 too large scanner-target distances were involved to be able to use the alternative amplitude weighted mean algorithm. The entire length of 70 m could only be sampled using a single algorithm if the proposed center extraction approach was introduced. As for the selection of the area for the distance estimation, the region shown in Figure 13 was chosen empirically for it best satisfies the criterion of homogeneity up to 70 m and even beyond where the laser spot diameter becomes bigger than 3 cm (at 70 m the spot diameter is ≈ 3 cm). Moreover, this region turns out to be the only one in which the residual pattern of the plane fitting process remains free of bias. The fact that the region lies on the retroreflective surface of the target was another reason to expect the occurrence of range errors. Hence, the scanning was done in the so-called *reflector* mode which generates the lowest pulse power compared to the other two modes³ available and is therefore most appropriate. The

³The *high-speed* and the *long-range* mode. The tests showed that using these two produced significantly larger range errors due to the higher pulse power.

question was how would this particular mode and the retroreflective character of the region shown in Figure 13 influence the range measurements.

After all scans were acquired, the reference distance measurements were performed again using the Leica TS30 tacheometer and the GPH1P reflector with the additive constant less than 0.1 mm. For each station, the distance to the prism was measured five times using the ATR functionality. The classical terrestrial measurements were carried out from the same tripod that was used for scanning and was stationed at one end of the 70 m corridor. The tripod carrying both instruments was also precisely levelled to make the comparison of distances possible. Because of the existing eccentricities at the reflector as well as the instrument side the slope distances could not be compared directly but only after computing the horizontal distances first. Concerning the eccentricities, the vertical offset was taken into account on the reflector side only. As for the eccentricity between the two instrumental coordinate origins, this could be also restricted to the vertical component by fixing both instruments into the same tribach. For this purpose alone a special adapter had to be attached to the scanner's base. During the seven-hour test the meteorological conditions were measured every hour but did not change significantly as expected (temperature change $\Delta T < 0.4$ °C, humidity change $\Delta \eta < 10$ % and air pressure change $\Delta p < 1.5$ mbar). However, if the results of this test, i.e., range corrections, are later to be applied in any outdoor test with varying atmospheric conditions from one epoch to another, the distances had to be corrected for the meteorological distance correction factors. It can be seen that the only significant error is the first velocity error which at the maximum distance was 1.4 mm for the tacheometer and 1.1 mm for the scanner.

In Figure 14 the standard deviations of the distances clearly indicate the difference in the quality between both instruments with respect to the rangefinder performance. The classical terrestrial

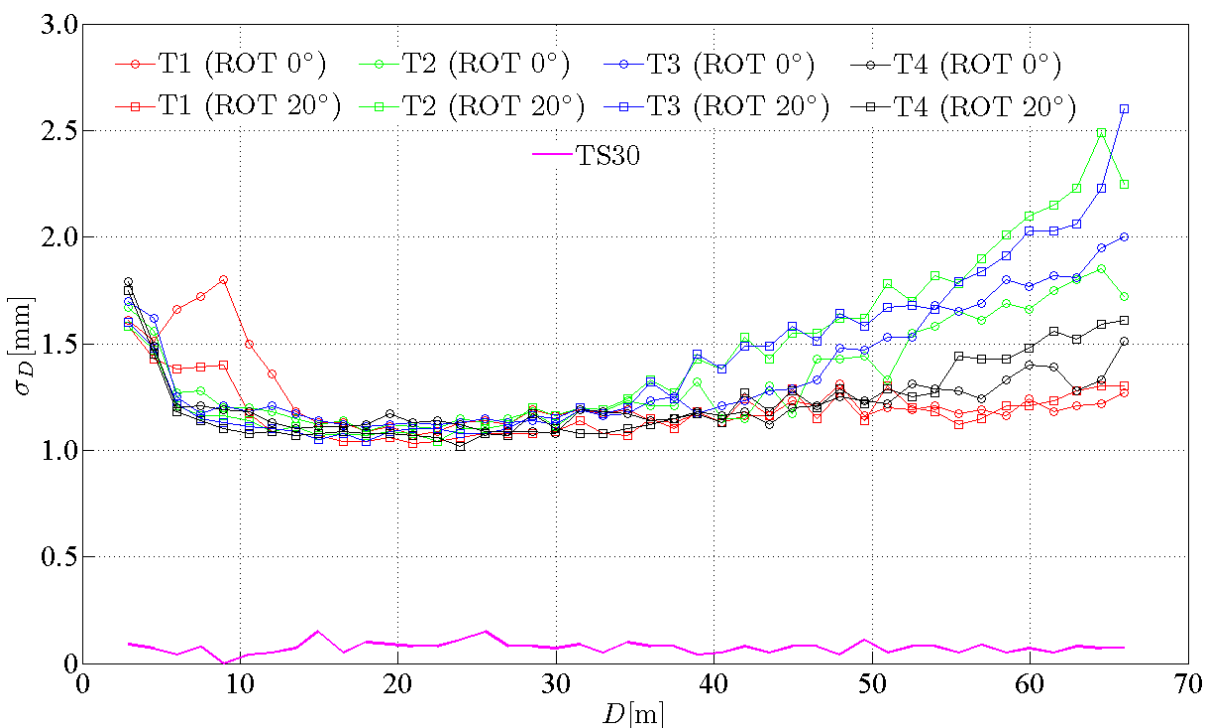


Figure 14: Standard deviations of distance measurements.

distance precision is at least ten times higher, which means these distances could be considered reference. Moreover, the TLS distance precision representing the level of noise at the target plane can be explained by examining the average amplitude each target produces in the selected region. The differences in average amplitude, which can be seen in Figures 16 and 17 on pages 37 and 38, lead to different noise levels. With respect to distance the TLS precision can be split into three different intervals. In the vicinity of the scanner ($D < 10$ m) the distance precision seems to reflect the fact that too much energy is returned back to the receiver under 0° incidence angle, resulting in higher noise level within the selected region. For T1 this interval stretches even little beyond 10 m because the target produces on average 20 % higher amplitudes than the other three. Rotating the target for 20° has positive effects since less energy is returned.

Next is the interval where the TLS distance precision becomes highest reaching up to $D \approx 35$ m. It is in this interval that the pulse power produces the smallest noise level for all targets despite the amplitude differences. Beyond 35 m the rangefinder performance start decaying fast particularly for T2 and T3, which produce the lowest amplitudes on average. In this farthest interval the differences in the targets' average amplitudes get more influencial due to the overall signal decay. Hence, more distinguishable standard deviations are obtained than below the 35 m where they appear much more consistent (with the exception of T1 in the close proximity). Of all the targets, the distance precision for T1 is the least affected by the distance. With the increase in distance the 20° rotation has the opposite effect producing more noise as the amplitude decreases even further.

Eventually the distances were levelled according to one of the three scenarios I, II, III shown in Figure 15 using only classical terrestrial measurements and known vertical eccentricities. Assuming

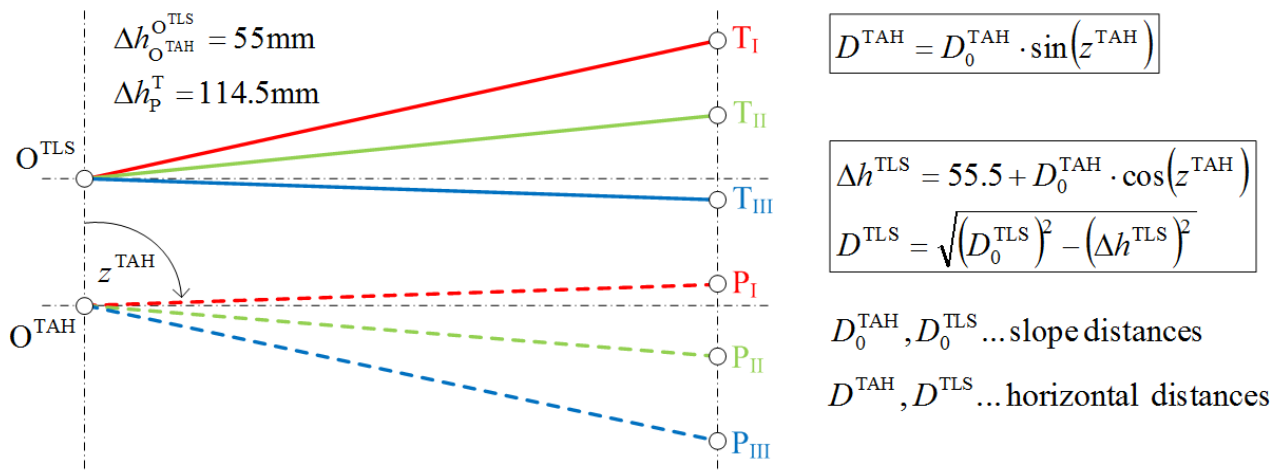


Figure 15: Slope distance levelling. P stands for the prism, T for the target.

small variations between the actual and ideal geometry of this levelling scheme exist (i.e., points $O^{\text{TAH}}, O^{\text{TLS}}, T, P$ lie in a plane and both vertical axes are parallel to each other), these have little effect on the calculated horizontal distances. The final distance comparison can now be presented with the range error computed as $\Delta D = D^{\text{TAH}} - D^{\text{TLS}}$.

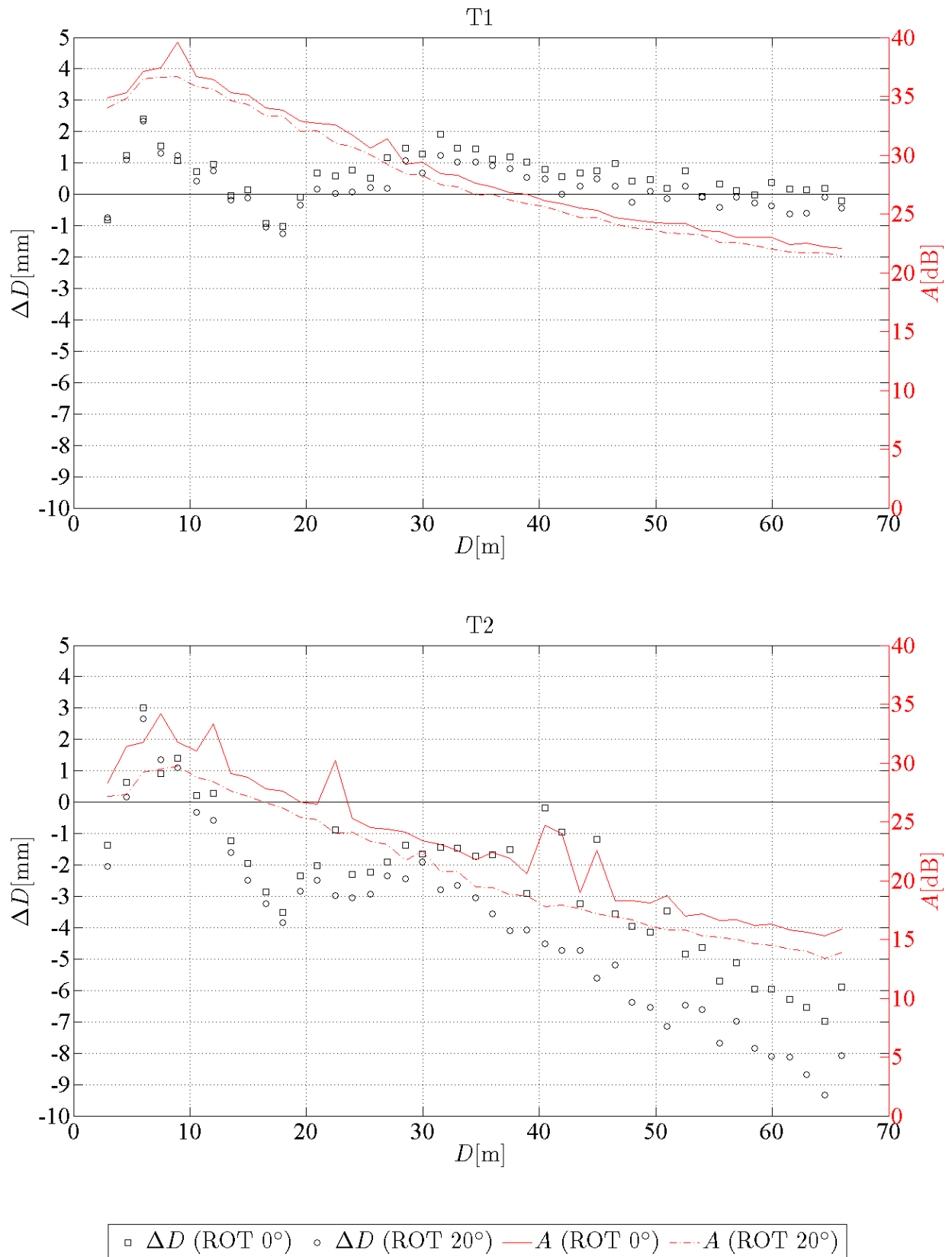


Figure 16: Range error and average amplitude as a function of the distance for T1, T2.

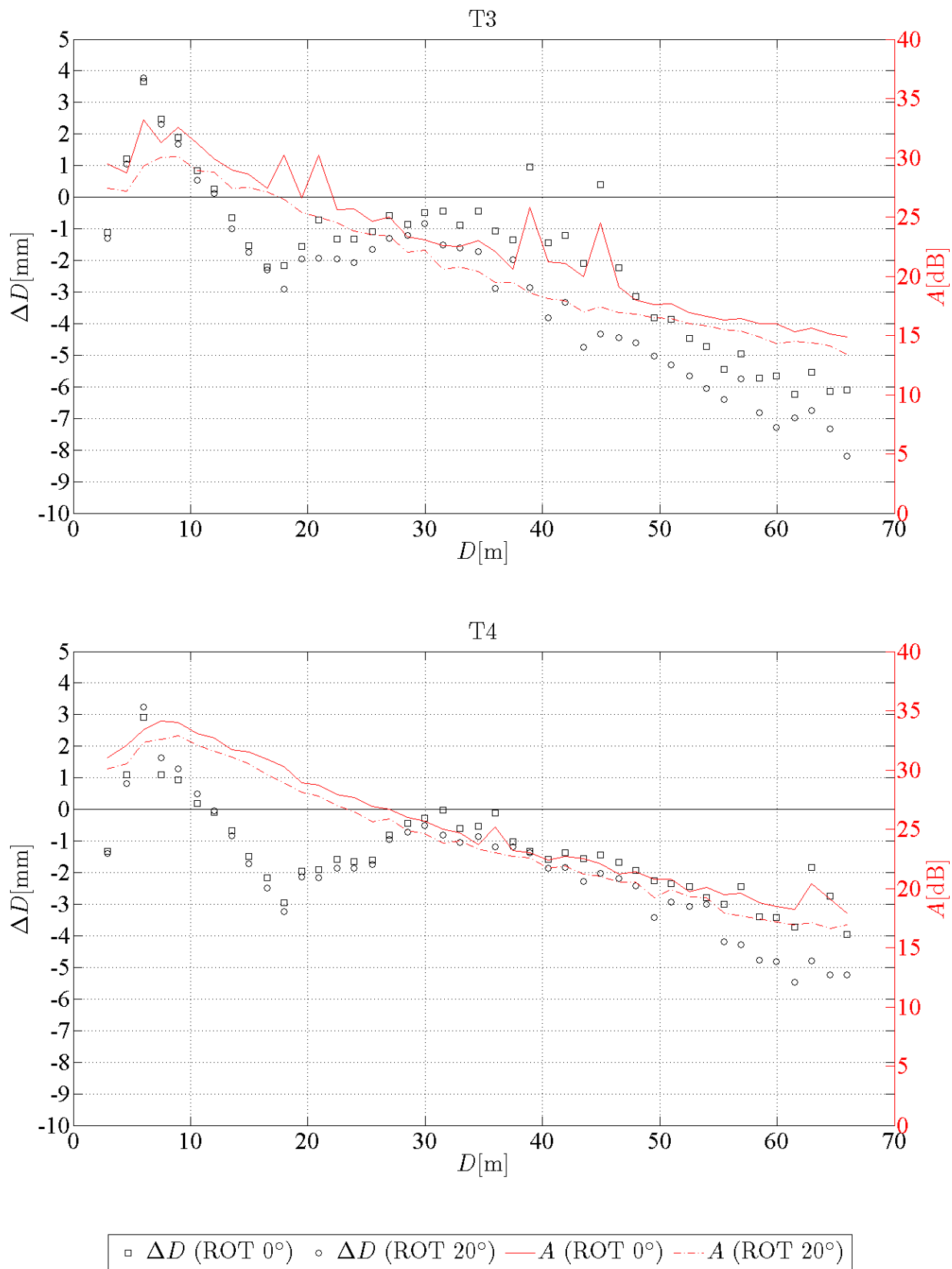


Figure 17: Range error and average amplitude as a function of the distance for T3, T4.

The inspection of the charts provides a confirmation of the existence of systematic range errors as well as the fact that in the millimeter domain these errors obviously behave differently for each target despite experiencing the same trend. The range errors are on average up to ten times bigger than the errors coming from the targets' mechanical deficiencies. The non-linear range error trend can be described by three local extrema, first at around 6 m, second at 18 m and last at 30 m. Clearly this trend originates from the instrument (i.e., *scanner effect*). Explaining the scanner effect would require the in-depth knowledge of the device itself and is therefore difficult to approach from the data side alone. On the other hand, the differences in ΔD originate from the variations in targets' amplitude behavior (i.e., *target effect*). If all targets would produce the same average amplitude⁴, ΔD would be the same. Consequently, the explanation of the target effect can be addressed by analyzing the amplitude variations.

Examining the amplitude plots, the $1/D^2$ decay starts dominating beyond the 10 m where the amplitude reaches maximum. Apparently the 10 m boundary represents the distance beyond which the whole pulse energy falls through the receiver's opening angle. Furthermore, local fluctuations in amplitude which can be seen particularly for T2 and T3 directly affect the distance estimation and finally also the range errors. The presence of these fluctuations is a problem reflecting the general instability of the rangefinder unit at the millimeter level, especially because they are not the outcome of single laser pulses but of the whole selected region containing around 4000 points. Because the occurrence of fluctuations is hard to predict, the modelling efficiency will be somewhat limited. The amplitude plots in turn offer no additional underlying information for the explanation of the scanner effect knowing that only one receiver unit is used for the near as well as the far field. Instead the amplitude and the range error are only correlated up to 18 m but beyond this, the correlation is lost. With the distance increasing, the difference between the amplitudes from both angular positions remains almost constant. The same is not true for the range error difference which increases with distance due to the overall amplitude decay. For T2 and T3, the range error difference grows more rapidly since these two experience larger amplitude difference ($\Delta A_{T2} = 2.4$ dB and $\Delta A_{T3} = 2.0$ dB compared to $\Delta A_{T1} = 0.8$ dB and $\Delta A_{T4} = 1.2$ dB). The reduction of the amplitude under 20° incidence angle pushes the range error in the negative direction and the range error difference can reach up to 2 mm for T2 at the maximum distance.

Besides the possibility of modelling the range error as a function of the distance, the intrinsic connection between the distance and the amplitude dictates an alternative way, which would be to model the error as a function of the amplitude. Figures 18 and 19 on pages 40 and 41 show that $\Delta D = f(A)$ does satisfy the criterion of a unique mapping. Moreover, in terms of modelling, this mapping is more suitable since only two distinct maxima are visible, which means the range error could be addressed by functions of lower degree than in the case of $\Delta D = f(D)$. For more clarity, in Figures 18 and 19, the local minimum is located closest to the scanner and the local maximum at around 30 m. The orientation of the black lines connecting the points at the same distance but different incidence angle is an indicator of the increase in the range error difference with distance.

⁴From here on the word 'average' will be left out.

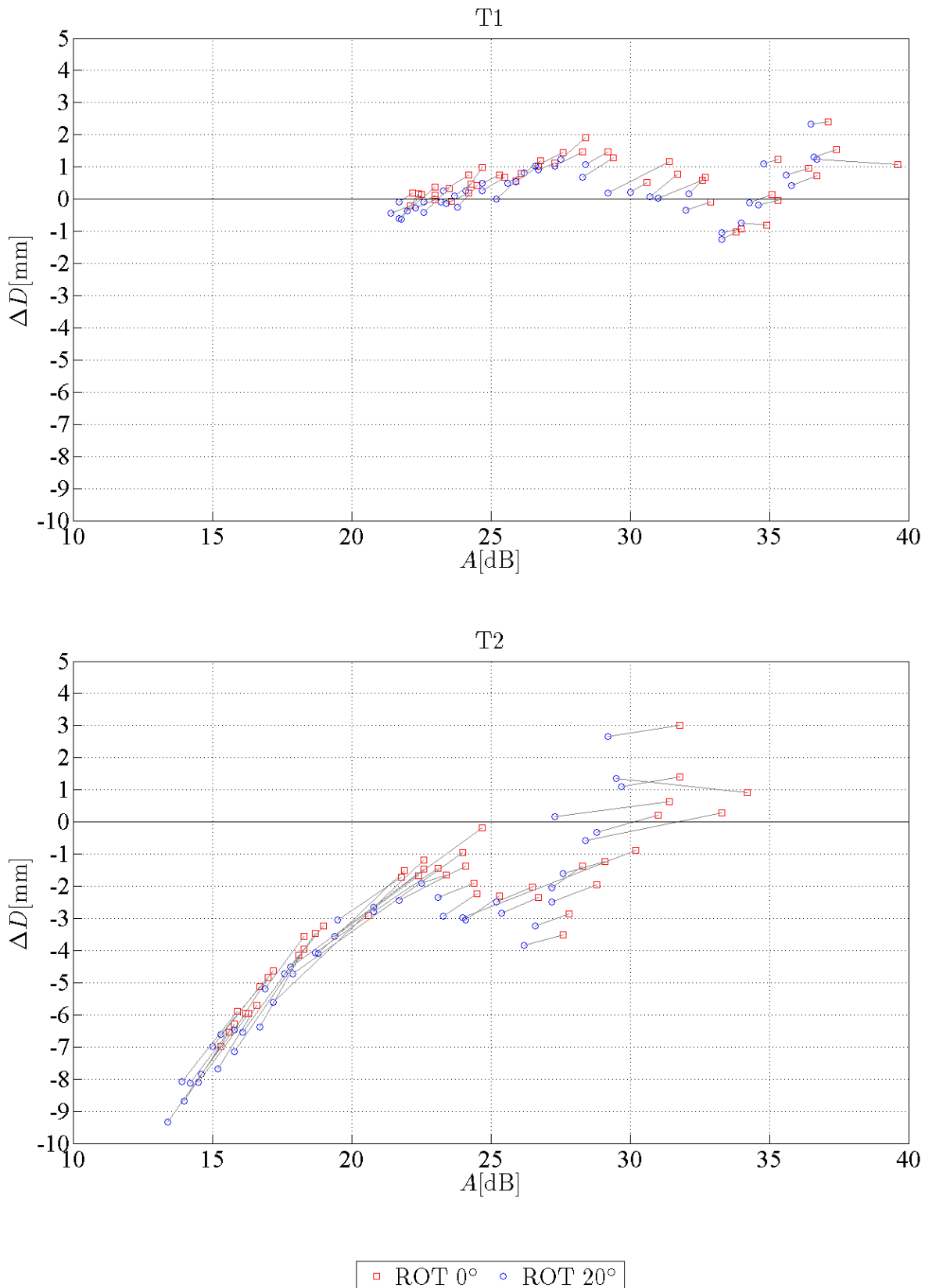


Figure 18: Range error as a function of the amplitude for T1 and T2. The black lines connect the point pairs.

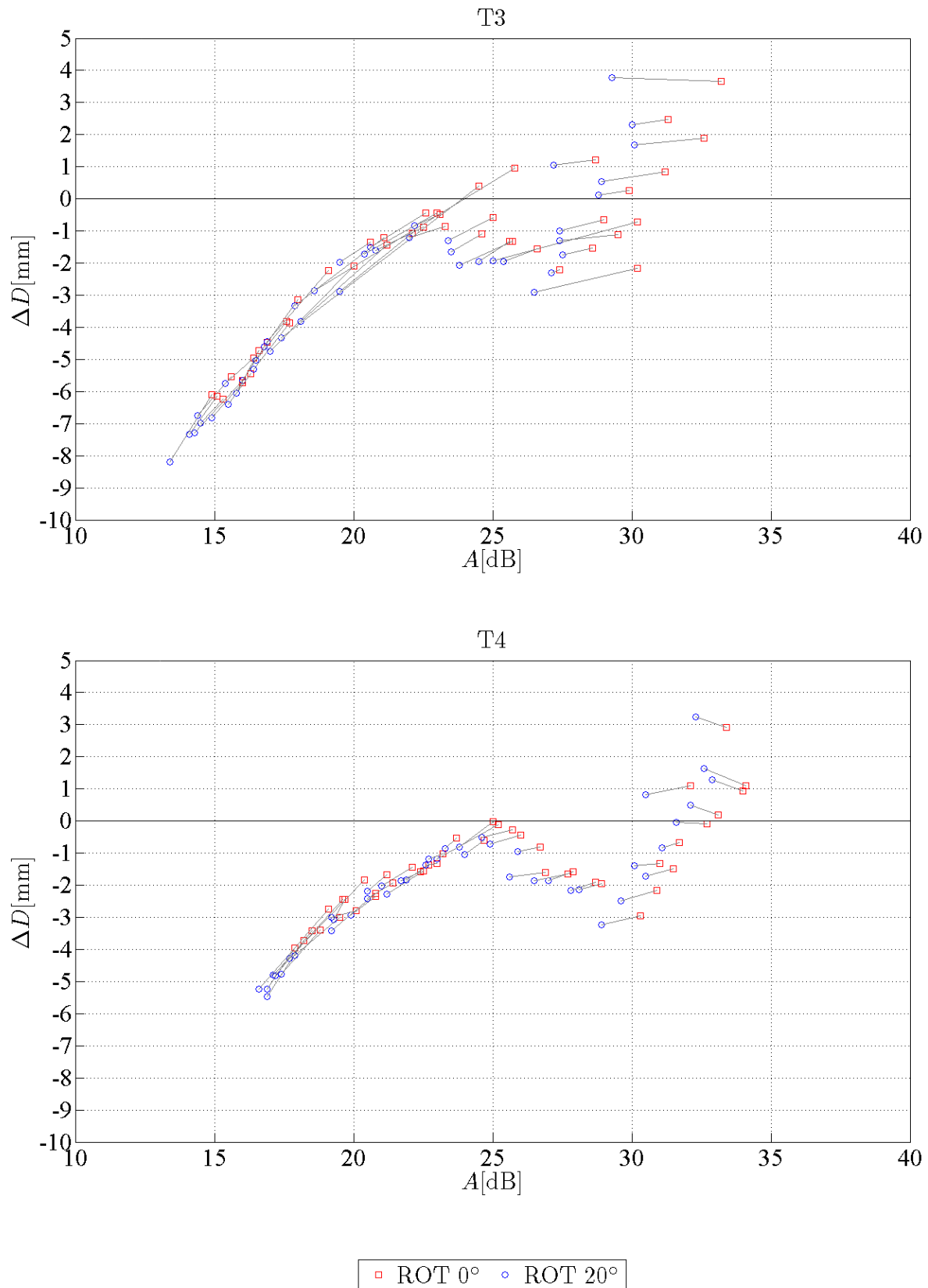


Figure 19: Range error as a function of the amplitude for T3 and T4. The black lines connect the point pairs.

Following the possibility of modelling the range error as a function of the amplitude with less parameters estimated in the adjustment was a decisive factor in the process. After choosing the amplitude instead of the distance domain, the initial idea behind the modelling was to try to separate the scanner and the target effect. This can be done by using a single function (*kernel* function) to represent the first effect and by introducing some additional parameters for the second one, i.e., $F(X, L) = F([x_1 \dots x_{u_0}, x_{u_0+1} \dots x_u], L) = 0$ where X is the vector of parameters and L the vector of observations. The parameters $x_{k,k=1\dots u_0}$ belong to the kernel function, whereas $x_{k,k=u_0+1\dots u}$ are the additional parameters providing the kernel with the necessary flexibility to incorporate the individual target characteristics.

Concerning the kernel function, first different degree polynomials were tested but eventually rational functions proved to be more capable of absorbing the trend. Rational functions are locally much more flexible but less robust, which means good approximate values of the parameters are expected to reach the convergence. The kernel consists of the 3rd degree polynomial in the numerator and the 2nd degree polynomial in the denominator⁵:

$$\Delta D = f(A) = \frac{P(A)}{Q(A)} = \frac{p_3 \cdot A^3 + p_2 \cdot A^2 + p_1 \cdot A + p_0}{A^2 + q_1 \cdot A + q_0} \quad (21)$$

In order to avoid the inherent scaling problem of this model q_2 was set to one (could be any other parameter). If not, the result would be a homogeneous system with trivial or infinitely many solutions. With two additional parameters s and t , one for scale and the other for the translation, the condition equation becomes:

$$\Delta D_{ij} = s_j \cdot \frac{A_{ij}^3 + p_2 \cdot A_{ij}^2 + p_1 \cdot A_{ij} + p_0}{A_{ij}^2 + q_1 \cdot A_{ij} + q_0} \cdot \cos(\alpha_{ij}) + t_j \quad (22)$$

In equation 22, $i = 1 \dots 344$ denotes the observation index and $j = 1 \dots 4$ the target index. For s_j to be considered a unique parameter, also p_3 has to be set to one. Hence, in the adjustment 13 parameters would be estimated altogether. The $\cos(\alpha_{ij})$ is introduced here in order to account for the incidence angle effect. The latter may be hard to evaluate based on two angles only but appears to be quite minute (see Figures 20, 21, 22 and 23 at the end of this section). The assumption about the Lambertian scattering properties of the targets could be violated due to the retroreflective character of the region for the distance estimation. Therefore, the $\cos(\alpha_{ij})$ can be modified to $\cos(m_j \cdot \alpha_{ij})$ with four more parameters to be considered in the adjustment.

Despite the advantages of this model in terms of using a single kernel and separating the instrument and the target effect, testing the model on the datasets was not very successful. The additional parameters did not provide the kernel with the desired flexibility to absorb the differences between the targets illustrated in Figures 18 and 19, which are presumably caused by the target effect. One possible reason for such an outcome may not be due to the parameters alone but also due to the

⁵In case the modelling would be approached in the distance domain, the kernel's numerator would be of degree four and the denominator of degree five.

approximate values of the unknowns which are difficult to find and lead to a local rather than a global minimum of the model function. No significant progress was achieved even after the final extension of the model where the functional argument A was replaced by $(A - T_j)$ adding another four new translation parameters to the adjustment. Going beyond the final number of parameters is not beneficial for it may lead to overparameterization of the system.

After the extensive testing of the single kernel model with various modifications and different sets of approximate values, the lack of any promising results lead to the abandonment of this initial idea. Instead the modelling was approached separately for each target but using the functional model presented in equation 21. The results of this separated adjustment scheme were better with respect to the overall modelling efficiency and were therefore considered final. The estimated values of the model parameters along with the corresponding a posteriori standard deviations for each target are listed in Table 3. In these separated model functions, also the incidence angle was left out because

Table 3: Estimated values of parameters of the range error functions and a posteriori standard deviations.

	T1	T2	T3	T4
p_3	0.304762	0.894525	0.847888	0.601716
p_2	-27.460037	-67.284268	-63.487416	-49.524117
p_1	812.467947	1677.293026	1573.560883	1349.126127
p_0	-7865.659127	-13926.696980	-12952.431721	-12191.481641
q_1	-66.824233	-49.207920	-49.067752	-55.238595
q_0	1128.073586	634.306982	630.330465	779.205941
$\hat{\sigma}_0$ [mm]	0.5	0.9	0.9	0.7

its absence basically did not change the adjustment results. The a posteriori standard deviations representing one quality measure of the modelling efficiency are below 1 mm. However, the residual patterns, shown in Figures 20, 21, 22, 23 on pages 44, 45, 46 and 47 reveal the fact that placing the targets closer than 20 m is not recommended due to generally larger residuals which indicate the inefficiency of modelling in that area. The question is whether in that area there is some underlying trend which could be observed only if the range would be sampled more densely or the range error variations simply follow no explicit pattern. On the other hand, beyond the 20 m range the residuals are for most part well below the 1 mm boundary. From the estimated values of the model parameters (see Table 3) some conclusion may be drawn in terms of why the chosen set of additional parameters, introduced in the initial modelling approach, was not successful. The differences in the parameter values may not be overcome by scaling and shifting the kernel alone. However, at least some knowledge on the scanner effect was gained during the experiment, uncovering the behavior of this particular instrument. Eventually, the cause of some concern are not so much the errors but more the error fluctuations because they cannot be tamed by the modelling process as can be seen in the following figures where the results of the final separated adjustment are presented graphically.

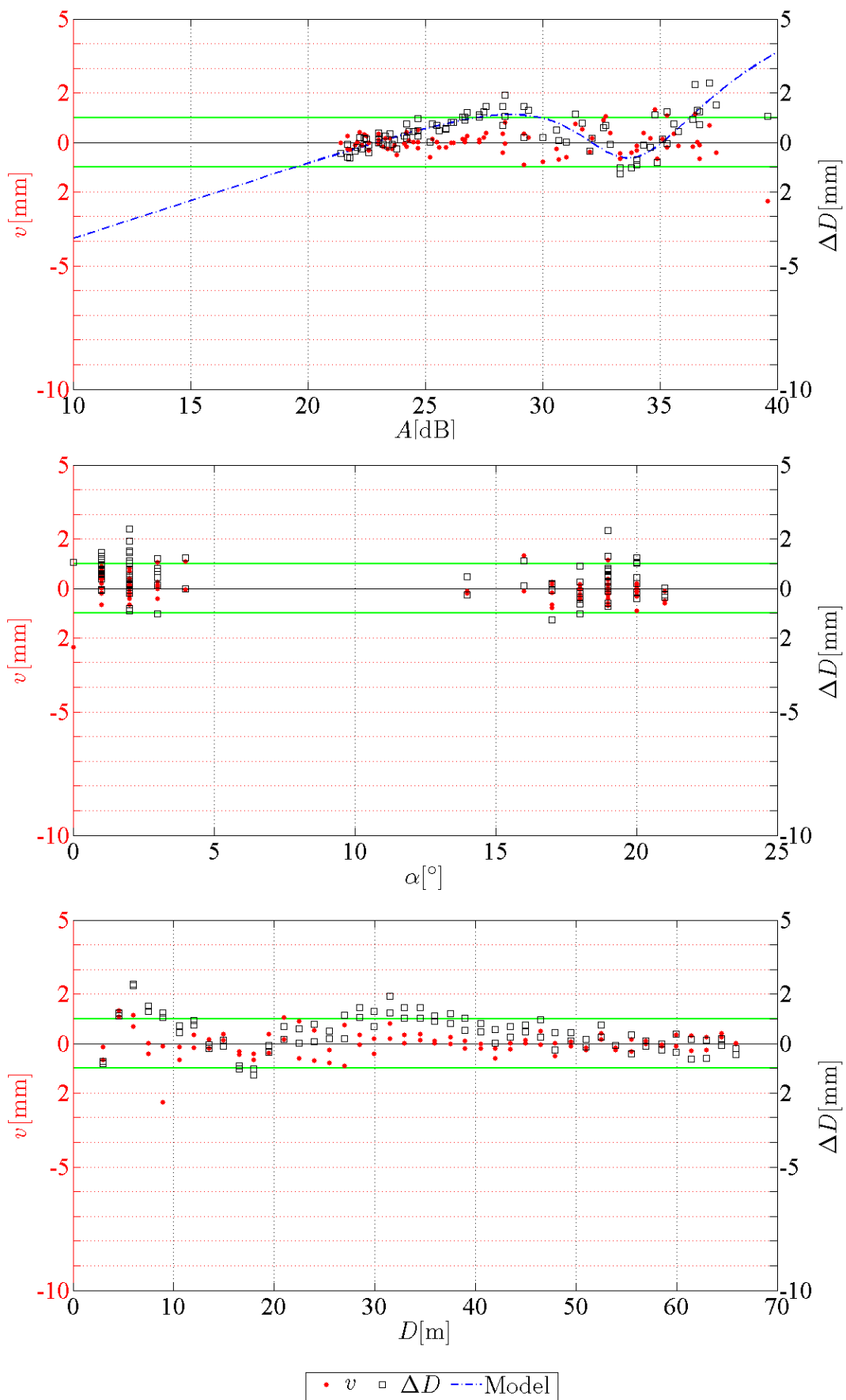


Figure 20: Residual pattern for T1.

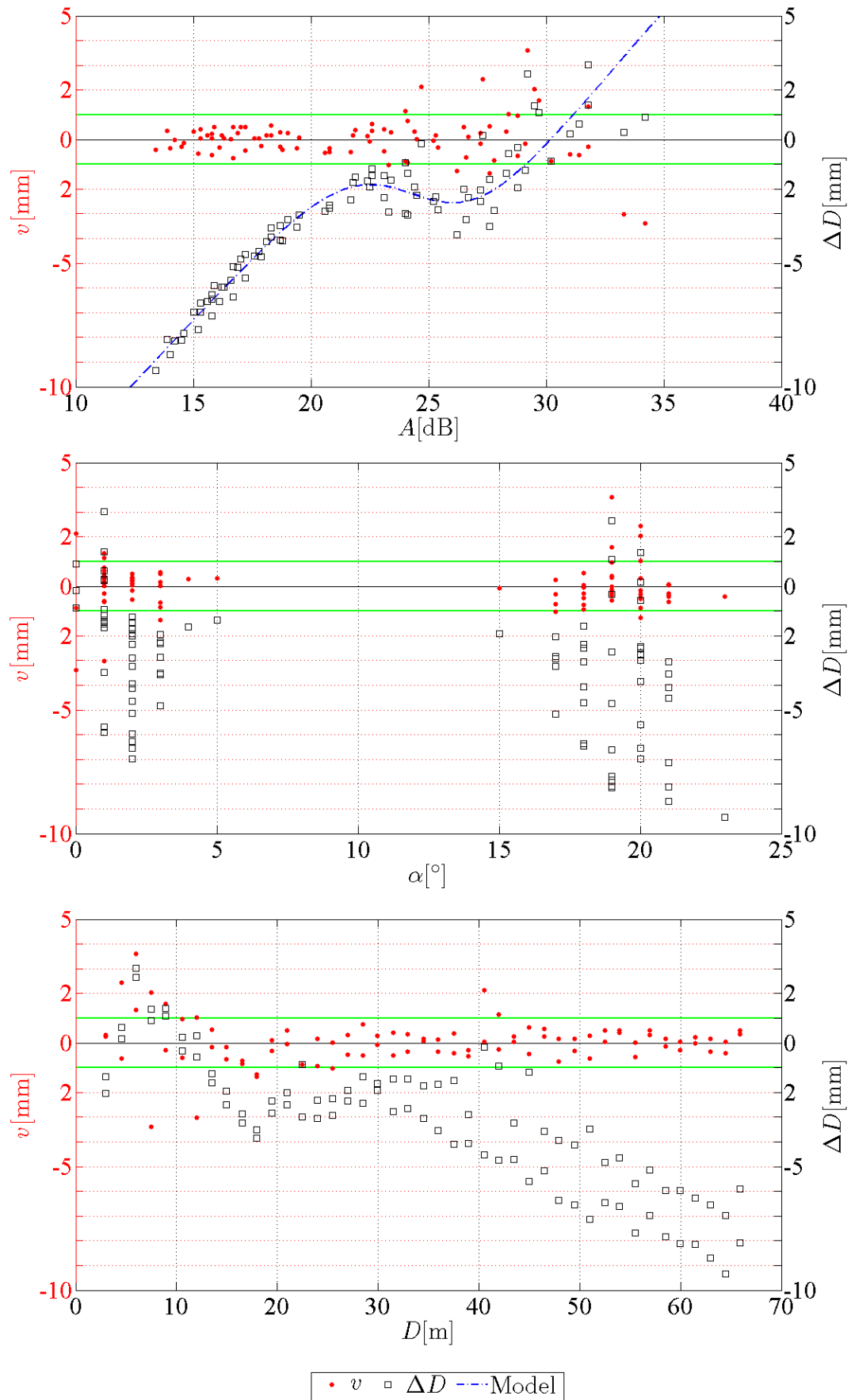


Figure 21: Residual pattern for T2.

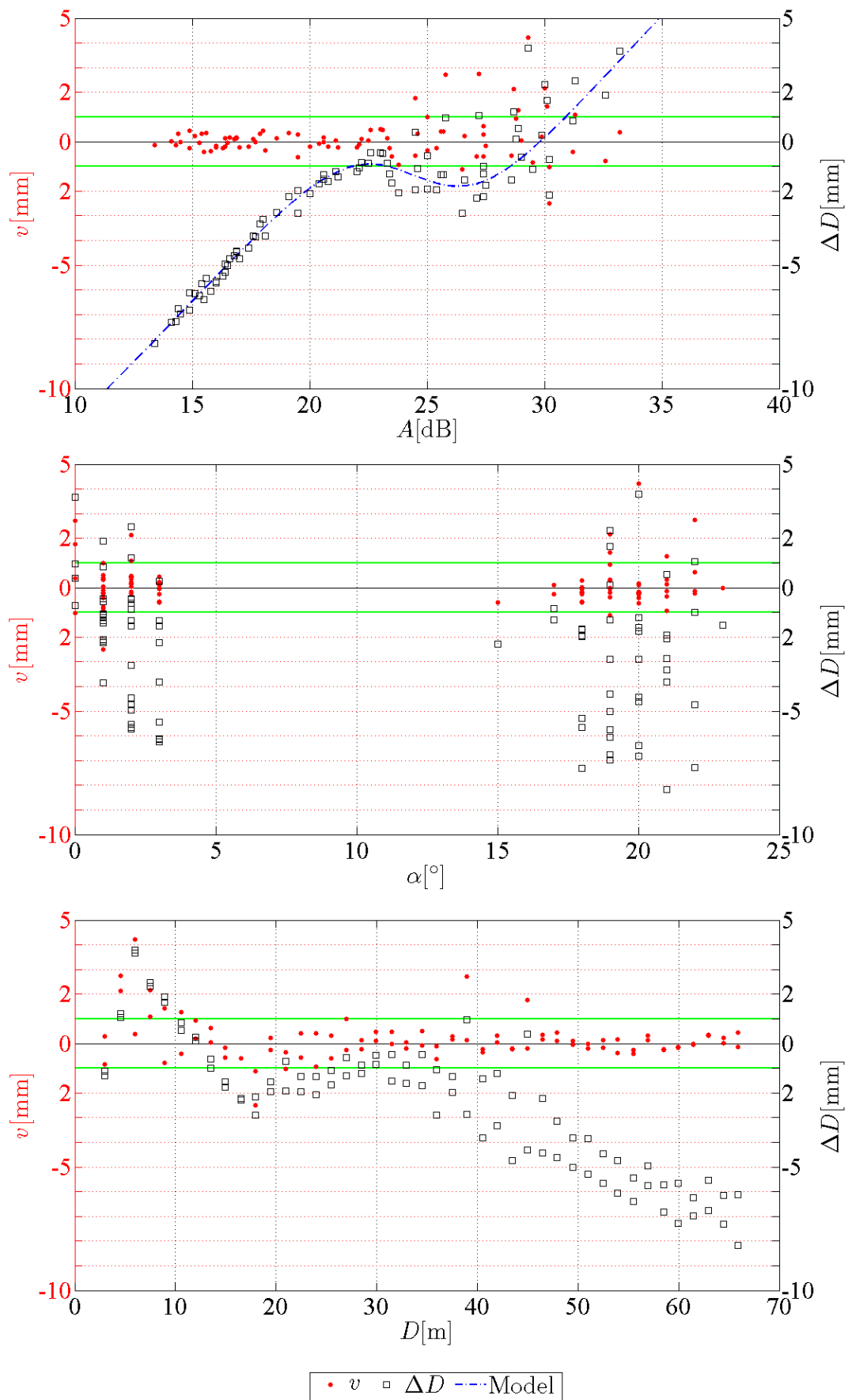


Figure 22: Residual pattern for T3.

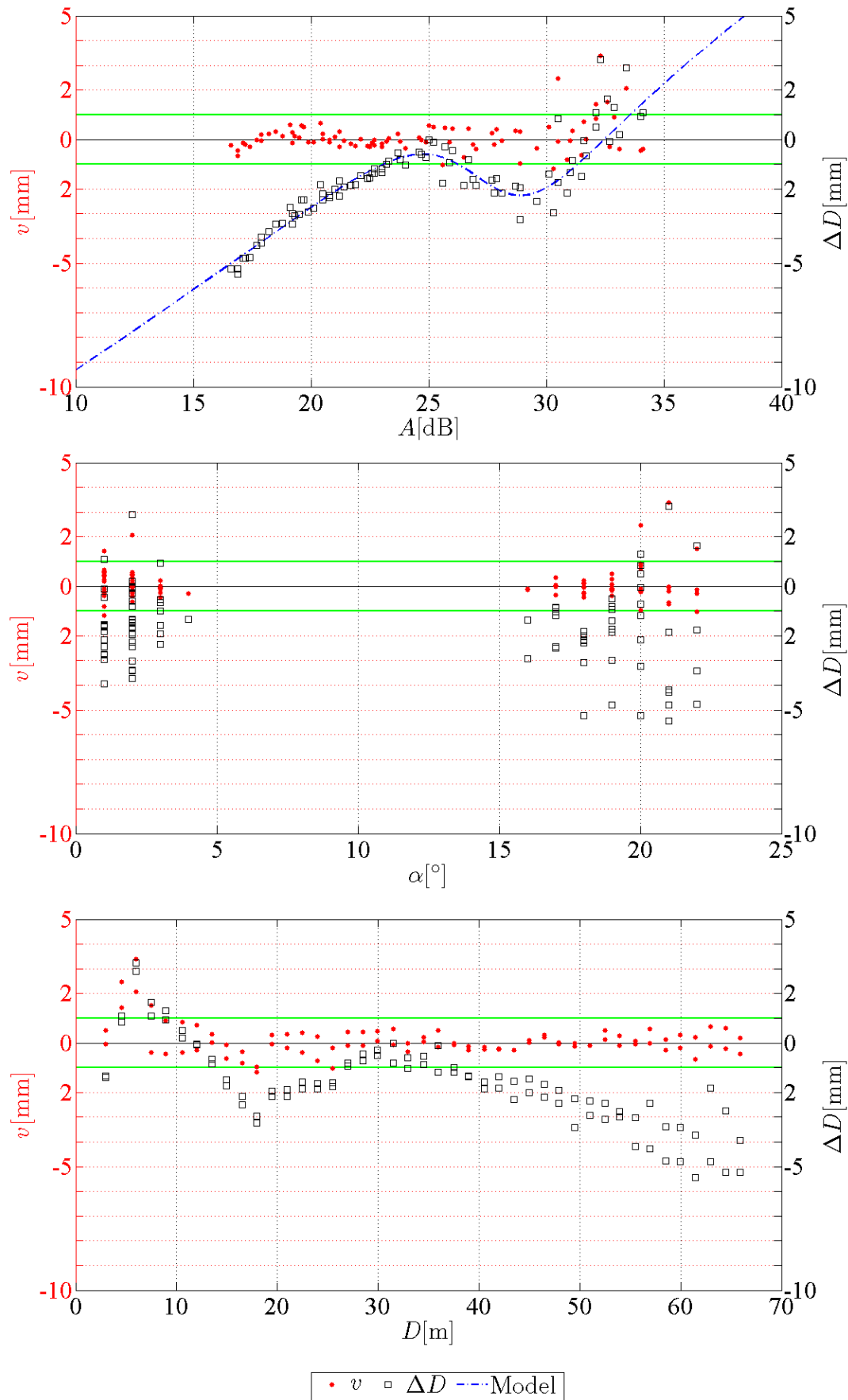


Figure 23: Residual pattern for T4.

3.2 Surface material response

Following the experiences from the last experiment it was also important to test the scanner's response to the variations in the surface properties. These results will be important for outdoor test 2 where the research objectives and characteristics dictate that the range precision and consequently the level of the instrument's detectivity should be tested with respect to the object's surface.

To be able to analyze how the reflectorless ranging precision in test 2 will be affected, six different samples denoted by S1 to S6 have been investigated in this test. The samples were carefully designed to replicate the most common surface conditions in the field. In Figure 24 the close-up images of the samples are shown to emphasize their distinct features. The samples represent not

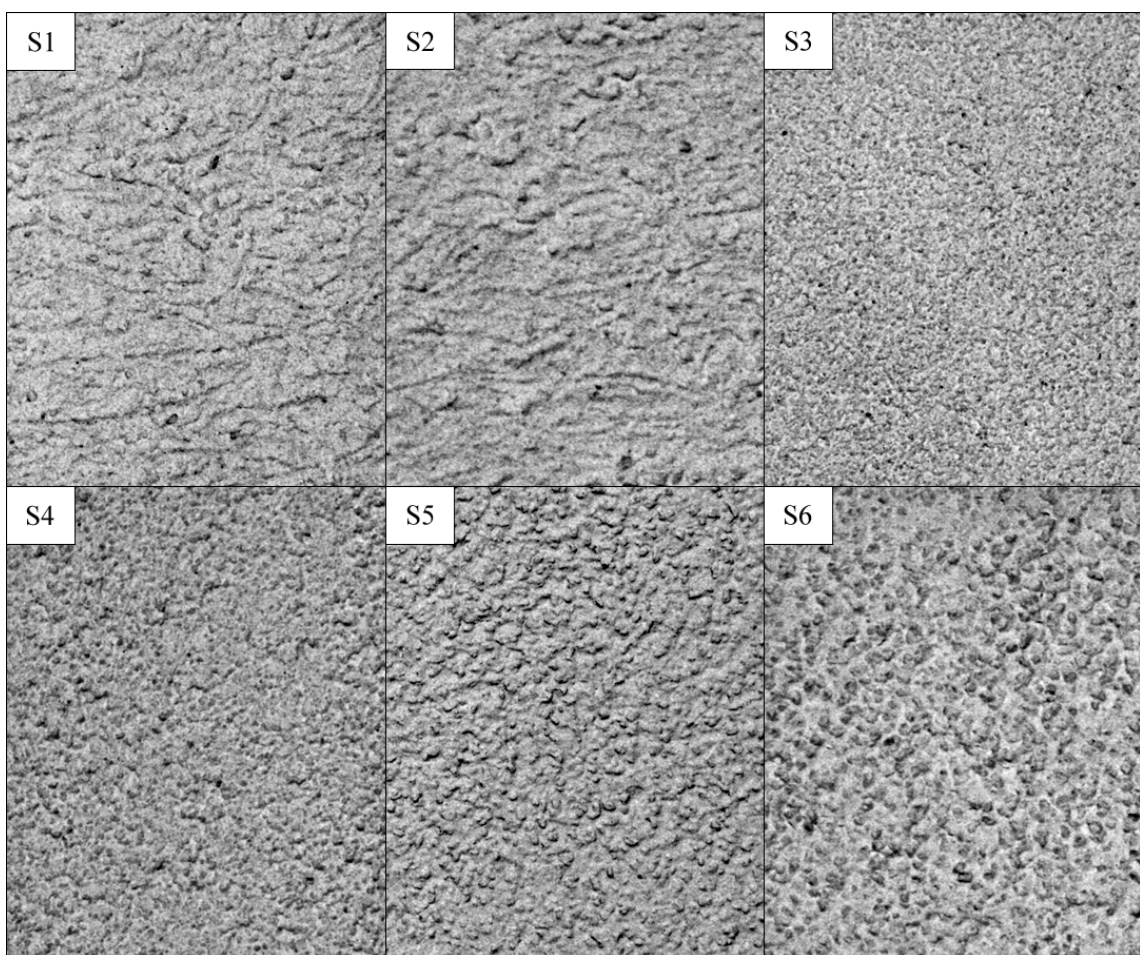


Figure 24: Close-up images of the tested samples each covering $\approx 5\%$ of the original sample area. The dimensions of the images are 12 cm x 9 cm.

only various levels of granulation but also differ by the way the grains are distributed. The top left two samples, S1 and S2, resemble the more non-uniform distribution achieved by scrubbing both surfaces. Compared to these two, all other samples were polished to result in a more homogeneous distribution. As for the grain size, four levels were used, i.e., 1.0 mm, 1.5 mm, 2.0 mm and 2.5 mm (see Table 4). The grains were finally embedded into plaster and brought onto the $\frac{1}{4} \text{ m}^2$ square

plates which can be seen in Figure 26 on page 50. Obviously, the size of the grains themselves and the surface roughness⁶ (σ_h) after the plate's assembly are not the same because of the plaster on the one hand and also because the latter was brought onto the plates by hand.

To estimate the actual surface roughness, each plate was scanned with the Metris D50 measuring arm (Nikon, 2010) which employs the triangulation principle to describe the object's geometry and has a specified single point precision below the $50 \mu\text{m}$, making it an appropriate device for the task. The results were high density point clouds containing more than one million points each. Due to the very low noise level of the instrument with respect to the grain size, most surface features of the individual plates could clearly be distinguished in the datasets. The resulting point clouds were then split into $2 \text{ cm} \times 2 \text{ cm}$ sized patches in order to determine also the local variations in surface roughness across the entire sample. On average the patch contained about 3000 points, which were used to estimate the reference planes, again based on the total least squares approach. These reference planes represent the mean height in the corresponding patches. By estimating local reference planes instead of only one for the whole sample, the effect of the plate's surface bending can practically be avoided. Finally, in Table 4 the information on the samples' properties is summarized. Clearly, the differences in $\bar{\sigma}_h$ are small, which raises a question whether or not this would lead to

Table 4: Sample properties. $\bar{\sigma}_h$ is the average surface roughness computed from 400 patches of each sample. In general, the average roughness represents 15 % of the grain size.

Sample	Grain size [mm]	$\bar{\sigma}_h$ [mm]	Note
S1	2.0	0.32	scrubbed
S2	2.5	0.36	scrubbed
S3	1.0	0.17	polished
S4	1.5	0.21	polished
S5	2.0	0.25	polished
S6	2.5	0.35	polished

different light scattering behavior for each sample, which could in addition also affect the distance precision. According to the Rayleigh criterion (Rees, 2001) all samples can be considered rough surfaces for the standard laser wavelengths but some deviations from an ideal Lambertian scatterer are expected. In contrast to the average roughness, the variations in the σ_h per patch are shown in Figure 25 reflecting the fact that the plaster was spread over the plates by hand. If the samples are to resemble the actual surface conditions in the field where such variations are always present, these should be included in the samples as well.

With the surface roughness analysis completed, the focus can now be shifted to the test which took place in the same 70 m corridor where the targets' calibration test was done. This time three tripods were placed approximately 20 m, 40 m and 65 m from one end of the corridor where an additional tripod was placed for the measuring instruments. Again, all the tripods were levelled with precise tubular levels. At each of the three stations, the plates were installed into a *fork-like* holder that could

⁶Here surface roughness is simply described as the standard deviation of the height variations from the mean height.

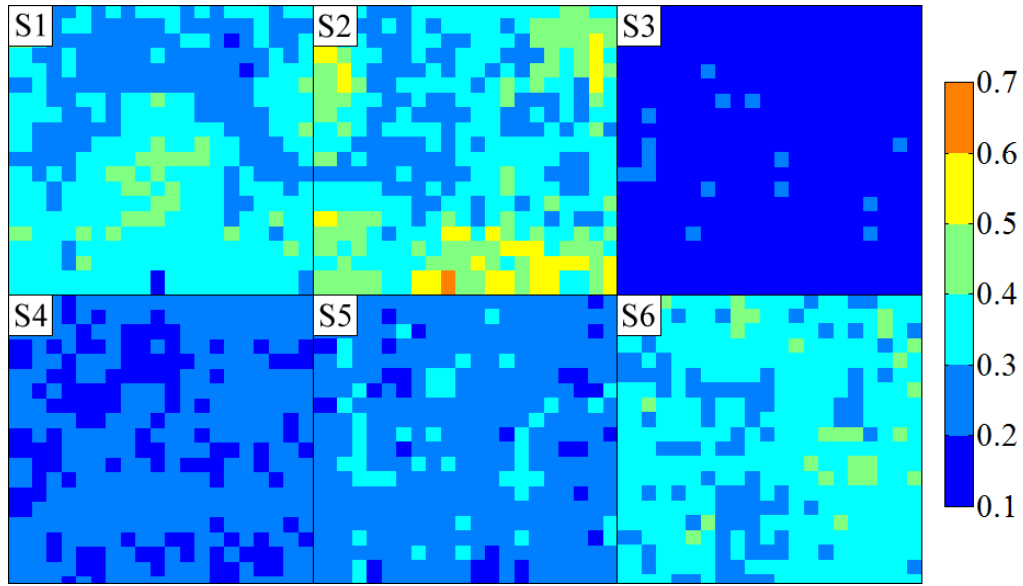


Figure 25: Surface roughness variations in [mm] – front view.

further be attached onto movable guide of a specially designed metal platform (see Figure 26). By

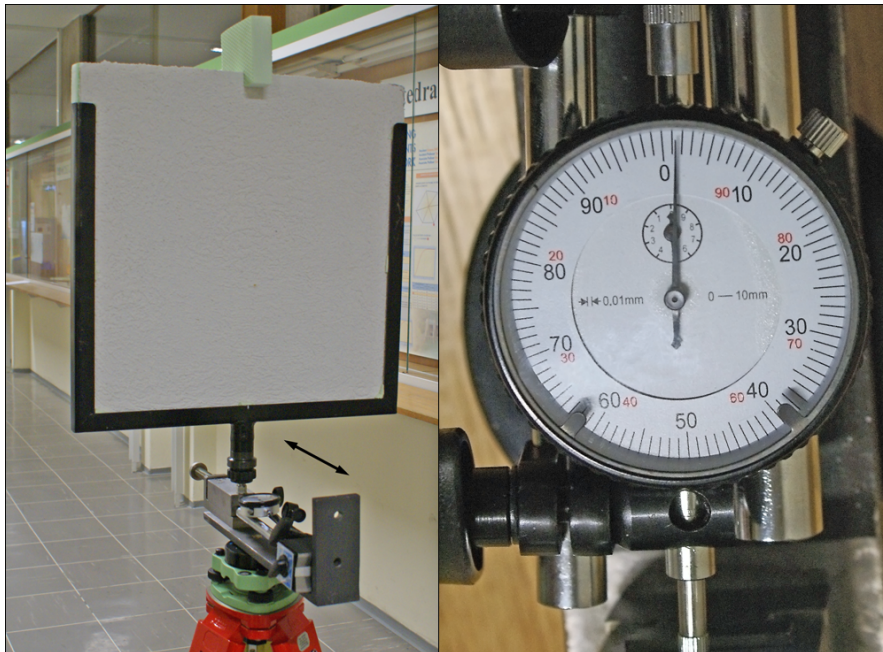


Figure 26: The plate holder and the measuring clock.

rotating the screw on one side of the platform the guide is able to slide along a single direction as indicated by the arrow in Figure 26. The last component is a measuring clock compressed between the guide and the other end of the platform which is bent upwards. One full turn on the clock represents a 1 mm shift as can be seen in Figure 26. Moreover, the holder could be rotated around the vertical axis; hence at every station the plates were scanned under three different incidence angles (20° , 45° and 60°) to see how the energy decrease would affect the distance precision not only with respect to distance but also in terms of the incidence angle. Finally, at each station and under every

incidence angle the plates were scanned in four guide positions; in the initial (reference) position and after the guide was displaced by 1 mm, 2 mm and 5 mm. This simulated displacement sequence was realized along the direction towards the scanner, which means the platform had to be oriented accordingly. The divergence between both, i.e., the sliding direction and the direction towards the scanner, had to be minimized but has little effect at this small displacement level. For example, the displacement of 5 mm on the clock along the 10° divergent sliding direction is less than 0.1 mm shorter than the displacement along the direction towards the scanner. Therefore, even the manual orientation of the platform, if careful, would introduce no significant impact on the results. Under the 45° and 60° incidence angle the plates were scanned in all guide positions only once, whereas under the 0° incidence angle five repeated scans were acquired in each guide position to analyze also the reproducibility and stability of the scanner. Following the presented measurement scheme, it took around six hours for the Riegl VZ-400 to finish the entire acquisition process. Afterwards, the clock's performance was checked also by classical terrestrial distance measurements with the GPH1P reflector attached onto the guide. At every station the distance was measured five times in all guide positions using the Leica TS30 tacheometer. The differences in the average distances and the clock's readings differed for less than 0.2 mm.

Obviously, the measurement scheme enables the evaluation of displacements relative to the initial guide position, whereas the scanner and the classical terrestrial measurements are not comparable at the millimeter level. All plates were scanned with a 5 mm raster resulting in approximately 6000 (0° angle), 4500 (45° angle) and 3000 (60° angle) points per scans with those lying close to the sides excluded from the analysis. Next, the planar model was fitted to the remainder of points. Even if the plates are not perfectly flat, this plays no role in the displacement calculation if their integrity remains unchanged. The estimated model parameters (centroids and normal vectors) provided the necessary input for the displacement calculation based on model 1, presented in section 2.8.1. Employing this deformation model it is only possible to determine displacements along some specified direction, in this case the initial normal vector. Hence, the direction of the initial normal vector has to coincide with the guide's sliding direction for the calculated displacements to correspond to the readings on the clock. This is not true under the 45° and 60° angles therefore all normal vectors must be divided by $\cos(\alpha)$.

The results of the test show that the incidence angle realization was within $\pm 2^\circ$. Furthermore, the ratios $\frac{A_{45^\circ}}{A_{0^\circ}}$ and $\frac{A_{60^\circ}}{A_{0^\circ}}$ indicate that on average 10 to 20 % more energy is returned as it should if the samples were ideal Lambertian surfaces. Despite these deviations, all samples produce similar scattering behavior, which means that the differences in surface roughness have little effect. Consequently, the similarities in amplitude can also be observed in the distance domain with the amplitude following the $1/D^2$ decay. Such an outcome suggests no significant difference between the samples should exist in terms of plane noise and in addition also of the level of agreement between the calculated displacements and the clock readings. Indeed, the analysis revealed that $\hat{\sigma}_0$ of the plane fitting process remained almost constant from one sample to the next. Moreover, the noise did not change very much up to 70 m under the 0° but it did as the angle was switched to 45° or 60° because the

level of reflected energy was now influenced by both parameters. In conclusion, the average $\hat{\sigma}_0$ of all the planes was around 1.6 mm and could reach up to 2.2 mm at 65 m and under 60° incidence angle. As for the level of agreement between the calculated displacements and the clock readings, this can be seen in Figure 27. The analysis of results in the time domain further suggests that some

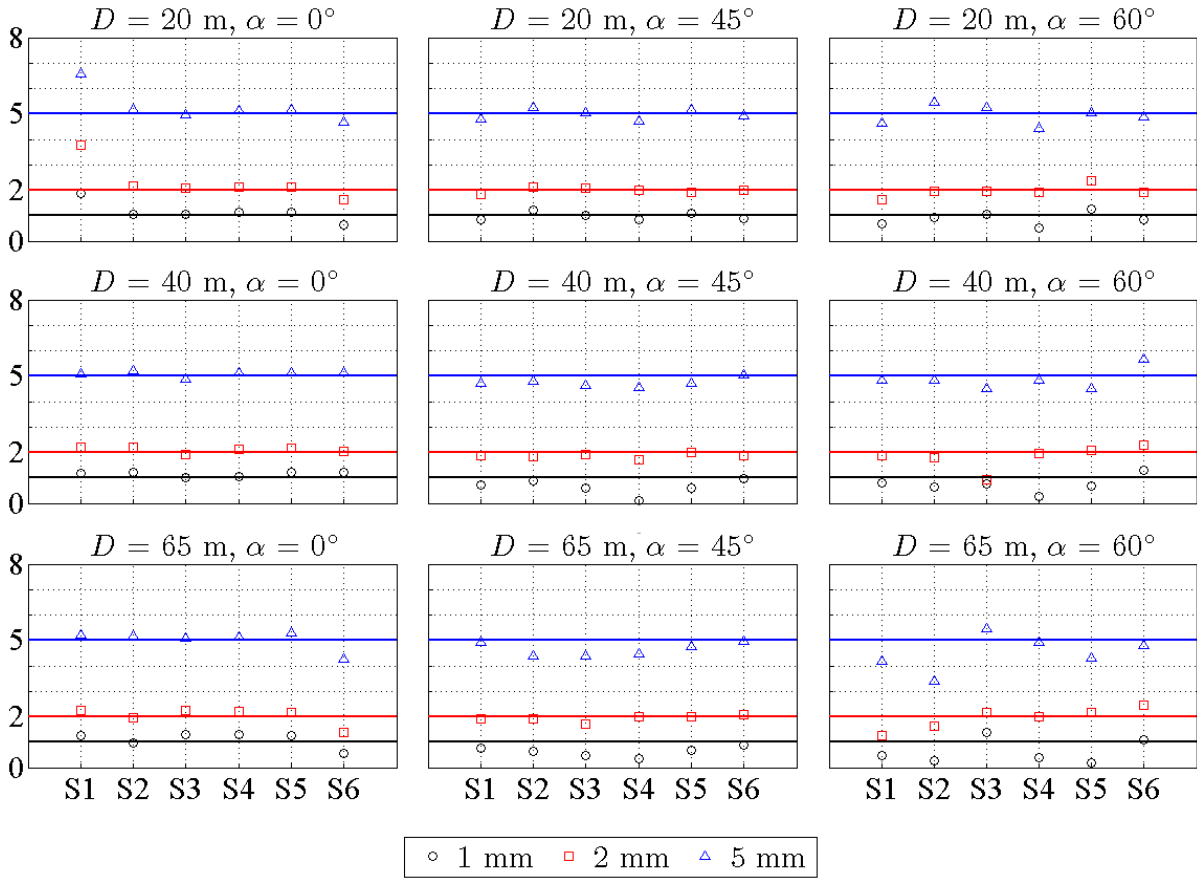


Figure 27: Displacement results in [mm]. Under $\alpha = 0^\circ$ the displacements are the result of averaging the five consecutive scans in each guide position.

deviations from the clock's readings could be produced by the power supply fluctuations since the scanner was running on batteries. This is most evident for S1 at 20 m and $\alpha = 0^\circ$ or S6 at 65 m and $\alpha = 0^\circ$, and can be explained by the very low battery power after few hours of scanning. Consequently, such periods of power shortages as well as the warm-up periods related to the instrument should be avoided. Based on the results in Figure 27, the calculated displacements become quite noisy at the 60° incidence angle, particularly at the distance of 65 m. On the other hand, the 2 mm and 5 mm displacements can be distinguished up to the 45° incidence angle regardless of the distance. As assumed, the quality of the displacement estimation is more or less the same for all samples with the deviations from the clock's readings reflecting the rangefinder deficiencies at this small scale level.

Finally, the results of scanning the multiples under the 0° incidence angle are shown in Figure 28 to reveal the reproducibility of the scanner. Clearly there is a slight deterioration in reproducibility with the increase in distance. In addition, the numbers related to the scanning sequence indicate

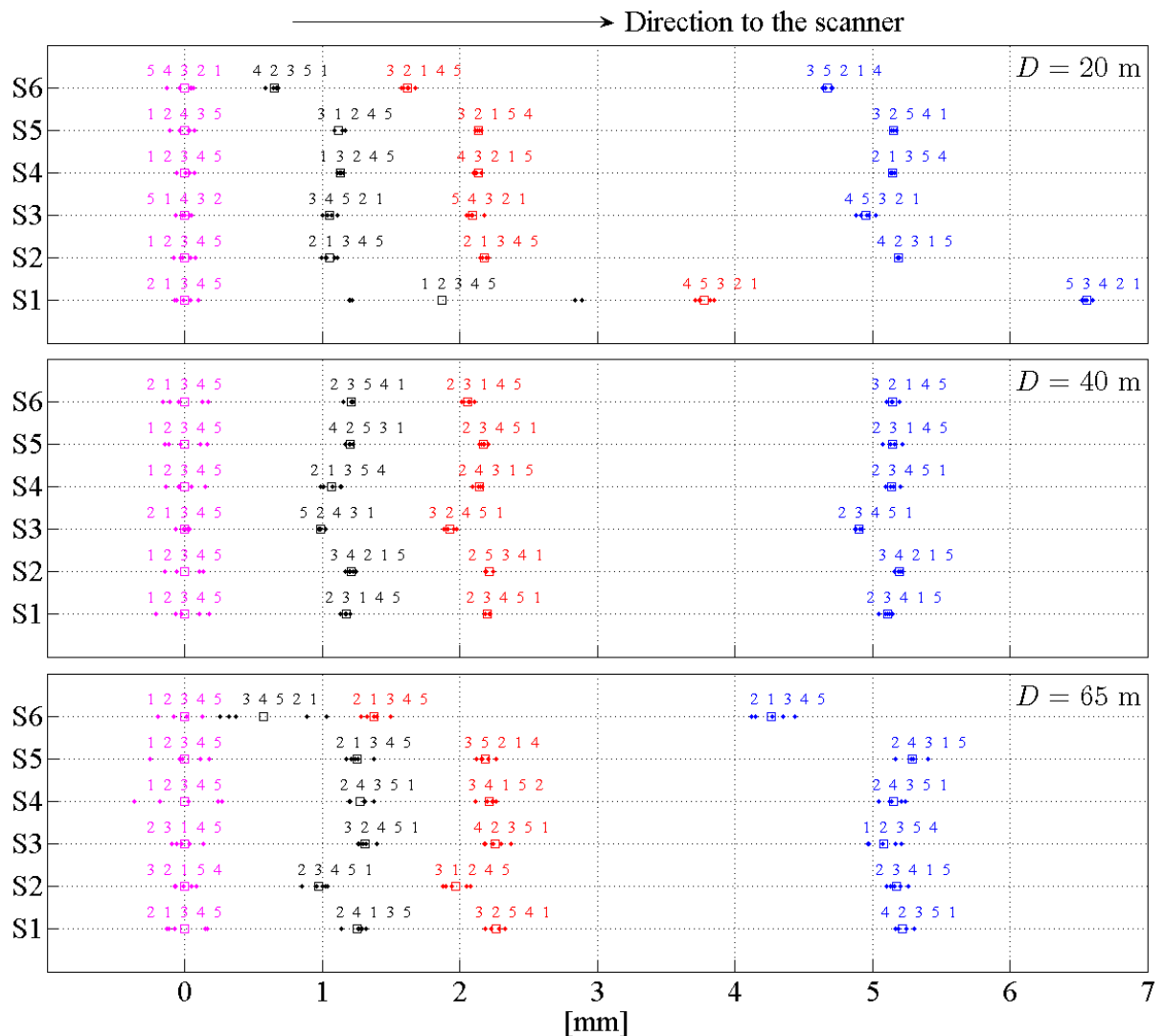


Figure 28: Multiples under 0° incidence angle. The numbers next to the dots represent the scanning sequence at a particular guide position. The average plane positions, already shown in Figure 27, are marked here by the squares.

the presence of systematic patterns at the initial guide positions, i.e., at the start of the acquisition process (see, e.g., S_1 at 40 m). In these cases the planes are initially furthest away and then shifting towards the scanner. Gradually, the patterns seem to disperse as the plates get displaced. So do the deviations from the mean planes, which are very small even at 65 m. In conclusion, averaging the results had no significant impact on the calculated displacements.

Based on the test results, the overall impression is that the average accuracy of displacements is well below the 1 mm boundary excluding the results at 60 m and 60° incidence angle. In order to evaluate the stability of deviations from the clock's readings with respect to the size of the scanned surface (and consequently the number of points), the initial area was reduced to 10 %. The average deviation remains almost the same at 20 % of the original window size as can be seen in Figure 29. Provided the surface was scanned with the 5 mm raster, the 20 % reduction level corresponds to the patch size which covers less than $10 \times 10\text{ cm}$ and contains around 250 points under 0° angle,

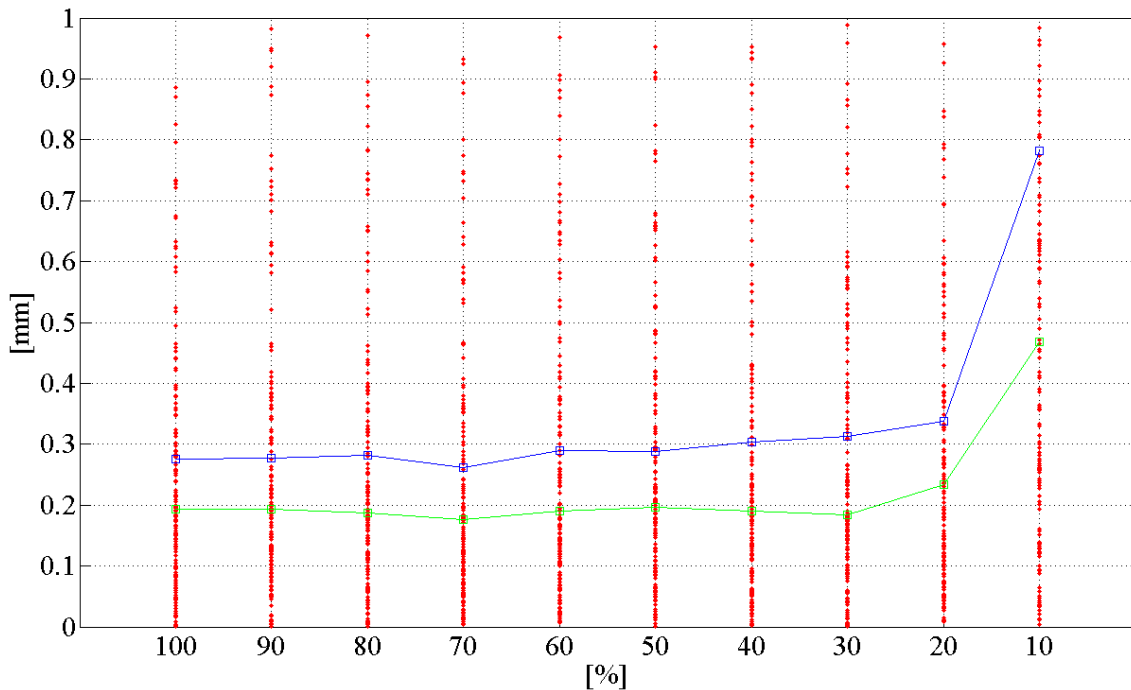


Figure 29: Deviations from the clock's readings at various reduction levels. The red dots represent the absolute values of all deviations, i.e., all samples at every station under the three incidence angles. The blue line indicates the average deviation and the green the median.

180 points under 45° angle and 100 points under 60° angle. This information was important when deciding on the point density in outdoor test 2 where this scanner was used as it showed how many points such a small patch should contain if the accuracy of displacements is to remain below the 1 mm boundary. Moreover, the scanner should be stationed near the object of study (e.g., $D < 50$ m) and the points scanned under the incidence angles larger than 45° should be excluded from the final deformation analysis. This way, the level of the instrument's detectivity would be the least affected by the rangefinder deficiencies and at least the 2 mm and 5 mm displacements, if they occurred, within its capabilities.

3.3 Outdoor test 1: Pipeline

3.3.1 The test field and its characteristics

The pipeline used in the outdoor research for the evaluation of deformations is part of the Slovene natural gas distribution network operated by the company Geoplin, the biggest distributor of natural gas in Slovenia. This network has been established for the transmission of gas for industrial facilities only, therefore the pressure inside the pipeline is very high (5000 kPa). Due to the high pressure level and variations in geomorphology, some parts of the network must be monitored con-

tinuously (annually) for possible displacements and deformations. The monitoring seems even more justifiable since in many of these critical locations the pipeline runs close to permanent human settlements. For the test field, the most problematic of these locations, which is situated about 30 km east of Ljubljana, was chosen (Figure 30). From Figure 30 it may be concluded that the pipeline

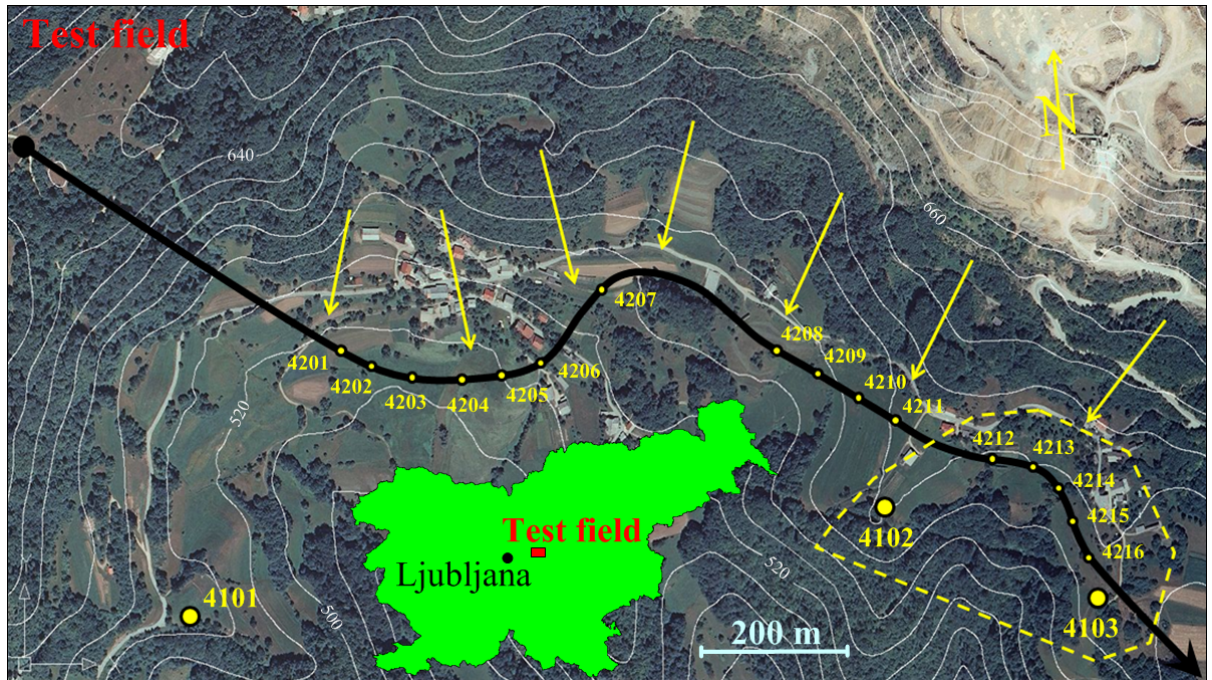


Figure 30: Orthophoto image of the test field. Due to the size of the test field and the research nature of this research project, only the area indicated by the dashed line was examined.

orientation is approximately parallel to the contour lines, making it extremely vulnerable to perpendicular tensions of the earth masses above the level of the pipeline (indicated with arrows). The height of the terrain decreases from north to south, with an average elevation being approximately 600 m. The sliding of the ground layers becomes even more intense during periods of heavy rainfall, particularly in spring and autumn. Therefore, the pipeline manager has already built a drainage system in some parts of the area in order to draw off the excessive water volume.

At the time of the construction in the late 1970s, when the pipeline was placed underground, special concrete pillars directly connected to the pipeline below were installed for geodetic observations. In Figure 30 these observation pillars are indicated as dots numbered from 4201 to 4216. The detailed presentation of the design of the observation pillars is depicted in Figure 31. Additionally, three different locations were chosen according to the preceding geological survey of the site where reference pillars 4101, 4102 and 4103 were grounded (Figure 30). These pillars were placed on a presumably stable ground in order to function as reference points for the comparison of displacements of the observation pillars and were not connected to the pipeline. However, the stability of the reference pillars had never been tested before this research was conducted.

As shown in Figure 31, the top of the reference and observation pillars is equipped with a metal platform and a screw, which is not completely in line with the pillar axis, used for mounting a sur-

veying instrument (e.g., an electronic tacheometer or a GNSS antenna) or a reflector. The steel bar connecting the observation pillars to the pipeline is about 8 cm in diameter and can be taken as solid, thus preventing occurrence of bending of the pillar axis when exposed to ground layer movements. The pipeline itself is also made of steel with 15 cm in diameter, which has to compensate for the tensions of the surrounding masses. So-far the stability of the observation pillars has been

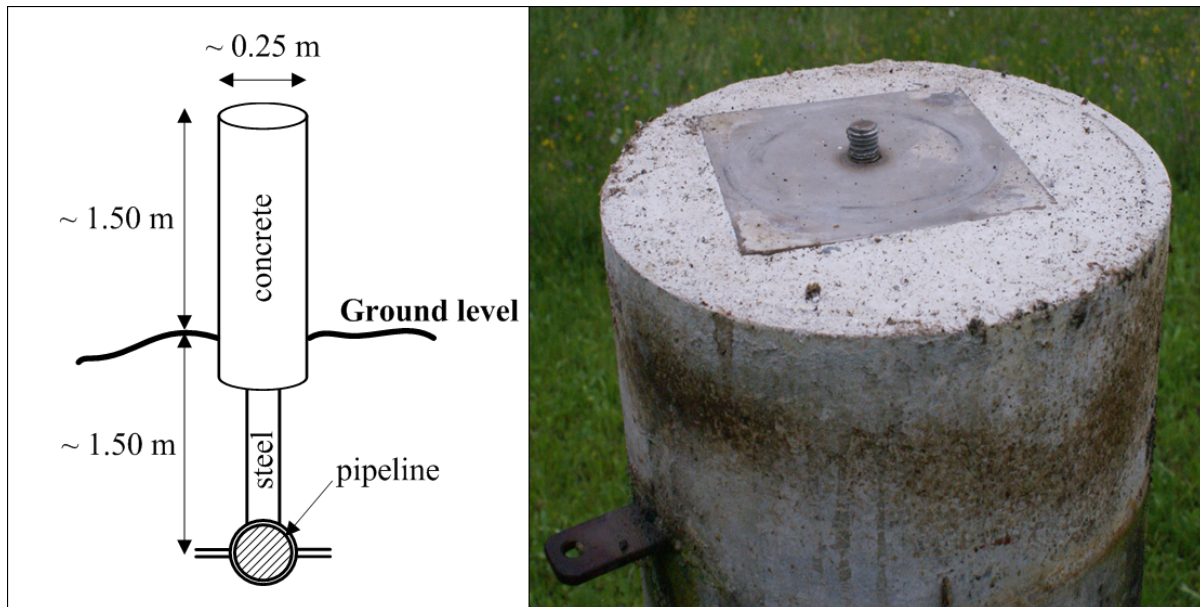


Figure 31: Pillars used for monitoring the movements of the underground pipeline.

investigated by means of simple tacheometric approach. The positions of the observation points were determined from the reference pillars 4101 and 4102 or from 4103, which were assumed to be stable. The observation points are located at the intersections of the screws and the top planes of the observation pillars, about 1.5 m above the ground level (Figure 31). If these pillars are exposed to inclinations produced by the sliding of ground masses, then the displacements of observation points cannot be taken as reliable measures of the actual movements of the pipeline underground. The inability to access the underground pipeline directly has therefore contributed to the conclusion that the representative points (section 2.8.2) for the displacement analysis could only be obtained on the basis of modelling the shape of the above-ground part of the observation pillars (Figure 31, left).

3.3.2 Field work

According to the methodology presented in Chapter 2, two measurement campaigns were carried out, the first at the beginning of June and the second at the beginning of November 2008, together reflecting the six-month period of possible deformation process. Due to the openness of the area and the lack of reliable orientation points, GNSS appeared to be more convenient for the reference frame realization. The short time span available between both measurement campaigns suggested only the occurrence of very small deformations (in the millimeter domain). Therefore it was assu-

med that the initial hypothesis could be put to a test.

Before the second measurement campaign in September and October 2008, several periods of high rainfall further increased the possibilities of the occurrence of landslides at the site of the research. The meteorological conditions were also quite complementary, the air temperature in particular, therefore the acquisition of physical properties of the atmosphere was necessary in order to compute the atmospheric distance corrections. The detailed values of the measured meteorological parameters of both surveying campaigns are summarized in Table 5. A precise Assmann psychrometer for the acquisition of air temperature and psychrometric difference was used (with the thermometer resolution of 0.1 °C). The air pressure was obtained using digital barometer Paroscientific, model nr. 760-16B, with the resolution of 0.01 mbar and relative precision of 0.01 %. When deploying the

Table 5: Atmospheric parameters of the two surveying campaigns, average values. All the atmospheric parameters were measured at the site of the instrument only.

Campaign date	Temperature [°C]	Humidity [%]	Air pressure [mbar]
June 2008	23.4	92.0	948.9
November 2008	-1.2	87.8	953.9

methodology into the field, it was obvious that if the high end precision of the representative points was to be achieved, it would have taken more than one day per epoch to measure all the observation pillars from Figure 30. Because the main goal of the research was to assess the capability of the proposed methodology for the deformation monitoring purposes, the decision was made to focus only on the easternmost part of the test field (the area indicated by the dashed line in Figure 30); therefore, only five observation pillars were used in the analysis of possible displacements (pillars 4212, 4213, 4214, 4215 and 4216). However, the GNSS observations were performed on all three reference pillars 4101, 4102 and 4103 to assure better geometry and more reliable displacement estimation. The geodetic network established for the purpose of the point cloud to the reference frame connectivity and the determination of the positions of observation points located on top of each pillar is shown in Figure 32. To exclude the possible errors due to variations in the network configuration, scanner targets were placed in the same locations in both epochs. Apart from the observation pillars (Figure 32), the scanner targets were placed onto the tripods. In the process of classical terrestrial measurements, also the reference pillars 4102 and 4103 were included which made it possible to compare the adjusted base distance 4102–4103 with the GNSS data.

In the geodetic network, all possible angles and distances were observed with altogether 19 instrumental stations in five sets of angles on each station, providing a high redundancy for the adjustment process, presented in subsection 3.3.3.2. The Leica TCRP 1201 electronic tacheometer, which is equipped with the ATR functionality, was used. The modulation frequency, additive constant, vertical index error and collimation error were tested beforehand by the official Leica representative; therefore, the instrument was working according to the manufacturer's specifications. For the signalization of network points, the Leica reflectors GPH1P, GPR121 and GMP101 were used. The additive constants of all reflectors were also determined prior to each measurement campaign. The

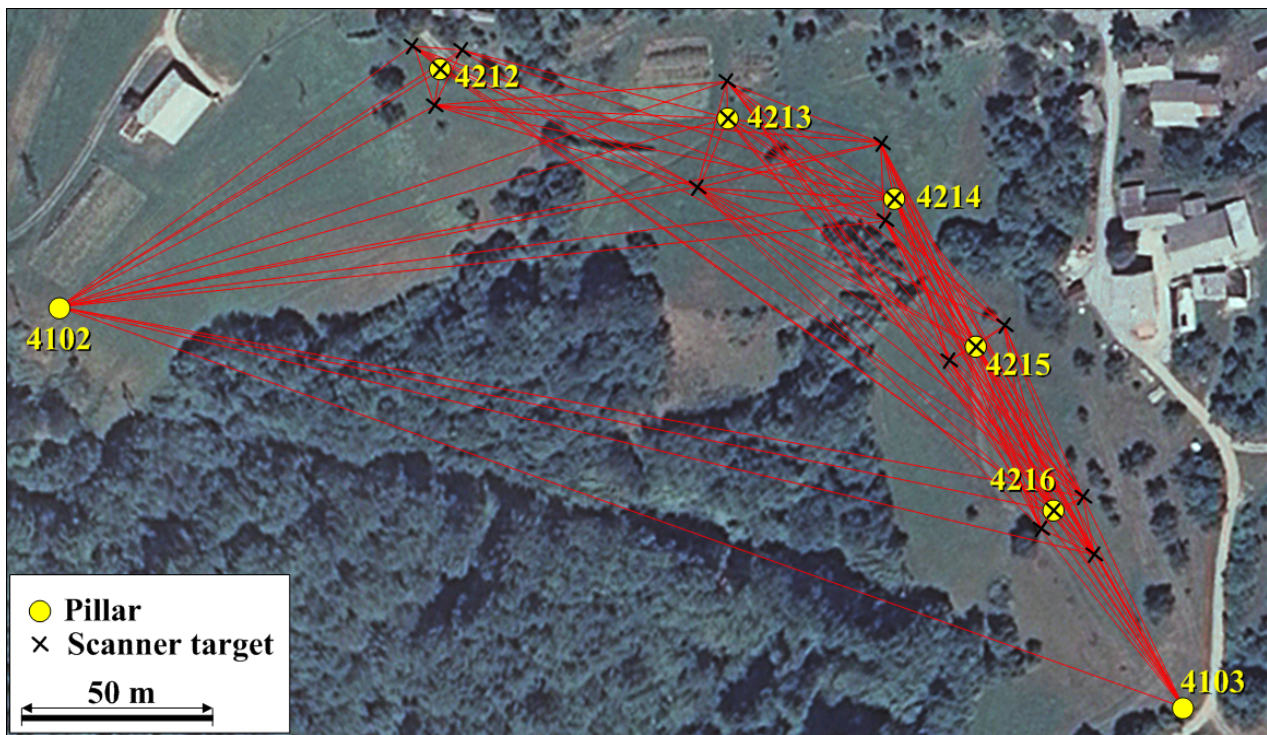


Figure 32: The geodetic network designed near the object of the study.

leveling of the instrument and reflectors was performed with precise tubular levels. After leveling all the tribrachs, they were not moved any more to avoid the occurrence of possible instrumental centering errors.

The scanning was performed from three different viewing angles for each observation pillar (Figure 33), using the Leica Scanstation 2 terrestrial laser scanner with stations regularly arranged around each pillar. At every scanner station, 4 to 5 Leica flat targets from Figure 2 (leftmost) were scanned. The average distance from the scanner to the pillar was about 10 m with the 2 mm raster on the pillar's surface, thus resulting in a very dense point sampling of each observation pillar. Compared to the electronic tacheometer, the scanner was not calibrated before each measurement epoch. One of the main reasons is that it was provided by the official Leica representative in Slovenia and was therefore assumed to be working according to the manufacturer's specification. The processing steps applied to the TLS data are presented in subsection 3.3.3.3. Altogether it took one whole day to perform the classical terrestrial and the TLS measurements in the field.

In each measurement campaign, the GNSS equipment was installed onto the reference pillars shortly after the classical terrestrial and TLS measurements were performed. The observations were carried out continuously for 2 to 3 additional days, using dual frequency Trimble 4000 SSE/SSI receivers with Trimble Compact L1/L2 with ground plane antennas or Trimble Geodetic L1/L2 with ground plane antennas. The minimum elevation angle was chosen on the basis of recommendations for high precision processing (found in IGS, 2009 and EPN, 2009) and software processing characteristics (Dach et al, 2007). It was set to 0° to estimate troposphere parameters and height with higher reli-

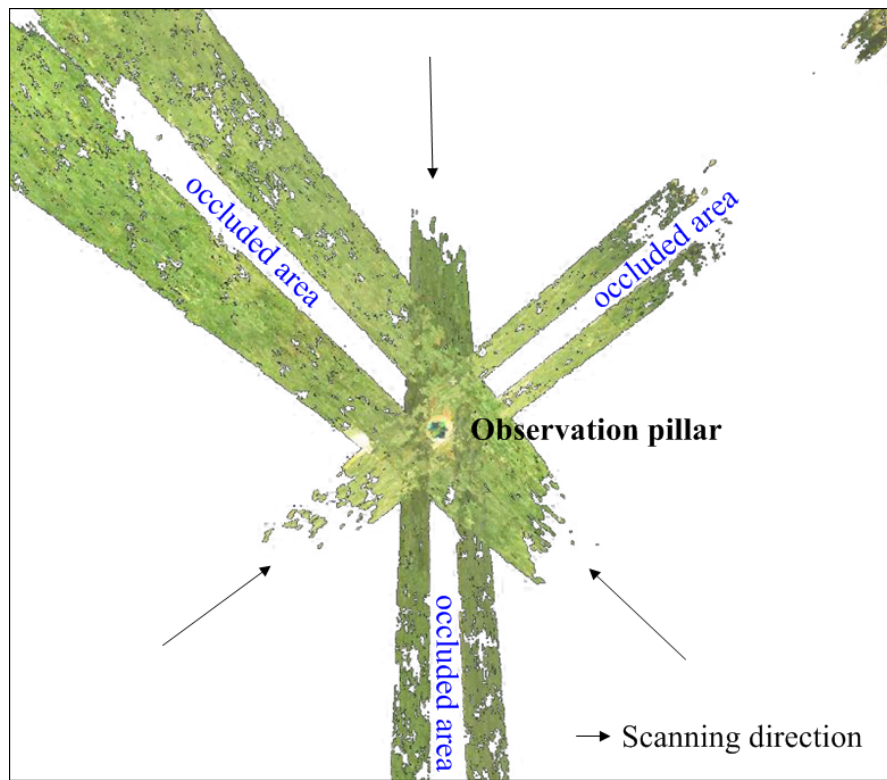


Figure 33: Scanner positions with respect to the observation pillars (top view). The adjacent point clouds had an overlap of approximately 30 %.

ability (Even-Tzur et al, 2004). The sampling interval was set to 15 s. The characteristics of both campaigns are listed in Table 6. The tribrachs on pillars 4102 and 4103 previously used for classical

Table 6: GNSS campaign characteristics.

Campaign date	Min. elevation angle/Sampling rate	Duration
June 2008	0°/15 s	48 hours
November 2008	0°/15 s	72 hours

terrestrial measurements were removed only after the GNSS observations had been finished to assure no centering error was embedded when switching the instruments. In both campaigns enough GNSS observations were collected for high precision position determination.

3.3.3 Results

After the data acquisition phases had been completed, the next step implied the processing of the raw measurements in order to obtain the input parameters for deformation model 2 (representative points, section 2.8.2). The alternative model (truncated direction, section 2.8.1) was not used in this test. Each measurement technology involved was processed separately. First the coordinates of the reference pillars had to be determined on the basis of GNSS observations. These were later supplied

to the classical terrestrial adjustment computation resulting in scanner target positions used for the absolute orientation of the point clouds as well as observation points located on top of each pillar. Finally, the pillar shape models were determined in a further adjustment procedure. The following subsections are devoted to a more detailed presentation of the data processing characteristics of the individual technologies involved.

3.3.3.1 GNSS

Following the recommendations from section 2.2, the realization of the reference frame in a homogenous way was ensured by tying the reference points (step 1 of the general workflow, section 2.1) to the global IGS network of permanent GNSS stations. For wider local stability of the reference frame also nearby GNSS stations from Slovene permanent network called SIGNAL (2009) were included in the processing of the observations. Furthermore, it was important to decide which of these stations should be treated as reference and which as control stations. The selection criteria were based on the station installation epoch, location and quality of stations as proposed in Bergeot et al (2009). The permanent stations GRAS, MATE, PENC, SOFI, WTZR and ZIMM were treated as the reference stations while all others were defined as the control stations. The ITRF2005 (Altamimi et al, 2007) was chosen as the reference coordinate frame (ITRF, 2009). The locations of all permanent stations used in GNSS data processing are presented in Figure 34. In each measurement

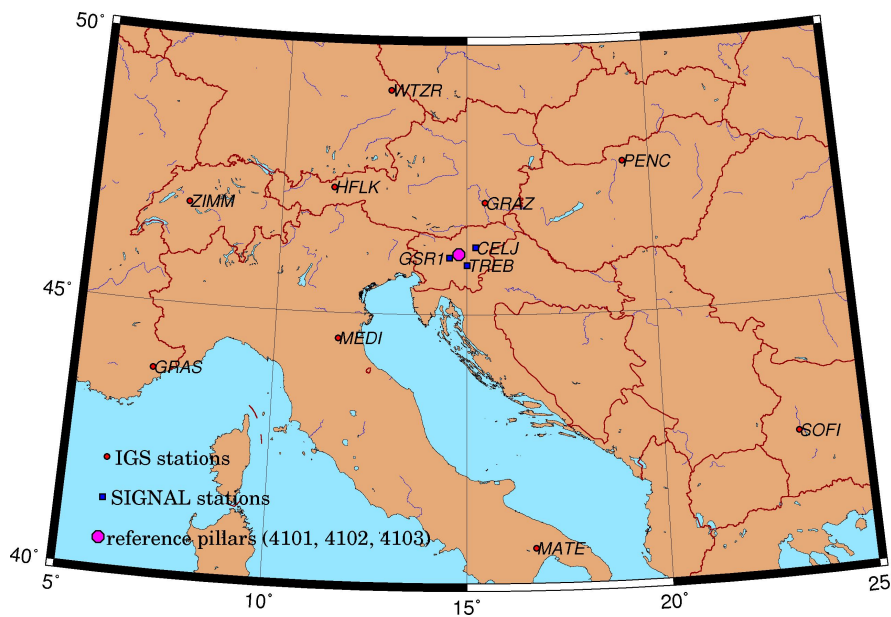


Figure 34: Locations of permanent GNSS stations.

campaign, the data was processed in one step on the basis of ionosphere free linear combination and ambiguities fixed as integer values. The software used was Bernese GPS Software, Version 5.0 (Dach et al, 2007). The precise IGS orbits were considered (Beutler et al, 1999) with corresponding Earth Orientation Parameters. Additionally, the solid Earth tides and ocean tide loading were

applied as proposed by McCarthy and Petit (2009), with ocean tide loading coefficients obtained from Onsala Space Observatory (2009) and processed according to the GOT00.2 model. Next, the GNSS antenna phase center variations were modelled with the relative antenna calibration parameters provided by IGS. The estimation of zenith tropospheric delay was carried out according to the Saastamoinen a priori model and Niell mapping function (Niell, 1996) for each hour. The final solutions included modelling of tropospheric azimuthal asymmetries with gradient estimation model (Dach et al, 2007) and were based on the free net estimation.

Ambiguities as the integer values were estimated on the basis of two algorithms. For short baselines (up to 150 km), the SIGMA algorithm (Dach et al, 2007) was used in two steps; initially on the wide-lane linear combination (L5) and secondly on both carrier frequencies, i.e., L1 and L2, based on wide-lane ambiguities. Long baselines (over 150 km) were resolved on the basis of QIF algorithm (Mervat, 1995).

As mentioned, the final coordinates are estimated in the ITRF2005 reference frame for both campaigns. Due to tectonic motions of the Eurasian plate, the transformation of the estimated coordinates into ETRF89 was performed (Boucher and Altamimi, 2008). Finally, the 3D geocentric ETRF89 coordinates were transformed to the state planar coordinates (e.g., transverse Mercator projection) where they can be further used for the classical terrestrial surveying (step 2 of the general workflow). In order to assure identical coordinates in both campaigns for further processing of classical terrestrial and TLS measurements, a rigid translation of 4102 and 4103 station coordinates from November to June coordinate values was performed. In Table 7, the estimated coordinates with corresponding standard deviations of the reference pillars for both campaigns on the state projection plane are given. Because heights of the network points were determined on the basis of

Table 7: Estimated coordinates of reference pillars.

Pillar	E [m]	σ_E [mm]	N [m]	σ_N [mm]	Epoch
4101	482 459.5975	1.0	108 430.2116	2.0	Jun 2008
	482 459.6140	1.0	108 430.1959	1.0	Nov 2008
4102	483 370.3219	1.0	108 571.3014	2.0	Jun 2008
	483 370.3219	1.0	108 571.3017	1.0	Nov 2008
4103	483 681.1483	1.0	108 464.2422	2.0	Jun 2008
	483 681.1483	1.0	108 464.2419	1.0	Nov 2008

trigonometric levelling (section 3.3.3.2), they are not presented in Table 7. The standard deviations presented in table 7 are the outcome of multiplying the coordinate precisions obtained by Bernese GPS Software, Version 5 processing with a factor of 10 as proposed in Mao et al (1999).

3.3.3.2 Classical terrestrial method

By performing the classical terrestrial measurements in five sets of angles, the first step of the data processing phase included the computation of mean values of individual measurements. In order to

properly reduce the slope distances, the meteorological distance correction factors were computed using temperature, air pressure and partial water vapor pressure provided by the psychrometric and barometric measurements. For the computation of the partial water vapor pressure, the Sprung equation was employed for the Assmann aspiration psychrometer. The saturated vapor pressure was computed according to the Magnus-Tetens equation. The standard and the actual refraction indexes of the atmosphere were determined according to Ciddor (1996) and Ciddor and Hill (1999). In the process of applying the distance correction factors, only the first velocity errors were taken into account. The second velocity errors were neglected since for the distances at the range of 400 m the value of the second velocity error is approximately 10^{-5} mm.

Furthermore, the error caused by the bending of the laser ray in the atmosphere was also skipped since it accounts for about 10^{-6} mm at 400 m, which is more than the largest measured distance. The corrected distances were then reduced to the pillar level using the measured instrument/reflector height. Contrary to that, no height offset was measured when placing the instrument/reflector on the tripods. Finally, the distances were first transformed onto the reference ellipsoid surface and next onto the national cartographic projection plane. The first transformation was only possible after the determination of the height differences between all points.

For the computation of height differences, the trigonometric levelling method was utilized. The computed height differences were then adjusted according to the least squares adjustment principles, using point 4102 as a reference. In this way, the heights of the network points above sea level were obtained along with the precision parameters. According to the results, the average standard deviation of the height in the first campaign was 0.5 mm and 0.4 mm in the second. If we were to get the correct heights of the scanner targets needed for the absolute positioning of the point clouds, also the vertical offset between the targets and the reflectors would have to be taken into consideration.

The last part of the classical terrestrial processing involved the least squares adjustment of all of the measured and properly reduced quantities for the estimation of the planar coordinates of the network points. All angles were assigned equal weights since the conditions throughout the individual campaigns did not change substantially. Equal weights were also applied to the network distances being relatively short and measured with almost the same precision. The observations were first adjusted as a free network with the minimum trace of the cofactor matrix of coordinate unknowns. Only in this way it is possible to obtain the precision of the measured quantities independently of the network datum. Moreover, the Baarda's Data Snooping was employed for the detection of potential gross errors, providing information on the internal and external reliability of the network (Caspary, 1988). In the next step, the adjustment was repeated with point 4102 assumed to be stable and the direction angle from 4102 to 4103. The two reference points showed no displacements between both epochs, as it was concluded from the GNSS observations (see section 4.1.1). The results of the final adjustment are shown in Table 8.

Table 8: Results of the adjustment using minimum datum parameters: a posteriori standard deviations, precisions of the adjusted observations and positional precisions of the network points.

Epoch	$\hat{\sigma}_0$	$\hat{\sigma}_{H_z}$ ["]	$\hat{\sigma}_D$ [mm]	$\hat{\sigma}_{\text{pos,max}}$ [mm]	$\hat{\sigma}_{\text{pos,min}}$ [mm]	$\hat{\sigma}_{\text{pos,avg}}$ [mm]
Jun 2008	0.99994	1.4	0.5	0.3	0.2	0.2
Nov 2008	1.00002	1.3	0.4	0.2	0.1	0.2

3.3.3.3 Terrestrial laser scanning

The initial phase of the TLS data evaluation included the point cloud positioning process (section 2.5). The average absolute orientation accuracy, including both campaigns, was $\sigma_{AO} = 1$ mm. Once again, in this test, the extraction of the target centers was done based on the amplitude weighted mean algorithm using a target scanning mode which produces a dense point pattern of the inner part of the target area only. In this scanning mode, the range error was applied simultaneously using the in-built correction factors provided by the manufacturer which are stored in the scanner. Therefore, compared to the Riegl scanner, no separate tests had to be done beforehand in order to estimate and model the range biases. The absence of any significant systematic errors originating in the absolute orientation was confirmed by the extensive visual analysis in the overlapping sections of adjacent point clouds. After positioning, the data not belonging to the pillar surface was manually removed from the point clouds, resulting in about 250 000 points per pillar which were then used for modelling the shape of the pillars.

According to step 6 of the general workflow, the pillars were modelled by using the cylinder model determined in the least squares adjustment process, as described in Luhmann et al (2006). To compute the cylinder parameters, a minimum of 5 points is required, minimizing the orthogonal distances of points $P_i(x_i, y_i, z_i)$ from the corresponding best-fit surface (see Figure 35):

$$d_i = r_i - r \quad (23)$$

where:

$$r_i = \frac{\sqrt{u_i^2 + v_i^2 + w_i^2}}{\sqrt{a^2 + b^2 + c^2}} \quad (24)$$

and:

$$\begin{aligned} u_i &= c \cdot (y_i - y_0) - b \cdot (z_i - z_0) \\ v_i &= a \cdot (z_i - z_0) - c \cdot (x_i - x_0) \\ w_i &= b \cdot (x_i - x_0) - a \cdot (y_i - y_0) \end{aligned} \quad (25)$$

Despite the fact that the cylinder is defined by:

- the point on the axis: $P_0(x_0, y_0, z_0)$,
- the direction vector: $\vec{s}(a, b, c)$,

- radius: r ,

only five of these parameters are linearly independent (x_0, y_0, a, b, r). Since the minimization function d is nonlinear, the unknown parameters are computed in an iterative procedure. The adjust-

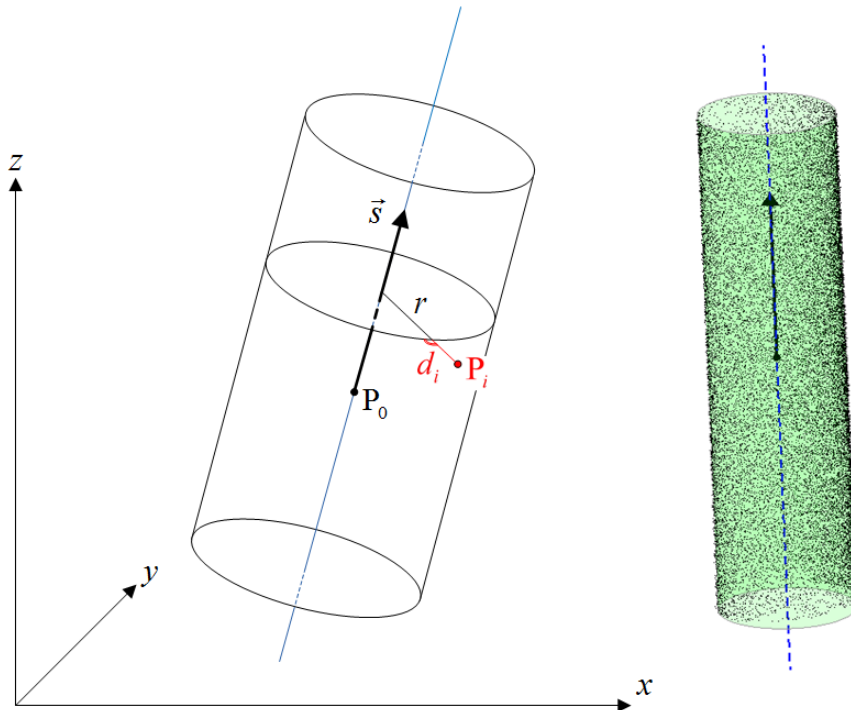


Figure 35: Cylinder parameters, determined in the adjustment process (left) and one example of the results in MATLAB, showing the estimated cylinder axis (right; only every 10th point is drawn).

ment process resulted in the average a posteriori value of 1.3 mm in both campaigns including all observation pillars ($\hat{\sigma}_{0,\min} > 1.1$ mm, $\hat{\sigma}_{0,\max} < 1.5$ mm). All values are well below the noise level of 2 mm stated by Leica Geosystems for the Scanstation 2 scanner. Additionally, the histograms of residuals d_i indicated that no blunders were present in the data, which was also confirmed by the Gaussian probability distribution of the remaining errors. The spatial distribution of residuals suggests that the selection of the scanner locations, as shown in Figure 33, actually compensated for the considerable errors of individual scans in the scanning direction, which is one of the downsides of the time-of-flight type scanners. In this way, the influences of the range inaccuracies had a more or less homogeneous effect on the computed cylinder parameters. An example can be seen in Figure 36 showing the spatial distribution of residuals and its schematic explanation in the case of pillar 4212. The same outcome was observed for other observation pillars. The examination of the spatial distribution of residuals in the overlapping areas provided an additional confirmation of the quality of absolute orientation which could finally be considered free of systematic errors.

Next, the validity of the models was investigated. The analysis of the quality of the fitting (i.e., residual patterns) indicated that the pillar shapes are almost cylindrical with small systematic deviations below ± 1.5 mm. However small, these error trends became clearly visible after switching to

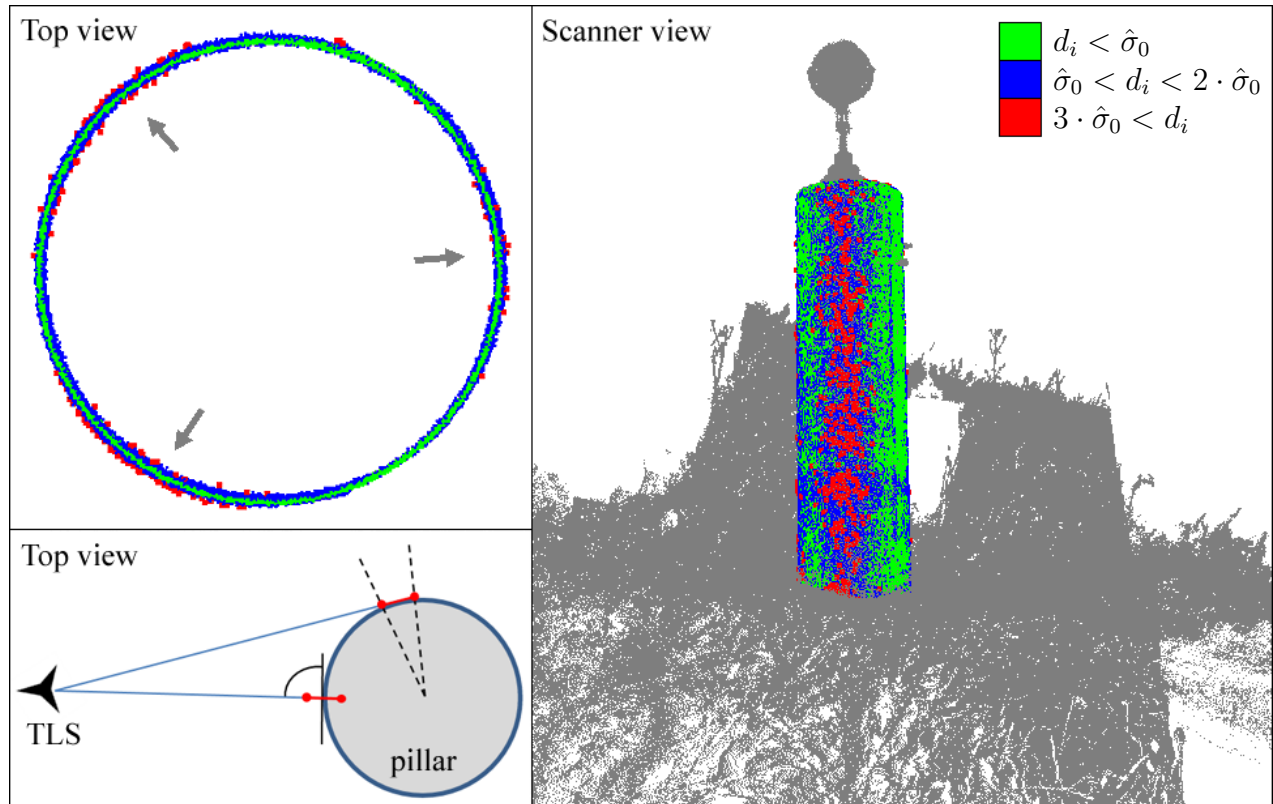


Figure 36: Example of the spatial distribution of residuals superimposing the point clouds (right image). The largest residuals occur in the scanning directions, indicated by the arrows in the upper left image. Despite similar range inaccuracies, minimizing the orthogonal distances r_i resulted in smaller residuals near the sides of the pillars (lower left image).

cylindrical coordinate system (Θ, z, d_i) suggesting the pillars were somewhat but not exactly elliptical in the azimuthal direction. In the height direction, some pillars widened from top to bottom while others had a more convex surface. At this small deviation level none of the patterns followed a simple mathematical description. In general, pillar 4212 experienced the largest whereas pillars 4215 and 4216 the smallest deviations. Pillar 4212 also had the most distinct elliptical pattern in the azimuthal direction.

In terms of temporal stability, the patterns of individual pillars were consistent in both epochs, therefore affecting the cylinder parameters in the same way. Consequently, the actual shape of the above ground part of the observation pillars was not deformed due to any external force. The consistency of individual patterns was not only tested visually but also by subtracting the pairs of November and June grids created from cylindrical coordinates of corresponding point clouds. Figure 37 shows the two grids for pillar 4212 with a cell size of 5 cm. Before the subtraction, the Gaussian low-pass filter was applied to the grids in order to preserve most of the actual trend but avoid local fluctuations coming from measurement errors. The grids shown in Figure 37 are the result of employing this filter, revealing the near elliptical surface of pillar 4212. Subtracting the grids, the trends were minimized well into the submillimeter domain therefore it was concluded that the shape was left un-

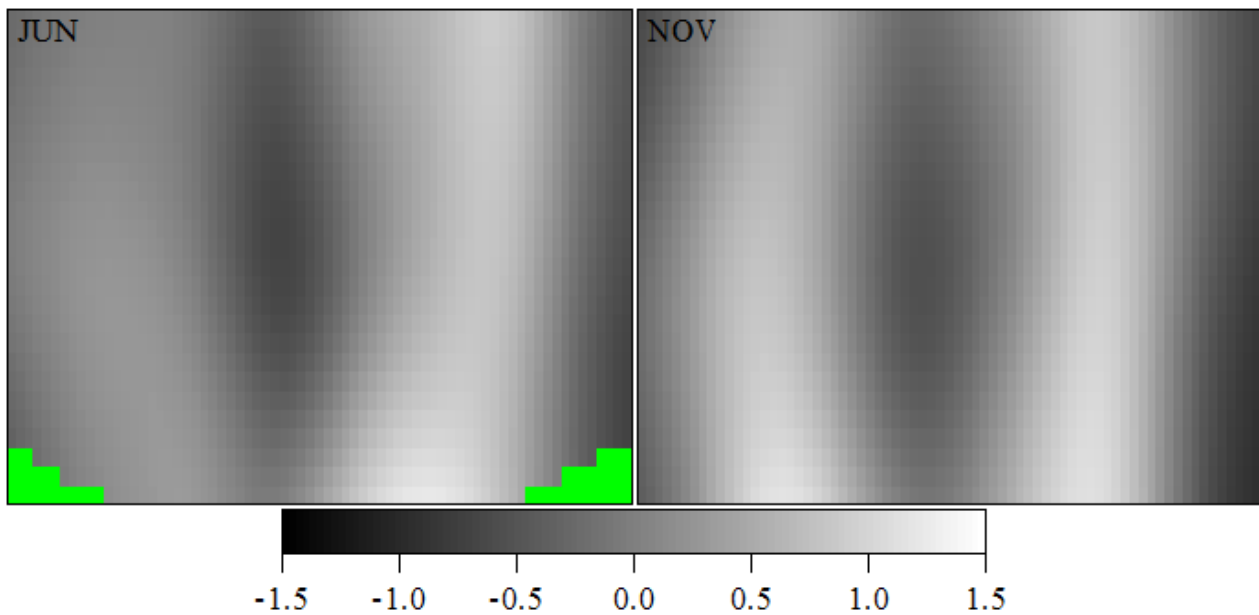


Figure 37: Residual pattern grids for 4212. The green represents the missing data due to high grass in the June campaign.

changed. The question remained if the estimated cylinder parameters were in any way affected by a particular scanning direction. In both measurement campaigns the locations of the scanner stations did not vary much but were not precisely the same. To provide answers, an additional survey was carried out at the site of pillar 4212 since it was this pillar that experienced the largest deviations from the model. Should the scanning direction have any significant effect, it would be exposed at pillar 4212.

The additional survey resulted in point clouds which had been acquired from nine different stations, regularly arranged around the pillar. The surface of the pillar was scanned with the same sampling interval of 2 mm as before. In terms of data processing steps, the only difference in this case was that one of the station's coordinate system was chosen as reference. This time no absolute orientation was needed for concluding the analysis. On the other hand, the relative orientation was performed in two consecutive steps. Initially, the transformation parameters were estimated according to equations presented in section 2.5 with the help of four targets scanned at each station. Afterwards, the point clouds as well as the estimated target centers were all transformed to the reference system providing the necessary input for step two. In step two, the relative orientation was refined with the Iterative Closest Point (ICP, Besl and McKay, 1992) algorithm estimating 60 unknowns in total. Besides the transformation parameters (48 unknowns for 8 stations) also the target coordinates (additional 12 unknowns) were estimated within this final adjustment involving all station measurements simultaneously. Using the ICP was beneficial because the LSA now minimized both, the target coordinate differences and the distances between point pairs along the normal vector directions. Hence, the normal vectors of all points had to be estimated beforehand. The adjustment was terminated after 20 iterations resulting in $\hat{\sigma}_0 = \sigma_{\text{RO}} = 0.5$ mm estimated with very high redundancy

due to the large number of points. The results of the ICP and the station configuration can be seen in Figure 38. With relative orientation concluded, the estimation of cylinder parameters of four station

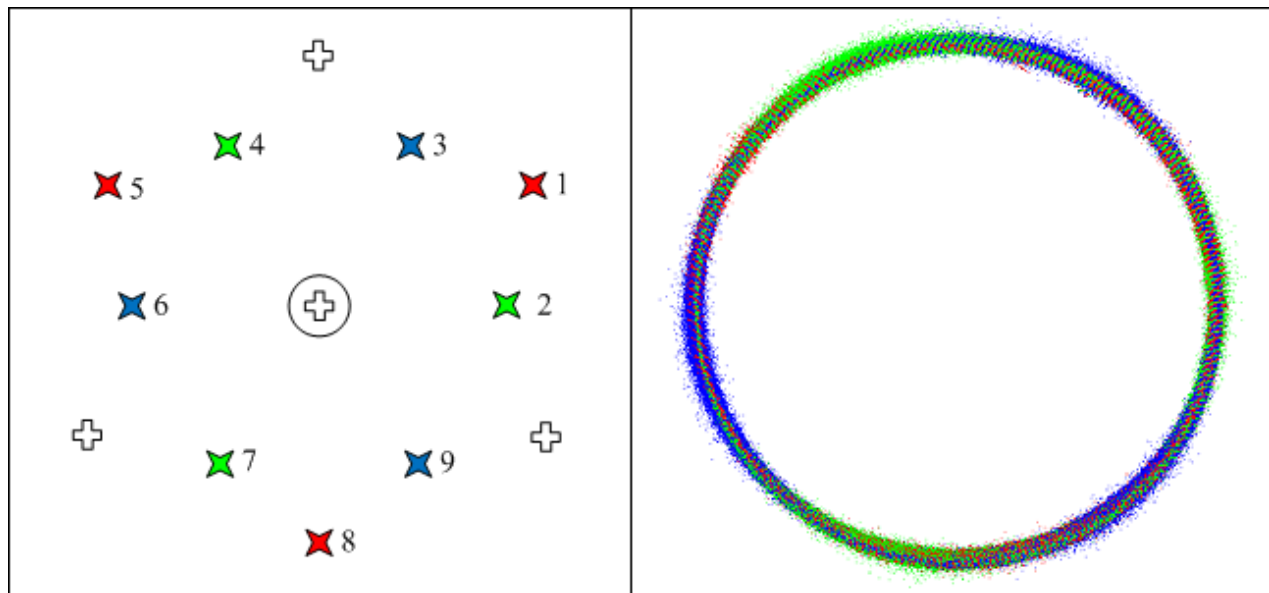


Figure 38: Station configuration (top view with pillar in the center) and ICP results. The star represent the station, whereas the cross the location of the target.

configurations was carried out based on equations 23–25. The adjustment results are summarized in Table 9. The first three configurations were chosen because they simulate similar surveying con-

Table 9: Adjustment results estimated from four station configurations. The coordinates of P_0 are not comparable because they depend on point distribution. D is the station distance to the pillar.

Configuration	D [m]	a	b	c	r [m]	$\hat{\sigma}_0$ [mm]
1,5,8	12	-0.08368	0.03192	0.99598	0.1254	1.4
2,4,7	8	-0.08377	0.03193	0.99597	0.1255	1.5
3,6,9	8	-0.08376	0.03196	0.99597	0.1257	1.6
1-9	/	-0.08373	0.03193	0.99598	0.1256	1.5

ditions as in the June and November campaigns (i.e., three stations per pillar with an overlap of $\approx 30\%$, see Figure 33). The last configuration can be considered as a control one, showing that using all the point clouds in the cylinder adjustment process provides no gain. Based on the results from Table 9 an important outcome of this analysis is that in the two field campaigns, the cylinder axes (including all observation pillars) most likely had not been affected by the variations in the scanning geometry. Compared to this test, the variations in the scanning geometry between June and November survey were much smaller since the establishment of the same surveying conditions was considered part of the general workflow recommendations (section 2.1). The axis direction components a , b and c , which play a role in the final displacement analysis, differ very little from

the first configuration to the last. Consequently, even if the variations of axes parameters in the June and November campaign would be as big as those in Table 9 they would have no influence on the computation of representative points which will eventually be presented in section 4.1.2.

In the last part of the TLS data processing stage, the reliable precision values of the cylinder parameters had to be estimated from very high point redundancy as indicated in section 2.7.2. Using all the points in the adjustment, the error propagation law clearly lead to the overestimation of Σ_{xx} . All of the obtained standard deviations were below the order of $10 \mu\text{m}$ with the direction cosines, which are non-unit values, most precisely determined. Next, the whole adjustment computation was repeated using only 8 points per pillar (four on the top and four on the bottom of each point cloud with equal radial arrangement) to get a first impression of the size of the overestimation factor. According to section 2.7.2, the point clouds of each pillar were finally split into adjacent regions and the adjustment re-computed in 18 consecutive steps. At every step, the model parameters were estimated from 100 subsets constructed by randomly selecting an equal number of points from each region. The number of points per region per step was $n_{i,i=1\dots 18} = 1, 2, 3 \dots 10, 15, 20 \dots 50$. In terms of region size, the adjustment was performed with two different region sizes. Initially, the point clouds were split into larger and then into smaller regions to see if this has any effect on results. As it turned out, both adjustment approaches (8 points/random samples) indicated the reduction of the cylinder precision parameters for the factor of 100. In this way, the upper and lower boundaries were computed, framing the quality of the adjusted quantities and offering a firmer and more reliable foundation for the deformation analysis. The analysis also showed that increasing the point number beyond 35 points per region has almost no benefit because the correlation between point becomes so high that the individual parameter estimates do not change any more. Applying the overestimation factor it becomes evident that the precision measures of cylinder parameters are very much comparable to the results provided by classical terrestrial method despite the obvious difference in the instruments' performance. In Figure 39 the results of this process are illustrated for pillar 4216. The same outcome was obtained for other pillars as well. Eventually, also the weight matrix was introduced to the adjustment process. Weights took into account only the incidence angle α since it was α that varied much more than the distances to the object assumed to be measured with more or less the same precision. However, introducing the weights $p_i = \cos(\alpha)$ did not change the outcome of this analysis nor did it influence the cylinder parameters with any significance. The axes direction vectors remained by far the most precisely determined parameters. Therefore, the employment of TLS has proved its value, especially when analyzing only the trends in the pillar inclination in order to get a better understanding of how the terrain sliding affects the observation pillars. Last but not least, from the computed inclinations it is possible to derive the conclusions on whether the displacements of the observation points on the top of the pillars reflect the actual movements of the pipeline.

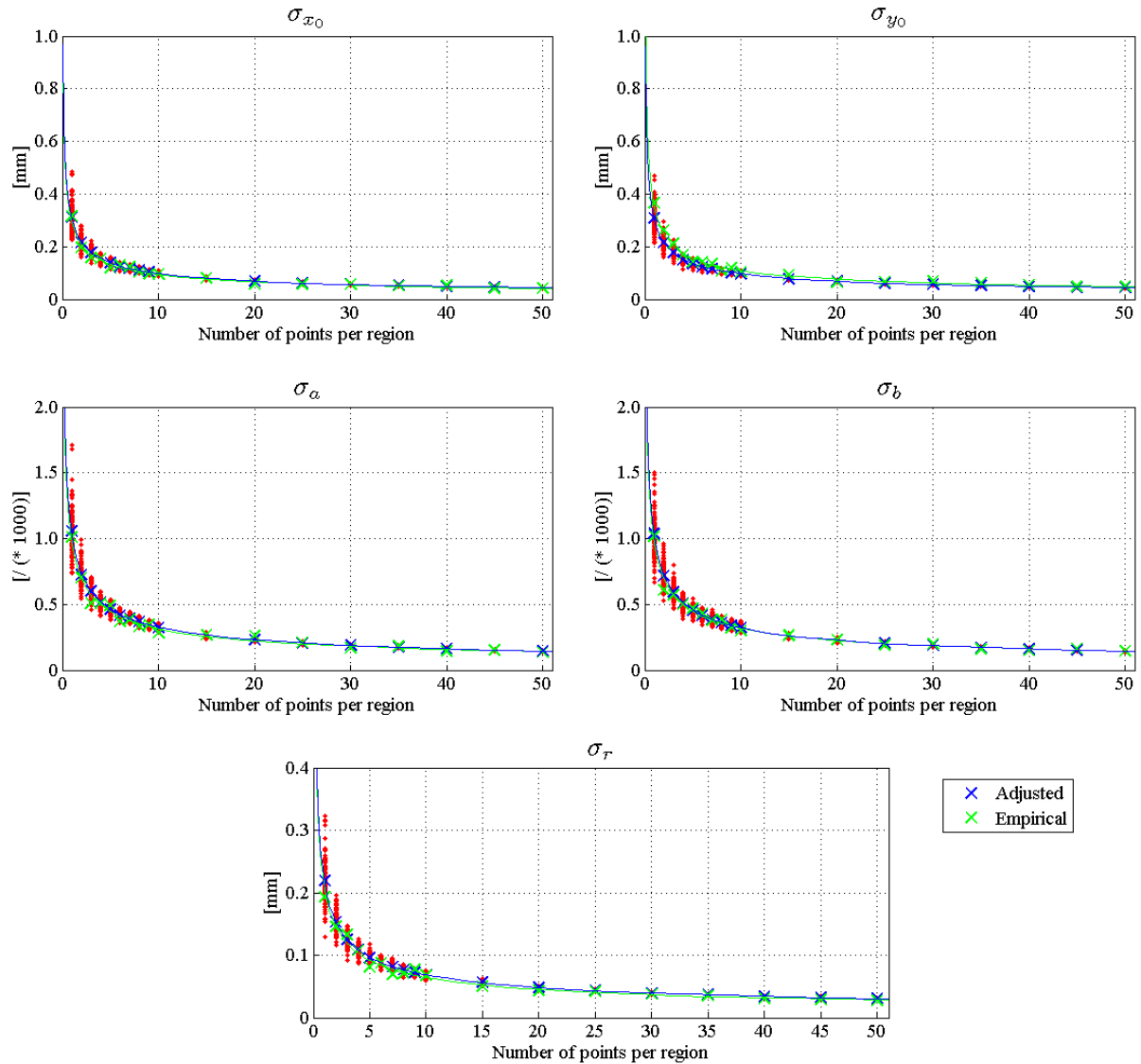


Figure 39: The standard deviations of the cylinder parameters after subsampling. The red dots represent the results from the 100 random subsets in each step. The blue crosses indicate the average standard deviations obtained from the adjustment of the 100 subsets. The green crosses represent the standard deviations of the estimated values of each cylinder parameter, i.e. empirical standard deviations. Eventually, the radius of the pillar will not be included in the deformation model presented in the last chapter.

3.4 Outdoor test 2: Supporting wall

3.4.1 The test field and its characteristics

Compared to test 1, the characteristics in this test were in many ways different as already indicated at the start of this chapter. Following this fact, also the ability of TLS in terms of small scale

displacement and deformation detection would be challenged a step further.

At the beginning of 2010, a tunnel construction project began at the Slovenian coast, establishing the remaining part between two already built sections of the highway that will eventually connect central Slovenia to the Croatian border. Since the area above the excavation site is densely populated a decision was made to monitor the effects of the excavation not only inside the tunnel but also on the surface. The above-ground monitoring would include all man-made structures with a firm and well-defined geometry, i.e., buildings, supporting walls, roads etc., to provide a complete surveillance of the possible damages caused by the underground construction works. Despite drilling into a stable rock, the height from the tunnel ceiling to the surface is not very high in some parts (the minimum height is only 15 m) which turned out to be a decisive factor for the monitoring to take place. Figure 40 shows the individual sectors of the entire area where the monitoring is to take place. It is in these sectors that the tunnel runs closest to the surface. With the geological survey of the site



Figure 40: Sectors selected for monitoring excavation effects. So-far only Sector 1 was excavated, limiting the deformation inspection of the thesis to this particular area. The red lines represent the two tunnel axes.

concluding that the rock was stable enough, the question remained whether there are no local gaps in this stable rock which could collapse during the excavation, damaging not just infrastructure but threatening lives as well. Besides these gaps, the impact of the excavation in general was supposed to be absorbed by the stable rock, therefore if any displacements or deformations would occur on the surface, they would be small in size. Such a prediction was again the basis for the hypothesis to be put to test.

Focusing on Sector 1 for the rest of the thesis (the sector excavated so-far), three different structures were examined, namely a large supporting wall, one building and a road, all shown in Figure 41. The analysis herein put a special emphasis on the wall since it contained the highest amount of surface features for the employment of both deformation models presented in section 2.8. From the perspective of the initial hypothesis and its evaluation within this research project where larger structures were involved in the monitoring process, the results could shed more light on the answer as well as provide the information on the effectiveness of the proposed methodological workflow. Before the excavation began, three concrete pillars (1000, 479 and 474 in Figure 41) were grounded



Figure 41: Objects of interest and stabilized pillars in Sector 1. Only about 25 % of the entire wall can be seen which stretches about 130 m in length and 10 m in height. The black line in the right image indicates the field of view of the left image.

around the tunnel entrance to navigate the progress of the underground works and to monitor the displacements of the tunnel walls during the construction. An additional pillar 481 was stabilized right above one of the tunnel axis to be able to monitor displacements during the initial stage of drilling and later when constructing the tunnel entrance (portal). These pillars were designed to enable forced centering of the measuring equipment.

After extensive considerations in the phase of planning the geodetic network, pillar 1000, stationed furthest away from the sector of interest (right next to the coastline), was chosen as a reference point. Moreover, this pillar was selected because it is the only one stabilized away from the tunnel entrance area where the ground could possibly be exposed to movements caused by all kinds of working machinery. Compared to the two pillars near the entrance area (479 and 474), the reference pillar 1000 also was placed into a more solid rocky ground of the artificially settled coastline belt. Due to the fact that pillars 479 and 474 were so exposed, a decision was made that the network orientation should be realized by observing a distant signal (in this case a church top situated about 10 km away), which was in the line of sight of pillars 1000 and 474. Besides pillar 1000, all other pillars were considered control points included in the network merely to strengthen its geometry. The visibility between all network points (target stations and pillars) could not be assured due to the vegetation buffer separating the objects of interest from the coast (see Figure 41, right image). The protective fences placed around the entrance area were further obstructing the visibility between pillars 1000, 479 and 474, preventing the realization of optimal measuring conditions among the network points.

Additional compromises had to be made in terms of selecting the scanner and target station locations near the objects of interest since the house could only be approached from one side. On the other hand, the road going through Sector 1 was not closed during the two field campaigns. Consequently, if the wall and the road were to be scanned with no resulting occlusions, multiple scans would have to be performed at some stations to fill the missing gaps. In conclusion, employing the proposed methodology into the field was challenging due to all these limitations alone but would provide more practical experiences that should be useful during the final evaluation of the hypothesis.

3.4.2 Field work

Using the same methodological steps from Chapter 2 as well as in test 1, two measurement campaigns were carried out, the first in May 2010, before the excavation of the tunnel in Sector 1 began, and the second in February 2011, right after this sector was excavated. Each campaign was finished within a period of a single day, including precise classical terrestrial method and laser scanning. Contrary to test 1, this time the stability of the reference frame was not further analyzed by any geodetic observation technology. Based on the location and ground stability around the network's reference point as well as the point of orientation it was in this case assumed that the datum parameters could be considered unchanged between both measurement campaigns.

By performing observations of the two campaigns in different seasons it was again necessary to measure the atmospheric conditions in order to correct the observed distance measurements for all systematic effects. In Table 10 the measured meteorological parameters of both surveying campaigns are summarized. The same precise Assmann psychrometer for the acquisition of air temperature and psychrometric difference was used as in test 1 (with the thermometer resolution of 0.1 °C). The air pressure was again obtained using digital barometer Paroscientific, model nr. 760-16B, with the resolution of 0.01 mbar and relative precision of 0.01 %. The geodetic network designed

Table 10: Atmospheric parameters of the two surveying campaigns, average values. All the atmospheric parameters were measured at the site of the instrument only.

Campaign date	Temperature [°C]	Humidity [%]	Air pressure [mbar]
May 2010	19.0	79.8	1003.0
February 2011	9.8	66.2	1024.1

to connect the point clouds to the reference frame consisted of 12 points, including four pillars (1000, 479, 474 and 481), one orientation point and seven target stations. Apart from pillar 481, the targets were placed onto the tripods whereby the locations of the tripods again remained the same in both campaigns. In Figure 42 the geodetic network is shown along with the lines indicating the visibility between points. In the geodetic network, the angles and distances were observed along the red lines (see Figure 42) in both measurement campaigns. As for the point of orientation, only angular measurements were carried out from pillars 1000 and 474. Again the high redundancy of

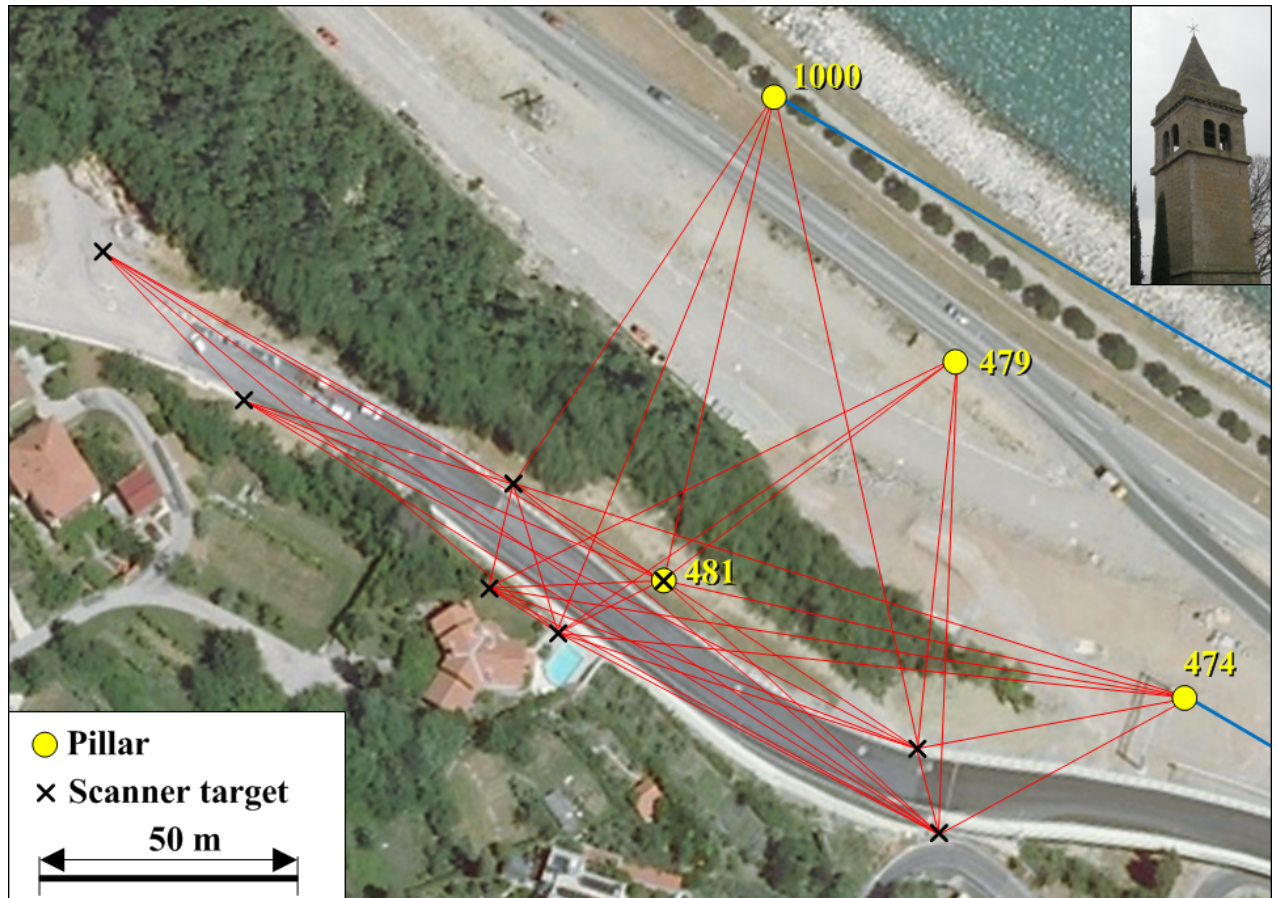


Figure 42: The geodetic network designed near the objects of the interest. The blue lines indicate the direction to the orientation point – a church top about 10 km away, upper right corner.

observations was assured by performing measurements in seven sets of angles at each station. In this test, the Leica TS30 electronic tacheometer was used and its ATR functionality employed at all stations not including of course the observations to the orientation point which had to be done manually. Before each campaign, the instrument's modulation frequency, additive constant, vertical index error and collimation error were tested by the official Leica representative; hence, the instrument was working according to the manufacturer's specifications. For the signalization of network points, the same Leica reflectors as in test 1 were used, i.e., GPH1P and GPR121, with all the additive constants determined prior to each campaign. Furthermore, the same precise tubular levels used in the first outdoor test for the leveling of the instrument and reflectors were also used in this test. After leveling the tribrachs, they could be left untouched during each campaign due to the compatibility of all the measuring equipment including the scanner (Riegl VZ-400) after attaching a special adapter to its base. This way the centering errors were again minimized.

Using the Riegl scanner in this test meant that each of the four Leica flat targets had to be labeled beforehand to keep track of their location, so that the corresponding parameters of each range error function (listed in Table 3) could be applied in the data processing phase. The fact of using these

range error functions in test 2 also meant that in the data processing phase (section 3.4.3.2), the coordinates of the target centers will have to be estimated according to the proposed two step algorithm described in section 2.4.1. The extraction of the centers based on the amplitude weighted mean algorithm was not possible here since the scanner-target distances were too big.

The scanning of the objects of interest was carried out from nine stations, depicted in Figure 43. The road was scanned from stations 1, 2, 3 and 9. The first three stations were located on the top of

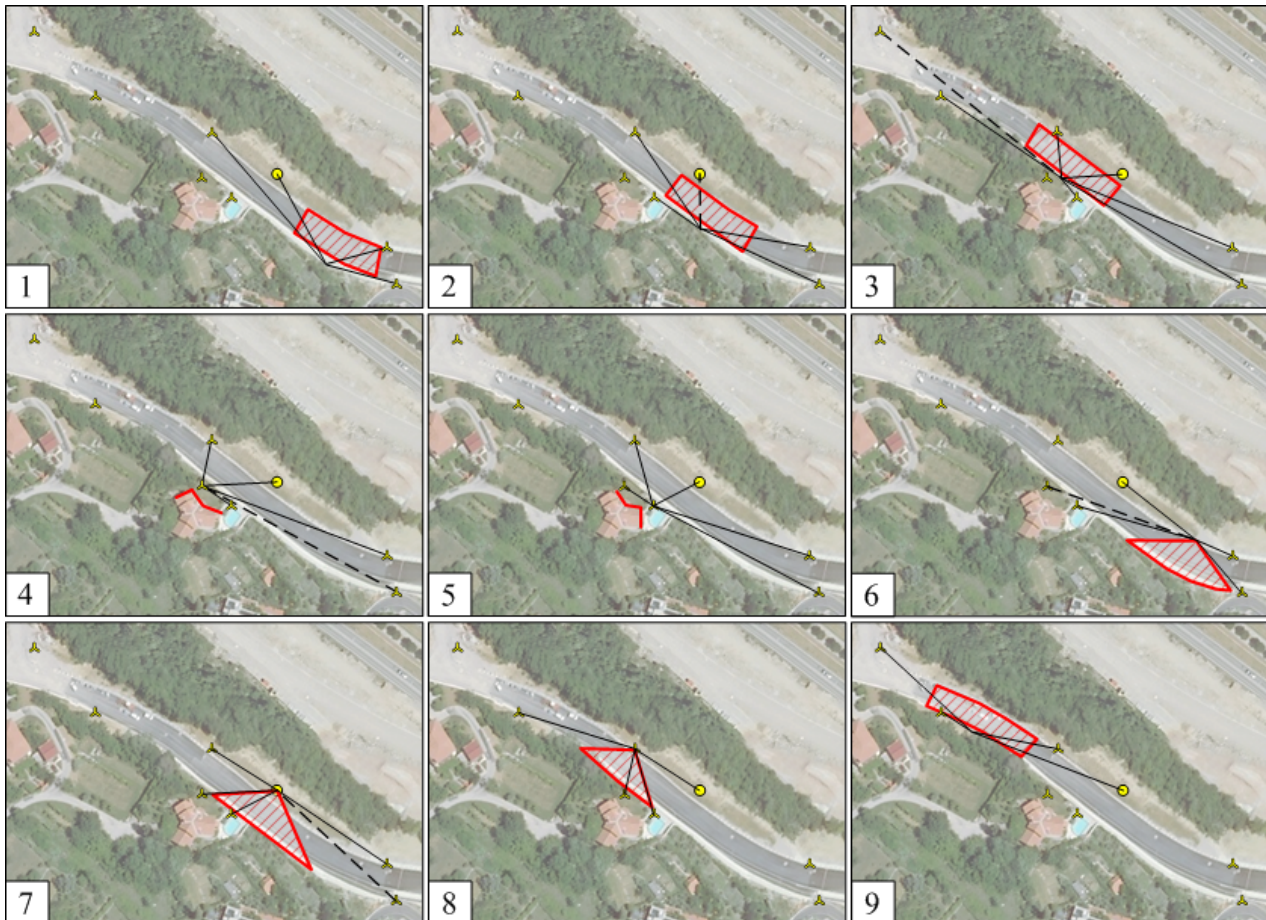


Figure 43: Scanner stations in the two measurement campaigns. The red lines indicate the scanned surface, whereas the black lines point towards the targets. The dashed black lines represent additional targets which were scanned in the second campaign only.

the supporting wall, whereas the last one on the pavement beside the road. From stations 4 and 5, the approachable part of the house was scanned by fixing the instrument onto the two tripods near the house, which were otherwise used as target stations. Finally, the supporting wall was scanned from stations 6, 7 and 8 again using two of the target stations to fix the scanner (i.e., stations 7 and 8 – pillar 481). The objects of interest were scanned with approximately a 5 mm raster producing high density point clouds containing up to 10 million points. The locations of the scanner stations were selected in such a way that the object distance and consequently the point density did not vary too much. Besides the two stations that were used for scanning the house, up to five multiple scans

of the objects' surface were acquired at all other stations due to the constant traffic producing gaps in data.

At every scanner station, 4 to 7 targets were scanned with a 1 mm raster on the targets' surface just like in the range error experiment presented in section 3.1.2. To assure the identical surveying conditions also in terms of target configuration, it was important that each of them (with its unique label) was placed on the same tripod in both campaigns. This way the remaining systematic errors (those that could not entirely be eliminated by modelling) would have similar effects on the results. At stations 3, 4, 6 and 7, one additional target was scanned in the second campaign only (the dashed black lines in Figure 43) since the vegetation was low. With respect to the scanner stations, the target station configurations were far from ideal and limited by many physical obstacles. Furthermore, it was also not always possible to avoid scanning the targets from less than 20 m distance despite the fact that the range error modelling was less efficient within this range (see Figures 20–23 on pages 44–47).

The calibration of the scanner was performed by its manufacturer concluding that it was working according to specifications. Among the components tested were the rangefinder and beam deflection unit performance as well as the angular readings. Besides this, no additional in-depth calibration was carried out.

3.4.3 Results

After completing both acquisition phases, the next two subsections will again be devoted to the presentation of the data processing steps aimed at computing the input parameters for the final displacement and deformation analysis which will eventually be presented in Chapter 4. Compared to test 1, both deformation models presented in section 2.8 were used in this test to analyze the wall, whereas the house and road were only evaluated within the truncated direction model (section 2.8.1). The first subsection focuses on the estimation of the scanner target positions based on the classical terrestrial measurements. The second subsection will then focus on the analysis of the absolute orientation and finally all the subsequent steps of the TLS data processing.

3.4.3.1 Classical terrestrial method

After computing the mean values of individual measurements from seven sets of angles, in this test the coordinates of the network points (targets and pillars) were estimated by considering the network as three-dimensional. Hence, the coordinate estimation was not approached separately for the planar coordinates and height differences like in test 1. Instead, the least squares adjustment included all measured quantities simultaneously, i.e., the horizontal angles, the zenith distances and slope distances. The same data processing steps, described below, were performed in both campaigns.

Before the adjustment, the slope distances had to be corrected for the meteorological distance co-

rection factors in order to be treated as straight lines. These correction factors were computed using temperature, air pressure and partial water vapor pressure provided by the psychrometric and barometric measurements following the same steps as in test 1. Hence, the partial water vapor pressure was calculated according to the Sprung equation for the Assmann aspiration psychrometer. The saturated vapor pressure was computed according to the Magnus-Tetens equation, whereas the standard and the actual refraction indexes of the atmosphere were again determined according to Ciddor (1996) and Ciddor and Hill (1999). The maximum measured distance in the network did not exceed 200 m which means that of all the distance correction factors, only the first velocity errors were of any significance. The second velocity errors and the error caused by the bending of the laser ray in the atmosphere could be skipped in this test as well.

Besides the slope distances, the correction of the measured zenith distances z_m was also considered, taking into account the earth curvature and refraction ($z_{corr} = z_m - D \cdot \frac{1-k}{2R}$, where R is the Earth radius and k the refraction coefficient). This correction factor directly influences the height differences and can reach up to 3 mm even at 200 m.

Finally, the error equations were derived for each measured and properly corrected quantity type (horizontal angle, zenith distance and slope distance) as presented in Kuang (1996) to be able to estimate the 3D positions of the network points. The a priori standard deviation σ_0 was calculated by averaging the standard deviations of all the observations. In both campaigns, equal standard deviations were assigned to all observations within each quantity type since they were measured with nearly the same precision. The observations were again initially adjusted as a free network with the minimum trace of the cofactor matrix of coordinate unknowns. Next, the Baarda's Data Snooping was employed for the detection of potential gross errors. In the last step, the adjustment was repeated by considering pillar 1000 as a reference point and the direction angle from pillar 1000 to the orientation point as reference direction. The adjustment results of the classical terrestrial measurements are listed in Table 11.

After the final adjustment was carried out, the network point heights were recalculated using the

Table 11: Results of the adjustment using minimum datum parameters: global model test, precisions of the adjusted observations and positional precisions of the network points in [mm].

Epoch	$\hat{\sigma}_0^2/\sigma_0^2$	$\hat{\sigma}_{Hz}$ ["]	$\hat{\sigma}_z$ ["]	$\hat{\sigma}_D$ [mm]	$\hat{\sigma}_{pos,max}$	$\hat{\sigma}_{pos,min}$	$\hat{\sigma}_{pos,avg}$
May 2010	1.00	0.6	1.0	0.1	0.9	0.5	0.7
Feb 2011	1.04	0.6	1.0	0.1	0.8	0.6	0.7

known vertical offset between the targets and the reflectors. For all pillars, except 481 (used as target station), the adjusted height values were reduced to the pillar level using the measured instrument/reflector height.

3.4.3.2 Terrestrial Laser Scanning

From the high density point clouds it was in the first step necessary to exclude all the points not belonging to the objects of interest. These points were filtered out manually. Next the scan multiples were joined to fill the gaps caused by the traffic occlusions. Following the latter step, the points which were further than 30 m away were then also filtered out, a perimeter selected according to the results of testing the instrument's detectivity capabilities (section 3.2). After the computation of normal vectors for the remaining points only those below 45° incidence angle were finally subtracted from the point clouds. The incidence angle threshold was again selected based on the scanner's performance tested on the six material samples S1–S6 (Figure 24). It seemed obvious that the displacement and deformation inspection should be performed on surfaces which resemble the samples' surface characteristics. Such surface conditions could be found on parts of the house as well as of the entire supporting wall. However, the road was considered an exception since the asphalt with its low albedo was not included in the samples. Despite the remark, the most interesting part of the road right above the two tunnel axes was analyzed anyway, assuming that by applying the range and incidence angle threshold beforehand, the rangefinder performance would not be decreased significantly when scanning this particular surface type.

The examination of the point clouds during this initial processing phase revealed the presence of irregularities causing some scan profiles to be shifted away from their correct position. The effect can be seen in Figure 44. It shows the effect is caused by the instrument rather than by scanning

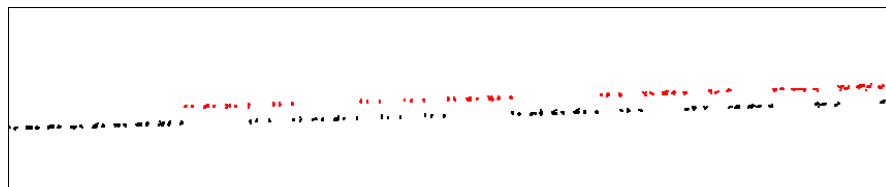


Figure 44: Profile irregularities. The profiles colored in red are erroneous.

a particular surface. Moreover, this profile shift could be observed even within one rotation of the 3-facet mirror that deflects the beam along the vertical direction producing characteristic triplets of scan profiles seen in Figure 44. The size of the shift depends on the incidence angle (the larger the incidence angle the more evident the shift becomes). In Figure 44 the erroneous profiles deviate for about 1 cm from the rest, a shift which remains constant since the incidence angle does not vary much. One possible explanation of this systematic effect is that the mirror's angular velocity experienced fluctuations which occurred only when the mirror was in the rotating mode (the fluctuations did not occur when the mirror was oscillating). Consequently, the pulses would be sent out at a wrong vertical angles causing the distances to be extended or shortened. However, to define the true origin of the effect, more tests would have to be performed with this instrument to prove whether the shift patterns are systematic or random in nature. The presence of such effects indicates the instability of the scanner despite the fact that it was tested by the manufacturer. To be able to

carry out all the subsequent steps of the data processing as well as the final deformation analysis, the erroneous profiles had to be filtered out. Finally, the distances to each of the leftover points were corrected for the meteorological distance correction factors which turned out to be smaller than 0.5 mm for the maximum point distance of 30 m.

After the preparation of the point clouds during the initial phase, the focus was shifted on analyzing the quality of the absolute orientation needed to establish the link to the common reference frame for each epoch measurements. To do so, the target centers at every scanner station had to be estimated according to the proposed two step algorithm. Next, the distances to the targets had to be corrected for all systematic errors (i.e., first the meteorological correction factors and in addition the range errors examined in section 3.1.2, which are caused by scanning the retroreflective target area with this scanner). Without applying particularly the parameters of the range error functions from Table 3, the target distance errors could reach up to 1 cm, a level that had to be reduced prior to the estimation of the transformation in the following step.

Due to the limited conditions in the field in terms of the scanner-target configuration and target distance⁷ (Figure 43), the analysis of the quality and stability of the transformation had to be examined in detail. Moreover, such an examination seemed reasonable to avoid the occurrence of possible temporal fluctuations in amplitude observed during the indoor target calibration test which could significantly reduce the quality of the transformation. Therefore, at each scanner station, the transformation parameters (rotation matrix R and the translation vector t ; scale was not estimated) were computed from all possible target combinations. For example, a station with n targets would produce $\sum_{k=3}^n \binom{n}{k} = \sum_{k=3}^n \frac{n!}{k!(n-k)!}$ sets of transformation parameters (R_i, t_i) in total including the one based on all n targets. Since $n_{\max} = 7$, the maximum number of sets was 99. Once the transformation parameters along with σ_{AO} were estimated for each set, the overlapping areas could be examined to see how the adjacent point clouds fit together after being transformed with various sets of (R_i, t_i) beforehand. Hence, the quality of the transformation was monitored in very much the same way as in test 1 (at the target and the object side), the only difference was that here the object side could not be monitored only visually but required also a numerical approach due to the extensiveness of the whole process. The discrepancies between the adjacent point clouds in the overlapping areas were therefore measured by first subdividing the areas into patches of 20 x 20 cm, estimating local planes for each patch and finally calculating the distances along the normal vector directions just like in the deformation model 1. The only difference is that in this case all the point clouds belonged to the same epoch. In Figure 45 the resulting σ_{AO} is shown for each target combination at all scanner stations of both measurement campaigns. Based on results from Figure 45, the absolute orientation accuracy at stations 1 to 5 was severely influenced by the scanner-target configuration, particularly in the second measurement campaign. The large deviations in σ_{AO} at these stations were considered an indicator of the instability of the transformation. Once the values

⁷The closest target was well below the perimeter of 20 m where the range error modelling efficiency was limited. On the other hand, few target distances exceeded the perimeter of 70 m which meant that the range error had to be estimated by the extrapolation.

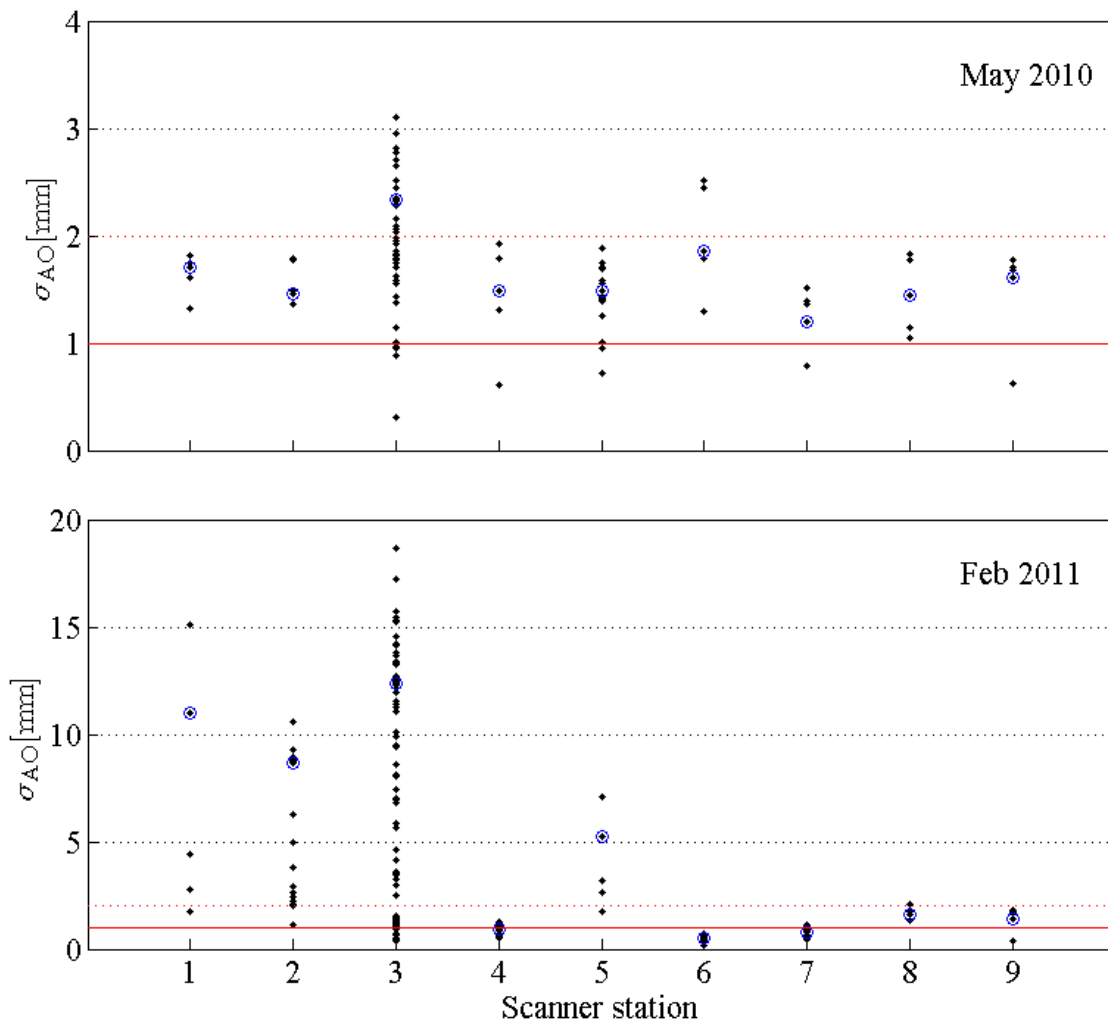


Figure 45: The overview of the absolute orientation accuracy. The blue circles represent the combination where all targets at a certain station were used to estimate the transformation parameters. Note the different interval for σ_{AO} on the y-axis.

of σ_{AO} were combined with the values of discrepancies, measured at the object side, the instability of the transformation for stations 1 to 5 was re-confirmed. The discrepancies between the overlapping point clouds were experiencing shifts of up to 1 cm from one set of transformation parameters to the next. As a result, these station measurements could not be positioned within the reference frame with the required accuracy and therefore had to be excluded from any further analysis. At stations 4 and 5 from which the house was scanned, the discrepancies on the object side could be reduced below the 1 mm level in each campaign. However, when comparing the point clouds from the first and the second epoch, the result made no sense since the first epoch measurements were located above the ones from the second. Clearly, the problem was in the transformation having all the targets on one side of the horizon and the object of interest on the other. In such case, even with the presence of small deviations at the target side, these can become significant at the object side. Compared to stations 1 to 5, the examination showed that the quality and particularly the stability of the transformation for stations 6 to 9 was much better. These four station measurements could be

used in the displacement and deformation analysis enabling the reconstruction of the entire supporting wall as well as the interesting part of the road surface right above the two tunnel axes. Out of all the sets of transformation parameters (R_i, t_i), estimated at stations 6 to 9 in both epochs, the optimal target configuration was selected with respect to both quality criteria, the orientation accuracy and the average patch discrepancy within the overlapping areas. In Table 12 the values of the two criteria are summarized along with the average deviations between the coordinates of network point and the targets after being transformed with the chosen set of transformation parameters. The chosen

Table 12: The quality of the absolute orientation process for stations 6 to 9 in [mm]. Δ denotes the average patch discrepancy in the overlapping areas shown in Figure 46. The superscripts a to e next to the values of Δ were added to be able to match the values from the table to the areas in the figure.

Epoch	Station	σ_{AO}	dx	dy	dz	$dxyz$	Δ		
May 2010	6	1.3	0.4	1.1	0.2	1.2	0.9 ^a	-	-
	7	0.8	0.5	0.3	0.3	0.8	1.5 ^b	0.5 ^c	-
	8	1.0	0.7	0.6	0.1	0.9	-	0.6 ^d	
	9	0.6	0.5	0.2	0.1	0.5	-	-	0.3 ^e
Feb 2011	6	0.6	0.3	0.4	0.2	0.6	0.6 ^a	-	-
	7	1.0	0.7	0.5	0.2	1.0	0.3 ^b	1.6 ^c	-
	8	1.8	1.4	0.7	0.2	1.6	-	0.8 ^d	
	9	1.4	1.2	0.6	0.7	1.6	-	-	0.3 ^e

optimal sets of transformation parameters (with their quality measures presented in Table 12) were calculated from 3 to 4 targets per station in both epochs. The distances to the targets at each station were ranging from 20 to 70 m, the perimeter where the range error modelling was expected to be most efficient (below the 1 mm level). Concerning the values of Δ , the point clouds from stations 6 and 7, as well as 7 and 8, were overlapping in two areas, one found on the road and the second on the supporting wall (hence the two values). On the other hand, the point clouds from stations 8 and 9 were overlapping on the road only. These values were obtained from a large number of 20 x 20 cm sized patches excluding the ones where the local planes were estimated from less than 100 points as well as those with the plane noise above the 5 mm level (e.g., edges on the wall). To be able to consider the values of Δ as representative, the discrepancies were re-calculated for each overlapping area, this time with the 10 x 10 cm patch, the minimum point number of 50 per patch and the plane noise level of 3 mm. The values of Δ did not change significantly.

After the selection of the optimal sets of transformation parameters, the overlapping areas were finally examined also visually to be sure the point clouds were actually fitting together in a smooth way and could therefore be treated as one joint entity. Figure 46 shows the overlapping areas that were examined during the evaluation of the quality of absolute positioning process in both campaigns. In Figure 46, the two missing parts of the supporting wall (gaps in the yellow points) could not be examined any further due to the occurrence of scan profile irregularities discovered in the measurements of the second field campaign.

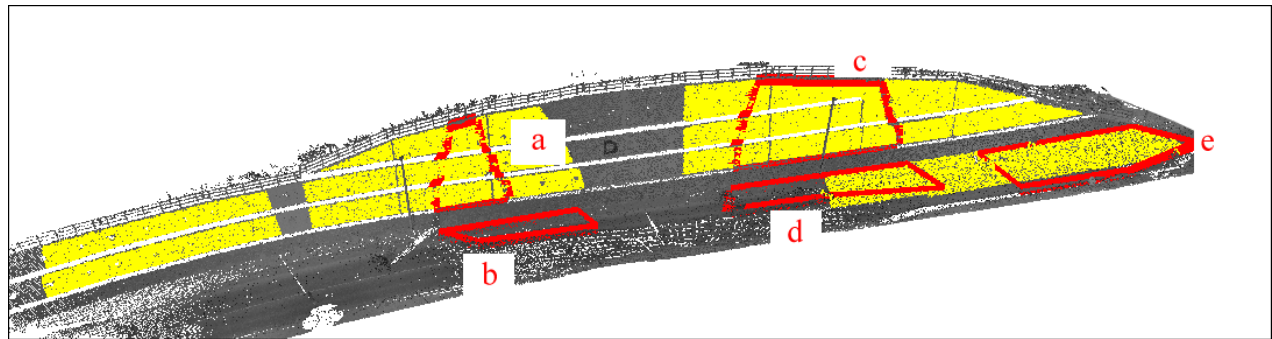


Figure 46: The overlapping areas on the wall (a and c) and the road surface (b, d and e) defined at stations 6 to 9. The yellow points on the wall and the road belong to the regions that will eventually be examined in the remaining part of the thesis. The gray colored points were added only to strengthen the visual perception.

In the last part of this section, the yellow points shown in Figure 46 were used to model the shape of the objects of interest (step 6 of the general workflow). Only then could the surface models be evaluated within the deformations models, presented in section 2.8. Both objects could be modelled in the same way, i.e., by splitting the point clouds into smaller segments (patches) according to coordinate axes and approximating the shape locally by a planar model as described in section 2.7.1. Furthermore, surface features could be found on the wall that enabled the modelling process to be approached also through segmentation. These features are shown in Figure 47. On the smooth part

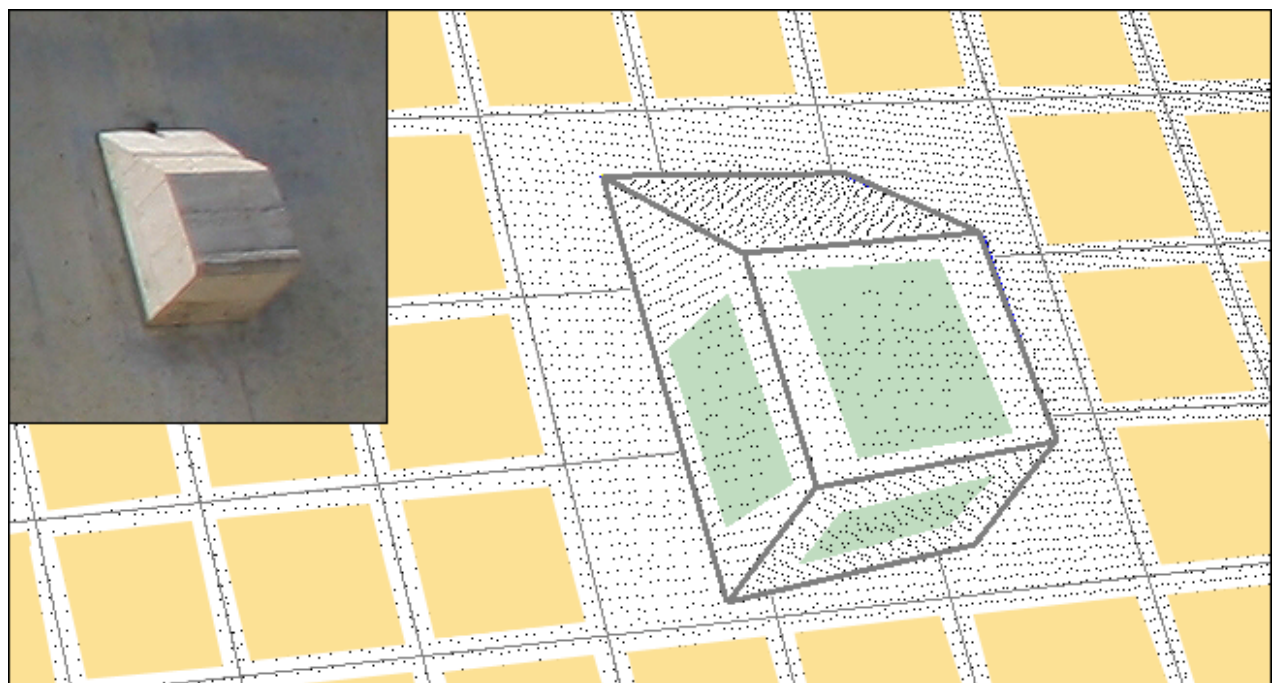


Figure 47: Modelling of the wall with a planar model. The orange planes were determined by splitting the point cloud into segment, whereas the green ones are the outcome of applying the segmentation algorithm presented in section 2.7.1.

of the wall (orange planes, Figure 47), the modelling was approached by using a 20 x 20 cm sized patch. The size of the patch was selected after analyzing the residual patterns of the plane fitting process in order to justify the use of the planar model. Furthermore, only those regions on the wall were modelled which contained more than 400 points per patch. This point number threshold was used also during the segmentation with the extracted planes on the wall features shown in Figure 47 (in green color). Next to the point number threshold also the plane noise threshold of 3 mm was implemented in the modelling algorithm in order to exclude those patches which contained points considered gross errors.

The resulting models were now ready for change inspection presented in the last chapter of the thesis (section 4.2). Besides the surface feature shown in Figure 47 which enables the extraction of representative points (deformation model 2, section 2.8.2) the rest of the wall's surface could only be examined with the truncated direction model (deformation model 1, section 2.8.1) due to the lack of any distinct detail. For the same reason, the truncated direction model was the only option to examine the road surface which has been modelled by using the same patch size and thresholds as in the case of the wall.

4 ANALYSIS AND DISCUSSION

This last chapter summarizes the results of the last step of the general workflow, i.e., the displacement and deformation analysis of the surface models from the outdoor tests 1 and 2 based on the two proposed models, presented in section 2.8. In the first part of the chapter, the pillars from the outdoor test 1 will be examined within the deformation model 2 (representative points). In the second part, the wall and the road from the outdoor test 2 will be evaluated within both deformation models (the truncated direction model and the model based on representative points).

4.1 Outdoor test 1

Due to the test field characteristics of this outdoor experiment the quality and stability of reference pillars was monitored by means of GNSS observations. The results of the networks's datum stability are presented in the next subsection. The results of the pillar displacements are following in the second and third subsections.

4.1.1 The datum stability

The results of the GNSS campaigns presented in Table 7 indicate that statistically identical coordinates are obtained for reference pillars 4102 and 4103. On the other hand, reference pillar 4101 shows a displacement of more than 1 cm between both GNSS campaigns. From these results it was concluded that both reference pillars 4102 and 4103, directly used in this research for further classical terrestrial observations and laser scanning, can be assumed as stable. In Figure 48, the analysis of the stability of the reference frame is shown graphically. Since the base distance between the stable reference pillars 4102 and 4103 (see Figure 32) was observed in the geodetic network with precise classical terrestrial method, this provided yet additional information on the stability of these two reference points. The difference between the adjusted base distances 4102–4103 of the two measurement campaigns as obtained from classical terrestrial observations was less than 1 mm, a level considered as being a result of the measurement uncertainty rather than the movement of any of the two reference pillars. This difference in the base distance was the same, whether the geodetic network was adjusted as a free network or with the minimum datum parameters.

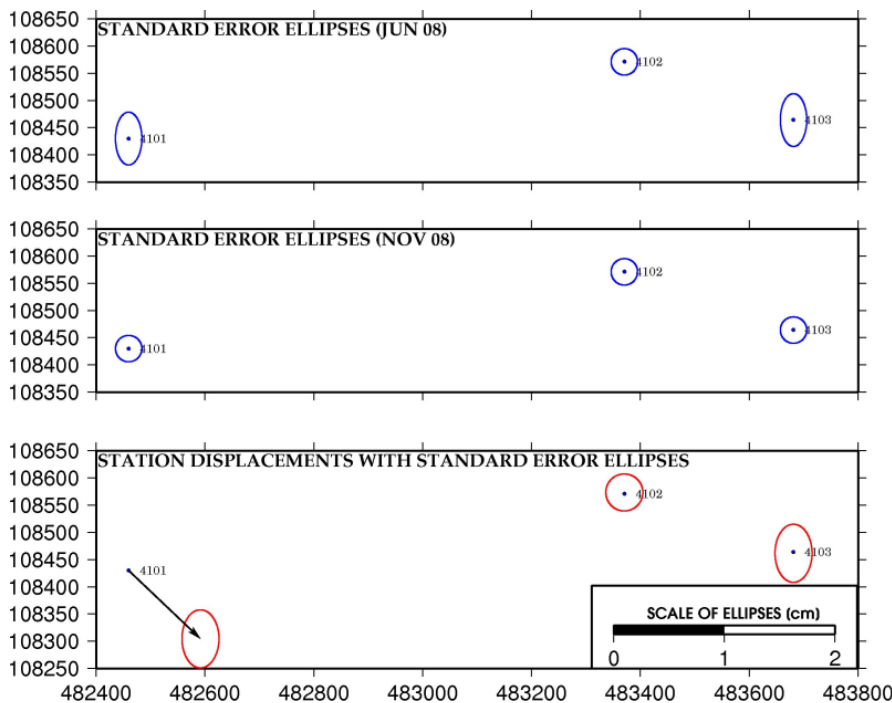


Figure 48: Graphical results of reference pillar displacements.

4.1.2 Determination of representative points

Based on the pillars' shape, the input quantities for the determination of the unique representative points consist of:

- the observation point locations which were treated as control points supporting the representative points computation as will be described below. The positions of these points were estimated from classical terrestrial measurements only;
- pillar axes (parameterized by points on the axes and direction vectors) as obtained from the TLS adjustment results.

In order to assure that the points to be used for the displacement computation are actually identical in both campaigns, the observation pillar control points were first projected onto their axes, using the shortest distance criterion (along the perpendicular line). As mentioned before, these control points do not lie directly on the pillar axes. The orthogonal distances from the axes range from 2 to 16 mm, depending on the particular observation pillar.

Furthermore, all representative points were determined by extrapolating downwards to the center of the pipeline with the help of the axes direction vectors. Additional analysis has proved that the distance of the control points from the axes had not changed (the integrity of the pillars remained unaffected). Therefore the projected points can be taken as the origins for the extrapolation. If only the pillar axes data computed from the point clouds were used, the equality of the extrapolated points could not be guaranteed because the points on the axes (P_0 in equations 23–25) are not comparable. In Figure 49, the calculation of the representative points is presented together with the extrapolation

step of 20 cm and the maximum distance of 3 m from the origins, corresponding to the approximate distance of the pipeline centers from the pillar top ends.

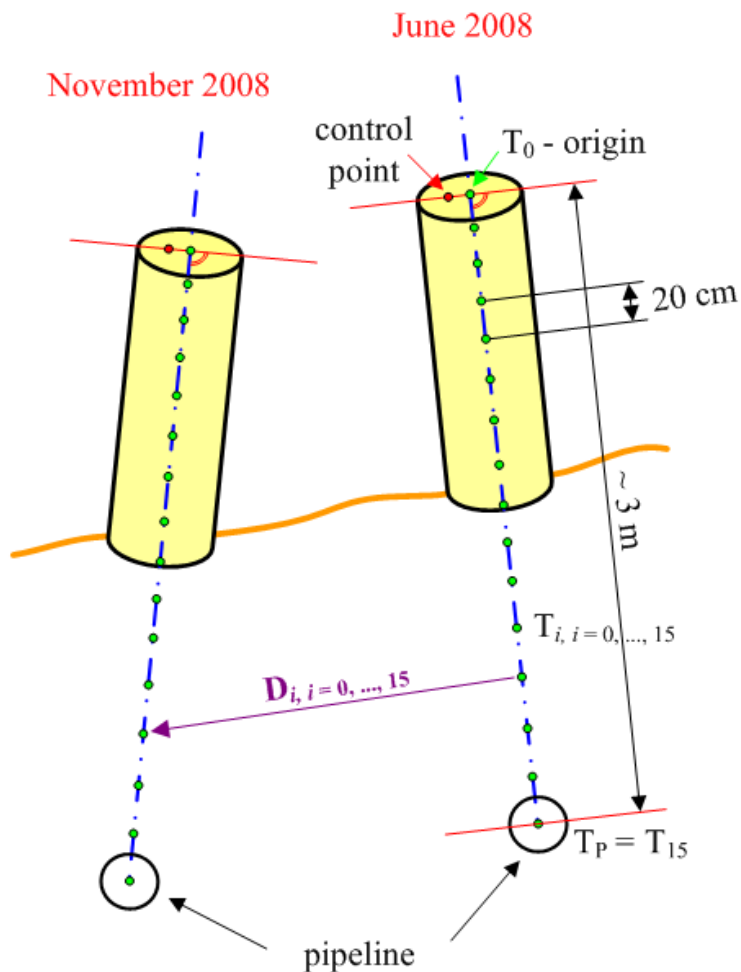


Figure 49: Identical points for the determination of displacements D_i , including the origin T_0 and the point in the center of the pipeline T_P .

4.1.3 Displacement evaluation

The results of employing the approach described in the previous section have shown that pillars 4212, 4213, 4214 and 4215 have moved and pillar 4216 has not. The sizes of displacements are presented in Figure 50. The displacement of representative points on the cylinder axes is not a linear function of the distance from the corresponding origins. In the case of the pillars where the shape has not changed in the period between both measurement campaigns also the analytical function of the displacements could be used to visualize the results presented in Figure 50. However, following the proposed methodology presented in section 2.8.2, in the case of more complex objects which deform their shape and require the representative points to be determined on the surface itself

the analytical function of the displacements would be difficult if not impossible to find. In Figure

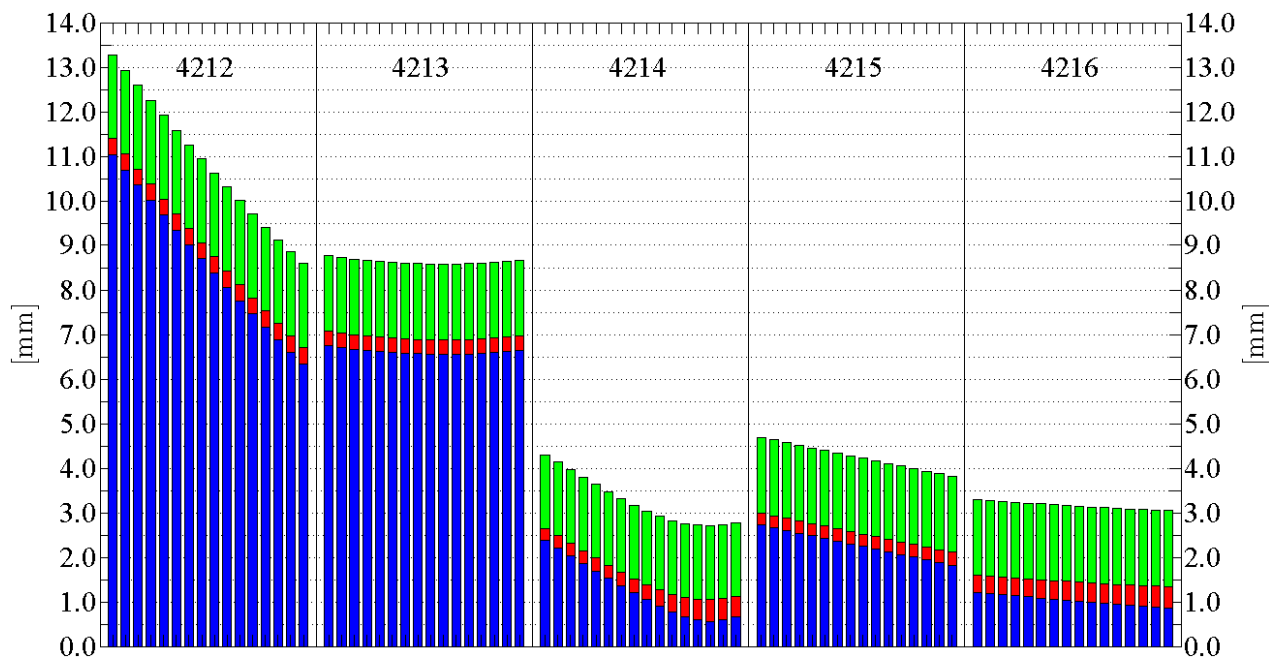


Figure 50: Pillar 3D displacement vectors (blue bars), standard deviations of displacements (red bars) and positional standard deviations of representative points T_i used for the calculation of displacement vectors (green bars, maximal values of $T_{i,\text{JUN}}$ and $T_{i,\text{NOV}}$ standard deviations are shown). The identical points T_0 to $T_P = T_{15}$ go from left to right for each observation pillar.

50, for all positional standard deviations of the representative points $T_{i,i=0\dots 15}$, the three-sigma rule was applied, expanding the confidence area up to 99.73 %. This way it is clear that pillars 4212 and 4213 have been exposed to the biggest movements ranging from more than 1 cm to 6.4 mm for pillar 4212 and about 6.5 mm for 4213. By examining the trends of displacements, it is also possible to conclude that pillar 4212 has inclined, resulting in the decreasing values of displacements from top downwards. The movement of the pipeline under 4212 is consequently only 57 % of the movement of the origin at the top, which means that the inclinations may have quite significant impacts on the values of displacements. Therefore, by observing only pillar peaks we cannot get accurate and reliable information on the movements of the pipeline itself. This fact is very important and may avoid or prevent false alarming from the pipeline manager side. The same inclination pattern cannot be seen for pillar 4213. The displacements indicate that all 16 points along the axis have moved almost equally and no considerable inclination effects were present.

The other two pillars, 4214 and 4215, were experiencing less impact from the ground movements, especially pillar 4214 where only the upper four points T_0 to T_3 have moved and the others have not. The displacements of the lower points are below the level of their corresponding end point precisions. Again, the inclination of 4214 has resulted in the reduction of displacements of about 21 % when comparing T_0 and T_3 , but no movements were detected for the pipeline center T_P .

The pillar 4215 displacements were between 2.7 and 1.8 mm, decreasing from top downwards and showing that here, too, the inclination of the pillar affected the pipeline level a little less than the top with the reduction of 33 %. Yet no displacements were detected at the site of pillar 4216 since no displacement vector was larger than the corresponding end point confidence areas.

The presented results were obtained by employing all TLS points and the standard deviations of the cylinder parameters obtained through the subsampling approach presented at the end of section 3.3.3.3. By decreasing the number of points up to 50 %, the same conclusions could be drawn from the displacement analysis. Hence, the presented results show a high degree of reliability with the average standard deviation of displacements of 0.4 mm. However, when reducing the number of TLS points in the computation of cylinder parameters below 50 %, the results are affected to such an extent that the displacement pattern cannot be sustained. Additionally, the results presented in Figure 50 were also compared to the axes direction vector analysis in order to confirm the pillar inclination characteristics. Finally, the directions of the displacements were checked, i.e. how they coincide with the terrain directions. Both tests have proved the quality of the results and the trends to be undisputable.

4.2 Outdoor test 2

The inspection analysis will first focus on the wall since both deformation models could be used in the process. Starting with the truncated direction model, this model could only detect displacements and deformations in the direction perpendicular to the wall's surface. In each patch the estimated parameters of the best-fitting planes (centroids and normal vectors) from the two measurement campaigns were used to calculate displacements along the reference directions, i.e., the normal vectors of the first epoch. The resulting displacements represent the distances from the first epoch centroids to the points at the intersections of the reference directions and the planes from the second epoch (see Figure 9). Around 4500 patches (segments) were found on the wall that could be examined in the model, since they contained enough points and passed the model validity test (with respect to the noise level and the residual pattern). In Figure 51 the results of the truncated direction model are shown in a form of a histogram. Based on the truncated direction model results, most of the displacements of the wall's surface patches are statistically not significant. Hence, the magnitude of the patch displacements perpendicular to the wall seems to be too small to be considered an actual movement. The few patches above the 4 mm level which are significant are simply not indicating any obvious trend that could be regarded as realistic. Concerning the dotted red and green lines in Figure 51 these are the outcome of the error propagation process, beginning with the polar coordinates of each point in the instrument's coordinate system σ_{φ_i} , σ_{θ_i} and σ_{D_i} (each multiplied by a factor of 3) and proceeding all the way to the final points used to calculate the displacements, including the transformation as well as the modelling process. The red dotted line stands for the threefold joint positional precision $\sigma_{P_i} = 3 \cdot \sqrt{\sigma_{C_i}^2 + \sigma_{P_{i,int}}^2}$, where σ_{C_i} and $\sigma_{P_{i,int}}$ are the corre-

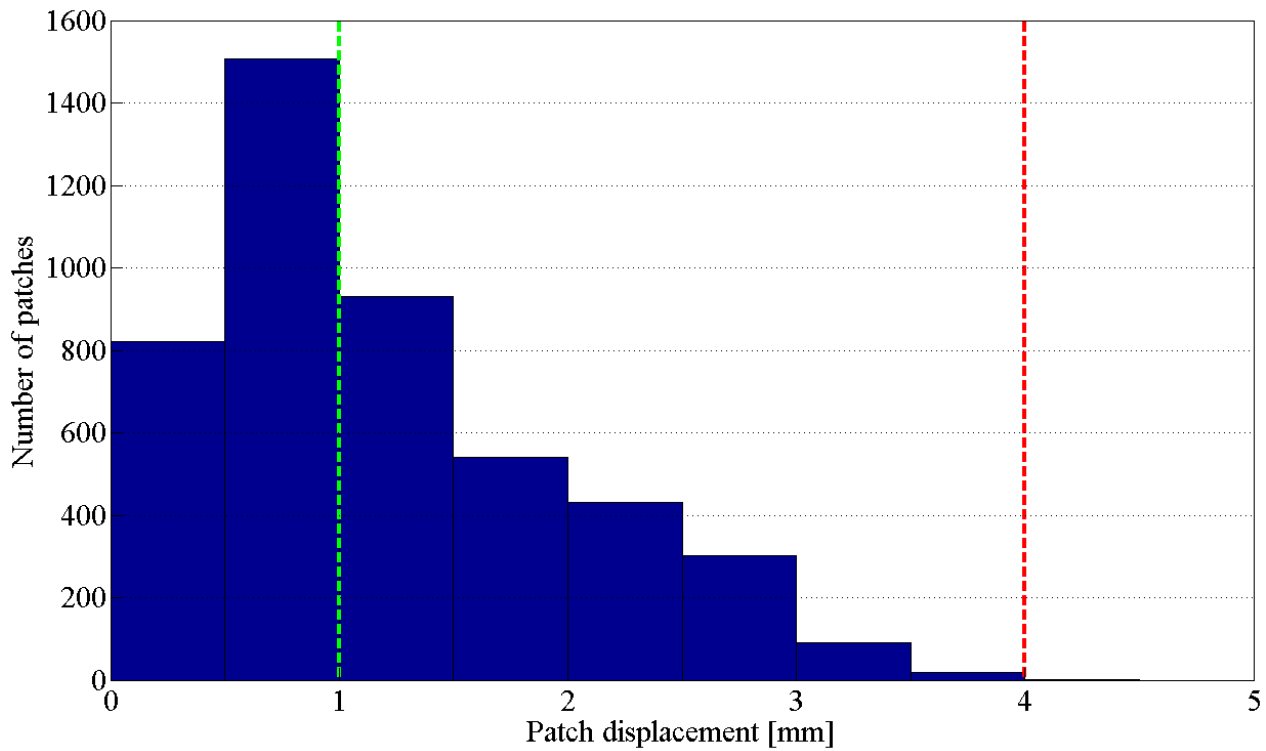


Figure 51: Histogram of the patch displacements from the truncated direction model. The red dotted line indicates the threefold joint positional precision of the pair of points used to calculate the displacements. The green dotted line represents the standard deviation of the estimated displacements.

sponding positional precisions of the centroids from the first epoch and the points of intersections of the reference directions and the planes from the second epoch. The calculations also reveal that the standard deviations of the displacements (green dotted line) are as big as most of the patch displacements. In conclusion, the analysis of the results from the truncated direction model shows that surface conditions on the smooth part of the wall (not including the surface features from Figure 47) remained unchanged up to the 4 mm level, a level predicted by the error propagation process. If any changes did occur, these would be undetected by TLS measurements.

Focusing now on the second deformation model, the unique representative points could be determined on the wall's surface features (see Figure 47) by intersecting adjacent planes extracted on different sides of each of them according to the segmentation algorithm described in section 2.7.1. These single representative points were obtained by intersecting various plane triplets, resulting in about 100 points on the entire wall which enabled the estimation of displacements in the same way as in the case of the point-wise monitoring approach (as three-dimensional vectors). Of all the extracted planes during the modelling process, only those satisfying strict segmentation thresholds were used to calculate the intersection points avoiding the outliers and the edges with further considerations of the spatial distribution of residuals for each plane. Finally, the points in the intersections

of each plane triplet P_i were computed as follows:

$$P_i = \frac{-d_1(\vec{n}_2 \times \vec{n}_3) - d_2(\vec{n}_3 \times \vec{n}_1) - d_3(\vec{n}_1 \times \vec{n}_2)}{\vec{n}_1 \cdot (\vec{n}_2 \times \vec{n}_3)} \quad (26)$$

where \vec{n}_1 , \vec{n}_2 and \vec{n}_3 are the normal vectors each corresponding to one of the planes in the triplet. The d_1 , d_2 and d_3 are the free plane parameters calculated from the normal vector components and the planes' centroids. In this second deformation model, the same strategy in terms of the error propagation was performed as in the truncated direction model. The only difference in model 2 was in the last part of the propagation process where equation 26 replaced the ones used in model 1. The results of deformation model 2 are shown in Figure 52. The histogram of the results from

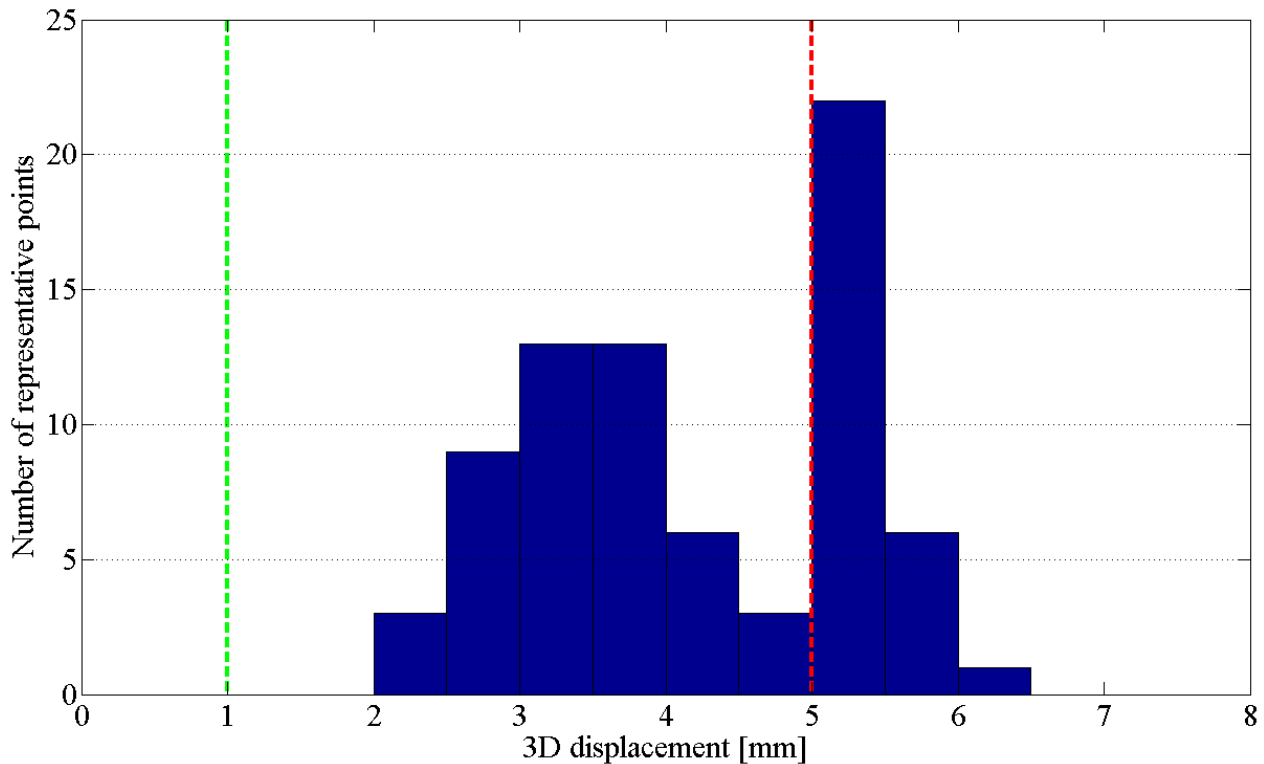


Figure 52: Histogram of the wall's displacements calculated in model 2. The red and the green dotted lines indicate the same quality thresholds as in Figure 51, i.e., the threefold joint positional precision and the standard deviation of the estimated displacements.

this deformation model is characterized by two peaks of which only one is statistically significant, i.e., the one above the red dotted line. These representative points have experienced displacements large enough to be considered as actual movements. With respect to the direction of the movements these points, the results indicate that it is the vertical component of the displacement vectors which is predominant, meaning that all the points associated with displacement larger than 5 mm have moved downwards. Even more interesting is the fact that the significant displacements were found on the part of the wall right above the tunnel axes, as can be seen in Figure 53. In Figure 53, the red dots with no vector association (blue lines) are the ones that have moved less than 5 mm, a

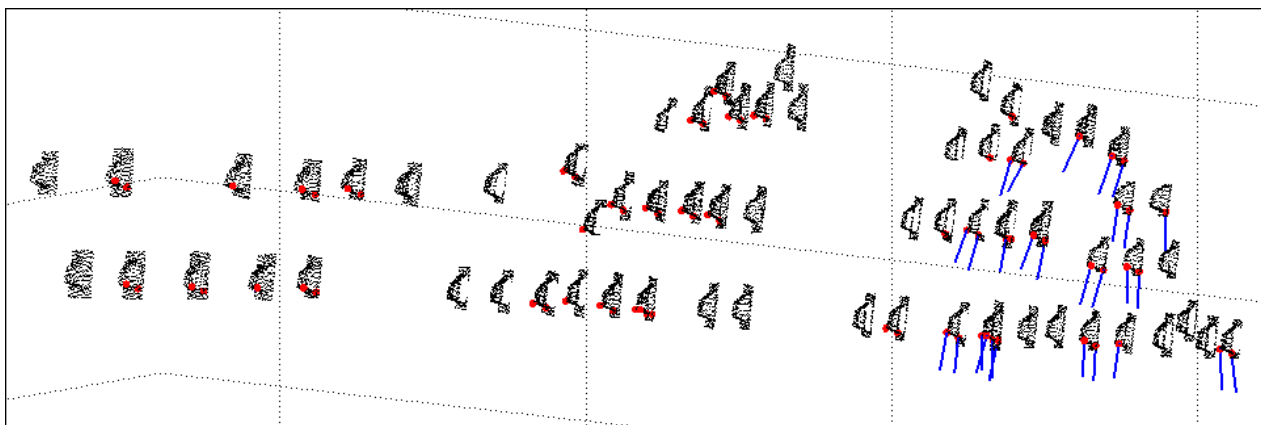


Figure 53: The directions of the displacement vectors for the wall's representative points. The black dots representing the point clouds of the wall features are for orientation purposes only. The red dots are the 100 points that were determined at the intersections of the plane triplets. Of all these 100 points only those with the significant magnitude of the displacement were associated with their corresponding directions, i.e., blue lines which have been expanded 200 times to be able to see the results.

level separating the significant displacements from the rest. Based on the results of this analysis, a high possibility exists that the part of the wall from Figure 53 has been displaced in the range from 5 to 6 mm. The remaining little doubt would be severely reduced if the obtained results could be compared to an alternative measurement source, e.g., precise classical terrestrial method.

On the other hand, should the vertical component of the displacement vectors be significant at one part of the wall, it is possible that by examining the road next to it (see Figure 46) one would expect the trend to be seen here as well. If the results are coinciding, this could strengthen the outcome of the analysis. Indeed, as seen in Figure 54, where the displacements of the road's surface are shown as obtained after applying the truncated direction model, some of the patches have experienced displacements at the level significant to be considered an actual displacement also at the location of the road. For the examination of the road's surface, the deformation model 1 was the only option available due to the smoothness and the lack of any surface detail on the road to be able to extract the representative points. Based on results shown in Figure 54, the patches which have been displaced for more than 4 mm could be regarded as significant movements since by using the same processing approach as in the case of the wall, the error propagation results were nearly the same. This means the positional precision of 4 mm and the standard deviation of the displacements at around 1 mm. Moreover, all of the point displacement vectors point in the same direction as the ones estimated for the wall's features, i.e., direction downwards. Despite having no alternative source of information, this would mean that the outcome of the analysis was at least observed not only at two different locations but also employing two different deformation models. The remaining small gap towards the solid belief in the results can basically only be filled by some control measurements or by more field campaigns. This other options represents an additional possibility since the continuation of

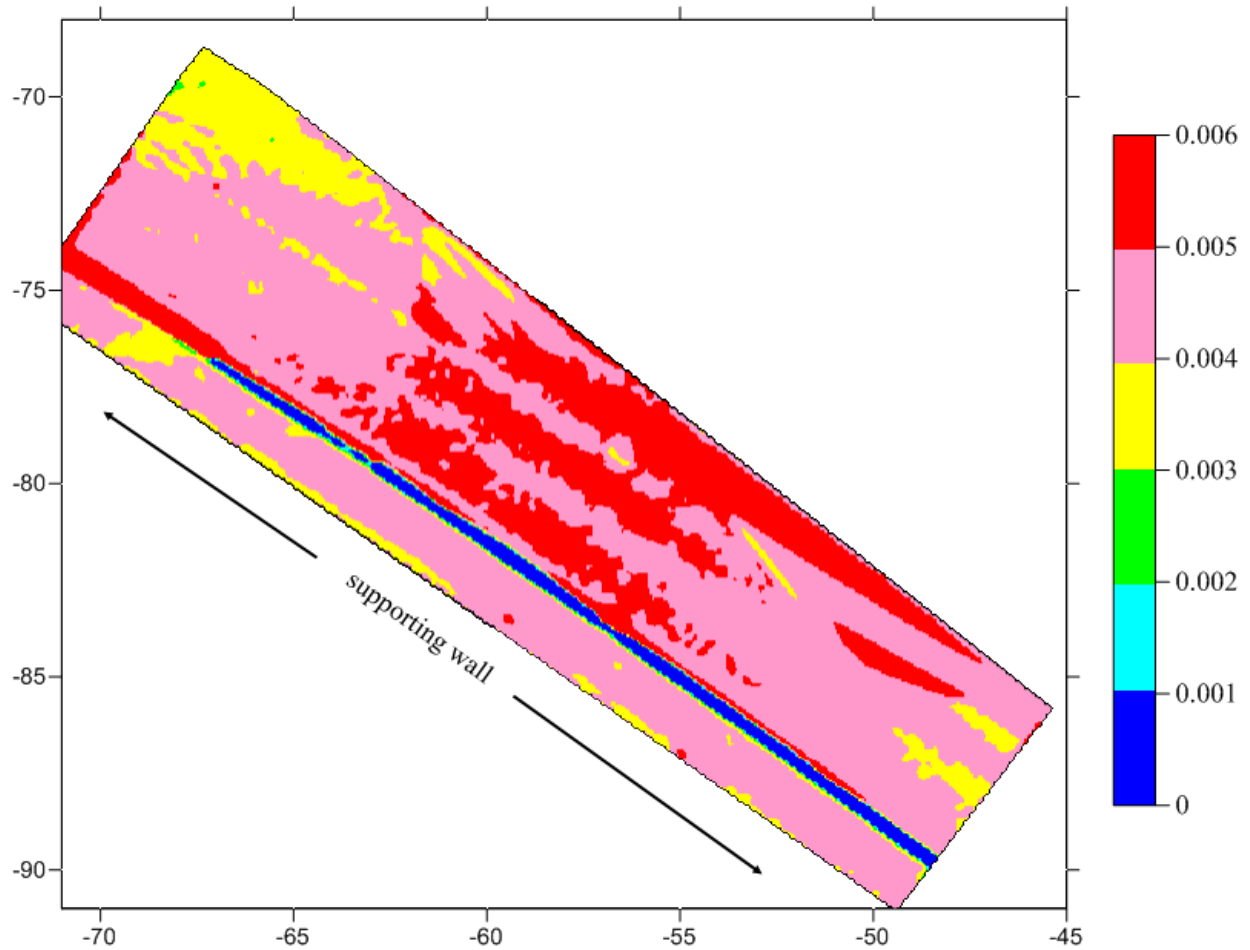


Figure 54: The magnitude of displacements of the roads surface. The frame numbers represent the coordinate system and the values in the legend are in [m]. The location of this section of the road is shown in Figure 46.

measurements is important as in any monitoring scheme and can over time (short or long period, depending on the interval between the field campaigns) reveal whether the displacements trends can be observed more than once. For now, the conclusions of the analysis speak in favor of the statement that a part of the wall and the road have been displaced downwards for about 5 mm.

During this extensive analysis, an additional and final interesting outcome involving the road's surface was observed after transforming the point clouds into the gridded form and subtracting the cell heights along the vertical direction. Most obviously the tire track areas have systematically sunk for up to 2 mm due to the constant traffic on this road. Such small displacements may well be below the significant level, but when examined visually, the pattern becomes evident. In Figure 55 the sinking of the road track areas is indicated by the dark stripes standing out from the rest of the road. Discovering this pattern is important for two reasons. It could only be detected by a surface-wise measurement technology such as TLS. Furthermore, it offers more confidence in the instrument's detectivity level itself since this small change in the road's surface condition did not go by unno-

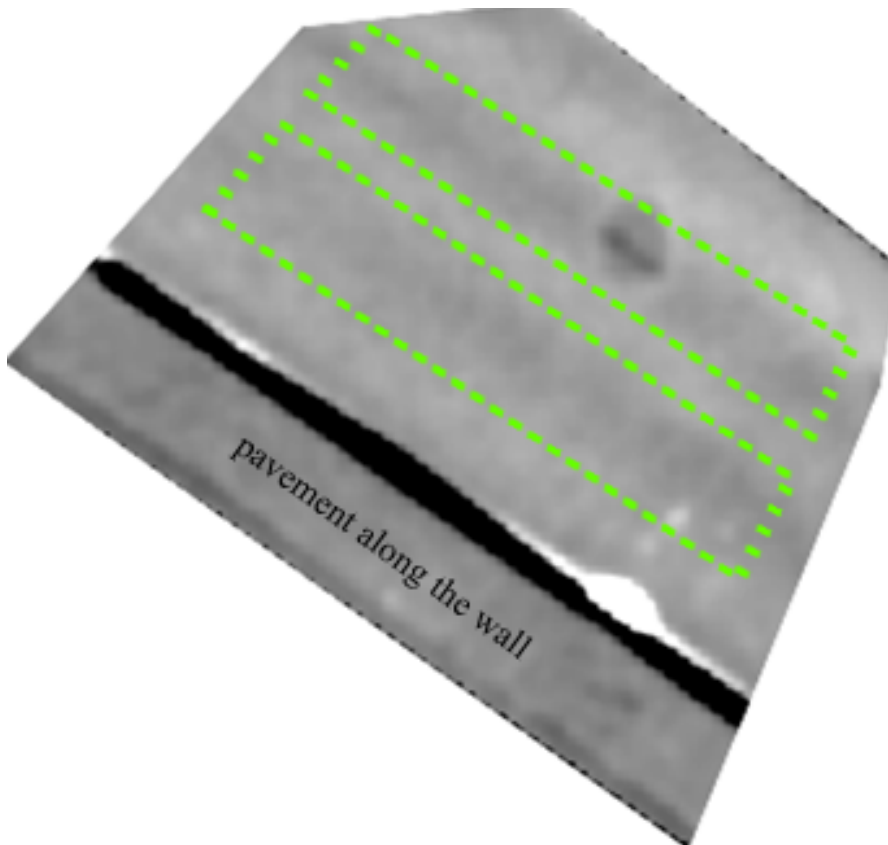


Figure 55: The road tracks' sinking pattern in the form of a grid shown from a close distance.

ticed. Consequently, the involvement of the TLS in the geodetic monitoring can in many ways be beneficial and may lead to some surprising results.

4.3 The indoor test evaluation

Finally, a short evaluation of the indoor tests should be done to summarize their overall quality and efficiency already indicated in sections describing the experimental results. In order for the results of these tests to be free of errors produced by the realization process itself they had and were carried out with utmost care. It is firmly believed that the results, whatever they are, are not the outcome of errors introduced by the careless experimental set-up. Moreover, also the conceptual design of the indoor tests with its simplicity can be treated as reliable enough to provide the necessary high quality results.

Despite the credible execution of these tests, the measurement uncertainty at such a small error level would require the repetition of especially the first indoor test, during which the targets' mechanical imperfections were analyzed by the manual observation process. Repeating the measurement process under various conditions would contribute to the reliability of results but the final conclusions of this test would probably not be altered. The fact is that the four targets used in the experiments are of slightly different mechanical quality and that the errors produced by the two degree rotation

are very difficult to model. Most of these errors seem to be confined to the ± 1 mm boundary, within which the center deviation patterns should be verified regardless of the quality of the instrument used to carry out the observations. So-far, only the observed 1 mm vertical eccentricity error for target T4 was taken into account due to its apparent stability (see Figure 11 on page 32). The rest of the errors could not be modelled successfully, which means that probably some of their effect can only be minimized through the transformation process.

Compared to the level of errors from the first test, a much larger error level was uncovered during the second indoor test. Since both of the two tests were designed to analyze the influences of errors that eventually affected the quality of transformation parameters in the outdoor test 2, not modelling the range errors would have much more impact on the quality of the transformation. The extension of the maximum range from the scanner to the target came at a cost of scanning the retroreflective part in order to estimate the target distance. Selecting the points on the retroreflective part of the target surface can lead to distance errors of up to 1 cm, almost ten times higher than those from the first indoor test. In general, the correction functions from Table 3 can reduce the range errors below the millimeter level but the efficiency of modelling these errors can decrease if the error behavior becomes unstable. The uncovered instability of the error behavior is presumably caused by the retroreflective part of the target but could also arise from the scanner side. Therefore, further tests are needed to find out why these error fluctuations occur. It is possible that the inability of modelling such fluctuations with enough efficiency contributed to the exclusion of some of the station measurements in the outdoor test 2. Most likely the amplitude fluctuations could only be avoided by replacing the retroreflective tape on the target with a less “aggressive” one. Either way, the quest for finding a better target type, as well as the implementation of the modelling approach where the scanner and target contributions to the range errors are separated, remains open.

Concerning the indoor test where the scanner’s detectivity level was analyzed with respect to various surface conditions, the results of the test provide valuable information when deciding on scanner-object distance, incidence angle limitations and the point density. Based on the conclusions from the final indoor test, the scanning geometry and parameters in the outdoor test 2 were adjusted (maximum range of 30 m from the object, maximum incidence angle of 45° and the point density corresponding to a minimum of 400 point per patch). Furthermore, the a posteriori standard deviations, estimated for each material sample (ranging from 1.6 to 2.2 mm), can be used to upgrade the variance-covariance matrices of the scanner’s direct measurements (particularly for the distance component) when performing the error propagation process. On the basis of the estimated a posteriori values, the modelling process in the outdoor test 2 was adjusted in order to exclude the patches with the planar noise higher than 3 mm. The results of the final indoor test further indicated the potentially negative effects caused by the scanner’s power supply. Therefore, the power shortages as well as the warm-up periods related to the instrument were avoided in the outdoor test 2 in order to minimize the impact on the stability of the scanner’s detectivity level. As already mentioned, the results of the final indoor test indicated that the 2 mm and 5 mm displacement level are well distinguishable, in turn supporting the findings from the deformation analysis.

5 CONCLUSIONS

The experimental results presented in the thesis must now be evaluated with respect to the initial hypothesis outlined in section 1.2. Moreover, the results offer a possibility to measure the quality of the methodological steps described in Chapter 2. Therefore, it is the purpose of this section to draw the final conclusions of the entire work described herein.

Based on the results of the thesis, clear evidence exists for significant confidence in accepting the working hypothesis. Following the proposed methodology can lead to a high precision deformation determination in the long-term for objects and not only for signalized (i.e., marked) points. TLS has proved to be capable of providing high precision data and therefore could be considered a complementary surveying technique which cannot only be combined with other well established high precision surveying technologies but can also contribute to a more complete understanding of deformations. However, the analysis shows that working in the millimeter domain with TLS comes with a certain price since the field work as well as the processing of the measurements has to be done with a lot of care. Furthermore, the level of detectable deformations in the millimeter domain can be influenced by many factors, such as:

- the selection of the surveying equipment (a scanner, targets);
- the conditions in the field (surface properties, distance to the object, incidence angle, geodetic network geometry);
- the efficiency of the modelling of systematic error (calibration parameters);
- the proper error propagation schemes incorporating all the subsequent data processing steps.

The estimation of displacements and deformations below the scanner's nominal capabilities can be achieved in general. This fact has been proved in the outdoor test 1 where the TLS has been used to determine the pillar axes. In this test the TLS results did match the ones from the precise classical terrestrial method to a very high degree. The analysis of the data from test 1, which have been first described in Vezočnik et al (2009), was taken a step further in the thesis but the final results published in the paper remain unchanged. On the other hand, the role of TLS in the outdoor test 2 was even bigger and despite some problems with the instrument as well as with the absolute orientation, the final results are promising in terms of the ability of TLS to be used for the high precision monitoring tasks. In both outdoor experiments, the establishment of the same surveying conditions in the field and following the same data processing algorithms was considered an important aspect of the general workflow in order to avoid the accumulation of any additional errors. For the monitoring to be effective in the long run, these errors have to be minimized as much as possible.

The modelling of systematic errors and obtaining the calibration parameters for all the measuring equipment is also a necessity. Without this step implemented in the workflow, the capabilities of deformation inspection in the millimeter domain may be severely reduced. Not only should the

modelling of systematic errors be considered in the process, but the calibration parameters (e.g., range error functions for the TLS targets, scanner systematic errors) would have to be determined by frequent tests in order to be estimated from highly redundant observations (and possibly different ambient conditions) and particularly to see how their temporal stability is behaving. Moreover, tests are definitely needed also in terms of the surface material response to evaluate the stability of the instrument's detection capabilities.

The extraction of the significant displacements and deformations cannot be approached without the proper error propagation process. During the modelling stage it is also important to consider the introduction of proper stochastic models as well as the estimation of realistic precision parameters for all the input quantities of both deformations models so as to not be deceived by too optimistic standard deviations, which are in many cases simply the outcome of highly redundant TLS measurements. According to the results presented in Chapter 4 such error propagation schemes revealed that TLS can in certain cases reach below the 5 mm level in the displacement and deformation detection, but to go as far as 1 mm would not be possible after applying the threefold point precision. With respect to the magnitude of detectable deformations, a 5 mm level is more realistic when dealing with objects larger in size and non-ideal surveying conditions. The detectivity level may be slightly extended by scanning the object with multiple scans and averaging the results. Scan multiples can also contribute to the stability of the deformation detection as shown during the surface material response test.

The surveying conditions can eventually decide whether the data can be used for the change inspection at this small scale level. In the outdoor test 2, the non-ideal conditions with respect to the number of TLS targets and the network geometry did contribute to the exclusion of some of the station measurements. To overcome this obstacle, using more targets per station is advisable in order to increase the quality and stability of the estimated transformation parameters. Not to increase the overall time spent in the field to perform the classical terrestrial measurements, some of these targets do not necessarily have to be included into the geodetic network but can be used for the relative orientation purposes only. The quality of the relative orientation can further be increased by the proper integration of targets and the ICP algorithm (Haring, 2007). Once the relative orientation parameters between the adjacent scanner station would be estimated, the whole block (i.e., all the TLS station measurements) could be transformed into the reference frame simultaneously. In order to be able to analyze the quality of the transformation also at the object side, the size of the overlapping areas has to be taken into consideration. With today's scanner providing very fast scanning rates, the size of the overlapping areas can be increased beyond 50 % with no significant time delays. The more such areas and the bigger they are, the better control could be established over the quality of transformation.

Finally, to strengthen the confidence in the results of the deformation analysis it may be sometimes advisable to install some control points onto the object of inspection and estimate their positions by means of an alternative surveying technology. This multi-sensor monitoring approach is most certainly one of the nowadays trends and will be important also in the near future. The involvement

of control points and complementary geodetic techniques does not decrease the quality of the proposed methodological workflow but can ultimately contribute to the level of trust in the outcome of such intricate geodetic tasks regardless of the type of technology employed.

5.1 Outlook

Despite the work presented in the thesis, some of it remains for the near future. These future objectives will be focused around the following topics, which can all contribute to the final quality of the TLS deformation monitoring approach:

- the positioning of the point clouds within the reference frame;
- the temporal stability of the calibration parameters (for the scanner and the targets as well);
- testing the scanner's performance on more material samples of various surface properties;
- the minimization of the overall time needed to acquire and process the data;
- the development of *ad hoc* multi-sensor monitoring configurations.

The first objective is related in particular to the quest of finding the optimal targets that would not be only associated with high quality in terms of systematic errors but would possibly be integrated with other reflectors within a single composition. This would also minimize and control the eccentricity offsets and make sure that no errors are introduced when switching one reflector with another. Based on the results presented in the thesis, it is fair to conclude that classical terrestrial coordinate estimation of the network points can be much higher than the coordinate estimation of the targets by the TLS measurements. Many times the main reason is not the quality of the center extraction algorithms themselves but the poor modelling efficiency of the systematic errors produced on the target side. Consequently, the inability of controlling and minimizing these systematic errors will affect the overall quality of transformation. Therefore the development of efficient models for the minimization of errors during the transformation estimation process has to be tackled as one of the future steps.

The in-depth calibration of the scanner still remains on the horizon as one important task to accomplish. Scanners employed in the experiments have only been calibrated by their manufacturers, therefore more knowledge is needed in terms of the detection and modelling of any additional or remaining systematic errors. Furthermore, tests should be designed to investigate the temporal stability of the scanner's calibration parameters as well as the stability of the systematic errors on the target side (e.g., range error function parameters). The temporal stability of these parameters will eventually give information on the quality of the selected TLS surveying equipment and dictate the conditions of its use in the monitoring tasks (also with respect to the level of detectable displacements and deformations). By the appropriate configuration of scanner stations during the field campaigns, the large data redundancy could eventually be used to perform an on-the-job calibration, such as those presented in e.g., Dorninger et al (2008), Molnár et al (2009) or Bae and Lichti (2010).

Next, more material samples of various surface properties should be tested to see how they affect the ranging precision of the scanner. Samples of different chemical composition, color, roughness and surface moisture should be included in order to establish a database that would help deciding which materials are appropriate and under what conditions they should be scanned (e.g., from how far away and under what incidence angle). Testing the scanner's response on more samples will provide further insights into the limitations of TLS for the long-term deformation monitoring.

Finally, the overall time needed to acquire and process the data should be optimized to such an extent that the millimeter level of deformations could be maintained. However, it is worth noticing that the millimeter level requires the work to be performed with a lot of care, thus preventing a radical reduction of the field work and data processing time. Still, it would be worth simplifying the data processing phase in order to achieve the ease of use. This way, less trained personnel would be required. As for now, the overall time for the data acquisition and processing could be compared to any other high precision engineering task. But in the future, the trends will definitely be oriented towards a more automated monitoring approach including multi-sensor compositions each operating for a specific and dedicated task, thus providing more frequent observations of the object of inspection. Such compositions could also be free of the target scanning and extraction process and all the errors it introduces. The idea is to permanently install the scanner onto a fixed platform (e.g., pillar) near the observable structure to provide the full coverage of the surface with the TLS measurements. The stability of the scanner's platform would be controlled from distant stations placed on stable ground using precise classical terrestrial method. The classical terrestrial measurements would not only monitor the stability of the scanner's platform from a distance but would be designed to perform frequent and automated observations between these distant stations in order to monitor their stability as well. The automated process of observations would reduce the amount of field work and allow the study of the structure's instantaneous condition on the basis of more frequent surface-wise observations ultimately contributing a great deal to the level of confidence and understanding of the final results of the deformation analysis.

6 SUMMARY

Monitoring displacements and deformations of anthropogenic spatial structures and objects represents one of the most intricate areas in geodetic surveying. In recent years, terrestrial laser scanning (TLS) has become increasingly used in different engineering surveying applications, including the field of displacement and deformation monitoring. Despite the growing number of presented solutions, the millimeter domain in displacement detection is still an open area of investigation, which is one of the reasons for the evaluation of the potential use of this tempting measurement technology at such a small scale level. Compared to other sensor technologies and point-wise monitoring approaches, where deformation evaluation is limited to a few discrete and well signalized, TLS is characterized by the following advantages:

- rapid and surface-wise measurement process;
- the ability to model the shape of the objects on the basis of huge data redundancy;
- non-contact nature demanding no direct object accessibility.

Based on the current research status, it was reasonable to try to evaluate the working hypothesis stating that TLS can be used for the millimeter size detection of displacements and deformations in the long-term perspective. Such an evaluation required the integration of TLS with other geodetic measurement technologies (GNSS, precise classical terrestrial method) in order to assure the quality and stability of the reference frame. The thesis tries to address these problems by introducing the proposed methodological workflow.

The proposed methodological workflow is divided into seven different steps, all of which had to be analyzed in detail and eventually modified to be able to meet the desired high precision demands. These steps can be treated as a sort of guidelines that would apply to any kind of TLS monitoring task regardless of the object of interest and the level of surface detail. The first step addresses the part of the workflow which is one of most elusive ones to be performed in the long-term perspective, namely the possibilities of controlling the quality and stability of the reference frame. The reference points should be located outside the area subdued by deformations, which can be in certain cases far away from the objects under inspection. Therefore, in order to assure the long-term connectivity between these reference points and the point clouds of the objects' surfaces, the target based point cloud positioning approach is the most reliable. Step 2 proposes the targets (which are placed near the object of study) to be included in the geodetic network consisting also of reference and control points. Furthermore, the target positions have to be estimated at each scanner station from the high density point clouds as well. Hence, step 3 addresses the possibilities for this estimation process proposing an alternative center extraction and estimation algorithm for the target type used in the thesis. In step 4 the transformation needs to be estimated based on which point clouds of the object's surfaces can finally be positioned within the reference frame. Once the connection to the reference frame is established, the focus of the remaining steps of the workflow is first shifted to the

description of how the surfaces under inspection must be scanned in order assure a homogeneous point coverage and to what limitations are governing the TLS acquisition process. Next come the guidelines to the surface modelling process, which is a vital part of the workflow if the large data redundancy is to be exploited in full scale. The surface models are eventually evaluated within the two proposed deformation models, again designed to be applicable in the most general of circumstances. The decision on which deformation model to use depends only on the amount of surface detail. The first model is always applicable, whereas the second one requires enough distinct surface features. Regardless of the model, the error propagation has to be performed alongside in order to be able separate the actual displacements from the measurement errors.

The proposed methodological steps were employed in the two outdoor tests studying the displacements and deformations of three objects (the pipeline in test 1, the supporting wall and the road surface in test 2). Prior to the outdoor tests, three additional indoor tests were carried out in order to evaluate two of the most vital components of the workflow:

- the quality of the targets;
- the performance of the scanner's rangefinder with respect to various surface conditions.

The quality of the targets was analyzed within two separate tests, i.e., the test for the evaluation of the targets' mechanical imperfections and the test for the analysis of the behavior of systematic range errors, which occurred due to scanning of retroreflective part of the target surface with the scanner used in the outdoor test 2. The results of the first of the two tests reveal the differences between the four used targets despite the fact that they are of the same type. The second test was definitely reasonable since it exposed large systematic range errors that had to be modelled for each target separately. The results of both tests provided an important insight into the extent of the influences of errors that will eventually affect the quality of transformation parameters. Next, for the outdoor test 2 alone also the scanner's performance was tested with respect to how the distance measurements are affected when scanning objects of different surface properties. The most common surface conditions of the outdoor test 2 were included in the test samples. The results of this indoor experiment could be used when deciding on the scanner-object distance, incidence angle limitations and the point density. Based on the knowledge from the indoor tests, the field work of the two outdoor tests could be adjusted in order to minimize the introduction of errors. Following the methodological workflow recommendations, in both outdoor tests the same surveying conditions were assured in two field campaigns for each test. Compared to the outdoor test 1 where the quality and stability of the reference points was analyzed by GNSS observations, this same step was avoided in test 2 due to the assumed ground stability. In the data processing phase of both outdoor tests, the classical terrestrial observations between network points were adjusted with high quality using the measurements of the instantaneous atmospheric conditions. After transforming the objects' point clouds to the reference frame, the shape of the surfaces under inspection was modelled using a simple cylindrical model in test 1 and a planar model in test 2. Due to the size of the objects in test 2, the modelling process was carried out whether by splitting the original point

clouds into surface segments or by the help of the segmentation algorithm proposed in step 6 of the methodological workflow. The final results of both outdoor tests, i.e., the surface models and their estimated precision parameters represented the input for the deformation analysis.

In the outdoor test 1, the surface models could be reduced to single representative points not lying on the surface at all since the shape of the models did not deform. The determination of these representative points required the support of the networks' control points estimated from the classical terrestrial measurements. The classical terrestrial as well as the GNSS observations agreed on the stability of the networks' reference points between both field campaigns. On the other hand, the analysis revealed that the objects of interest have been displaced in the range from 2 to 10 mm. The error propagation process in test 1 suggested that the displacements larger than ≈ 2 mm could be regarded as significant. In the outdoor test 2, the supporting wall could be analyzed in both deformation models. The results from the first model revealed the absence of any kind of displacements and deformations. However, the results of the second deformation models exposed the presence of displacements in the range from 5 to 6 mm in the vertical direction of the wall. These results were confirmed also by the analysis of the road surface, which was analyzed within the first deformation model. The magnitude and direction of displacements was therefore calculated with two different approaches (deformation models) involving two neighboring objects. In the outdoor test 2, the error propagation suggested that the displacements larger than 4 mm (for the first deformation model) and 5 mm (for the second deformation model) could be treated as significant. According to the results from the indoor calibration tests, this displacement level should be within reach of the scanner's and the targets' performance. Finally, during the analysis of the road surface it was revealed that the tire tracks areas have systematically sunk for up to 2 mm within the period of less than one year.

Based on the results of the thesis, clear evidence exists for significant confidence in accepting the working hypothesis. Following the proposed methodology can lead to a high precision deformation determination in the long-term for objects and not only for signalized (i.e., marked) points. TLS has proved to be capable of providing high precision data and therefore could be considered a complementary surveying technique, which cannot only be combined with other well established high precision surveying technologies but can also contribute to a more complete understanding of deformations. However, the extraction of the significant displacements and deformations cannot be approached without the proper error propagation process. During the modelling stage it is also important to consider the introduction of proper stochastic models as well as the estimation of realistic precision parameters for all the input quantities of both deformations models so as to not be deceived by too optimistic standard deviations, which are in many cases simply the outcome of highly redundant TLS measurements. According to the results, such error propagation schemes revealed that TLS can in certain cases reach below the 5 mm level in the displacement and deformation detection, but to go as far as 1 mm would be extremely challenging. With respect to the magnitude of detectable deformations, a 5 mm level seems to be more realistic when dealing with objects larger in size and non-ideal surveying conditions.

7 REFERENCES

- Alba, M., Fregonese, L., Prandi, F., Scaioni, M., Valgoi, P. 2006. Structural monitoring of a large dam by terrestrial laser scanning. In: Proceedings of International Archives of Photogrammetry, Remote Sensing and Spatial Information Sciences. Dresden, Germany, September 25–27. Vol. XXXVI, Part 5 on CD-ROM.
- Altamimi, Z., Collilieux, X., Legrand, J., Garayt, B., Boucher, C. 2007. ITRF2005: A new release of the international terrestrial reference frame based on time series of station positions and earth orientation parameters. *Journal of Geophysical Research*, Vol. 112, No. B09401: 1–19.
doi: 10.1029/2007JB004949
- Austin, R. L., Schultz, R. J. 2006. Guide to Retroreflection Safety Principles and Retroreflective Measurements. American Traffic Safety Services Association. Fredericksburg, Virginia.
<http://atssa.com/galleries/default-file/RetroreflectionGuide-ATSSA.pdf> (accessed on 7.11.2010).
- Bae, K. H., Lichti, D. D. 2010. On-site self-calibration using planar features for terrestrial laser scanners. In: Proceedings of the ISPRS Workshop – Laser Scanning 2007 and SilviLaser 2007. Espoo, Finland, September 12–14. Vol. XXXVI, Part 3: p. 14–19.
- Bergeot, N., Bouin, M. N., Diament, M., Pelletier, B., Régnier, M., Calmant, S., Ballu, V. 2009. Horizontal and vertical interseismic velocity fields in the Vanuatu subduction zone from GPS measurements: Evidence for a central Vanuatu locked zone. *Journal of Geophysical Research*, Vol. 114, No. B06405: 1–20.
doi: 10.1029/2007JB005249
- Besl, P. J., McKay, H. D. 1992. A method for registration of 3-D shapes. *Pattern Analysis and Machine Intelligence*, Vol. 14, No. 2: 239–256.
- Beutler, G., Rothacher, M., Schaer, S., Springer, T. A., Kouba, J., Neilan, R. E. 1999. The International GPS Service (IGS): An interdisciplinary service in support of Earth sciences. *Advances in Space Research*, Vol. 23, Issue 4: 631–653.
- Boucher, C., Altamimi, Z. 2008. Memo: Specification for reference frame fixing in the analysis of a EUREF GPS campaign, Version 7.
<http://etrs89.ensg.ign.fr/memo-V7.pdf> (accessed on 24.10.2008).
- Caporali, A., Aichhorn, C., Barlik, M., Becker, M., Fejes, I., Gerhatova, L., Ghitau, D., Grenerczy, G., Hefty, J., Krauss, S., Medak, D., Milev, G., Mojzes, M., Mulic, M., Nardo, A., Pesec, P., Rus, T., Simek, J., Sledzinski, J., Solaric, M., Stangl, G., Stopar, B., Vespe, F., Virag G. 2009. Surface kinematics in the Alpine-Carpathian-Dinaric and Balkan region inferred from a new multi-network GPS combination solution. *Tectonophysics*, Vol. 474, Issue 1-2: 295–321.

Caspary, W. F. 1988. Concepts of Network and Deformation Analysis, Monograph 11. School of Surveying. The University of New South Wales: p. 68–96.

Chatfield, C. 1995. The Analysis of Time Series, An Introduction. Fifth Edition. The University of Bath, Chapman & Hall: p. 18–25.

Chrzanowski, A. 2006. Tasks and achievements of the FIG Working Group on deformation measurements and analysis. In: Proceedings of 3rd IAG Symposium of Geodesy for Geotechnical and Structural Engineering and 12th FIG Symposium on Deformation Measurements. Baden, Austria, May 22–24.

http://www.fig.net/commission6/baden_2006/pdf/oc/chrzanowski_fig.pdf (accessed on 24.10.2008).

Ciddor, P. E. 1996. Refractive index of air: new equations for the visible and near infrared. *Applied Optics*, Vol. 35, No. 9: 1566–1573.

Ciddor, P. E., Hill, R. J. 1999. Refractive index of air. 2. Group Index. *Applied Optics*, Vol. 38, No. 9: 1663–1667.

Dach, R., Hugentobler, U., Frizez, P., Meindl, M. 2007. Bernese GPS Software, Version 5.0. University of Bern, Astronomical Institute.

Dorninger, P., Nothegger, C., Pfeifer, N., Molnar, G. 2008. On-the-job detection and correction of systematic cyclic distance measurement errors of terrestrial laser scanners. *Journal of Applied Geodesy*, Vol. 2, Issue 4: 191–204.

EUREF Permanent Network. Guidelines for EPN Analysis Centres.

http://www.epnccb.oma.be/_organisation/guidelines/guidelines_analysis_centres.pdf.
(accessed on 12.3.2009).

Even-Tzur, G., Salmon, E., Kozakov, M., Rosenblum, M. 2004. Designing a geodetic-geodynamic network: A comparative study of data processing tools. *GPS Solutions*, Vol. 8, No. 1: 30–35.

Gonzales-Aguilera, D., Gomez-Lahoz, J., Sanchez, J. 2008. A new approach for structural monitoring of large dams with a three-dimensional laser scanner. *Sensors*, Vol. 8, No. 9: 5866–5883.

Gordon, S. J., Lichti, D. D. 2007. Modelling of terrestrial laser scanner data for precise structural deformation measurement. *Journal of Surveying Engineering*, Vol. 133, Issue 2: 72–80.

Haring, A. 2007. Die Orientierung von Laserscanner- und Bilddaten bei der fahrzeuggestützten Objekterfassung. Dissertation. Vienna University of Technology, Institute of Photogrammetry and Remote Sensing: 156 p.

Hoover, A., Jean-Baptiste, G., Jiang, X., Flynn, P. J., Bunke, H., Goldgof, D. B., Bowyer, K., Eggert, D. W., Fitzgibbon, A., Fisher, R. B. 1996. An Experimental Comparison of Range Image Segmentation Algorithms. *IEEE Transactions on Pattern Analysis and Machine Intelligence*, Vol. 18, No. 7: 673–689.

Horn, B. K. P. 1987. Closed-form solution of absolute orientation using unit quaternions. *Journal of the Optical Society of America*, Vol. 4, No. 4: 629–642.

Horn, B. K. P. 1988. Closed-form solution of absolute orientation using orthonormal matrices. *Journal of the Optical Society of America*, Vol. 5, No. 7: 1127–1135.

International Terrestrial Reference Frame.

<http://itrf.ensg.ign.fr> (accessed on 10.9.2009).

International GNSS Service.

<http://igscb.jpl.nasa.gov/igscb/center/analysis> (accessed on 10.9.2009).

Jelalian, A. V. 1992. Laser Radar Systems. Boston, Artech House: 292 p.

Joeckel, R., Stober, M. 1989. Elektronische Entfernungs- und Richtungsmessung. Stuttgart, Wittwer: p. 152–176.

Kersten, T., Sternberg, H., Mechelke, K., Acevedo Prado, C. 2004. Terrestrial laserscanning system MENSI GS 100/GS 200 – accuracy tests, experiences and projects at the Hamburg University of Applied Sciences. Panoramic Photogrammetry Workshop 2004, organized by TU Dresden, University of Stuttgart and ISPRS WG V/1. February 19–22.

http://www.commission5.isprs.org/wg1/workshop_pano/papers/PanoWS_Dresden2004_Kersten.pdf (accessed on 5.11.2007).

Kogoj, D. 2005. Measuring distances with electronic distancemeters. Ljubljana, Faculty of Civil and Geodetic Engineering: p. 111–147 (in Slovene).

Kraus, K., Pfeifer, N. 1998. Determination of terrain models in wooded areas with airborne laser scanner data. *ISPRS Journal of Photogrammetry and Remote Sensing*, Vol. 53, Issue 4: 193–203.

Kuang, S. 1996. Geodetic network analysis and optimal design: concepts and applications. Chelsea, Ann Arbor Press, Inc.: p. 83–92.

Laser Scanning Europe GmbH.

<http://www.laserscanning-europe.com> (accessed on 12.1.2011).

Leica Geosystems AG.

<http://www.leica-geosystems.com/en/index.htm> (accessed on 9.1.2011).

- Lichti, D. D. 2007. Error modelling, calibration and analysis of an AM-CW terrestrial laser scanner system. *ISPRS Journal of Photogrammetry and Remote Sensing*, Vol. 61, Issue 5: 307–324.
- Lovas, T., Berényi, A. 2009. Laser scanning in deformation measurement. *GIM International*, Vol. 23, Issue 3: 17–21.
- Luhmann, T., Robson, S., Kyle, S., Harley, I. 2006. *Close Range Photogrammetry. Principles, Methods and Applications*. Dunbeath, Whittles Publishing: p. 87–88.
- Mao, A., Harrison, C. G. A., Dixon, T. H. 1999. Noise in GPS coordinate time series. *Journal of Geophysical Research*, Vol. 104, No. B2: 2797–2816.
doi:10.1029/1998JB900033
- Mervat, L. 1995. Ambiguity Resolution Techniques in Geodetic and Geodynamic Applications of Global Positioning System. Dissertation. University of Bern, Astronomical Institute: 155 p.
- McCarthy, D. D., Petit, G. IERS Conventions (2003), IERS Technical note 32.
<http://www.iers.org/MainDisp.csl?pid=46-25776> (accessed on 23.1.2009).
- Molnár, G., Pfeifer, N., Ressl, C., Dorninger, P., Nothegger, C. 2009. On-the-job Range Calibration of Terrestrial Laser Scanners with Piecewise Linear Functions. *Photogrammetrie, Fernerkundung, Geoinformation*, Issue 1: 9–22.
- Niell, A. E. 1996. Global mapping functions for the atmosphere delay at radio wavelengths. *Journal of Geophysical Research*, Vol. 101, No. B2: 3227–3246.
doi:10.1029/95JB03048
- Nikon.
<http://www.nikonmetrology.com> (accessed on 29.9.2010).
- Onsala Space Observatory.
<http://www.oso.chalmers.se/> loading (accessed on 9.3.2009).
- Park, H.S., Lee, H. M. 2007. A new approach for health monitoring of structures: Terrestrial laser scanning. *Computer Aided Civil and Infrastructure Engineering*, Vol. 22, Issue 1: 19–30.
- Pesci, A., Teza, G. 2008. Terrestrial laser scanner and retro-reflective targets: an experiment for anomalous effects investigation. *International Journal of Remote Sensing*, Vol. 29, Issue 19: 5749–5765.
- Rees, W. G. 2001. *Physical Principles of Remote Sensing*, Second Edition. Cambridge, Cambridge University Press: p. 46–61.

Reshetyuk, Y. 2009. Terrestrial laser scanning: Error sources, self-calibration and direct georeferencing. Saarbrücken, VDM Verlag Dr. Müller Aktiengesellschaft & Co. KG: p. 63, 28–29, 32–64, 41.

Riegl, J., Bernhard, M. 1974. Empfangsleistung in Abhängigkeit von der Zielentfernung bei optischen Kurzstrecken-Radargeräten. *Applied Optics*, Vol. 13, No. 4: 931–936.

Rottensteiner, F. 2003. Automatic generation of high-quality building models from lidar data. *IEEE Computer Graphics and Applications*, Vol. 23, Issue 6: 42–50.

Savšek-Safić, S., Ambrožič, T., Stopar, B., Turk, G. 2006. Determination of point displacements in the geodetic network. *Journal of Surveying Engineering*, Vol. 132, Issue 2: 58–63.

Schenk, T. 1999. Digital photogrammetry, Volume I, Backgrounds, Fundamentals, Automatic Orientation Procedures. Ohio, The Ohio State University, Terrascience: p. 248–249.

Slovenian GNSS Network SIGNAL.

<http://www.gu-signal.si/index.php> (accessed on 12.9.2009).

Soudarissanane, S., Van Ree, J., Bucksch, A., Lindenbergh, R. 2007. Error budget of terrestrial laser scanning: Influence of the incidence angle on the scan quality. In: Proceedings of 3D-NordOst. Berlin, Germany, December 5–8: p. 73–81.

Soudarissanane, S., Lindenbergh, R., Gorte, B. 2008. Reducing the error in terrestrial laser scanning by optimizing the measurement set-up. In: The International Archives of the Photogrammetry, Remote Sensing and Spatial Information Sciences. Beijing, China, July 3–11. Vol. XXXVII, Part B5: p. 615–620.

Tsakiri, M., Lichti, D., Pfeifer, N. 2006. Terrestrial laser scanning for deformation monitoring. 3rd IAG/12 FIG Symposium. Baden, Austria.

<http://www.ipf.tuwien.ac.at/np/Publications/tsakiriLichtiPfeifer FIG.pdf> (accessed on 15.6.2008).

Van Gosliga, R., Lindenbergh, R., Pfeifer, N. 2006. Deformation analysis of a bored tunnel by means of terrestrial laser scanning. In: Proceedings of International Archives of Photogrammetry, Remote Sensing and Spatial Information Sciences. Dresden, Germany, September 25–27. Vol. XXXVI, Part 5 on CD-ROM.

Vezočnik, R., Ambrožič, T., Sterle, O., Bilban, G., Pfeifer, N., Stopar, B. 2009. Use of Terrestrial Laser Scanning Technology for Long Term High Precision Deformation Monitoring. *Sensors*, Vol. 9, No. 12: 9873–9895.

Vosselman, G., Maas, H. G. 2010. Airborne and Terrestrial Laser Scanning. Dunbeath, Whittles Publishing: p. 109–119.

Wagner, W., Ullrich, A., Ducic, V., Melzer, T., Studnicka, N. 2006. Gaussian Decomposition and Calibration of a Novel Small-Footprint Full-Waveform Digitising Airborne Laser Scanner. ISPRS Journal of Photogrammetry and Remote Sensing, Vol. 60, Issue 2: 100–112.

Wagner, W. 2007. Grundzüge der Fernerkundung für Studierende des Bakkalaureatstudiums Geodäsie und Geoinformatik. Vienna, Institute for Photogrammetry and Remote Sensing, Vienna University of Technology: p. 152–158.

Zogg, H. M., Ingensand, H. 2008. Terrestrial laser scanning for deformation monitoring – load tests on the Felsenau viaduct (CH). In: The International Archives of the Photogrammetry, Remote Sensing and Spatial Information Sciences. Beijing, China, July 3–11. Vol. XXXVII, Part B5: p. 555–562.

Univerza
v Ljubljani
Fakulteta
za gradbeništvo in
geodezijo



PODIPLOMSKI ŠTUDIJ
GEODEZIJE

DOKTORSKI ŠTUDIJ

Kandidat:

ROK VEZOČNIK, univ. dipl. inž. geod.

**ANALIZA TEHNOLOGIJE TERESTRIČNEGA
LASERSKEGA SKENIRANJA ZA SPREMLJANJE
DEFORMACIJ NA OBJEKTIH**

Doktorska disertacija štev.: 218

KAZALO VSEBINE

1	UVOD	117
1.1	Motivacija	117
1.2	Raziskovalni cilji	118
1.3	Pregled sorodnih del	119
1.4	Struktura naloge	120
2	METODE	123
2.1	Splošni metodološki pristop	123
2.2	Referenčni sestav	123
2.3	Razvoj geodetske mreže	124
2.4	Skeniranje in ocena položajev tarč	125
2.4.1	Ploske tarče	126
2.5	Umeščanje meritev TLS v izbrani referenčni sestav	129
2.6	Skeniranje objekta	134
2.6.1	Fizikalne omejitve	134
2.6.2	Geometrija skeniranja	136
2.7	Modeliranje oblike objekta	137
2.7.1	Segmentacija na osnovi ravninskega modela	138
2.7.2	Pravilnost modela in ocena modelnih parametrov	139
2.8	Deformacijski modeli	140
2.8.1	Model 1: model z omejeno smerjo	141
2.8.2	Model 2: reprezentativne točke	142
3	REZULTATI TESTOV	145
3.1	Testi kalibracije tarč	145
3.1.1	Mehanske nepopolnosti	146
3.1.2	Modeliranje dolžinskega pogreška	149
3.2	Odzivnost površinskega materiala	164
3.3	Test v naravi 1: Plinovod	170
3.3.1	Testno polje in njegove posebnosti	170
3.3.2	Terenska izmera	172
3.3.3	Rezultati	175
3.3.3.1	Opazovanja GNSS	175
3.3.3.2	Klasična terestrična izmera	177
3.3.3.3	Terestrično lasersko skeniranje	178
3.4	Test v naravi 2: Podporni zid	185
3.4.1	Testno polje in njegove posebnosti	185

3.4.2	Terenska izmera	187
3.4.3	Rezultati	190
3.4.3.1	Klasična terestrična izmera	190
3.4.3.2	Terestrično lasersko skeniranje	192
4	ANALIZA IN DISKUSIJA	199
4.1	Test v naravi 1	199
4.1.1	Stabilnost datuma	199
4.1.2	Določitev reprezentativnih točk	200
4.1.3	Analiza premikov	201
4.2	Test v naravi 2	203
4.3	Ovrednotenje laboratorijskih testov	208
5	ZAKLJUČKI	211
5.1	Smernice nadaljnega raziskovalnega dela	213
6	POVZETEK	215
7	VIRI	219

KAZALO SLIK

Slika 1: Točkovni in ploskovni način spremljanja objekta	118
Slika 2: Tarče TLS	126
Slika 3: Primeri prileganja modela	128
Slika 4: Diagram pozicioniranja meritev TLS	130
Slika 5: Ocenjevanje časa in amplitude	136
Slika 6: Vplivi na gostoto točk	137
Slika 7: Antropogeni objekti, zajeti z metodo TLS	138
Slika 8: Rezultati segmentacije	139
Slika 9: Segmentni način ugotavljanja premikov	142
Slika 10: Testiranje konstrukcijskih napak tarč	146
Slika 11: Rezultati ekscentričnosti	148
Slika 12: Zasnova testa dolžinske napake	149
Slika 13: Območje oblaka točk izbrano za oceno dolžine	150
Slika 14: Standardne deviacije merjenih dolžin	151
Slika 15: Horizontiranje poševnih dolžin	152
Slika 16: Pogrešek dolžine in povprečna vrednost amplitudo kot funkcija razdalje za T1, T2	153
Slika 17: Pogrešek dolžine in povprečna vrednost amplitudo kot funkcija razdalje za T3, T4	154
Slika 18: Pogrešek dolžine kot funkcija amplitudo za T1 in T2	156
Slika 19: Pogrešek dolžine kot funkcija amplitudo za T3 in T4	157
Slika 20: Vektor popravkov za T1	160
Slika 21: Vektor popravkov za T2	161
Slika 22: Vektor popravkov za T3	162
Slika 23: Vektor popravkov za T4	163
Slika 24: Povečane slike testnih vzorcev	164
Slika 25: Razlike hrapavosti površine	166
Slika 26: Držalo za plošče in merska ura	166
Slika 27: Rezultati premikov	168
Slika 28: Večkratni skenogrami pri vpadnem kotu 0°	169
Slika 29: Odstopanja od odčitkov na merski uri pri različnih nivojih redukcije točk	170
Slika 30: Ortofoto posnetek testnega polja	171
Slika 31: Stebri za spremljanje premikov podzemnega cevovoda	172
Slika 32: Geodetska mreža razvita v bližini obravnavanega objekta	173
Slika 33: Položaji skenerja glede na opazovalni steber	174
Slika 34: Lokacije permanentnih postaj GNSS	176
Slika 35: Parametri valja	180
Slika 36: Primer prostorske razporeditve vektorja popravkov	181
Slika 37: Mrežni model vektorja popravkov za 4212	182

Slika 38: Razporeditev stojišč in rezultati ICP	182
Slika 39: Standardne deviacije parametrov valja po vzorčenju	184
Slika 40: Sektorji izbrani za spremljanje posledic gradnje	185
Slika 41: Obravnavani objekti in stabilizirani stebri v sektorju 1	186
Slika 42: Geodetska mreža razvita v bližini obravnavanih objektov	188
Slika 43: Položaji skenerja v obeh terminskih izmerah	189
Slika 44: Nepravilnosti profilov	192
Slika 45: Pregled natančnosti absolutne orientacije	194
Slika 46: Območja preklopov na zidu in na površini ceste	196
Slika 47: Modeliranje zidu s pomočjo ravninskega modela	196
Slika 48: Grafična predstavitev rezultatov premikov referenčnih stebrov	200
Slika 49: Identične točke za določitev premikov	201
Slika 50: Premikov stebrov	202
Slika 51: Histogram premikov površinskih segmentov kot rezultat modela z omejeno smerjo	204
Slika 52: Histogram premikov zidu pridobljen iz modela 2	205
Slika 53: Smeri vektorjev premikov reprezentativnih točk na zidu	206
Slika 54: Velikost premikov površine ceste	206
Slika 55: Vzorec ugrezanja kolesnic v obliki mrežnega modela	207

KAZALO PREGLEDNIC

Preglednica 1: Lastnosti okrogle ploske tarče	127
Preglednica 2: Rezultati občutljivosti tarč na vrtenje	147
Preglednica 3: Ocenjene vrednosti parametrov funkcij pogreška dolžine	159
Preglednica 4: Lastnosti vzorcev	165
Preglednica 5: Test v naravi 1: atmosferski parametri dveh terminskih izmer	173
Preglednica 6: Lastnosti terminskih izmer GNSS	175
Preglednica 7: Ocenjene vrednosti koordinat referenčnih stebrov	177
Preglednica 8: Rezultati izravnave z minimalnim številom datumskih parametrov	178
Preglednica 9: Rezultati izravnave ocenjeni na osnovi štirih razporeditev stojišč	183
Preglednica 10: Test v naravi 2: atmosferski parametri dveh terminskih izmer	188
Preglednica 11: Rezultati izravnave z minimalnim številom datumskih parametrov	191
Preglednica 12: Kakovost postopka absolutne orientacije	195

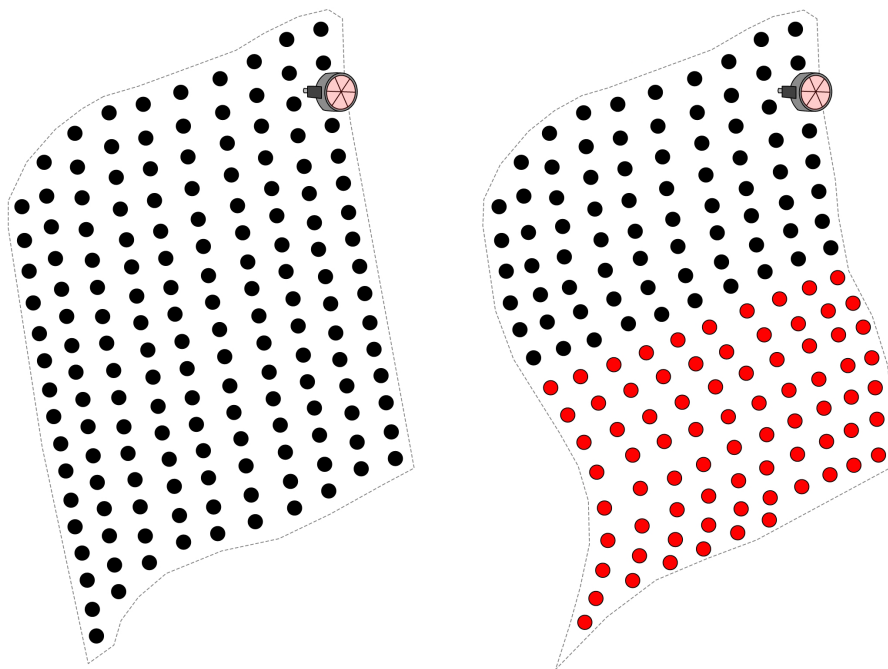
1 UVOD

1.1 Motivacija

Spremljanje premikov in deformacij antropogenih prostorskih struktur in objektov predstavlja eno izmed najbolj zahtevnih področij v geodeziji. Poznavanje tipov, lastnosti in velikosti strukturnih deformacij je poglavito pri opredelitvi njihove narave in posledično pri potrditvi potencialnih možnostih poškodb ali celo uničenja objektov. V klasični geodeziji so bili v ta namen razviti različni pristopi deformacijske analize (npr. Delft, Fredericton, Hannover, Karlsruhe, München, glej Chrzanowski, 2006). Vse te metode so usmerjene v zagotavljanje varnega delovanja in uporabe obravnavanih objektov. Drugi pomemben vidik je tesno povezan s stroškovno učinkovitim procesom gradnje in upravljanjem. Stroški obnove so namreč lahko zelo veliki, zato je vzroke za pojav deformacij s pazljivo zasnovanimi strategijami geodetske spremljave treba pravočasno odkriti in odpraviti.

V zadnjih nekaj letih je terestrično lasersko skeniranje (TLS) postalo pospešeno vključeno v različne naloge inženirske geodezije, vključno s področjem spremljanja premikov in deformacij. Kljub naraščajočemu številu predstavljenih rešitev pa ostaja odkrivanje milimetrskih premikov še vedno zelo aktivno področje raziskovanja. Sposobnost hitrega in gostega zajema ogromne količine objektnih točk je mamljiva prednost metode TLS pred ostalimi senzorskimi tehnologijami in točkovnimi načini spremljanja, kjer je ugotavljanje deformacij omejeno na nekaj diskretnih in dobro signaliziranih točk (slika 1 na strani 118). Za razliko od manjše natančnosti posameznih skeniranih točk, ki bi sicer onemogočala njihovo uporabo v nalogah velike natančnosti, je učinkovito spremljanje deformacij na celotni površini objektov možno na podlagi izkoriščanja velike redundance podatkov. TLS spada med tehnologije daljinskega zaznavanja, kar pomeni, da neposreden dostop do objekta ni potreben, poleg tega pa se zmanjša tudi vpliv namestitve kontrolnih točk oziroma drugih senzorskih kompozicij na opazovano površino.

V procesu dolgoročnega spremljanja premikov in deformacij igra bistveno vlogo tudi kakovost in stabilnost izbranega referenčnega sistema, tj. geodetski datum. Geodetski datum je realiziran na osnovi geodetskih točk, ki morajo biti stabilizirane na geološko stabilnih tleh, če hočemo preprečiti podvrženost deformacijskih parametrov (translacij, rotacij in drugih strukturnih distorzij, določenih na podlagi primerjave 3R ploskovnih modelov iz podatkov TLS) premikom datumskih točk. Zaradi tega postane povezava med TLS in ostalimi geodetskimi merskimi tehnikami neizogibna. Z integracijo metode TLS in ostalih geodetskih tehnik v multisenzorsko mersko zasnova se lahko izognemo pomanjkljivostim posamezne tehnike, hkrati pa njihove prednosti s pridom izrabimo za celovito analiziranje deformacij na celotni površini obravnavanih objektov.



Slika 1: Točkovni in ploskovni način spremeljanja objekta. Količina informacij o spremembah stanja objekta je bistveno manjša v primeru prvega načina spremeljanja. Točke ponazarjajo gost snemalni vzorec TLS, pri čemer so tiste, ki odražajo deformacije, obarvane z rdečo barvo.

1.2 Raziskovalni cilji

Primarni cilj naloge je ovrednotenje hipoteze, ki pravi, da je **z vidika dolgoročnega spremeljanja možno ugotavljati premike in deformacije v območju milimetrov, in sicer po celotni površini objektov in ne samo na manjšem številu signaliziranih (tj. stabiliziranih) točk**, kar je značilno pri uporabi točkovnih geodetskih tehnik. Naloga se bo osredotočila predvsem na analizo podatkov impulznih sistemov TLS, saj je ta merski princip najbolj pogost in primeren zaradi širokega spektra uporabe, vendar po drugi strani manj natančen, kar bo predstavljalo dodatno omejitev v postopku potrjevanja hipoteze. Z vidika obravnavanih objektov so za takšen namen primerni samo tisti, ki imajo dobro opredeljeno in čvrsto površino.

Znotraj opisanega raziskovalnega okvirja bo naloga usmerjena v predstavitev celovitega in učinkovitega metodološkega pristopa prostorsko-časovne analize sprememb, ki bo vključevala komplementarne merske tehnike. Slednje so uporabljene z namenom vzpostavitve in kontrole kakovosti ter stabilnosti referenčnega sestava, ki služi za ovrednotenje premikov in deformacij ploskovnih modelov metode TLS. Če hočemo pristopiti k analizi deformacij v območju milimetrov, potem je najprej treba podrobno preučiti obstoječe pristope in jih nato po potrebi izpopolniti oziroma nadgraditi, da bodo ustrezali zahtevam po veliki natančnosti. Na podlagi obsežnih testiranj, ki so bila izvedena z namenom podrobnega analiziranja predlaganega metodološkega pristopa, bo doktorska naloga ne samo ovrednotila delovno hipotezo, ampak poskusila odgovoriti na naslednja vprašanja:

- kateri so poglaviti deli predlaganega pristopa;
- kje so meje današnjih impulznih sistemov TLS;
- ali je metoda TLS dovolj natančna, da jo lahko postavimo ob bok z geodetskimi merskimi tehnikami, ki omogočajo odkrivanja premikov na nivoju milimetrov.

1.3 Pregled sorodnih del

Zanimanje za morebitno uporabo tehnologije TLS na področju inženirske geodezije velike natančnosti je botrovalo vzpostavitvi posebne delovne skupine znotraj organizacije FIG (6.1.5 Terestrično lasersko skeniranje za spremeljanje deformacij), kar nakazuje pomembnost vključevanja te brezkontaktne metode v geodetsko prakso (Tsakiri in sod., 2006). Delovna skupina 6.1.5 sodeluje z delovno skupino V/3 Terestrično lasersko skeniranje organizacije ISPRS na različnih raziskovalnih področjih kot tudi pri izmenjavi idej, metodologije ter praktičnih izkušenj v raziskovalnih in uporabnih študijah. Vsaka organizacija ima nekoliko drugačen pogled na analizo deformacij meritev TLS, saj prva izhaja neposredno iz geodezije, medtem ko druga izvira iz fotogrametrije in daljinskega zaznavanja. Interdisciplinarno sodelovanje teh dveh področij meroslovja je ključno pri obravnavanju možnosti uporabe tehnologije TLS za spremeljanje strukturnih deformacij. Večina dosedaj opravljenih raziskav se strinja z ugotovitvijo, da je mogoče na osnovi velike redundance opazovanj, ki jo zagotavlja TLS, ugotavljati deformacije precej pod nominalno natančnostjo posameznih točk TLS. Od začetkov uvedbe metode TLS na področje spremeljanja deformacij je bila le-ta uporabljena v različnih nalogah in obremenitvenih testih, ki zajemajo tako laboratorijske raziskave kot tudi teste v naravi. Obravnavani objekti vključujejo jezove, predore, viadukte, stolpe in druge zgradbe. Vsak avtor praktično predstavi svoj lasten pristop k analizi deformacij, kar na nek način otežuje njihovo ovrednotenje z vidika učinkovitosti in celovitosti. To je eden izmed razlogov za definiranje splošnega metodološkega pristopa, ki bo predstavljen v okviru naloge.

Eden izmed začetnih testov v naravi avtorjev Alba in sod. (2006) je podal rezultate spremeljanja deformacij z metodo TLS na betonskem jezu. Avtorji so predstavili dva pristopa k analizi deformacij. Prvi pristop je temeljal na določitvi najkrajše razdalje med zaporednima oblakoma točk (pri čemer je bil eden v obliki ploskovnega modela). Rezultat drugega pristopa pa so bili premiki, določeni s primerjavo dveh mrežnih modelov površine jezu. V okviru te študije so avtorji ugotovili, da je stabilnost referenčnih točk izredno pomembna, če želimo ločiti dejanske premike od napak, ki izvirajo iz postopka umestitve meritev TLS v izbrani koordinatni sestav.

Še en zanimiv pristop spremeljanja deformacij večjih jezov je bil opisan v Gonzales-Aguilera in sod. (2008), kjer so avtorji za predstavitev površine jezu uporabili funkcijo RBF (*Radial Basis Function*). Za kontrolo kakovosti umeščanja meritev TLS v izbrani referenčni sestav pa je bila uporabljena analiza re-WEOP (*re-Weighted Extended Orthogonal Procrustes*).

V Van Gosliga in sod. (2006) so bili predstavljeni rezultati simulacije deformacij na steni predorske cevi in uporabe statističnih postopkov analize meritev (metoda Delft). V tem članku je bila skeni-

rana površina modelirana na osnovi cilindričnega modela, pri čemer so avtorji analizo deformacij izvedli s pomočjo primerjave površinskih segmentov.

V Lovas in sod. (2009) so opisani izsledki nadzorovanega obremenitvenega testa mostu. Rezultati meritev TLS so primerjani z meritvami zelo natančnih induktivnih merilnikov, ki so bili pritrjeni na konstrukcijo mostu. Avtorji so predlagali, da se metoda TLS v obremenitvenih testih lahko uporabi kot dopolnilna merska tehnologija, saj zagotavlja uporabne informacije, vendar ne more v celoti zamenjati klasičnih točkovnih merskih tehnik.

V Zogg in sod. (2008) je predstavljena še ena študija obremenitvenega testa viadukta v Švici, kjer so avtorji uporabili fazni skener. Ta raziskava se zaključi z ugotovitvijo, da se metoda TLS lahko uporabi za odkrivanje deformacij v območju milimetrov, vendar so v takšnih primerih komplementarne merske metode (v njihovem primeru precizni nivelman) nepogrešljive, če želimo oceniti natančnost meritev TLS in potrditi pravilnost končnih rezultatov.

Poleg zgoraj navedenih študij so različni avtorji uporabili metodo TLS za analiziranje deformacij v nadzorovanih okoljih oz. v okviru testov s simuliranimi premiki, npr. Park in sod. (2007) ali Gordon in sod. (2007). Na ta način je precej lažje ločevati dejanske premike od napak meritev, ne nazadnje tudi zato, ker lahko zanemarimo vpliv meteoroloških pogojev na opazovanja. Hkrati kakovost in stabilnost referenčnega sestava ni posebej obravnavana v nobeni od teh študij (predpostavlja se stabilnost referenčnih točk), predvsem zato, ker je za primerno obravnavo problema dатuma treba vključiti komplementarne merske tehnike, kar bo sicer naloga poskušala zajeti v okviru predlaganega metodološkega pristopa.

1.4 Struktura naloge

Doktorska naloga je strukturirana po običajni obliki večine znanstvenih del, in sicer po formatu IMRAD (*Introduction, Methods, Results and Discussion*).

Poglavlje 1: Uvod

Namen uvodnega poglavja je v predstavitev motivacije za raziskovalno delo in definiranju delovne hipoteze, ki bo ovrednotena glede na rezultate testov. Dodano je poglavje o pregledu sorodnih del z namenom opisa stanja na obravnavanem raziskovalnem področju in predstavitevjo del drugih avtorjev, kar bo omogočilo umestitev vsebine naloge v znanstveno raziskovalni okvir.

Poglavlje 2: Metode

Uvodnemu poglavju sledi poglavje 2, kjer bodo predstavljeni metodološki koraki. Slednji predstavljajo osnovno teoretsko podlago za oblikovanje zasnove testnih meritev, ki bodo služile za ovrednotenje delovne hipoteze. Poglavlje 2 se začne z opisom splošnega metodološkega pristopa k analizi deformacij, ki ga lahko obravnavamo kot neke vrste izvleček celotnega poglavja. V nadaljevanju so na podrobnejši način predstavljeni posamezni deli metodološkega pristopa, začenši z referenčnim

sestavom in razvojem geodetske mreže. Nato se naloga posveti tarčam TLS, ki jih potrebujemo za relativno/absolutno orientacijo oblakov točk, ki bo predstavljena v naslednjem podoglavlju. Temu sledi predstavitev skeniranja objekta in postopek modeliranja njegove oblike. Poglavlje se zaključi s predstavitvijo dveh deformacijskih modelov, ki sta bila zasnovana za izvedbo prostorsko-časovne analize sprememb. S konceptualnega vidika pokriva vsebina tega poglavja naslednje teme:

- zasnova referenčnega sestava,
- umeščanje meritev TLS v izbrani referenčni sestav,
- skeniranje in modeliranja površine objekta,
- predstavitev deformacijskih modelov.

Poglavlje 3: Rezultati testov

V tem poglavju so opisane eksperimentalne meritve, ki zajemajo tri laboratorijske teste in dva testa v naravi. Prvi trije testi so bili zasnovani za namene analiziranja ključnih delov metodološkega pristopa, tj. kakovosti tarč TLS, sistematičnih napak in odzivnosti površinskega materiala na vpadno lasersko svetlobo. Zaključke teh treh testov je bilo treba upoštevati v okviru obeh testov v naravi, kjer je bila predlagana metodologija preizkušena v celoti ob različnih in omejenih pogojih na terenu ter na različnih objektih (plinovod in podporni zid). Podoglavlji, ki opisujeta oba testa v naravi, se zaključita z določitvijo vhodnih količin za predlagana deformacijska modela.

Poglavlje 4: Analiza in diskusija

V tem poglavju so predstavljeni in analizirani rezultati uporabe deformacijskih modelov na objektih obeh testov v naravi. Poglavlje se zaključi s kratkim opisom ugotovitev laboratorijskih testov.

Poglavlje 5: Zaključki

V zadnjem poglavju so povzeti zaključki ovrednotenja delovne hipoteze in smernice nadaljnjega raziskovalnega dela.

Poglavlje 7: Viri

Seznam v nalogi uporabljenih virov.

2 METODE

2.1 Splošni metodološki pristop

V splošnem lahko predlagani pristop k analizi deformacij meritev TLS razdelimo na naslednjih sedem korakov:

1. vzpostavitev mreže referenčnih točk;
2. razvoj geodetske mreže v okolini opazovanega objekta;
3. skeniranje tarč in ocena njihovega položaja za povezavo z referenčnim sestavom;
4. vzpostavitev povezave z referenčnim sestavom na osnovi ustreznih ocen transformacije;
5. skeniranje obravnavanih objektov z ustrezno gostoto točk;
6. modeliranje oblike obravnavanih objektov s primernimi ploskvami;
7. primerjava ploskovnih modelov v okviru različnih deformacijskih modelov.

Poleg teh grobih smernic je pomembna tudi kalibracija vseh vključenih instrumentov ter njim pripadajoče merske opreme. Kljub temu avtorja Lichti (2009) in Dorninger (2008) ugotavlja, da bo analiziranje časovne stabilnosti sistematičnih pogreškov skenerjev ostalo aktivno področje raziskovanja tudi v bodoče. Ne nazadnje je tudi izmero na terenu treba izvesti na zelo pazljiv in dosleden način, pri čemer je posebno pozornost treba posvetiti realizaciji enakih snemalnih pogojev v vseh terminskih izmerah ter slediti enakim postopkom obdelave podatkov. Snemalni pogoji seveda ne vključujejo meteoroloških pogojev, ki jih ni mogoče nadzorovati. Opisani merski pristop omogoča celovito in učinkovito kontrolo nad posameznimi segmenti kot tudi nad procesom prenosa pogreškov. V nadaljevanju tega poglavja bodo sledili podrobnejši opisi predstavljenih korakov splošnega metodološkega pristopa.

2.2 Referenčni sestav

Opazovanja GNSS (*Global Navigation Satellite Systems*) predstavljajo eno izmed učinkovitih metod za kontrolo kakovosti in stabilnosti referenčnega sestava, saj je trenutno edina časovno neprekinjena geometrična geodetska tehnika opazovanj, ki zagotavlja določitev absolutnega položaja v dobro opredeljenem geocentričnem referenčnem sistemu. Ta metoda je omejena na odprta območja, kjer ne prihaja do prekinitev satelitskega signala. Za potrebe izmer večje natančnosti mora strategija planiranja in obdelave opazovanj GNSS temeljiti na priporočilih za zelo natančno oceno koordinat, ki jih najdemo npr. v strategiji obdelave IGS (IGS, 2009), navodilih EUREF za analizne centre EPN (EPN, 2009) ali v zelo natančnih geodinamičnih raziskavah (Bergeot in sod., 2009; Caporali in sod., 2009). Namen opazovanj GNSS je tako v realizaciji stabilnega referenčnega sestava za nadaljnja

terestrična opazovanja v vseh terminskih izmerah.

Druga možnost kontroliranja referenčnega sestava je z uporabo precizne klasične terestrične metode. V tem primeru je kakovost in stabilnost referenčnih točk treba preverjati z metodami, omenjenimi v Chrzanowski (2006), poleg tega pa upoštevati tudi priporočila, opisana v poglavju 2.3. V primeru, da v tem koraku uporabimo klasično terestrično metodo, je pomembno, da imamo v vidnem območju na razpolago dovolj zanesljivih orientacijskih točk.

Na splošno je ta del metodološkega pristopa z vidika dolgoročne geodetske spremljave eden izmed najbolj problematičnih in je odvisen predvsem od karakteristik območja. Vzpostavitev stabilnega referenčnega sestava z zadostno natančnostjo je ključnega pomena in mora biti izvedena pred izvedbo skeniranja v analizo vključenih objektov. Če je mogoče, naj bodo referenčne točke izbrane na geološko stabilnih tleh in stabilizirane na primeren način (npr. steber), ki omogoča prisilno centriranje instrumentov in reflektorjev ter preprečuje pogreške centriranja.

2.3 Razvoj geodetske mreže

Referenčni sestav je povezan z meritvami TLS (tj. oblaki točk) na podlagi referenčnih točk, ki tvorijo geodetsko mrežo. Geodetska mreža mora tako vsebovati referenčne točke, položaje tarč ter kontrolne točke. Slednje lahko služijo za primerjavo z rezultati TLS, lahko pa sodelujejo pri določitvi reprezentativnih točk, opisanih v poglavju 2.8.2.

Pri razvoju mreže velike natančnosti v okolini obravnavanega objekta igra pomembno vlogo njena oblika, ki neposredno vpliva na kakovost absolutne orientacije zajetih oblakov točk. Na področju zelo natančne geodetske izmere je ta korak najpogosteje izведен s pomočjo precizne klasične terestrične metode. Če hočemo po metodi najmanjših kvadratov (MNK) oceniti koordinate točk v mreži z veliko natančnostjo, potem meritve navadno izvajamo v večih girusih, pri čemer meritve predstavljajo horizontalni in vertikalni koti ter poševne dožine. Mnogi precizni elektronski tahimetri danes omogočajo avtomatsko prepoznavanje tarč (APT), funkcionalnost, ki lahko bistveno zmanjša pogreške operaterja in pospeši merski proces. Na ta način lahko hkrati dosežemo veliko redundanco meritev, ki omogoča kakovostno in stabilno oceno koordinat točk. V primeru, da meritve izvajamo z uporabo avtomatskega prepoznavanja tarč, je standardne deviacije surovih meritev treba preveriti za prisotnost grobih pogreškov, ki se lahko pojavi zaradi avtomatskega procesa izmere (npr. v primeru, ko se dva reflektorja nahajata skoraj v isti smeri).

Poleg tega je meritve poševnih dolžin treba popraviti za vse sistematične pogreške, ki vplivajo na izmerjene vrednosti. Namen upoštevanja dolžinskih korekcij je v oceni koordinat točk v mreži samo na osnovi meritev, podvrženih slučajnim pogreškom. Pri določitvi korekcij moramo upoštevati atmosferske pogoje. Podrobni opis redukcije poševnih dolžin lahko najdemo v literaturi, npr. v Joeckel (1989) ali Kogoj (2005).

Če želimo oceniti položaje točk v mreži z veliko natančnostjo, je treba v postopku izmere uporabiti precizne reflektore z znanimi adicijskimi konstantami manjšimi od enega milimetra. Ob uporabi

teh reflektorjev lahko za običajne velikosti mrež, razvitih v okolini večine (tudi večjih) objektov, dosegamo natančnost koordinat na nivoju nekaj desetink milimetra. Tako velika natančnost ocene koordinat ne bi bila možna, če bi klasične terestrične meritve izvajali neposredno v povezavi s tarčami TLS. Zato je treba položaje tarč v mreži oceniti posredno, z oceno položajev centrov prizm v prvi fazi in nato z upoštevanjem ekscentritete med obema reflektorjema. Pri pogoju, da so reflektorji horizontirani, se ekscentriteta omeji na zgolj vertikalno komponento, ki jo je prav tako mogoče oceniti z natančnostjo pod nivojem milimetra. Na opisan način bo stopnja natančnosti ocene koordinat klasične terestrične izmere zagotavljala dobro opredeljen in kakovosten okvir za geolociranje oblakov točk na osnovi tarč, stopnjo, ki jo bo težko doseči pri ocenjevanju položajev tarč iz meritev TLS.

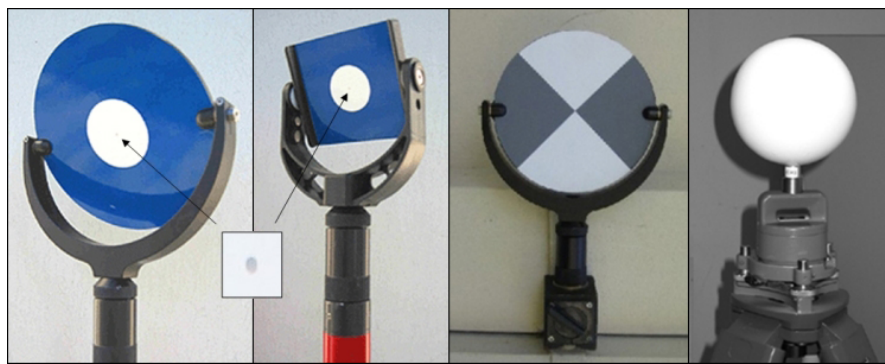
2.4 Skeniranje in ocena položajev tarč

Pri odločanju o primernosti določenega tipa tarč TLS za potrebe izmer velike natančnosti moramo upoštevati naslednje kriterije:

- tarče morajo biti stabilne in toge mehanske izdelave;
- njihova velikost in oblika morata biti usklajeni z maksimalno razdaljo od skenerja, če hočemo zmanjšati sistematične pogreške, ki izvirajo iz naraščajoče laserske pike, in hkrati zagotoviti dovolj gost vzorec točk TLS na njihovi površini;
- tarče morajo biti dobro opredeljene, da omogočajo modeliranje njihove oblike iz meritev TLS.

Glede na te dokaj samoumevne kriterije lahko hitro ugotovimo, da je število primernih in komercialno razpoložljivih tarč precej majhno. Poleg opisanih pogojev je kakovost končnega rezultata procesa ekstrakcije in modeliranja na vsakem stojišču skenerja, tj. ocnjene vrednosti centrov tarč, nadalje odvisna predvsem tudi od sistematičnih pogreškov, ki so rezultat kombiniranega vpliva skenerja ter odziva določene izbrane površine tarče. Rezultati eksperimentov, predstavljeni npr. v članku avtorjev Pesci in Teza (2008), so razkrili prisotnost velikih sistematičnih pogreškov izmere dolžine pri skeniranju retroreflektivnih površin tarč. Na podlagi njunih ugotovitev postane jasno, da lahko v večini primerov tarče uporabimo za precizno umeščanje oblakov točk v izbrani koordinatni sistem šele po predhodnem modeliranju sistematičnih pogreškov, ocenjenih v okviru pazljivo zasnovanih kalibracijskih testov, opisanih v poglavju 3.1. Po drugi strani je možno najti določene izjeme, kjer proizvajalci ponujajo posebne načine skeniranja oz. prilagodijo moč laserskega impulza za določen tip tarč in tako v veliki meri odpravijo nastale dolžinske pogreške. V vsakem primeru pa je sistematične pogreške dolžin TLS, ki izvirajo iz trenutnih pogojev v atmosferi, vedno treba odpraviti, kadar njihov vpliv ni zanemarljiv.

Med primernimi tipi tarč, ki se na široko uporabljajo v nalogah inženirske geodezije s poudarkom na zahtevi po večji natančnosti, so predvsem ploske in krogelne tarče (slika 2). Krogelne tarče imajo na eni strani to prednost, da je natančnost določitve centra neodvisna od vpadnega kota, seveda



Slika 2: Tarče TLS. Prve tri z leve strani so ploske tarče proizvajalca Leica Geosystems (2011). Krogelno tarčo, ki predstavlja alternativni tip, ponuja podjetje Laserscanning Europe (2011).

ob predpostavki, da ni prisotnih sistematičnih anomalij oblike tarče. Po drugi strani pa je navadno samo manjši del njihove površine uporaben za izračun centra, še posebno na razdaljah okoli 100 m od skenerja, ko lahko premer laserske pike naraste do velikosti nekaj centimetrov. V takšnem primeru je treba točkam bližje robovom krogle dodeliti ustrezne uteži glede na vpadni kot ali jih celo izključiti iz obdelave. Poleg tega je natančnost koordinat centra najbolje prilegajoče (izravnane) krogle odvisna od velikosti šuma laserskega impulza, kar lahko povzroči odstopanja tudi do 5 mm, kot so ugotovili Kersten in sod. (2004). Ne nazadnje je izdelava krogelnih tarč z zelo majhnimi anomalijami oblike (če je možno pod nivojem milimetra) zelo draga, hkrati pa je ravnanje z njimi oteženo, če postane njihova velikost prevelika.

Glede na navedene razloge in izpolnitve zgornjih treh kriterijev v največji meri so bile za ekstrakcijo in modeliranje izbrane ploske tarče. Ta tip tarč je bil analiziran tudi v okviru kalibracijskih testov in ne nazadnje uporabljen v dveh eksperimentih v naravi (glej poglavje 3).

2.4.1 Ploske tarče

Za razliko od kroglenih je pri ploskih tarčah v postopek ocene položaja centra vedno treba vključiti tudi radiometrične informacije o sprejetih impulzih, ki jih večina skenerjev beleži poleg polarnih koordinat. Jakost sprejetega signala na sprejemniku, imenovana amplituda (A), nudi ključno informacijo o položaju centra v ravnini tarče. Model za oceno položaja centra tarče je odvisen od njene izvedbe, saj imajo tarče različne razporeditve visoko in nizko odbojnih delov. Na podlagi dveh smeri rotacije je ploske tarče treba usmerjati proti skenerju na vsakem stojišču instrumenta. V doktorski nalogi je bila za modeliranje izbrana tarča, ki je na sliki 2 prikazana skrajno levo. V preglednici 1 pa so podane njene dimenzije in odbojne lastnosti. Kot ugotavlja Reshetyuk (2009), večina postopkov določitve centra ploskih tarč temelji na predpostavki, da se maksimalna amplituda registrira v njenem centru. V primeru tarče, ki je bila uporabljena v doktorski nalogi, je ta predpostavka celo vgrajena v njeni izvedbi, z visoko odbojno srebrno piko v sredini tarče, obkroženo z nizko odbojno belo podlago. Upoštevajoč to predpostavko, je ocena koordinat centra tarče določena

Preglednica 1: Lastnosti okrogle ploske tarče. R_A je koeficient retroreflektivnosti, kot ga opredelita Austin in Schultz (2006). Modri in srebrni material sta retroreflektorja sferičnega tipa.

Tip materiala	Premer [mm]	R_A	Opomba
Moder	152.4	10	Material, ki se uporablja za ozadja prometnih znakov.
Bel	50.8	/	Nima retroreflektivnih lastnosti.
Srebrn	2	75	Material, ki se uporablja za napise na prometnih znakih.

kot amplitudno uteženo povprečje točk TLS, tj. $x_c = \sum_{i=1}^n A_i \cdot x_i / \sum_{i=1}^n A_i$. Tukaj $x_c \in \mathbb{R}^3$ označuje koordinate centra tarče, $x_i \in \mathbb{R}^3$ so koordinate i -te skenirane točke, A_i pa njim pripadajoče amplitudo. Glede na način implementacije se lahko to uteženo povprečje izračuna na osnovi vseh točk na tarči oz. samo podmnogožici tistih z najvišjimi vrednostmi amplitude.

Podrobnejša analiza razkrije, da ima pristop k ocenjevanju centra tarče na osnovi amplitudno utežene povprečja nekatere slabosti, predvsem zaradi majhne velikosti srebrne pike. Ocenjevanje lahko postane precej nestabilno ali celo nemogoče, če oddaljnost tarče začne presegati 40 m, saj postaja 2-milimetrska srebrna pika v njenem centru čedalje bolj nevidna zaradi naraščanja premera laserske pike. V praksi velja, da je majhna oddaljenost tarč obratnosorazmerna s številom točk v geodetski mreži, kar pomeni, da je v fazo pozicioniranja oblakov točk treba vložiti več časa in virov (merske opreme), kadar so v proces geodetske spremljave vključeni večji objekti. Poleg tega je tudi pri oddaljenostih, ki so manjše od 40 m, premer srebrne pike veliko manjši od običajne velikosti laserske pike, kar lahko povzroča sistematična odstopanja koordinat centra, ki so odvisna predvsem od nepravilnosti skeniranega vzorca in načina obdelave sprejetih signalov, ki se hkrati odbijejo od visoko in nizko odbojnih območij, na strani sprejemnika.

Če želimo preseči opisane omejitve in razširiti območje uporabe preko meje "vidnosti" srebrne pike, je posebej za ta namen treba izdelati ustrezniji model za oceno centra tarče, ki je bil v okviru naloge tudi izdelan. Predlagana rešitev ocene centra v ravnini tarče temelji na modeliranju območja prehoda med modrim retroreflektivnim in belim materialom brez retroreflektivnih lastnosti. Za razliko od velikosti srebrne pike je premer tega območja precej večji, zato lahko oddaljenost tarče bistveno povečamo, tudi preko 100 m. V okviru predlagane rešitve je postopek ocene centra razdeljen na dva koraka, in sicer se v prvem oceni ravnina tarče, v drugem pa položaj centra v tej ravnini. Za oceno ravnine tarče v prvem koraku je predhodno treba izvesti dve dodatni fazi:

- ločitev meritev na površini tarče od okolice;
- ocena približnega položaja centra tarče.

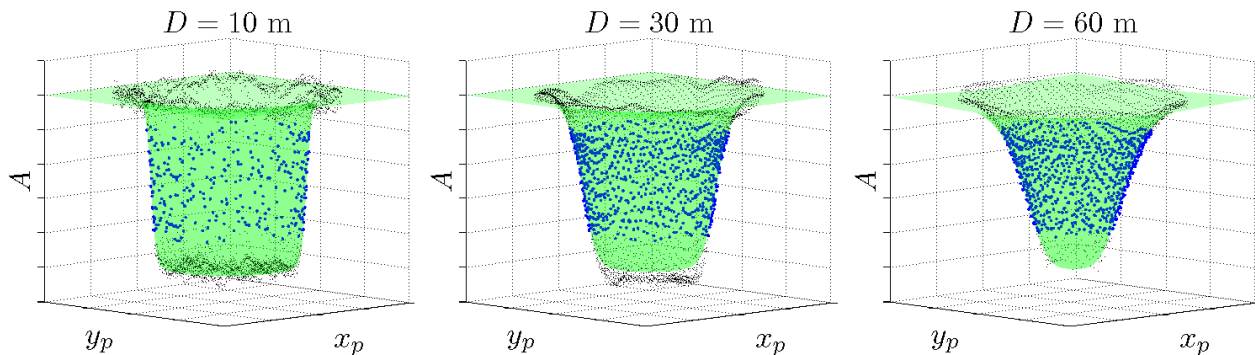
Avtomatsko ločitev meritev na površini tarče od okolice lahko izvedemo na osnovi analize histograma amplitud in znanih retroreflektivnih lastnosti površine tarče (modrega materiala). Po izločitvi okoliških točk je približne vrednosti koordinat centra v dolžinski sliki (sestavljeni iz polarnih koordinat φ_i , θ_i in D_i) mogoče določiti z uporabo preprostega slikovnega ujemanja z navzkrižno korelacijo (Schenk, 1999). Približne koordinate centra so na ta način v večini primerov dovolj

dober približek za izbiro ustreznih podmnožic točk $T_i = (x_i, y_i, z_i)^T$, ki služijo za oceno položaja in orientacije ravnine tarče po metodi najmanjših kvadratov. Pomembno je, da izberemo točke znotraj homogenega območja na površini tarče, če se želimo izogniti robovom in področjem prehoda med različnimi tipi materiala, kjer se lahko naraščajoča laserska pika hkrati odbije od različno odbojnih površin. V okviru metode najmanjših kvadratov je položaj ocenjene ravnine tarče določen s centroidom točk $T_c = \frac{1}{n} (\sum_{i=1}^n x_i, \sum_{i=1}^n y_i, \sum_{i=1}^n z_i)^T$, orientacija ravnine pa z normalnim vektorjem $\vec{n} = (n_x, n_y, n_z)^T$, ki pripada najmanjši lastni vrednosti matrike normalnih enačb $N = \sum_{i=1}^n T_i' \cdot T_i'^T$, kjer $T_i' = T_i - T_c$. Na ta način se minimizirajo pravokotne razdalje točk od izravnalne ravnine z vektorjem popravkov $v_i = \vec{n} \cdot (T_i - T_c)$, ki vsebuje informacije o kakovosti izravnave. Pred prehodom na drugi korak je v ravnini tarče treba vzpostaviti ravninski koordinatni sistem in točke transformirati v ortogonalni pogled ter tako odpraviti odstopanje orientacije ravnine tarče proti skenerju.

V drugem koraku je treba oceniti položaj centra v predhodno določeni ravnini tarče, in sicer ponovno na osnovi MNK, kjer postane vključitev registriranih amplitud impulzov neizogibna, če se hočemo izogniti singularnosti. Pri opredelitvi matematičnega modela za izvedbo tega koraka je zaželeno, da je model določen z majhnim številom parametrov, hkrati pa še vedno dovolj prilagodljiv za naraščanje premera laserske pike. V nalogi predlagani model je sposoben izpolniti omenjene zahteve, njegova oblika pa je določena z:

$$f(x_p, y_p) = A = \frac{1}{1 + \left(a \cdot \sqrt{(x_p - x_0)^2 + (y_p - y_0)^2} \right)^b} \quad (1)$$

kjer sta x_p in y_p koordinati točk v ravnini tarče. Neznanki x_0 in y_0 predstavljata ocenjeni vrednosti koordinat položaja centra v ravnini tarče, a in b pa neznanki, ki določata obliko modelne funkcije. Ta model izkorišča dejstvo, da amplituda narašča od belega proti modremu tipu materiala, kar vodi do *skledaste* oblike funkcije, prikazane na sliki 3. Model, predstavljen z enačbo 1, je na nek način



Slika 3: Primeri prileganja modela. Glajenje območja prehoda med modrim in belim tipom materiala je posledica naraščanja premera laserske pike s povečevanjem dolžine (D). Vrednosti amplitude so normirane med [0,1].

pospološena oblika utežne funkcije, ki sta jo prva predlagala Kraus in Pfeifer (1998), vendar je tukaj uporabljena za povsem drug namen. Neznanke (x_0, y_0, a, b) je treba oceniti na iterativnem način, pri čemer dobimo njihove približne vrednosti s pomočjo slikovnega ujemanja ter znanega polmera belega tipa materiala. Očitno je, da je funkcija simetrična glede na normalo ravnine tarče, zato je, kot že rečeno, točke predhodno treba transformirati v ortogonalno projekcijo, da bi se izognili asimetriji območja prehoda. V zaključni fazi mora biti položaj centra v ravnini tarče ocenjen na osnovi izključno tistih točk, ki ležijo blizu meje med belim in modrim materialom, kjer se vrednosti amplitudo spremenijo. Te točke so najpomembnejše v drugem koraku, zato je postopek ocene centra treba omejiti zgolj na izbrani amplitudni interval. Na sliki 3 so te točke, katerih amplituda pada na izbrani interval od [0.2,0.8], označene z modro barvo.

V primeru, da položaj centra ocenimo na podlagi enačbe 1, je vektor popravkov brez enot, saj se v okviru MNK minimizirajo vertikalne razdalje točk od modelne funkcije. Slednje lahko postane problematično pri ocenjevanju stohastičnih lastnosti modelnih parametrov x_0 in y_0 , ki sta izražena v metričnih enotah. Alternativno možnost predstavlja minimizacija horizontalnih razdalj točk, pri čemer je enačbo 1 treba preureediti:

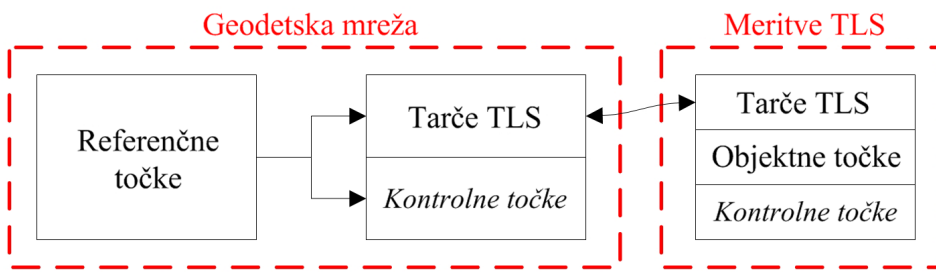
$$\sqrt{(x_p - x_0)^2 + (y_p - y_0)^2} - \sqrt[b]{\frac{\frac{1}{A} - 1}{a}} = 0 \quad (2)$$

Tudi v enačbi 2 se ocenijo iste neznanke kot prej, s to razliko, da je vektor popravkov tokrat v metričnih enotah in ga je zato lažje interpretirati. Izbira minimizacijske funkcije (enačba 1 oz. 2) ima zelo majhen vpliv na ocenjene vrednosti modelnih parametrov, kar je bilo potrjeno v okviru eksperimentov. Dvostopenjska narava predlaganega algoritma ocene centra vodi do pomembnega zaključka. Mere natančnosti (standardne deviacije) koordinat v ravnini tarče x_0 in y_0 so lahko tudi do desetkrat večje od standardne deviacije izravnane ravnine v prvem koraku, predvsem zaradi šuma razdaljemera. Z naraščanjem laserske pike vse več točk zaide v območje prehoda, ob pogoju, da se gostota točk z razdaljo ne spreminja (glej sliko 3). Posledično je z vidika konstrukcije tarče pomembno, da je beli tip materiala čim bolj okrogel in glede na center tarče ne leži ekscentrično. Zadnji pogoj mora biti izpolnjen tudi v primeru določitve centra tarče po začetno predstavljenem pristopu (amplitudno uteženo povprečje). Samo na ta način bo ocena centra nepristranska.

2.5 Umeščanje meritev TLS v izbrani referenčni sestav

Po vzpostavitvi geodetske mreže s precizno klasično terestrično metodo in oceni položajev centrov tarč na posameznem stojišču skenerja lahko ocenimo transformacijske parametre, ki omogočajo umestitev oblakov točk obravnavanih objektov v referenčni sestav. Ob predpostavki, da je zagotovljena velika natančnost centrov tarč (iz skenogramov tarč visoke gostote), je takšno točkovno umeščanje bolj priporočljivo od ostalih metod (npr. umeščanje na osnovi značilk ali iterativno ujemanje najbližjih točk (*Iterative Closest Point*), glej Vosselman in Mass, 2010), saj ponuja možnost

vzpostavitev nedvoumnih in neposrednih povezav med centri tarč, določenimi iz skenogramov in točkami v mreži (slika 4). Če za umeščanje ne bi uporabili tarč, bi bilo vzpostavljanje zvez



Slika 4: Diagram pozicioniranja meritov TLS. Tarče predstavljajo povezavo med oblaki točk in referenčnim sestavom. Kontrolne točke se lahko uporabijo za primerjavo premikov ali kot podpora pri določitvi reprezentativnih točk, opisanih v poglavju 2.8.2.

(točkovnih oziroma s pomočjo značilk) med skenogrami iz različnih časovnih obdobjij pri številnih nalogah spremeljanja deformacij težko izvedljivo z zadostno natančnostjo, predvsem tudi zato, ker se je težko odločiti, kateri objekti (ali njihovi deli) so ostali nespremenjeni in jih lahko privzamemo kot izhodišče za primerjavo. Ker je natančno pozicioniranje oblakov točk znotraj referenčnega sistema eden izmed najpomembnejših korakov, še posebej pri analizi deformacij v območju milimetrov, je uporaba tarč neizogibna.

Naslednja popularna metoda, čeprav slabša od uporabe tarč, je t. i. *direktno georeferenciranje*, ki je do podrobnosti opisano v Reshetuk (2009). Ta metoda temelji na postavitvi skenerja na znano točko, horizontiranju in orientiranju proti vsaj eni točki z znanimi koordinatami v izbranem referenčnem sistemu. Konceptualno se na enak način umeščajo meritve v klasični geodeziji. Kljub temu je direktno georeferenciranje za zelo natančno umeščanje oblakov točk manj primerno, saj v merski proces vnaša dodatne instrumentalne pogreške, kot sta pogrešek centriranja in horizontiranja, ki so lahko precej večji kot pri preciznih tahimetrih, in sicer tudi pri skenerjih z vgrajenimi kompenzatorji, saj le-ti niso dovolj natančni.

Če se sedaj osredotočimo na način umeščanja s pomočjo tarč, lahko dve množici točk, ki bosta tukaj označeni z $X_i, Y_i \in \mathbb{R}^3$ in se nanašata na isto fizično entiteto ter različni koordinatni sistem, povežemo na podlagi ocene prostorske 7-parametrične Helmertove transformacije v okviru MNK, pri čemer se minimizira vsoto kvadratov koordinatnih odstopanj:

$$\sum_{i=1}^n \|v_i\|^2 = \sum_{i=1}^n \|Y_i - sR(X_i) - t\|^2 \quad (3)$$

kjer je R rotacijska matrika, t vektor translacije in s faktor merila. Te neznake lahko ocenimo na osnovi najmanj treh parov točk. Kadar se neznanke ocenjuje na relaciji med sosednjimi stojišči skenerja, se ta postopek imenuje *relativna orientacija*. V primeru, da ima ena izmed množic točk položaje določene v predhodno opredeljenem referenčnem sistemu, pa se isti postopek imenuje *absolutna ali zunanjna orientacija*.

Vektor translacije

Za minimizacijo vsote kvadratov popravkov v enačbi 3 je v prvem koraku priporočljivo reducirati vse točke X_i in Y_i na pripadajoči težišči $X_c = \frac{1}{n} \sum_{i=1}^n X_i$ in $Y_c = \frac{1}{n} \sum_{i=1}^n Y_i$:

$$X'_i = X_i - X_c \quad Y'_i = Y_i - Y_c \quad (4)$$

Sedaj lahko enačbo 3 preuredimo s pomočjo enačbe 4 in dobimo:

$$\sum_{i=1}^n \|Y'_i - sR(X'_i) - t'\|^2$$

ozziroma:

$$\sum_{i=1}^n \|Y'_i - sR(X'_i)\|^2 - 2t' \cdot \sum_{i=1}^n [Y'_i - sR(X'_i)] + n \|t'\|^2 \quad (5)$$

kjer je $t' = t - Y_c + sR(X_c)$. Iz enačbe 5 je razvidno, da je vsota drugega člena nič, saj so točke reducirane na težišča (upoštevamo, da $\sum_{i=1}^n X'_i = 0$ in $\sum_{i=1}^n Y'_i = 0$). Poleg tega lahko vidimo, da prvi člen ni odvisen od t' , zadnji pa ne more biti negativen. Zato je vsota v enačbi 5 minimalna, ko $t' = 0$, kar pomeni, da je ocenjeni vektor translacije predstavljen kot razlika prvega in z merilom pomnoženega ter zarotiranega drugega težišča:

$$t = Y_c - sR(X_c) \quad (6)$$

Kot je ugotovil Horn (1987), je pri ocenjevanju translacije bolje uporabiti vse kot pa samo eno ali nekaj izbranih točk, ob pogoju, da so le-te po natančnosti ozziroma točnosti med sabo primerljive. Preden lahko izračunamo vektor translacije je treba oceniti merilo in matriko rotacije.

Ocenjevanje merila

Po vpeljavi težišč in določitvi vektorja translacije lahko enačbo 5, ki jo moramo minimizirati, preuredimo:

$$\sum_{i=1}^n \|Y'_i - sR(X'_i)\|^2 \quad (7)$$

Eračbo 7 lahko razširimo, upoštevajoč dejstvo, da je rotacija linearna transformacija, ki ohranja razdalje, tj. $\|R(X'_i)\|^2 = \|X'_i\|^2$ in dobimo:

$$\sum_{i=1}^n \|Y'_i\|^2 - 2s \sum_{i=1}^n Y'_i \cdot R(X'_i) + s^2 \sum_{i=1}^n \|X'_i\|^2 \quad (8)$$

ali krajše:

$$s^2 S_X - 2s D + S_Y \quad (9)$$

kjer je $S_X = \sum_{i=1}^n \|X'_i\|^2$, $S_Y = \sum_{i=1}^n \|Y'_i\|^2$ in $D = \sum_{i=1}^n Y'_i \cdot R(X'_i)$. Če s v enačbi 9 dopolnimo do polnega kvadrata, sledi zveza:

$$\left(s\sqrt{S_X} - \frac{D}{\sqrt{S_X}} \right)^2 + \frac{(S_Y S_X - D^2)}{S_X} \quad (10)$$

Očitno je glede na merilo zadnji izraz minimalen, ko je člen v oklepaju nič, to je $s = \frac{D}{S_X}$ ali:

$$s = \frac{\sum_{i=1}^n Y'_i \cdot R(X'_i)}{\sum_{i=1}^n \|X'_i\|^2} \quad (11)$$

V splošnem je ta asimetrična oblika faktorja merila v enačbi 11 odvisna od smeri. Če transformacijo izvedemo v obratni smeri, torej $X_i = \tilde{s}\tilde{R}(Y_i) + \tilde{t}$, potem ni za pričakovati, da bo $\tilde{s} = \frac{1}{s}$, $\tilde{t} = -\frac{1}{s}R^{-1}(t)$ in $\tilde{R} = R^{-1}$. Namesto tega dobimo:

$$\tilde{s} = \frac{\sum_{i=1}^n X'_i \cdot \tilde{R}(Y'_i)}{\sum_{i=1}^n \|Y'_i\|^2} \quad (12)$$

Če se zopet navežemo na Horna (1987), je eden izmed obeh faktorjev merila iz enačb 11 oziroma 12 primernejši, kadar so koordinate enega od sistemov ocenjene s precej večjo natančnostjo kot tiste iz drugega. To ugotovitev je smiselno po potrebi uporabiti v primeru absolutne orientacije z dobro opredeljenimi in zelo natančnimi klasičnimi terestričnimi koordinatnimi ocenami. Po drugi strani pa je ob primerljivi natančnosti koordinat v obeh sistemih bolj smiselno zagotoviti simetričnost merila (npr. pri relativni orientaciji). V tem primeru je enačbo 7 treba nekoliko spremeniti:

$$\sum_{i=1}^n \left\| \frac{1}{\sqrt{s}} Y'_i - \sqrt{s} R(X'_i) \right\|^2 \quad (13)$$

S podobno preureditvijo enačbe 13 kot v primeru enačbe 7 lahko v zadnjem koraku vidimo, da minimizacija glede na merilo s (le da v tem primeru simetrično) vodi do:

$$s = \sqrt{\frac{\sum_{i=1}^n \|Y'_i\|^2}{\sum_{i=1}^n \|X'_i\|^2}} \quad (14)$$

Prednost simetrične oblike merila je v tem, da predhodno ni treba oceniti rotacijske matrike. V vsakem primeru pa je ocena matrike rotacije neodvisna od izbire merila, preostala napaka pa bo minimalna takrat, ko bo D kar se da velik.

Ocena rotacijske matrike z enotskimi kvaternioni

V primerjavi z bolj poznanimi rotacijskimi matrikami ima predstavitev rotacij s Hamiltonovimi enotskimi kvaternioni številne prednosti. Na primer, veliko lažje je zagotoviti izpolnitev pogoja, da mora biti kvaternion enotski, kot pa pogoj, da mora biti rotacijska matrika ortonormalna (Horn,

1987). Poleg tega je sestavljanje kvaternionov enostavno, so numerično bolj stabilni, hkrati pa se z njihovo uporabo izognemo problemu kardanske zapore. Enotski kvaternion, ki predstavlja rotacijo za kot θ okrog osi $\vec{u} = (u_x, u_y, u_z)^T$, kjer $\|\vec{u}\| = 1$ je:

$$\dot{q} = \cos\left(\frac{\theta}{2}\right) + \sin\left(\frac{\theta}{2}\right)(iu_x + ju_y + ku_z) = \cos\left(\frac{\theta}{2}\right) + \sin\left(\frac{\theta}{2}\right)\vec{u} \quad (15)$$

V jeziku kvaternionov lahko točko v prostoru predstavimo kot čisti imaginarni kvaternion $\dot{r} = 0 + \vec{r}$, položaj točke po rotaciji pa z enačbo 15 v obliki:

$$\dot{r}' = \dot{q}\dot{r}\dot{q}^* = \left[\cos\left(\frac{\theta}{2}\right) + \sin\left(\frac{\theta}{2}\right)\vec{u} \right] \vec{r} \left[\cos\left(\frac{\theta}{2}\right) - \sin\left(\frac{\theta}{2}\right)\vec{u} \right] \quad (16)$$

kjer je \dot{q}^* konjugirana vrednost kvaterniona, ki jo dobimo z negiranjem imaginarnega dela \dot{q} . Razširitev enačbe 16 vodi do Rodriguesove rotacijske formule, ki posebno način predstavitev rotacije z uporabo kota in osi.

Če se vrnemo k problemu ocene rotacije, upoštevajoč, da bo končna minimizacija enačbe 7 oz. 13 dosežena, ko bo D kar se da velik, je treba poiskati takšen enotski kvaternion, ki bo maksimiral izraz:

$$\sum_{i=1}^n (\dot{q}\dot{r}_{X'_i}\dot{q}^*) \cdot \dot{r}_{Y'_i} \quad (17)$$

Namesto X'_i in Y'_i je v enačbi 17 uporabljen kvaternionski zapis, tj. $\dot{r}_{X'_i}$ in $\dot{r}_{Y'_i}$. Na osnovi zakonitosti kvaternionske metrike je Horn (1987) dokazal, da rešitev enačbe 17 predstavlja lastni vektor, ki ustreza najbolj pozitivni lastni vrednosti simetrične 4×4 matrike:

$$N = \begin{bmatrix} S_{xx} + S_{yy} + S_{zz} & S_{yz} - S_{zy} & S_{zx} - S_{xz} & S_{xy} - S_{yx} \\ S_{yz} - S_{zy} & S_{xx} - S_{yy} - S_{zz} & S_{xy} + S_{yx} & S_{zx} + S_{xz} \\ S_{zx} - S_{xz} & S_{xy} + S_{yx} & -S_{xx} + S_{yy} - S_{zz} & S_{yz} + S_{zy} \\ S_{xy} - S_{yx} & S_{zx} + S_{xz} & S_{yz} + S_{zy} & -S_{xx} - S_{yy} + S_{zz} \end{bmatrix} \quad (18)$$

kjer so $S_{xx} = \sum_{i=1}^n x'_{X_i}x'_{Y_i}$, $S_{xy} = \sum_{i=1}^n x'_{X_i}y'_{Y_i}$ in ostali elementi vsote produktov koordinatnih komponent v obeh sistemih, ki so bile predhodno reducirane na pripadajoča težišča. Iskani lastni vektor je dejansko enotski kvaternion $\dot{q} = q_0 + q_x + q_y + q_z$, ki predstavlja oceno rotacije. Po določitvi tega kvaterniona je izračun ocenjeni rotaciji ekvivalentne 3×3 rotacijske matrike trivialen:

$$R = \begin{bmatrix} q_0^2 + q_x^2 - q_y^2 - q_z^2 & 2(q_x q_y - q_0 q_z) & 2(q_x q_z + q_0 q_y) \\ 2(q_x q_y + q_0 q_z) & q_0^2 - q_x^2 + q_y^2 - q_z^2 & 2(q_y q_z - q_0 q_x) \\ 2(q_x q_z - q_0 q_y) & 2(q_y q_z + q_0 q_x) & q_0^2 - q_x^2 - q_y^2 + q_z^2 \end{bmatrix} \quad (19)$$

V zgoraj predstavljenem pristopu k oceni transformacije ne potrebujemo približnih vrednosti. Neznanke se določijo v zgolj enem koraku, upoštevajoč vse točke X_i in Y_i . S tem je zagotovljena optimalna ocena toge transformacije med dvema koordinatnima sistemoma ob predpostavki, da točke niso kolinearne. Robustnost te metode je njena pomembna prednost pred tistimi, kjer se rotacija oceni na osnovi ortonormalnih matrik (Horn, 1988). Po potrebi lahko v postopek vključimo tudi uteži, ki kompenzirajo nehomogeno natančnost točk X_i in Y_i (glej Horn, 1988).

Po oceni transformacijskih parametrov je slednje treba aplicirati na oblake točk, ki so rezultat skeniranja obravnavanega objekta. Poleg vektorja popravkov (enačba 3) oz. aposteriori standardne deviacije σ_{AO} (σ_{RO})¹, ki predstavlja merilo kakovosti transformacije, je treba analizirati tudi območja preklopov, če želimo ugotoviti, ali točke, zajete na različnih stojiščih skenerja, sovpadajo do zahtevane stopnje. V splošnem na transformirane položaje točk ne vpliva samo kakovost koordinatne ocene iz klasičnih terestričnih meritev in meritev TLS, ampak tudi geometrija mreže stojišč tarč in skenerja. Poleg tega je hkrati treba zagotoviti, da je razdalja od instrumenta do tarč in obravnavanega objekta primerljiva, saj lahko v nasprotnem primeru že manjša odstopanja med množicama točk X_i in Y_i po izvedbi transformacije povzročijo precej večja odstopanja na strani objekta. Pred izvedbo meritev v naravi lahko vplive določene geometrije mreže na transformirane položaje točk analiziramo z uporabo simulacij, kjer vsaki točki dodelimo slučajno generirani pogrešek. Rezultati takšnih simulacij omogočajo pridobitev informacij o občutljivosti transformiranih položajev točk na prisotnost vseh vplivnih faktorjev.

2.6 Skeniranje objekta

Skeniranje lahko obravnavamo kot geodetsko metodo, ki zaradi povsem avtomatiziranega merskega procesa na nivoju posameznih točk ne omogoča nobene redundancy. To dejstvo v določeni meri omejuje uporabo surovih meritev TLS (polarnih oziroma kartezičnih koordinat) v analizi premikov in deformacij, saj je težko oceniti njihove variančno kovariančne matrike (največkrat imamo namreč na razpolago le standardne deviacije meritev, ki jih podajo proizvajalci). Po drugi strani je redundancy meritev neprimerno večja, če razumemo ploskve kot posredno opazovane količine, kar je z vidika ugotavljanja sprememb veliko primernejše. Kot v vsakem merskem procesu je kakovost teh opazovanih količin podvržena merskim pogreškom, ki so na sistematičen način opisani v Reshetuk (2009). Pri impulznem TLS na opazovane količine vplivajo predvsem pogreški izmere dolžin, ki so rezultat fizikalnih omejitv brezkontaktnega merskega procesa. Za boljše razumevanje njihovih vplivov bodo te omejitve predstavljene v naslednjem podpoglavlju. Poleg tega pa je kakovost opazovanih količin odvisna tudi od geometrije skeniranja, kar bo predmet obravnave drugega podpoglavlja.

2.6.1 Fizikalne omejitve

Fizikalne omejitve brezkontaktne izmere dolžin s pomočjo impulznih laserjev so določene z modificirano radarsko enačbo, ki jo v literaturi najdemo v nekoliko različnih oblikah, večinoma izpeljanih iz dela Jelaliana (1992). Wagner (2007) je svojo različico predstavil z naslednjo enačbo:

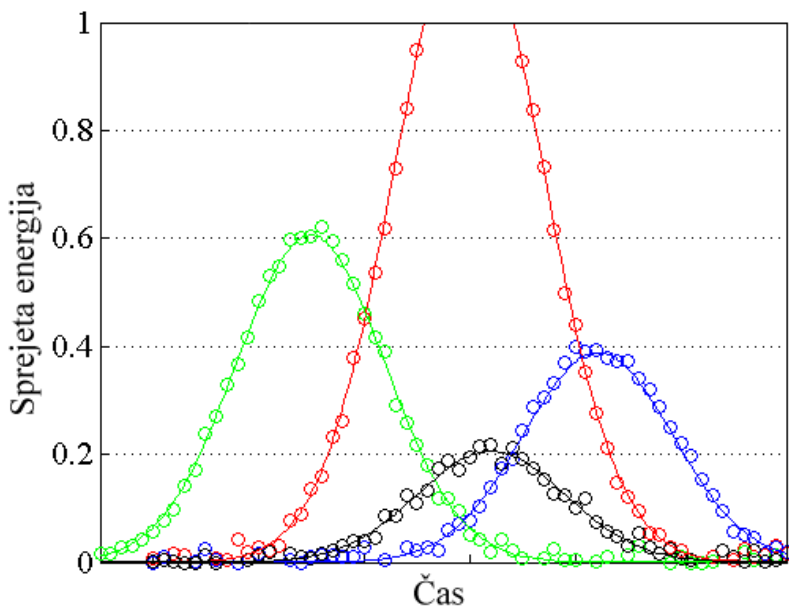
$$P_r = \frac{P_0 \cdot d_a^2}{(2D)^2} \cdot \rho \cdot \cos(\alpha) \cdot \eta_{ATM} \cdot \eta_{SYS} \quad (20)$$

¹AO – absolutna orientacija, RO – relativna orientacija

kjer je P_0 energija oziroma moč oddanega, P_r pa sprejetega laserskega impulza na razdalji D . d_a predstavlja premer zaslonke sprejemnika, ρ je koeficient odbojnosti površine in α vpadni kot². Faktorja atmosferske in sistemski transmitivnosti, η_{ATM} in η_{SYS} , označujeja energijske izgube pri širjenju valovanja skozi atmosfero ter oddajno-sprejemno optiko. Upadanje sprejete energije P_r s kvadratom razdalje lahko pričakujemo samo takrat, ko se celotna površina laserske pike odbije od površine objekta, sicer je treba upoštevati višje potence razdalje D . Poleg tega sta npr. Riegl in Bernhard (1974) demonstrirala, da je povezava energije in razdalje odvisna tudi od konfiguracije oddajnika in sprejemnika. Ne nazadnje se v enačbi 20 predpostavlja, da intenziteta (tj. gostota jakosti energijskega toka) odbite laserske svetlobe pada po Lambertovem zakonu, $I(\alpha) = I_0 \cos(\alpha)$, ki velja v primeru idealnega difuznega odboja (sevalnika), pri čemer je intenziteta neodvisna od odbojne smeri. Klub dejstvu, da je površina večine antropogenih objektov groba z vidika običajnih valovnih dolžin laserjev, vgrajenih v komercialne skenerje (z λ v vidnem oziroma infrardečem spektru svetlobe), je v praksi ta teoretični model odboja najverjetneje treba zamenjati z enim od bolj kompleksnih, npr. Minnaertovim ali Henyey-Greensteinovim modelom, ki jih najdemo v Rees (2001). Če želimo majhne premike in deformacije oceniti dovolj natančno, potem je pri izvedbi skeniranja na prvem mestu treba upoštevati zakonitosti iz enačbe 20. Sprejeta optična energija P_r se obdela (diskretizira v primeru povsem digitalnih sistemov) znotraj sprejemnika, posledično pa se ocenita čas potovanja impulza ter njegova amplituda. Rezultat tega procesa je na preprost, demonstrativen način prikazan na sliki 5, kjer sta čas in amplituda ocenjena v okviru MNK z uporabo Gaussove funkcije. Očitno je, da predstavljajo razdalja do objekta in lastnosti oddajnega ter sprejemnega sistema pomembne faktorje, ki ne samo vplivajo na kakovost ocene opazovanih količin (ploskev), ampak hkrati tudi omejujejo uporabo tehnologije TLS, kadar je odbojnost objekta prenizka ali kadar so izgube energije pri širjenju skozi atmosfero oziroma instrument prevelike. Poleg tega vpadni kot in odbojne lastnosti materialov (glede na barvo, kemično sestavo, hrapavost površine itd.) prav tako določajo količino in smer porazdeljenosti energije na strani objekta, kar povzroča dodatne omejitve pri kakovostnem in zanesljivem ocenjevanju dolžin. Nekatere sistematicne pogreške, kot so atmosferske korekcije, lahko upoštevamo na podoben način kot pri klasičnih terestričnih meritvah in jih je vedno treba vključiti, če njihovi vplivi postanejo dovolj veliki. Kar zadeva pogreške, ki imajo izvor v površinskih lastnostih materialov, lahko njihove vplive na natančnost izmere dolžin in hkrati stopnjo občutljivosti instrumenta testiramo v okviru eksperimentov (glej poglavje 3.2).

Vsi omenjeni, medsebojno tesno povezani parametri povzročijo, da je kakovost ocenjenih ploskev precej bolj podvržena sistematičnim pogreškom izmere dolžin kot obeh kotov. Tudi če impulzi niso oddani v popolnoma enakih kotnih intervalih, so nepravilnosti v nastalem skenogramu odvisne izključno od instrumenta in ne vplivajo na količino zajetega detajla. Tako lahko gost snemalni vzorec z majhnimi kotnimi koraki med zaporednimi laserskimi impulzi, ki so ga današnji sistemi sposobni zagotoviti, uporabimo za natančno predstavitev površin kljub vedno prisotnim kotnim nepravilnostim v snemальнem vzorcu. Poleg razumevanja fizikalnih omejitev brezkontaktne izmere dolžin, podanih z enačbo 20, je z vidika kotov pomembno upoštevati tudi postavitev skenerja glede

²Vpadni kot je kot med smerjo vpada laserskega impulza in normalo na ploskev v točki odboja.



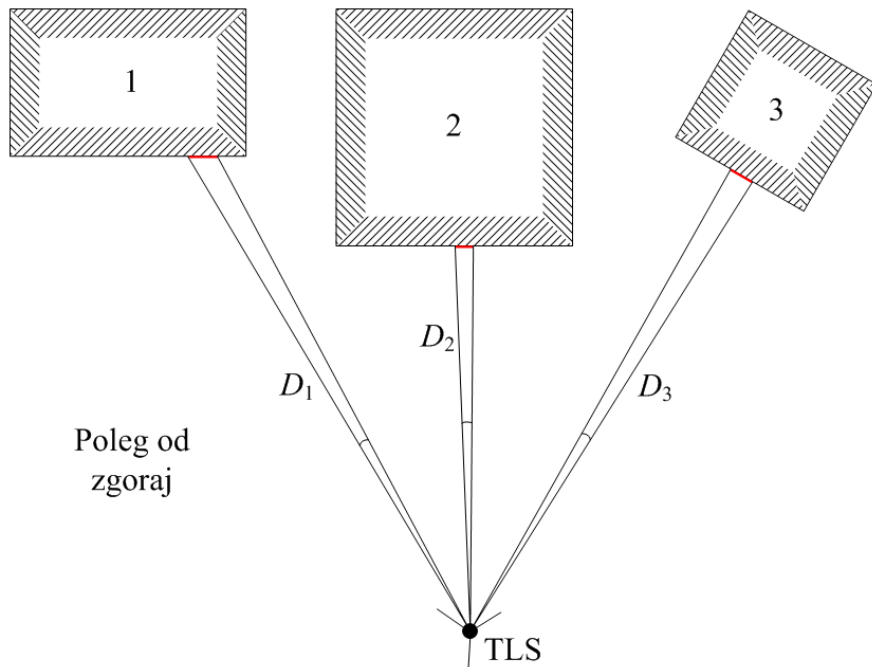
Slika 5: Ocenjevanje časa in amplitude. Pri impulznih sistemih impulz ni nikoli prava Diracova delta funkcija; izkaže se namreč, da je uporaba Gaussovega modela bolj realistična in široko uporabna (Wagner in sod., 2006). Točke predstavljajo diskretizirano obliko impulza na intervalu $[0,1]$, ki ustreza dinamičnemu obsegu sprejemnika.

na objekt, če hočemo zagotoviti zadostno pokritost njegove površine oziroma gostoto točk.

2.6.2 Geometrija skeniranja

Če naj bo gostota točk dovolj velika, je poleg predhodno izbranih parametrov skeniranja (kotne ločljivosti) treba vzpostaviti tudi primerno geometrijo zajema na osnovi analize vpadnih kotov in razdalj (slika 6). Izbira teh parametrov ima neposreden vpliv na kakovost oblakov točk, s ciljem, da se zagotovi razmeroma homogena razporeditev točk na celotni površini objekta. Hitrost upadanja gostote točk je lahko precej velika v primeru skeniranja večjih objektov iz neposredne bližine, npr. pri zajemu cest, predorov ali daljših zidov. Predvsem pri takšnem skeniraju iz neposredne bližine so Soudarissanane in sod. (2008) ugotovili, da lahko kakovost oblaka točk izboljšamo za okoli 25 % zgolj s tem, ko premaknemo skener za dva metra. Tudi analiziranje vplivov orientacije površine objekta na kakovost meritev lahko najdemo v različnih študijah, kot je npr. Soudarissanane in sod. (2007).

Pokritost objekta z meritvami TLS je ne nazadnje odvisna še od izbire stojišč instrumenta (skenerja), saj navadno celotnega objekta zaradi ovir na njegovi površini ali vzdolž posameznih vizur ni možno zajeti s samo ene lokacije. Nastale sence je treba zapolniti s točkami, izmerjenimi na sosednjih stojiščih, ki so bile predhodno umeščene v skupni referenčni koordinatni sistem. V območjih, kjer prihaja do preklopov med skenogrami, je na podlagi višje gostote točk mogoče pridobiti in-

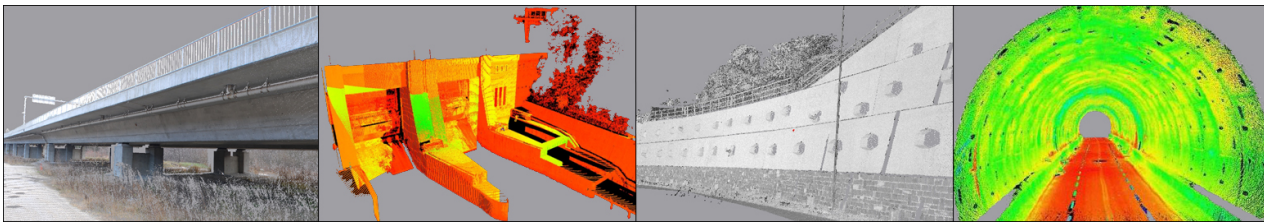


Slika 6: Vplivi na gostoto točk. Čeprav $D_1 \approx D_3$, večji vpadni kot na objektu 1 vodi do širšega razmika med posameznimi točkami.

formacije o kakovosti absolutne (relative) orientacije meritev TLS, procesu, ki je tesno povezan z ustrezno geometrijo položajev tarč v geodetski mreži. Velikost in kompleksnost objekta določata število stojišč skenerja, katerih rezultat je končna slika objekta z majhnimi variacijami dolžin in vpadnih kotov med posameznimi točkami. Nekateri izmed današnjih vrhunskih skenerjev so merški proces sposobni izvesti s kotno ločljivostjo, manjšo od ene ločne sekunde, ter tako zagotoviti milimetrski razmik med točkami na objektu v obeh smereh in po celotnem območju delovanja (Leica, 2011). Tako visoke ločljivostne sposobnosti vodijo do ogromnih lokalnih redundanc podatkov in k očitnemu zmanjšanju terenskega dela na splošno.

2.7 Modeliranje oblike objekta

Metodi TLS lastne in prednostne lastnosti lahko temeljito izkoristimo v fazi rekonstrukcije oblike objekta – postopek, ki ga običajno imenujemo modeliranje. Ploskovne modele lahko obravnavamo kot abstraktne matematične konstrukte, ki posnemajo dejansko geometrijo objekta. Velika razpoložljiva redundanca podatkov omogoča določitev precej večje natančnosti modelnih parametrov v primerjavi z relativno majhno natančnostjo posameznih koordinat točk, ugotovitev, ki je na nek način postala blagovna znamka metode TLS. Za razliko od bolj poljubnih oblik naravnih objektov oziroma struktur, z možnostjo vsebovanja kompleksnih detajlov (značilk), so antropogeni objekti v splošnem precej enostavnnejših oblik z dobro opredeljenimi in čvrstimi površinami. Samo takšni objekti so primerni za analiziranje premikov in deformacij v območju milimetrov in jih lahko uporabimo v vseh nadaljnjih korakih obdelave (slika 7). Obstaja veliko načinov predstavitev ploskev



Slika 7: Antropogeni objekti, zajeti z metodo TLS.

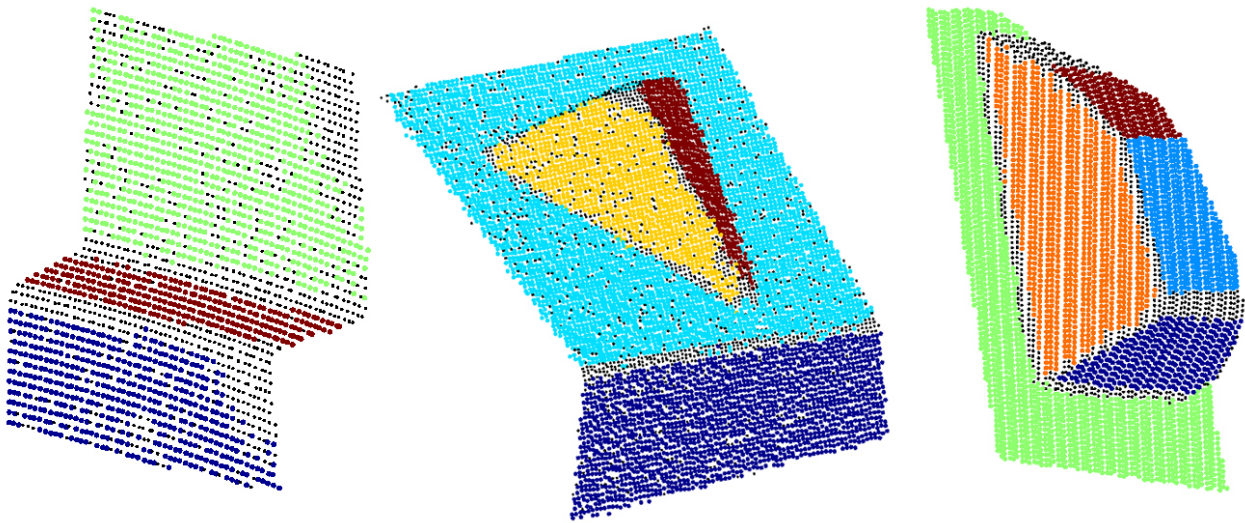
antropogenih objektov, od pravilnih geometričnih gradnikov, kot so ravnine, valji, stožci ali krogle, do bolj kompleksnih, na primer parametričnih zlepkov in pristopa NURBS (*Non Uniform Rational Basis Spline*), ki so bolj primerni za modeliranje kompleksnejših objektov z več površinskega detajla. Izbira ustreznega matematičnega opisa je v precejšnji meri odvisna od samega objekta, pri čemer mora njegov model do zahtevane stopnje Sovpadati z dejansko obliko. V veliko primerih lahko antropogene objekte modeliramo na osnovi pravilnih geometričnih gradnikov ob upoštevanju kriterijev skladnosti med dejansko in modelirano obliko površine. Pred odločitvijo o izbiri modela je potrebno tiste točke, ki ne pripadajo obravnavanemu objektu, izločiti iz obdelave. Enak postopek je treba uporabiti tudi za odstranitev t. i. mešanih pikslov (Reshetnyuk, 2009). Te točke so rezultat napak sistematične narave, ko se laserska pika v bližini robov razcepi in odbije od večih objektov, ki so medsebojno oddaljeni za manj kot polovico prostorske dolžine impulza. Za 5 ns trajajoč impulz mora biti ta oddaljenost večja od 0.75 m, če želimo, da bo položaj točke pravilno določen.

2.7.1 Segmentacija na osnovi ravninskega modela

Za zagotovitev večje kontrole nad kakovostjo modeliranja in vključitve vseh značilnih detajlov na objektu se nemalokrat izkaže, da je izvorni oblak točk večjih objektov, ki jih ne moremo predstaviti izključno z enim samim modelom, priporočljivo razdeliti na manjše segmente glede na koordinatne osi. Velikost segmenta je odvisna od gostote točk in vrste uporabljenega modela. Manjša kot je velikost segmenta (površinske zaplate), večja je verjetnost za aproksimacijo oblike s pomočjo preprostih gradnikov, kot so ravnine (ali celo tangentne ravnine). Uporaba linearnega modela ima svoje prednosti, saj je enostavna, hkrati pa je ob njegovem neustrezanju v začetno izbrani velikosti segmenta slednjega vedno mogoče razdeliti na še manjše enote. Velika redundanca točk, ki je običajno na razpolago, omogoča redukcijo velikosti segmenta do nekaj centimetrov, če se za to izkaže potreba.

Drug priročen način za iskanje ravninskih območij v oblaku točk je z uporabo postopkov segmentacije, ki so v podrobnosti opisani v Hoover in sod. (1996) in testirani predvsem na podatkih zračnega laserskega skeniranja za avtomatsko odkrivanje in modeliranje različnih struktur (za primer glej Rottensteiner, 2003). Vsi postopki segmentacije so usmerjeni v razdelitev nestrukturiranih oblakov točk v ločene regije, in sicer na podlagi različnih geometričnih kriterijev. Ob predpostavki, da ravninska območja obstajajo, se postopek začne z oceno normalnega vektorja (re-

ferenčne smeri) v okolini poljubno izbrane točke, ki prevzame vlogo izvorne točke segmentacije. Vsaka naslednje izbrana točka pripada izvorni ravnini samo pod pogojem, da leži dovolj blizu in da njena normala sovpada z normalo izvorne točke do predhodno določenega kotnega praga. Vsakokrat, ko na novo izbrana točka pade v izvorno ravnino, se referenčna smer ponovno izračuna na osnovi vseh trenutno pripadajočih točk ravnine. Če se hočemo izogniti podsegmentaciji, potem morajo na ta način določene regije vsebovati hkrati tudi zadostno število točk. Rezultati opisanega postopka segmentacije so prikazani na sliki 8. V primerjavi z načinom, kjer oblak točk enostavno



Slika 8: Rezultati segmentacije. Črne točke predstavljajo grobe napake, robeve ter mešane piksele in zato ne pripadajo nobenemu od ravninskih območij.

razdelimo na enake segmente, omogoča postopek segmentacije z razraščanjem ploskev s slike 8 možnost kontroliranja planarnosti točk tekom klasifikacijskega procesa s pomočjo ustreznih vhodnih parametrov. Ti parametri so odvisni od instrumentalnih pogreškov (natančnosti in točnosti izmere dolžin), gostote točk in meje, ki določa, kaj se dopušča kot dovolj ravno. Postopek segmentacije z razraščanjem ploskev je prav tako sposoben odkriti in odstraniti prisotnost mešanih pikslov ali kakršnih koli drugih točk, ki so grobo pogrešene in ne pripadajo nobeni ravninski regiji.

2.7.2 Pravilnost modela in ocena modelnih parametrov

Pred začetkom analiziranja premikov in deformacij je pravilnost ploskovnih modelov treba preveriti za prisotnost kakršnih koli sistematičnih pogreškov rekonstruirane površine. Rezultati izravnave v postopku modeliranja, tj. vektor popravkov, vsebujejo odstopanja med dejansko in idealizirano obliko objekta. Podrobna raziskava prostorske razporeditve vektorja popravkov je nujna, če hočemo oceniti (ne)pristranskost modeliranja. V nekaterih primerih lahko prostorski vzorec vektorja popravkov analiziramo v okviru modelnih koordinatnih sistemov (kot sta cilindrični ali ravninski), pri čemer lahko poleg vizualnega pregleda uporabimo tudi metode numerične statistike, npr.

avtokorelacijsko (Chatfield, 1995). Eden izmed pomembnih vidikov v analizah prostorskega vzorca vektorja popravkov pri časovno zaporednih skenogramih je v ugotavljanju morebitno nastalih deformacij površine objekta. V nasprotnem primeru mora vzorec popravkov ostati nespremenjen. V postopku izravnave je za pravilno ocenjevanje variančno kovariančnih matrik Σ_{xx} modelnih parametrov izbira primernega stohastičnega modela prav tako pomembna. Nepravilne stohastične lastnosti opazovanj imajo navadno majhen vpliv na ocenjene vrednosti modelnih parametrov, vendar lahko bistveno vplivajo na njihove mere natančnosti. V izračunu Σ_{xx} apriori (referenčno) varianco σ_0^2 običajno nadomestimo z aposteriori oceno $\hat{\sigma}_0^2$, saj prva od teh največkrat ni dobro poznana, medtem ko je druga ocnjena na osnovi velike redundance meritev TLS. V postopku modeliranja je po potrebi posameznim točkam mogoče predpisati tudi uteži, in sicer glede na dolžino ($p_{D_i} = 1/D_i^2$) in vpadni kot ($p_{\alpha_i} = \cos(\alpha_i)$), s predpostavko Lambertovega modela odboja. V primeru razdelitve oblaka točk na manjše segmente in uporabi lokalnih modelnih deskriptorjev, kot je bilo opisano v poglavju 2.7.1, je vsem točkam znotraj posameznega segmenta zaradi majhnih sprememb dolžine in vpadnega kota mogoče dodeliti enake uteži.

Še en zanimiv pojav, tesno povezan z realističnim določevanjem mer natančnosti ocenjenih vrednosti modelnih parametrov, je moč opaziti, ko je v postopek izravnave vključena velika redundanca podatkov, ki lahko vodi do preveč optimističnih vrednosti mer natančnosti. Kot so ugotovili že Van Gosliga in sod. (2006), je zaradi velike redundance meritev TLS natančnost modelnih parametrov precej večja od relativno majhne natančnosti koordinat posameznih točk. Ker je slednje dobro znana karakteristika metode TLS, je kljub temu treba preveriti, kako realistične so izračunane mere natančnosti, če hočemo na njihovi osnovi določene deformacije pravilno ovrednotiti. Za pridobitev bolj realističnih mer natančnosti lahko postopek izravnave ponavljamo v večih zaporednih korakih, pri čemer v vsakem uporabimo večje število naključno izbranih enako velikih vzorcev, iz koraka v korak pa povečujemo velikost vzorca. Ko so v obravnavo vključene samo slučajno pogrešene točke, potem lahko na osnovi takšnega empiričnega pristopa ne samo ugotovimo, pri katerih vrednostih se mere natančnosti ustalijo, ampak tudi pri kakšnem številu točk v vzorcu postane korelacija tako močna, da se posamezne ocenjene vrednosti modelnih parametrov ne spreminjajo več.

2.8 Deformacijski modeli

Pri točkovnem načinu geodetske izmere je izbiro položajev reprezentativnih točk treba izvesti pred izvedbo meritev, če hočemo kontrolirati integriteto obravnavanega objekta. Z vidika metode TLS pa je odločitev o načinu obravnave premikov in deformacij objekta možna šele po transformaciji skeniranih točk v ustrezno ploskovno obliko. V splošnem je pri analiziranju časovno različnih modelov TLS količina geometričnega opisa sprememb stanja objekta v veliki meri pogojena s količino detajla na opazovani površini. Iz tega razloga ni vedno mogoče pristopiti k obravnavi premikov in deformacij na enak način kot pri točkovnem načinu geodetskega spremmljanja, kjer signalizirane točke inherentno omogočajo določevanje premikov v vseh treh koordinatnih smereh. V namišljenem ek-

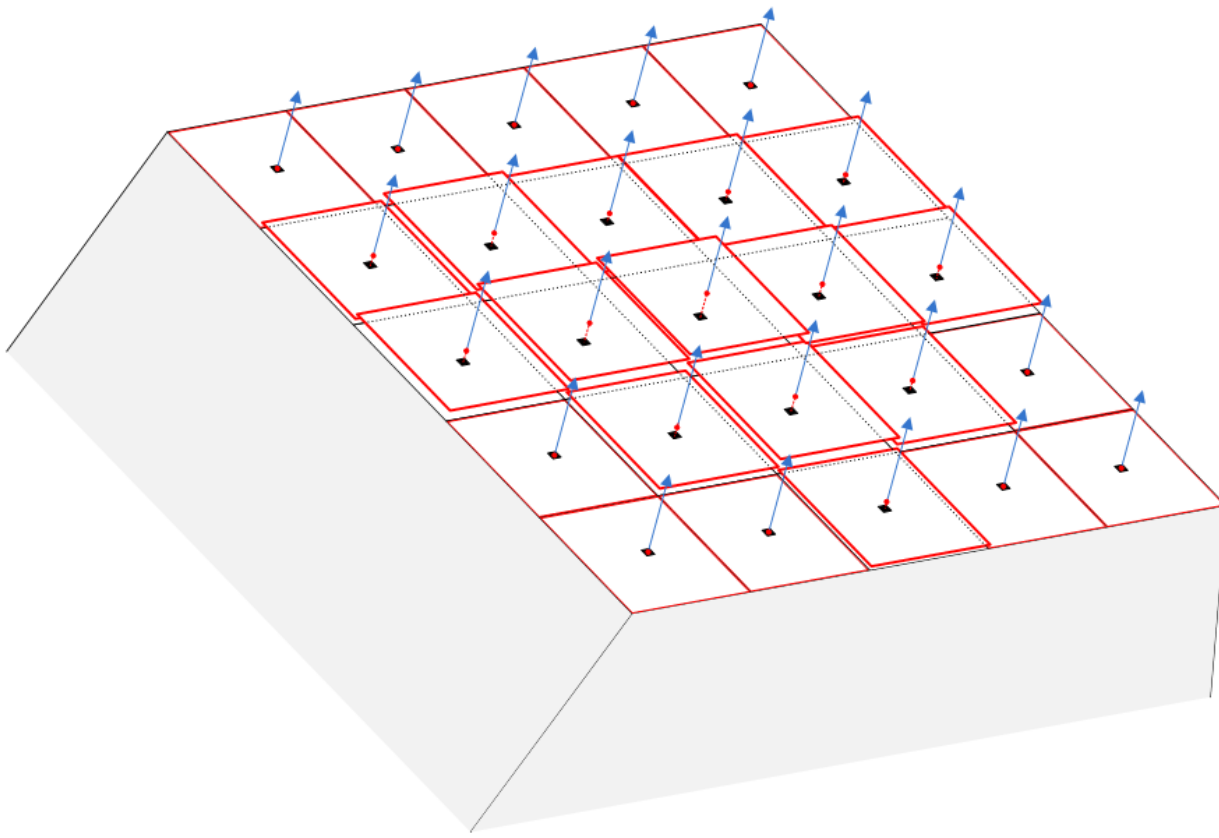
stremnem primeru, če bi skenirali povsem raven zid, instrument ne bi zaznal nikakršnih sprememb, ki bi se zgodile izključno znotraj ravnine zidu. Čeprav so takšni primeri redkost, je v teh situacijah edina možna rešitev v stabilizaciji kontrolnih točk neposredno na objekt. Večja verjetnost je, da je ob pomanjkanju detajla na objektu kljub temu možno pridobiti vsaj nekaj informacij o velikosti in smeri premikov posameznih ploskovnih segmentov. Če pa detajli na objektu obstajajo, lahko ploskovne modele v končnem reduciramo na nivo posameznih značilnih (reprezentativnih) točk ter tako spremljamo njihov položaj skozi čas. Zadnji dve situaciji sta v okviru t. i. deformacijskih modelov podrobnejše predstavljeni v zadnjem delu tega poglavja.

2.8.1 Model 1: model z omejeno smerjo

Omejena smer v imenu tega modela se nanaša na njegovo nezmožnost ugotavljanja premikov posameznih ploskovnih segmentov v vseh treh koordinatnih smereh, neodvisno od tipa oziroma izbire sistema (kartezičnega ali modelnega, kot je na primer cilindrični, ki se na široko uporablja pri modeliranju površine tunelov iz podatkov TLS). Ta slabost je neposredna posledica pomanjkanja kakršnih koli značilnih površinskih detajlov, ki preprečujejo reduciranje ploskovnih modelov do posameznih identičnih točk v vseh terminskih izmerah. Posledično je sledenje modelnih segmentov možno izključno vzdolž predhodno določenih smeri normalnih vektorjev (smeri sledenja), kot je prikazano na sliki 9. Na sliki 9 je velikost premikov posameznih ploskovnih segmentov predstavljena kot razdalja med točkami začetnih položajev segmentov (črne točke) in točkami v presečiščih premic, določenih z začetnimi normalnimi vektorji, in segmentov iz katere koli kasnejše izmere. Takšen pristop hkrati omogoča analiziranje neskladij med začetnimi in vsemi kasnejšimi normalami, kar nakazuje, kako deformacije napredujejo.

Pogoj za uporabo tega deformacijskega modela je, da so bili oblaki točk v prvem koraku razdeljeni in modelirani po posameznih segmentih, kot je bilo opisano v poglavju 2.7.1, saj v modelu potrebujemo vektorje normal. Več kot je na strani objekta na razpolago segmentov različnih orientacij, večje je tudi število smeri sledenja premikov. Skupni opis stanja objekta (položaja in integritete) ter njegovih sprememb je treba sestaviti na osnovi analize vektorskih polj, ki vsebujejo vse razpoložljive smeri sledenja, saj se lahko vplivi sil, ki delujejo na objekt, prenesejo na različno število smeri sledenja z različno magnitudo, odvisno od njihove narave. V določenih primerih lahko smer delovanja sil v veliki merisovpa s smermi sledenja, npr. pri spremeljanju vplivov vodnih zajetij na jezove hidroelektrarn ali pri testiranjih mostov, izpostavljenim sili gravitacije oziroma težkim obremenitvam. Kadar torej smeri sovpadajo, je ta model kljub svojim pomanjkljivostim lahko uspešen pri podajanju odgovorov o odzivih površine na prisotnost sil z izvorom v ali izven objekta.

Druga prednost modela, ki jo je vredno omeniti, pa je v velikem številu segmentov v primerjavi s številom reprezentativnih točk, ki jih je običajno mogoče določiti iz ploskovnih modelov antropogenih objektov in struktur. Zato je model z omejeno smerjo upravičeno obravnavati kot ploskovni deformacijski model, ki omogoča skoraj neprekinjeno analiziranje premikov in deformacij na opa-



Slika 9: Segmentni način ugotavljanja premikov. Smeri premikov določajo začetni normalni vektorji v posameznih segmentih.

zovanih površinah. Iz omenjenega razloga je, tudi ob prisotnosti reprezentativnih točk, prostorsko-časovno obravnavo sprememb ploskovnih modelov priporočljivo izvesti z uporabo tega modela, da potrdimo skladnost rezultatov obeh deformacijskih modelov.

2.8.2 Model 2: reprezentativne točke

Za razliko od modela z omejeno smerjo vodi redukcija ploskovnih modelov do posameznih značilnih točk k točkovni obliki analize premikov, ki omogoča pridobitev popolnih (3-razsežnih) geometričnih informacij o stanju objekta in njegovih sprememb brez potrebe po stabilizaciji kakršnih koli kontrolnih točk ali drugih senzorskih kompozicij na opazovano površino. Določitev *identičnih* reprezentativnih točk v vseh terminskih izmerah je izrednega pomena, če želimo premike obravnavati na pravilen način (tj. z navezavo na isto točko v vseh terminskih izmerah). Tudi pri tem modelu je način določevanja reprezentativnih točk odvisen od problema, čeprav lahko kljub temu podamo neke smernice o tem, kje in na kakšen način jih lahko pridobimo.

Pri izbiri lokacije točk je v primeru, ko se je oblika objekta deformirala, reprezentativne točke treba določiti neposredno na površini, pri čemer mora biti njihov položaj enolično določen. Pri takšnih

deformabilnih primerih je ob majhnem številu reprezentativnih točk rezultate tega modela zaželeno podkrepliti z rezultati modela 1. V nasprotnem primeru, če je oblika objekta ostala nespremenjena in se je spremenil samo njegov položaj, lahko objekt predstavimo na podlagi nekih značilnih točk na njegovi površini, pri tem pa upoštevati, da mora biti število točk odvisno od velikosti objekta. V posebnih primerih, ko spremljamo objekte z dobro opredeljeno geometrijo, katerih oblika se ne deformira, lahko reprezentativne točke izberemo tudi tako, da le-te nujno ne ležijo na površini objekta (npr. objektna os). Takšen primer bo opisan v poglavju 3.3.

V postopku določitve reprezentativnih točk je slednje mogoče pridobiti s presekanjem različnih vrst ploskovnih gradnikov, kot so ravnine oziroma premice, ki so bile predhodno modelirane in so njihovi parametri ocenjeni na osnovi nadštevilnih opazovanj. To lahko demonstriramo s pomočjo slike 8 na strani 139, kjer je reprezentativne točke možno določiti v presečiščih treh sosednjih ravnin. Če identične točke določamo na premicah (ali oseh), te določitve ne moremo izvesti neposredno, saj je položaj smernega vektorja na premici v različnih terminskih izmerah lahko malce drugačen, odvisno od razporeditve točk TLS. Edini način za izhod iz problema je v presekanju premice z drugim ploskovnim gradnikom (ravnino, premico itd.) ali s projekcijo točke z znanim položajem na premico. V primeru testa v naravi 1 je bilo to projekcijo možno izvesti samo z uporabo ene izmed kontrolnih točk v geodetski mreži, saj obravnavana površina objekta ni omogočala določitve enoličnih točk. Če ploskovni modeli vsebujejo strukturne (prelomne) črte, lahko tudi te vključimo v proces določitve reprezentativnih točk, upoštevajoč enake korake, kot so bili opisani zgoraj. V primeru prisotnosti določenih površinskih značilk, kot so krogle ali polkrogle, lahko ploskovne modele neposredno reduciramo do posameznih točk brez pomoči nekih dodatnih modelnih gradnikov.

Po določitvi reprezentativnih točk je eden izmed običajnih in enostavnih načinov za ugotavljanje premikov pravilo palca (Savšek-Safić, 2006). Pri tem načinu velja, da se je točka premaknila, če je velikost vektorja premika večja od položajne standardne deviacije krajinih točk, pomnožene s faktorjem 3 oz. 5. S faktorjem 3 pomnožene standardne deviacije se navadno privzamejo za mejo, do koder segajo slučajni pogreški ocene položaja. Kakršna koli večja odstopanja od ocenjenih vrednosti položaja običajno obravnavamo kot grobe pogreške oziroma dejanske premike točk. Ne glede na izbor deformacijskega modela za analizo premikov in deformacij je zanesljivost končnih rezultatov analize odvisna predvsem od vzporedno izvedenega in pazljivo zasnovanega prenosa pravih pogreškov.

3 REZULTATI TESTOV

Glede na opisano metodologijo in predlagani splošni pristop k analizi premikov in deformacij iz poglavja 2 sta bila v naravi izvedena dva eksperimenta, ki bosta opisana v okviru tega poglavja (glej poglavji 3.3 in 3.4). Lastnosti obeh testov v naravi so bile v marsikaterem pogledu precej različne, in sicer glede:

- posebnosti terena in stabilnosti tal,
- velikosti obravnavanih objektov,
- dostopnosti do objekta,
- omejitev pri razvoju geodetske mreže,
- kompleksnosti procesa analize premikov in deformacij.

Če na podlagi teh dejavnikov primerjamo v naravi izvedena testa 1 in 2, lahko ugotovimo, da je test 2 zagotovo veliko bolj zahteven, predvsem kar se tiče sprejema oziroma zavrnitve delovne hipoteze z dovolj veliko zanesljivostjo. Med izvedbo testov v naravi sta bila uporabljeni dva različna skenerja, in sicer Leicin skener pri testu 1 in Rielgov skener pri testu 2, oba predstavnika podobnega kakovostnega razreda. Zaradi uporabe prvega skenerja v kombinaciji s tarčami, ki prihajajo od istega proizvajalca, je to dejstvo v veliki meri vplivalo na učinkovito redukcijo sistematičnih pogreškov izmere dolžin, saj je bilo površino tarče mogoče skenirati s posebej za ta namen prilagojenim načinom izmere. Z uporabo tega načina skeniranja se centri tarč ocenijo na podlagi amplitudno uteženega povprečja točk, pristopa, ki je vgrajen v skenerjevo programsko opremo za obdelavo meritev. Po drugi strani je bilo treba obnašanje dolžinskih pogreškov testirati in modelirati pred izvedbo testa 2, da bi lahko ugotovili, na kakšen način se bo drugi skener odzval na ta isti tip tarč (glej poglavje 3.1.2). Posledično predstavlja združljivost skenerja in tarč še en dodaten dejavnik poleg zgoraj navedenih, ki ga je bilo treba analizirati izključno za potrebe testa 2. Ne nazadnje so bili pri testu 2 v obravnavo vključeni objekti iz različnih materialov in različne površinske hrapavosti, kar je zahtevalo tudi testiranje stopnje občutljivosti skenerja, da bi lahko določili njegove zmožnosti pri zaznavi majhnih premikov in deformacij (glej poglavje 3.2).

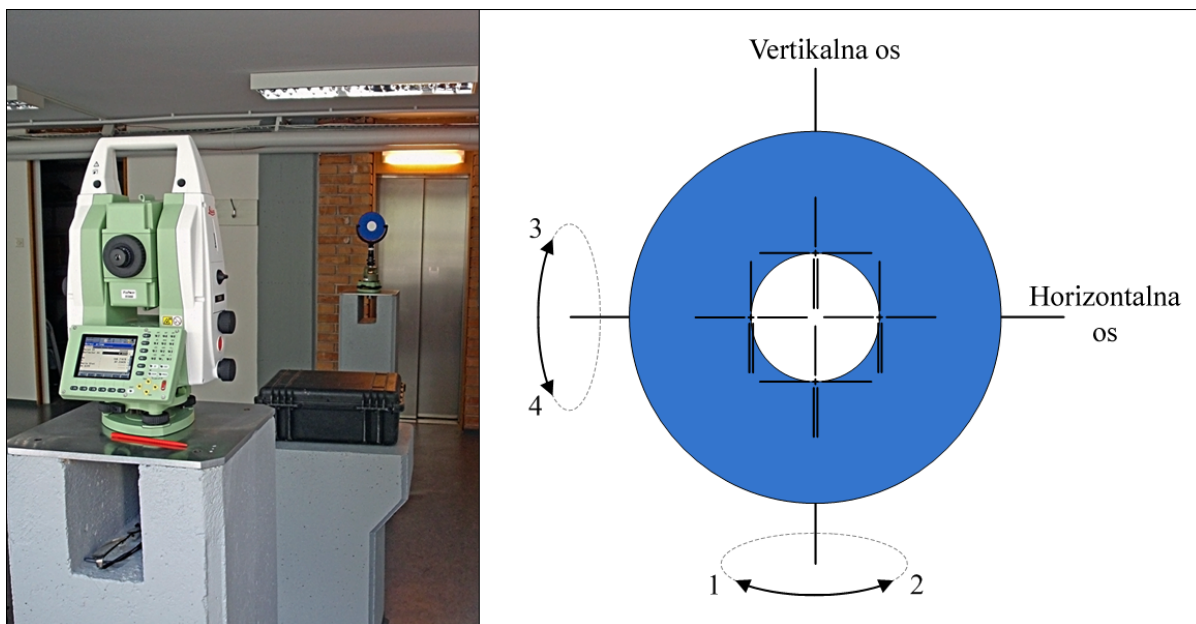
3.1 Testi kalibracije tarč

Shemo kalibracije tarč sestavljata dva ločena testa: test za določitev mehanskih nepopolnosti tarč in test za oceno morebitnih dolžinskih napak. Pod drobnogled so bile vzete skupno štiri tarče istega tipa (skrajno leva tarča na sliki 2), ki so bile kasneje uporabljene v testih v naravi. Lastnosti teh tarč so povzete v preglednici 1. Rezultati kalibracije bi morali doprinesti k določitvi optimalnega okvirja njihove uporabe, znotraj katerega bodo sistematični pogreški minimalni, s tem pa ocena transformacije čim bolj nepristranska.

3.1.1 Mehanske nepopolnosti

Namen tega enostavnega testa je dvojen. Najprej je pomembno ugotoviti, kako vrtenje vpliva na položaj centra tarče, še posebej zato, ker jo je treba na vsakem stojišču usmeriti proti skenerju. V idealnem primeru se položaj centra ne bi smel spremenjati, če tarčo vrtimo v katero koli od dveh smeri (horizontalno ali vertikalno). Ker pa ta idealni primer popačijo mehanske nepopolnosti, je potrebno pridobiti informacije o tem, kako naj bo usmerjanje tarč izvedeno, da bodo vplivi takšnih napak minimalni. V drugem delu testa pa je treba preveriti ekscentriciteto med tarčo in prizmo ter ugotoviti, ali je ta skladna z ekscentriciteto, določeno na osnovi tehničnih opisov obeh reflektorjev. Rezultati testa mehanske nepopolnosti so neodvisni od skenerja.

Da bi lahko odgovorili na zgornja vprašanja, je bilo treba izvesti laboratorijski test, prikazan na sliki 10 (levo). Dva stebra, postavljena približno 3 m narazen, sta bila uporabljena za pritrditev merskega



Slika 10: Testiranje konstrukcijskih napak tarč. Številke na desni sliki predstavljajo smeri vrtenja vsake izmed tarč, tj. najprej levo-desno nato navzgor-navzdol.

instrumenta na eni in tarče na drugi strani. Oba podnožja sta bila predhodno horizontirana s pomočjo preciznih cevnih libel. Za izvedbo opazovanj je bil izbran instrument Leica TS30, katerega kotna natančnost znaša $0.5''$, natančnost izmere dolžin pa $0.6 \text{ mm} + 1 \text{ ppm}$. V vsaki smeri 1, 2, 3 in 4 (slika 10) je bila tarča zavretena s korakom 10° do kota 40° , kar skupno predstavlja 17 položajev tarč, vključno s položajem, ko sta bila oba kota zasuka 0° . Nadalje je bil center tarče v vsakem kotnem položaju izračunan v dveh korakih. V prvem koraku sta bila na osnovi štirih odčitkov nitnega križa izračunana horizontalni in vertikalni kot točke centra, kot kaže slika 10. Odčitka levo-desno sta služila za izračun horizontalnega kota, odčitka zgoraj-spodaj pa za izračun vertikalnega kota. V drugem koraku je sledila izmera dolžine do centra s postavitvijo nitnega križa na sredino majhne (2 mm) srebrne pike v središču tarče. Takšen dvokoračni način se je izkazal za bolj nedvoumnega in

bolj natančnega od tistega, kjer se vse tri koordinatne komponente določijo z viziranjem na sredino srebrne pike. Tudi če dolžina v drugem koraku ni izmerjena vzdolž vizure, ki bi popolnoma sovpadala z vizuro, izračunano v prvem koraku, je razlika v dolžini zanemarljiva, saj izračunana vizura nikoli ne pade izven srebrne pike. Predstavljeno zaporedje izvedbe opazovanj in določitve centrov je bilo ponovljeno pri vseh štirih tarčah. Nazadnje so bila izvedena še opazovanja na reflektor Leica GHP1P z adicijsko konstanto pod 0.1 mm, da bi lahko določili ekscentriciteto med reflektorjem. Vsa opazovanja za izračun horizontalnega in vertikalnega kota centrov tarč v prvem koraku so bila izvedena brez nadštevilnosti. Dolžine do centrov v drugem koraku pa so bile ocenjene na osnovi petkratno ponovljenih meritev v vsakem položaju tarč. V primeru meritev na prizmo so bila opazovanja zopet izvedena z uporabo sistema APT, pri čemer so bile vse merjene količine, tj. oba kota in dolžina, opazovane v petih ponovitvah.

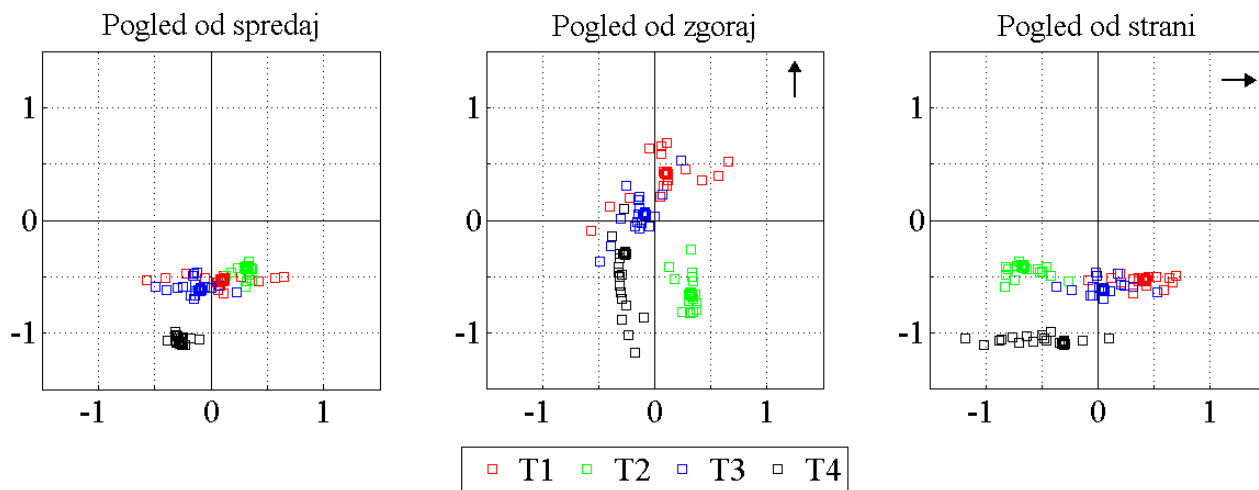
Rezultati testa potrjujejo, da so bile vse dolžine ocenjene z natančnostjo, ki ni nikoli presegla 0.2 mm. Te poševne dolžine so bile v zadnjem koraku pretvorjene v horizontalne dolžine in šele nato uporabljene za primerjavo. Kotne meritve na prizmo so bile ocenjene z natančnostjo 0.1" in 0.3", kar predstavlja zanemarljiva odstopanja na razdalji treh metrov. V preglednici 2 so prikazani rezultati tega testa z vidika občutljivosti tarč na vrtenje. V povprečju so položaji centrov tarč na vrtenje

Preglednica 2: Rezultati občutljivosti tarč na vrtenje. Δ_1 , Δ_2 , Δ_3 so razponi, znotraj katerih se gibljejo centri, pri čemer Δ_1 predstavlja smer *levo-desno*, Δ_2 smer *naprej-nazaj* in Δ_3 smer *navzgor-navzdol* gledano s strani opazovališča.

Tarča	Δ_1 [mm]	Δ_2 [mm]	Δ_3 [mm]
T1	1.2	0.8	0.2
T2	0.2	0.6	0.2
T3	0.7	0.9	0.2
T4	0.3	1.3	0.1

najbolj občutljivi v smeri *naprej-nazaj*, najmanj pa v smeri *navzgor-navzdol*. Če izvzamemo tarči T1 (Δ_1) in T4 (Δ_2) so vsi razponi centrov omejeni znotraj meje 1 mm, po prehodu v območje pod mejo enega milimetra pa se očitno tarče po občutljivosti malenkost razlikujejo. Podrobnejša analiza razkriva, da v tem majhnem velikostnem območju ni mogoče opaziti močne korelacije med vpadnim kotom in velikostjo premika centra v nobeni smeri Δ_i . Po drugi strani pa rezultati pokažejo, da vrtenje okoli vertikalne osi v večji meri vpliva na premike v smeri *naprej-nazaj* kot vrtenje okoli horizontalne osi. Posledično so vrednosti Δ_2 v preglednici 2 pretežno rezultat vrtenja okoli prve osi in so pri vrtenju okoli horizontalne osi še manjše. Na tej točki je težko podati zaključke o velikosti razponov premikanja centrov, če bi opazovanja izvedli z vrtenjem tarč okoli vertikalne osi v polnem krogu. Na podlagi rezultatov iz preglednice 2 bi verjetno nekaj vrednosti Δ_1 in Δ_2 prekoračilo mejo 1 mm v primerjavi z vrednostmi Δ_3 , ki so očitno 3- do 4-krat manjše in precej stabilne znotraj obravnavanega $80^\circ \times 80^\circ$ sfernega okna. Vendar pa takšna izvedba opazovanj z vrtenjem tarč v polnem krogu ni mogoča s samo enega stojišča instrumenta in v nalogu ni bila vključena. Če se sedaj osredotočimo na analizo ekscentricitete, lahko iz tehničnih opisov obeh reflektorjev

ugotovimo, da bi center tarče moral biti 114.5 mm (± 0.7 mm) nad centrom prizme, kar pomeni, da bi ekscentriciteta morala biti omejena zgolj na vertikalno smer. Rezultati, predstavljeni v preglednici 2, pa so pokazali, da v območju pod mejo enega milimetra ekscentriciteta ni reducirana izključno na to smer. Ta ugotovitev je ilustrirana tudi na sliki 11, kjer so prikazani položaji centrov tarč glede na položaj centra prizme, upoštevajoč vertikalni odmik 114.5 mm. Glede na sliko 11



Slika 11: Rezultati ekscentričnosti. Pogledi prikazujejo položaje centrov z vidika opazovališča. Za lažjo predstavo je smer proti točki opazovanja na sredinski in desni sliki nakazana s puščico. Odebeljeni okvirčki predstavljajo položaje, ko sta oba kota zasuka nič. Vse vrednosti na oseh so v [mm].

postanejo konstrukcijske razlike tarč jasno opazne in potrjene. Centri se po sistematičnem vzorcu grupirajo okoli izhodišča. Z vidika ekscentricitete so centri tarč T1, T2 in T3 okoli 0.5 mm nižje od navedene vrednosti, vendar znotraj dopustne meje. Enak zaključek ne velja za T4, katere centri se grupirajo približno okoli vrednosti 113.5 mm, tj. 1 mm nižje od navedbe iz tehničnega opisa. Vsaj pri T4 bi bilo treba ta pogrešek vertikalne ekscentricitete vedno upoštevati, kadar se tarčo uporablja, še posebej zato, ker se očitno zelo malo spreminja. Ekscentriciteta tarče T4 je v vertikalni smeri torej najmanj točna, medtem ko je pri vseh ostalih tarčah približno enaka.

Pri pogreških ekscentricitete v ostalih dveh prostorskih smereh je pomemben položaj razponov Δ_1 in Δ_2 glede na izhodišče. Na primer razpon 2 mm se prepolovi, če je glede na izhodišče postavljen centralno. To ugotovitev je mogoče opaziti pri tarči T1, katere razpon Δ_1 omejuje meja ± 1 mm. Grafi na sliki nakazujejo, da je od vseh najbolj natančna T2, vendar hkrati skoraj najmanj točna. T1 in T3 sta si podobni glede natančnosti, le da je T3 očitno bolj točna. Za tarčo T4 pa velja, da so njeni centri najbolj raztreseni, pri čemer nekateri padejo celo več kot 1 mm stran od izhodišča. Ti največji odmiki so rezultat vrtenja tarče okoli vertikalne osi na desno stran (smer 2 na sliki 10). Takšen rezultat za T4 govori v prid predpostavki, da bi bili odmiki pri vrtenju okoli vertikalne osi v polnem krogu za to tarčo najverjetneje vsaj tako veliki ali celo večji. Po drugi strani pa rezultati za T1, T2 in T3 znotraj tega $80^\circ \times 80^\circ$ sfernega okna močneje namigujejo, da bi bili pri opazovanju

centrov v polnem krogu njihovi položaji še vedno omejeni z mejo ± 1 mm. Ne nazadnje postane ob pregledovanju rezultatov tudi jasno, da bi bila uporaba kakršnih koli postopkov modeliranja za odstranitev takšnih pogreškov horizontalne ekscentritete zelo težavna, saj v tem velikostnem območju ni moč opaziti nobenih očitnih vzorcev. Zato tudi ni posebnega razloga, da bi z razširitvijo izvedbe opazovanj na polni krog s tem pripomogli k učinkovitosti modeliranja te vrste pogreškov. Očitno je, da lahko njihove vplive do določene mere odpravimo le v okviru ocene transformacije, če sploh (glej enačbo 3). Zaradi ročne izvedbe opazovanj in majhnega nivoja odstopanj bi lahko zanesljivost rezultatov ne nazadnje povečali s ponovitvami testa na enakih oz. različnih razdaljah instrument – tarča.

3.1.2 Modeliranje dolžinskega pogreška

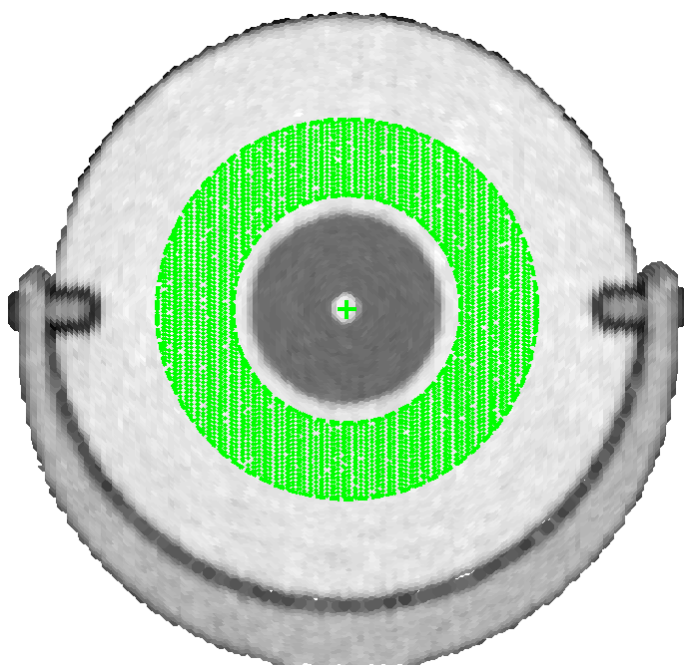
Kot je bilo omenjeno na začetku tega poglavja, je bilo obnašanje Rieglovega skenerja glede na Leicine ploske tarče analizirano v okviru laboratorijskega testa, z namenom ugotavljanja prisotnosti morebitnih sistematičnih dolžinskih pogreškov, ki bi jih bilo treba upoštevati takoj po izvedbi postopka ocene centrov tarč v testu 2, kjer je bil ta skener uporabljen. Dolžina objekta, v katerem je bil izveden ta laboratorijski test, je bila skoraj 70 m, zato je bilo pogrešek dolžine mogoče testirati izključno znotraj te razdalje. V tem 70-metrskem območju je bilo postavljenih skupno 43 stativov, in sicer na vsakih 1.5 m, z začetkom na treh pa vse do 66 m (slika 12). Stativi so bili



Slika 12: Zasnova testa dolžinske napake.

postavljeni skoraj v ravni črti in horizontirani s preciznimi cevnimi libelami. Na vsakem stojišču stativa je bila vsaka od štirih tarč skenirana v zaporednem vrstnem redu pri dveh vpadnih kotih, najprej pod kotom 0° in nato pod kotom 20° . Kot 20° je bil realiziran z zasukom tarče samo okoli vertikalne osi, kar je omogočilo analiziranje obnašanja pogreška pri nepravokotnem položaju tarče

glede na skener, ko se do njegovega sprejemnega sistema vrne manj optične energije. Poleg tega so izkušnje pokazale, da kot 20° predstavlja zgornjo mejo ročnega načina usmerjanja tarč, ki jo lahko zagotovimo ob skrbni in dosledni izvedbi terenskega dela. Rieglov VZ-400 skener je v celoti zajel 344 skenogramov, vsakič z ločljivostjo 1 mm na površini tarče v obeh kotnih smereh, kar predstavlja okoli 20 000 točk na skenogram. Za oceno položajev centrov tarč je bil uporabljen predlagani dvokoračni postopek (glej poglavje 2.4.1). Vse ravnine tarč v prvem koraku predlaganega postopka so bile ocenjene na osnovi pripadajočih podmnožic točk, prikazanih na sliki 13 (zeleno obarvane točke). Odločitev za izbor tega postopka ocenjevanja centra je bila motivirana iz pre-



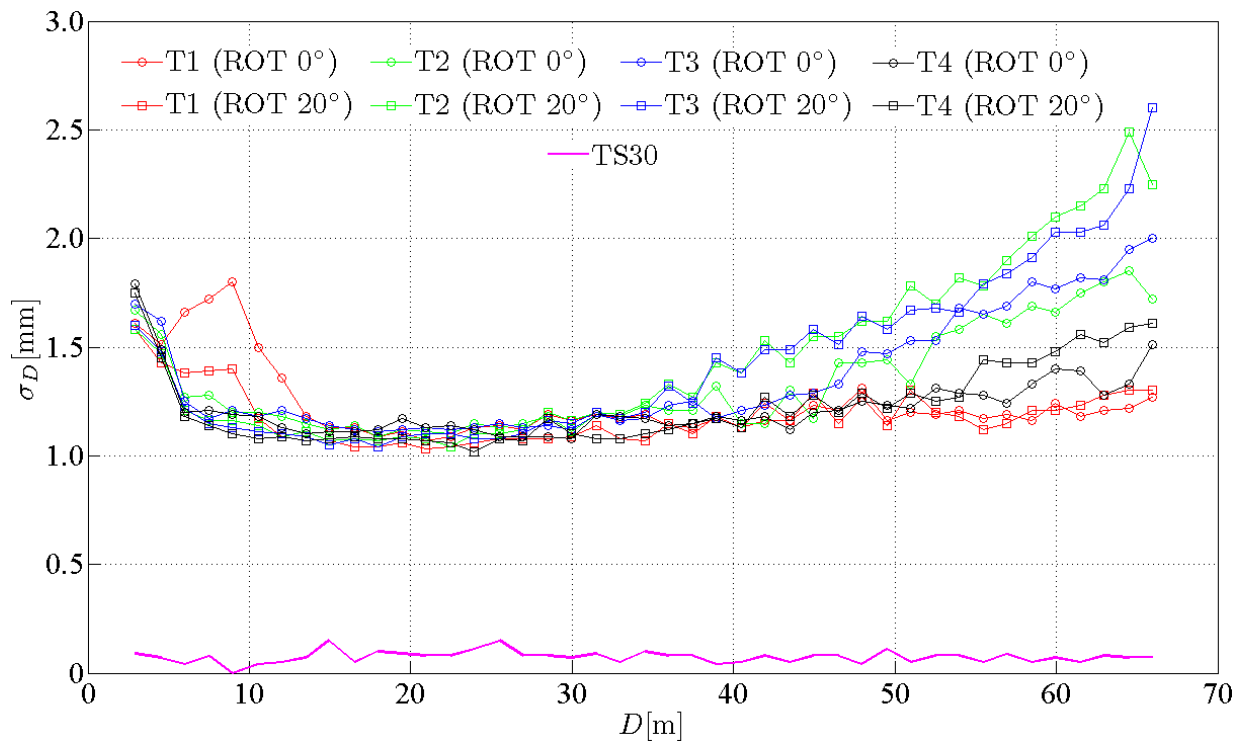
Slika 13: Območje oblaka točk izbrano za oceno dolžine. Točke so obarvane glede na amplitudo. Križec predstavlja približni položaj centra, izračunan z navzkrižno korelacijo.

prostega razloga, da so bile v okviru testa 2 razdalje skener – tarča prevelike in bi zato onemogočale uporabo alternativnega pristopa, ki temelji na amplitudno uteženem povprečju. Na celotni dolžini 70 m je bilo centre tarč mogoče oceniti na podlagi zgolj enega samega postopka samo v primeru uporabe predlaganega postopka določitve centra. Pri določitvi območja za oceno dolžine je bil pas, prikazan na sliki 13, izbran empirično, saj najbolje izpolnjuje kriterij homogenosti točk vse do dolžine 70 m in čez, kjer postane premer laserske pike večji od 3 cm (na razdalji 70 m je premer pike ≈ 3 cm). Poleg tega samo v tem območju vzorec vektorja popravkov izravnalne ravnine tarče ni podvržen sistematičnim vplivom. Dejstvo, da območje leži na retroreflektivni površini tarče, je predstavljalo dodaten razlog za pričakovanje prisotnosti dolžinskih pogreškov. Iz tega razloga je bilo skeniranje izvedeno v t. i. *reflektorskem* načinu, ki v primerjavi z ostalima dvema načinoma³ generira najšibkejše impulze in je posledično tudi najprimernejši. Vprašanje je bilo, kako bo ta

³Hitri način (*high-speed*) in način dolgega dometa (*long-range*). Testi so pokazali, da uporaba teh dveh načinov zaradi višje jakosti impulzov ni primerna, saj vodi do precej večjih dolžinskih pogreškov.

način skeniranja in retroreflektivne lastnosti območja, prikazanega na sliki 13, vplival na izmero dolžin.

Po zajemu vseh skenogramov so bile izvedene še referenčne meritve dolžin, ponovno z uporabo tahimetra Leica TS30 in reflektorja GPH1P z adicijsko konstanto pod 0.1 mm. Na vsakem stojišču stativa je bila dolžina do prizme izmerjena v petih ponovitvah, in sicer s pomočjo sistema APT. Klasične terestrične meritve so bile izvedene z istega stativa, ki je bil uporabljen za skeniranje in se je nahajal na enem od krajišč 70 m dolgega hodnika. Stativ za pritrdiritev obeh instrumentov je bil prav tako horizontiran, da bi bila s tem omogočena primerjava dolžin. Zaradi ekscentricitet, tako na strani reflektorjev kot tudi na strani instrumentov, poševnih dolžin ni bilo možno neposredno primerjati, ampak šele po izračunu horizontalnih dolžin. Pri ekscentriciteti na strani reflektorjev je bila upoštevana izključno vertikalna komponenta. Tudi ekscentriciteto med koordinatnima sistemoma obeh instrumentov je bilo možno s pritrdiritvijo v isto podnožje omejiti na vertikalno komponento. Izključno za ta namen je bil pod glavo skenerja pritrjen poseben adapter. Med sedem ur trajajočim testom so bili vsako uro izmerjeni meteorološki pogoji, ki se sicer po pričakovanjih niso bistveno spreminali (sprememba temperature $\Delta T < 0.4$ °C, vlažnosti $\Delta \eta < 10$ % in zračnega tlaka $\Delta p < 1.5$ mbar). V primeru uporabe rezultatov tega testa, tj. dolžinskih korekcij, v kasnejših izmerah v naravi s spremnjajočimi se pogojimi atmosferi v različnih terminskih izmerah, bi bilo dolžine treba popraviti za meteorološke popravke. Izkaže se, da je pomembno upoštevati predvsem prvi popravek hitrosti, ki je na največji razdalji znašal 1.4 mm za tahimeter in 1.1 mm za skener. Na sliki 14 standardne deviacije dolžin jasno nakazujejo razliko kakovosti med obema instrumentoma z vidika zmogljivosti razdaljemera. Natančnost klasičnih terestričnih dolžin je najmanj de-

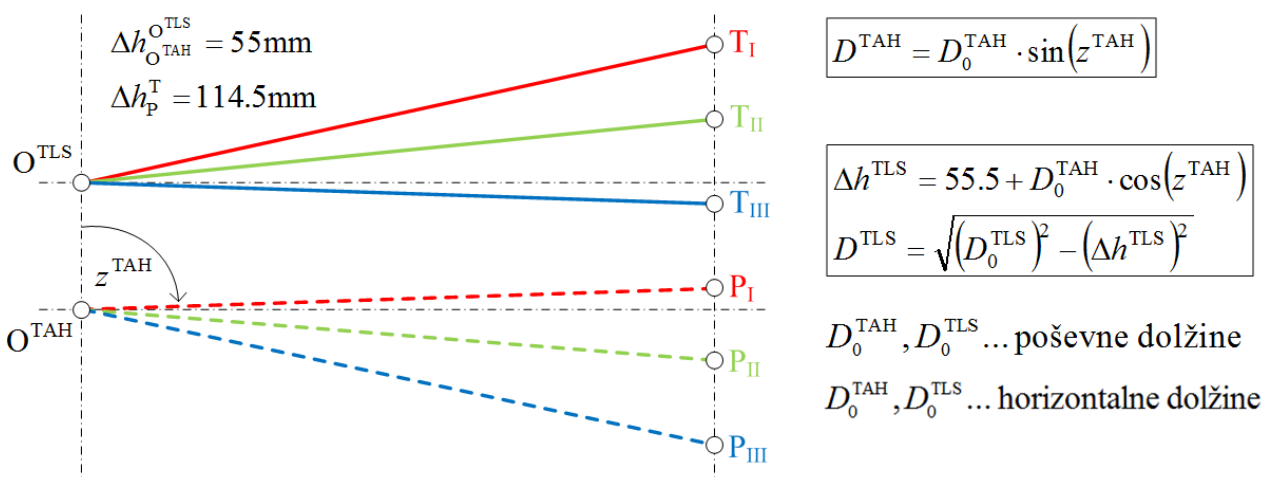


Slika 14: Standardne deviacije merjenih dolžin.

setkrat večja, kar pomeni, da lahko te dolžine obravnavamo kot referenčne. Poleg tega je natančnost dolžin TLS, ki predstavlja stopnjo šuma v ravnini tarče, mogoče razložiti z analiziranjem povprečne amplitud, ki jo posamezna tarča proizvede znotraj izbranega območja. Razlike povprečnih amplitud, ki jih lahko vidimo na slikah 16 in 17 na straneh 153 in 154, vodijo do različnih stopenj šuma. Glede na razdaljo lahko natančnost dolžin TLS razdelimo na tri ločene intervale. V bližini skenerja ($D < 10 \text{ m}$) se v natančnosti dolžin očitno odraža dejstvo, da se pri vpadnem kotu 0° do sprejemnika vrne preveč energije, kar znotraj izbranega območja povzroči večjo stopnjo šuma. Pri T1 se ta interval podaljša celo nekoliko čez 10 m , saj proizvede ta tarča v povprečju 20 % višje vrednosti amplitud od ostalih treh. Vrtenje tarče za 20° ima pozitiven vpliv, saj se vrne manjša količina energije.

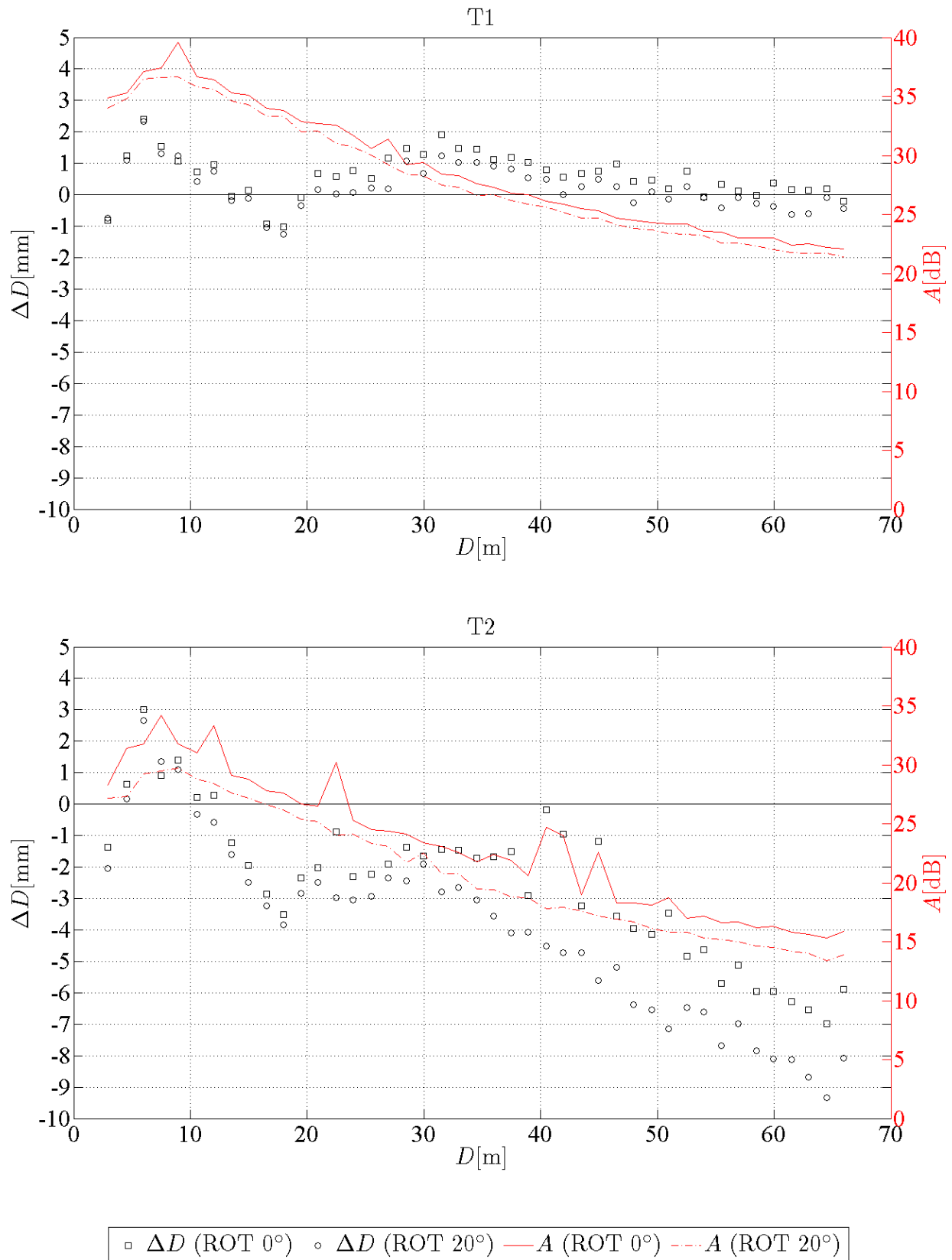
V naslednjem intervalu, ki sega do $D \approx 35 \text{ m}$, je natančnost dolžin TLS največja. Energija impulzov torej v tem intervalu proizvede najmanjšo stopnjo šuma, in sicer pri vseh tarčah ne glede na amplitudne razlike. Nad mejo 35 m začne zmogljivost razdaljemera hitro upadati, predvsem pri T2 in T3, ki proizvedeta v povprečju najnižje amplitude. V tem najbolj oddaljenem intervalu pridejo razlike povprečnih amplitud tarč zaradi splošnega upada energije impulzov precej bolj do izraza. Posledično se standardne deviacije bolj razlikujejo kot pod mejo 35 m , kjer so precej skladnejše (razen pri T1 v neposredni bližini). Od vseh tarč je pri T1 natančnost dolžin najmanj odvisna od razdalje. Z naraščanjem dolžine ima zasuk za 20° nasproten vpliv, saj zaradi čedalje nižje amplitudo proizvede več šuma.

V zadnjem koraku so se dolžine horizontirale glede na enega od treh scenarijev I, II in III, ki so prikazani na sliki 15, in sicer izključno na osnovi klasičnih terestričnih meritev in znanih vertikalnih ekscentricitet. Ob predpostavki, da med dejansko in idealno geometrijo te sheme horizontiranja ob-

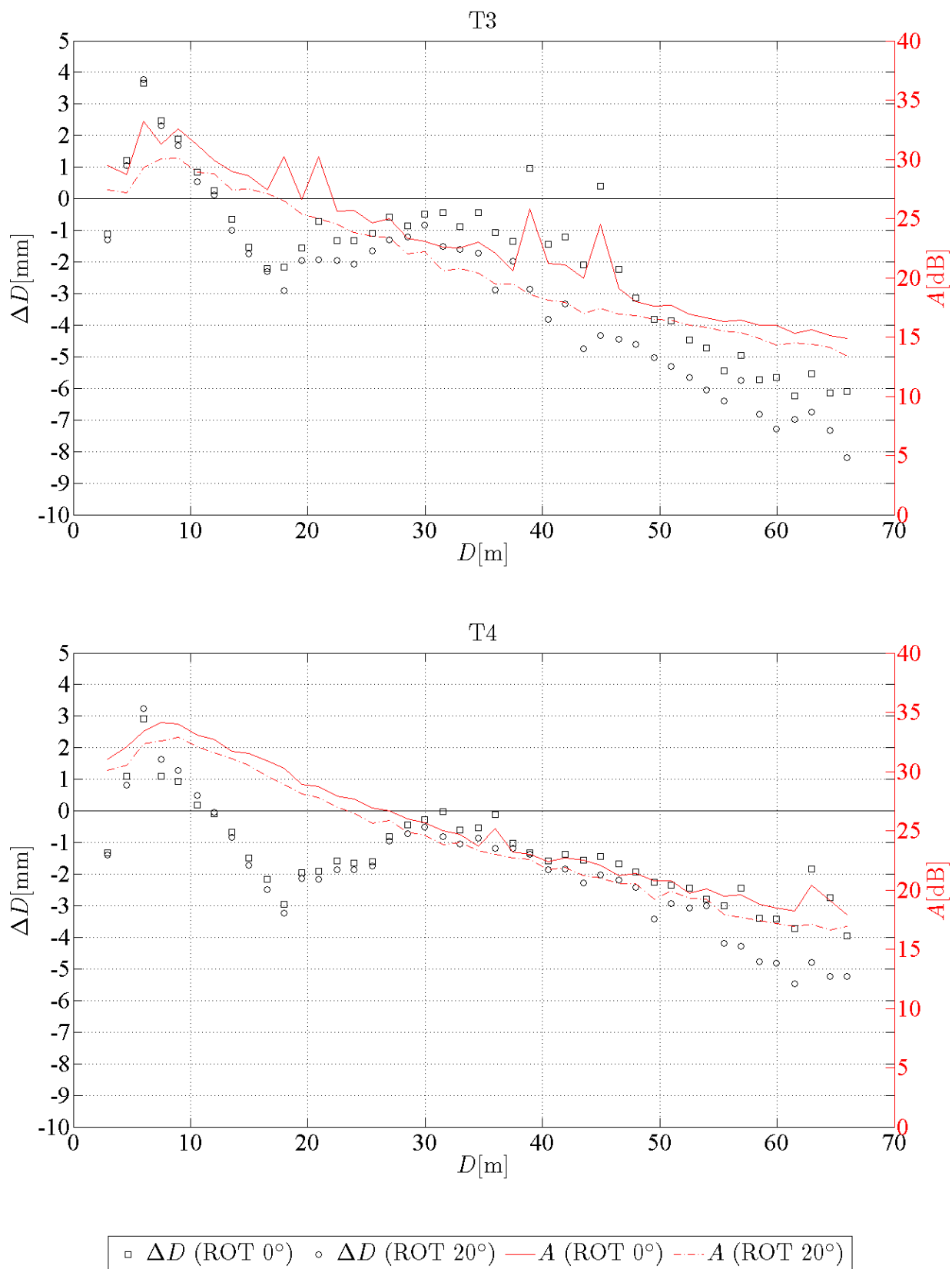


Slika 15: Horizontiranje poševnih dolžin. P označuje prizmo, T pa tarčo.

stajajo samo majhne razlike (tj. točke O^{TAH} , O^{TLS} , T, P ležijo v ravnini in obe vertikalni osi sta si vzporedni), imajo le-te zanemarljiv vpliv na izračunane horizontalne dolžine. Sedaj se dolžine končno lahko primerjajo, pri čemer je pogrešek dolžine izračunan kot $\Delta D = D^{\text{TAH}} - D^{\text{TLS}}$.



Slika 16: Pogrešek dolžine in povprečna vrednost amplitude kot funkcija razdalje za T1, T2.



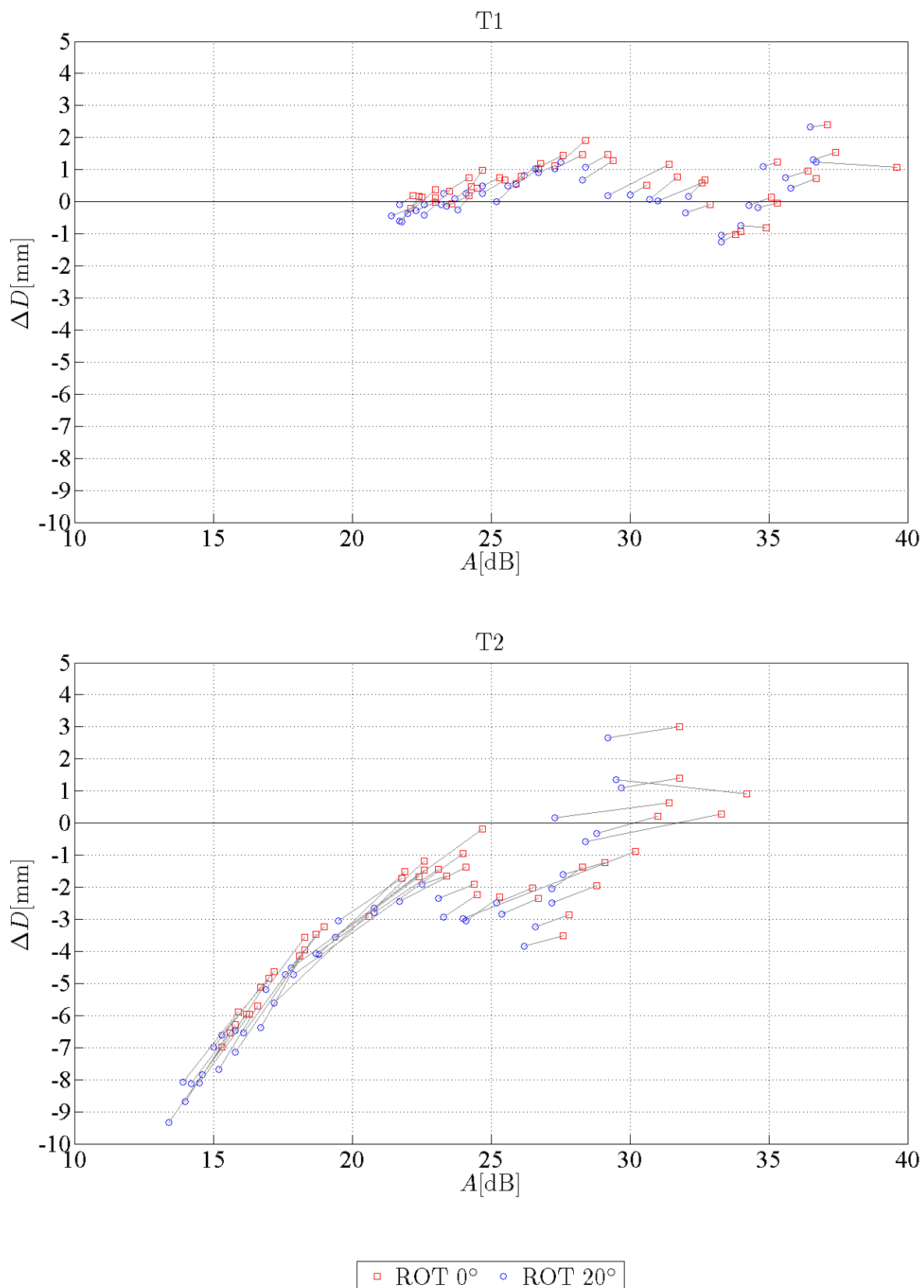
Slika 17: Pogrešek dolžine in povprečna vrednost amplitude kot funkcija razdalje za T3, T4.

Na podlagi pregleda grafov lahko potrdimo obstoj sistematičnih pogreškov dolžin kot tudi dejstvo, da se v območju milimetrov za posamezno tarčo ti pogreški obnašajo različno kljub podobnemu trendu. Pogreški dolžin so v povprečju do desetkrat večji od pogreškov mehanskih nepopolnosti tarč. Nelinearen trend pogreškov dolžin lahko opišemo s tremi lokalnimi ekstremi, prvim pri okoli šestih metrih, drugim pri osemnajstih metrih in zadnjim pri tridesetih metrih. Očitno ima ta trend izvor v instrumentu (tj. *vpliv skenerja*). Za razlago vpliva skenerja bi potrebovali poglobljeno znanje o sami napravi, zato ga je izključno s strani meritev težko razložiti. Po drugi strani izvirajo razlike v ΔD iz razlik v obnašanju amplitudo tarč (tj. *vpliv tarče*). Če bi vse tarče proizvedle enako povprečno amplitudo⁴, bi bil ΔD enak. Posledično lahko k razlagi vpliva tarče pristopimo z analiziranjem amplitudnih razlik.

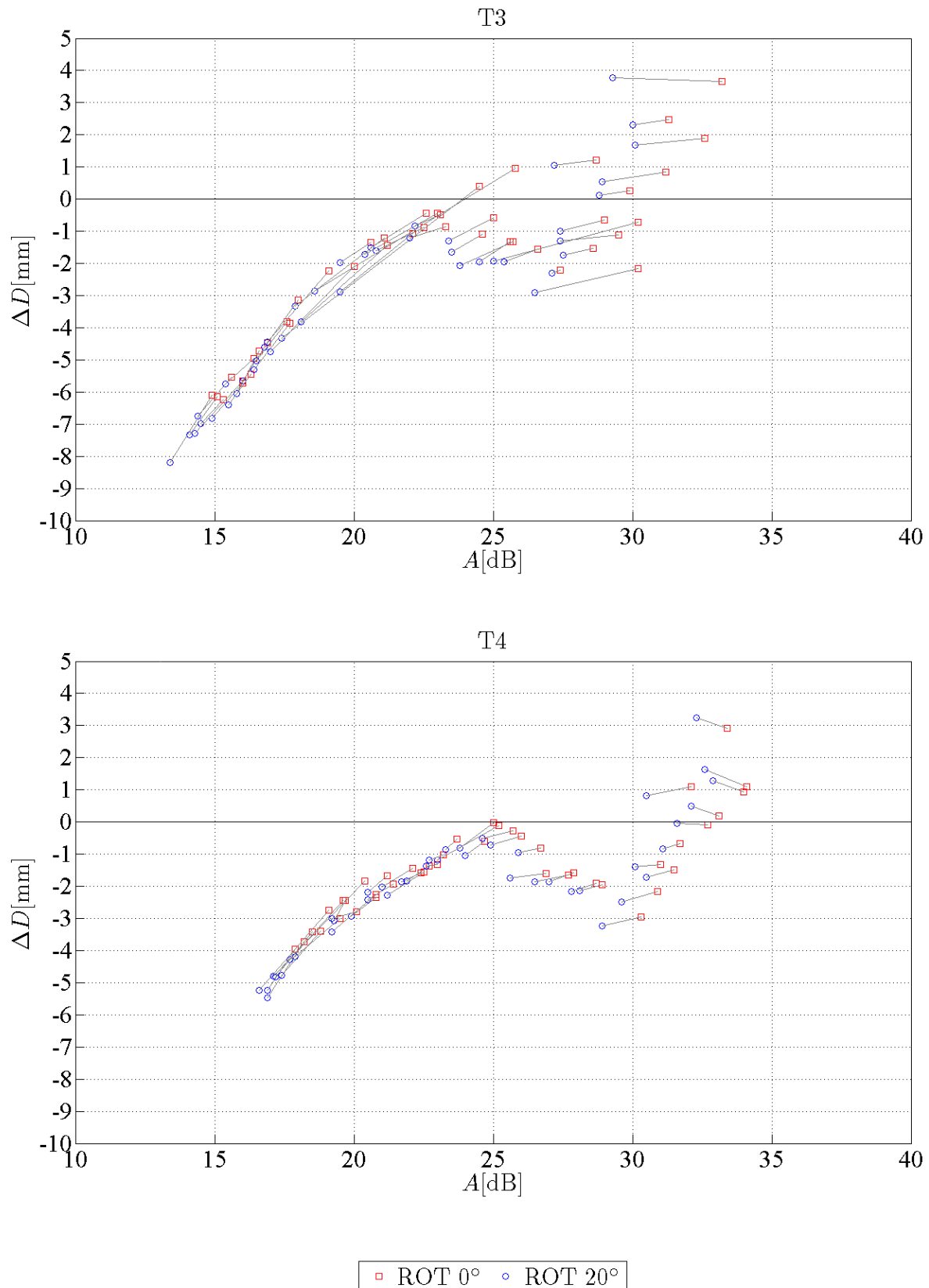
Pri proučevanju grafov amplitudo lahko zaključimo, da začne upad $1/D^2$ prevladovati pri razdaljah nad 10 m, kjer amplituda doseže maksimum. Najverjetneje predstavlja razdalja 10 m tisto mejo, nad katero pade celotna energija impulzov skozi sprejemnikov zaslonski kot. Prav tako velja, da lokalna nihanja amplitudo, ki so opazna predvsem pri T2 in T3, neposredno vplivajo na ocenjevanje dolžin in ne nazadnje tudi na pogreške dolžin. Prisotnost teh nihanj je problematična, saj ta na nek način odražajo splošno nestabilnost razdaljemera v območju milimetrov, predvsem zato, ker niso rezultat posameznih impulzov, ampak celotnega izbranega območja na tarči, ki vsebuje okoli 4000 točk. Ker je pojav nihanj težko napovedati, bo učinkovitost modeliranja do neke mere omejena. Na podlagi grafov amplitudo ni mogoče pridobiti dodatnih ključnih informacij za razlago vpliva skenerja, upoštevajoč, da se tako v bližnjem kot daljnem dosegu dolžine določijo z enim samim sprejemnim sistemom. Namesto tega sta amplituda in pogrešek dolžine korelirana do razdalje 18 m, nad to mejo pa se korelacija izgubi. Z naraščanjem dolžine ostane razlika med amplitudama iz obeh kotnih položajev skoraj enaka. To pa ne velja za razlike med dolžinskima pogreškoma, ki narašča z razdaljo zaradi splošnega upadanja amplitude. Pri T2 in T3 narašča razlika med dolžinskima pogreškoma hitreje, saj so pri teh dveh razlike med amplitudama večje ($\Delta A_{T2} = 2.4 \text{ dB}$ in $\Delta A_{T3} = 2.0 \text{ dB}$, medtem ko $\Delta A_{T1} = 0.8 \text{ dB}$ in $\Delta A_{T4} = 1.2 \text{ dB}$). Padec amplitude pri vpadnem kotu 20° potisne pogrešek dolžine v negativno smer, razlika med dolžinskima pogreškoma pa lahko za T2 na največji razdalji doseže do 2 mm.

Poleg možnosti modeliranja dolžinskega pogreška kot funkcije dolžine nam globoka medsebojna povezava med dolžino in amplitudo ponuja alternativni način, in sicer z modeliranjem dolžinskega pogreška kot funkcije amplitude. Glede na sliki 18 in 19 na straneh 156 in 157 se izkaže, da $\Delta D = f(A)$ izpoljuje kriterij prave funkcije. Hkrati je z vidika modeliranja ta funkcija bolj primerna, saj jo določata samo dva različna ekstrema, kar pomeni, da lahko pogrešek dolžine opišemo s funkcijami nižje stopnje kot v primeru $\Delta D = f(D)$. Za boljše razumevanje naj bo omenjeno, da se na slikah 18 in 19 lokalni minimum nahaja na najmanjši razdalji od skenerja, lokalni maksimum pa na razdalji okoli 30 m. Orientacija črnih črt, ki povezujejo točke na enaki razdalji, vendar pri različnem vpadnem kotu, je pokazatelj naraščanja dolžinskega pogreška z razdaljo.

⁴V nadaljevanju se bo besedo 'povprečna' izpuščalo.



Slika 18: Pogrešek dolžine kot funkcija amplitude za T1 in T2. Črne črte povezujejo pare točk.



Slika 19: Pogrešek dolžine kot funkcija amplitude za T3 in T4. Črne črte povezujejo pare točk.

Možnost modeliranja dolžinskega pogreška kot funkcije amplitude na podlagi manjšega števila parametrov, ki jih je v izravnavi treba oceniti, se je izkazala za odločilen dejavnik. Po izbiri modeliranja kot funkcije amplitude in ne razdalje, je bila začetna ideja izravnave ločiti vpliv skenerja in vpliv tarče. To je možno izvesti z uporabo ene funkcije (jedrne funkcije), ki bo predstavljala prvi vpliv, in z uvedbo določenega niza dodatnih parametrov za drugi vpliv, tj. $F(X, L) = F([x_1 \dots x_{u_0}, x_{u_0+1} \dots x_u], L) = 0$, kjer je X vektor parametrov, L pa vektor opazovanj. Parametri $x_{k,k=1\dots u_0}$ pripadajo jedrni funkciji, medtem ko so $x_{k,k=u_0+1\dots u}$ dodatni parametri, ki pri vključevanju lastnosti posamezne tarče jedrni funkciji zagotavljajo potrebno prilagodljivost.

V postopku izbire jedrne funkcije so bili sprva testirani polinomi različnih stopenj, vendar so se pri absorbiranju trenda v zadnjem koraku za bolj učinkovite izkazale racionalne funkcije. Slednje so lokalno veliko bolj prilagodljive, vendar manj robustne, kar pomeni, da potrebujemo za uspešno konvergenco dobre približne vrednosti parametrov. Jedrno funkcijo sestavljata polinom tretje stopnje v števcu in polinom druge stopnje v imenovalcu⁵:

$$\Delta D = f(A) = \frac{P(A)}{Q(A)} = \frac{p_3 \cdot A^3 + p_2 \cdot A^2 + p_1 \cdot A + p_0}{A^2 + q_1 \cdot A + q_0} \quad (21)$$

Če se hočemo izogniti inherentnemu problemu merila v tem modelu, je treba parameteru q_2 dodeliti vrednost ena (lahko bi uporabili kateri koli drug parameter). V nasprotnem primeru bi za rezultat dobili homogen sistem s trivialno oziroma neskončno mnogo reštvami. Z vključitvijo dveh dodatnih parametrov s in t , prvega za merilo in drugega za translacijo, dobimo spodnjo enačbo popravkov:

$$\Delta D_{ij} = s_j \cdot \frac{A_{ij}^3 + p_2 \cdot A_{ij}^2 + p_1 \cdot A_{ij} + p_0}{A_{ij}^2 + q_1 \cdot A_{ij} + q_0} \cdot \cos(\alpha_{ij}) + t_j \quad (22)$$

V enačbi 22 je z $i = 1 \dots 344$ označen indeks tarče. Če hočemo, da bo s_j postal pravi parameter, potem je tudi p_3 treba nastaviti na vrednost ena. Posledično se v izravnavi v celoti oceni 13 parametrov. Tukaj je $\cos(\alpha_{ij})$ dodan z namenom upoštevanja vpliva vpadnega kota. Slednjega je sicer na podlagi dveh kotov težko ovrednotiti, vendar izgleda precej majhen (glej slike 20, 21, 22 in 23 na koncu tega podpoglavja). Predpostavka o Lambertovih sevalnih lastnostih tarč zaradi retroreflektivnih lastnosti območja, ki služi za določitev dolžine, najverjetneje ne drži. Iz tega razloga lahko člen $\cos(\alpha_{ij})$ preuredimo v $\cos(m_j \cdot \alpha_{ij})$, kar v izravnavo vključi še štiri nove parametre.

Kljub prednostim opisanega modela z vidika uporabe ene jedrne funkcije ter ločitve vpliva instrumenta in tarče, testiranje modela na podatkih ni bilo preveč uspešno. Dodatni parametri jedrni funkciji niso zagotovili želene prilagodljivosti za absorpcijo razlik med tarčami, ki so prikazane na slikah 18 oziroma 19 in jih domnevno povzroči vpliv tarče. Eden od možnih razlogov za takšen izzid ni nujno izključno v parametrih samih, ampak je lahko tudi v približnih vrednostih neznank, ki jih je težko poiskati in lahko, namesto do globalnega, vodijo do lokalnega minimuma modelne funkcije. Nobenega posebnega napredka ni bilo doseženega z razširitvijo modela do končne oblike,

⁵V primeru modeliranja pogreška dolžine kot funkcije razdalje bi v števcu jedrne funkcije nastopal polinom četrte, v imenovalcu pa pete stopnje.

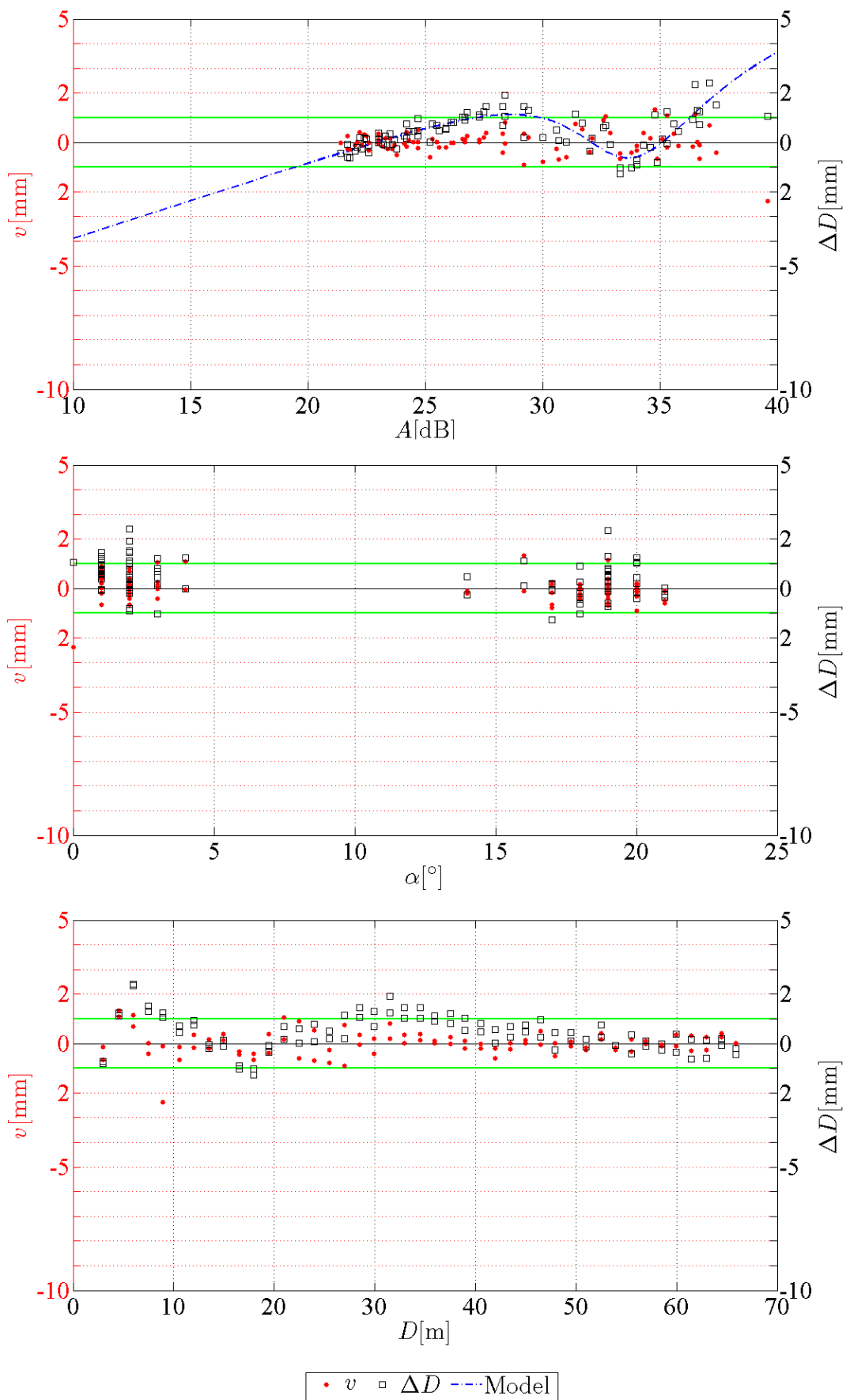
v kateri je funkcionalno spremenljivko A nadomestila ($A - T_j$), kar je v izravnavo dodalo še štiri nove translacijske parametre. Vključevanje parametrov preko končnega števila nima nobene koristi, saj lahko vodi do nadparametrizacije sistema.

Po izčrpnom testiranju enojedrnega modela z različnimi modifikacijami in z različnimi nizi približnih vrednosti je pomanjkanje kakršnih koli obetajočih rezultatov botrovalo opustitvi začetne ideje izravnave. Namesto tega se je k modeliranju pristopilo na ločen način, in sicer za vsako tarčo posebej, vendar še vedno z uporabo funkcionalnega modela iz enačbe 21. Rezultati tega ločenega pristopa so bili z vidika splošne učinkovitosti modeliranja boljši in so zato bili privzeti kot končni. Ocenjene vrednosti modelnih parametrov, vključno s pripadajočimi aposteriori standardnimi deviacijami za vsako tarčo, so podane v preglednici 3. Iz teh ločenih modelnih funkcij je bil vpadni

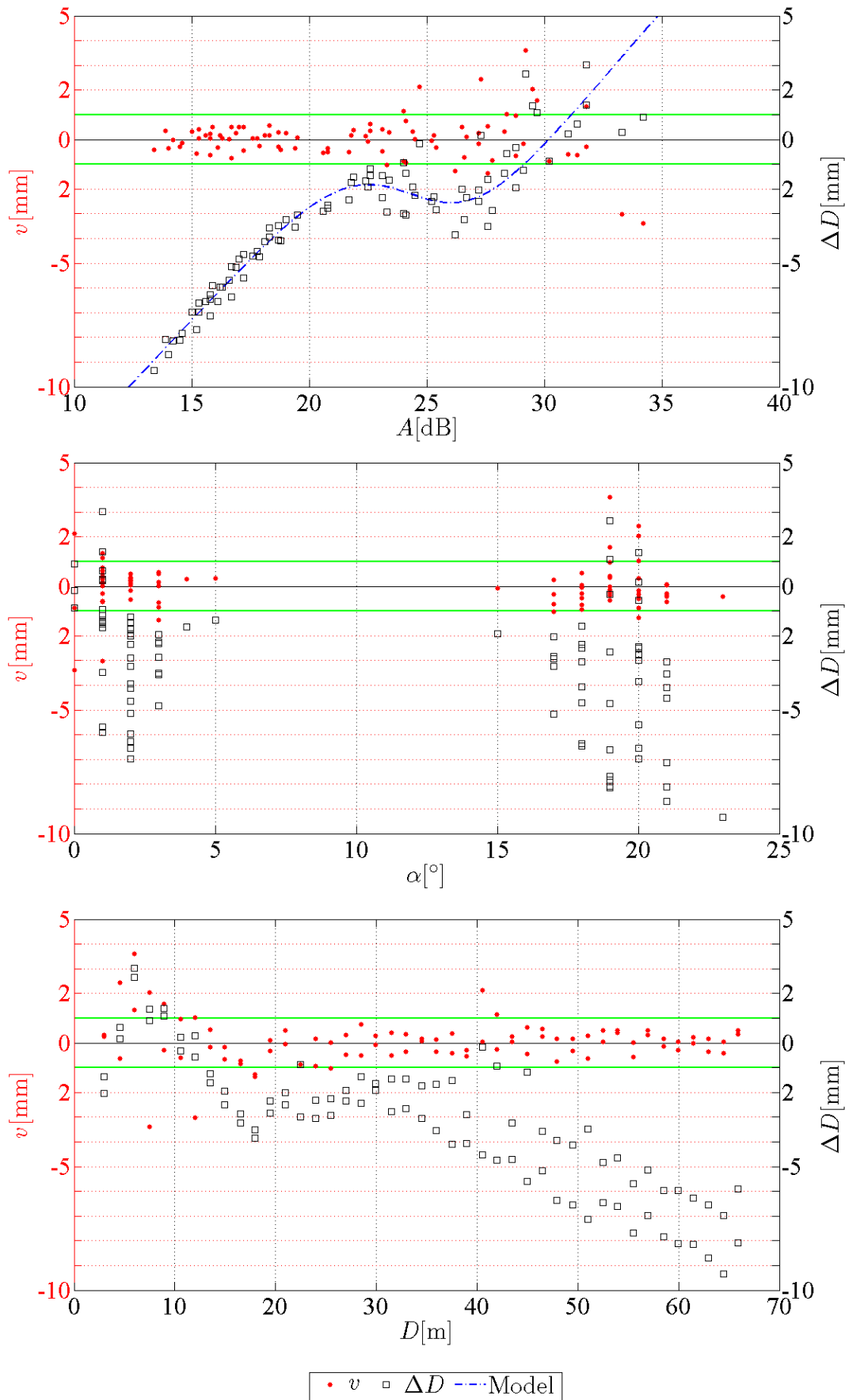
Preglednica 3: Ocenjene vrednosti parametrov funkcij pogreška dolžine in aposteriori vrednosti.

	T1	T2	T3	T4
p_3	0.304762	0.894525	0.847888	0.601716
p_2	-27.460037	-67.284268	-63.487416	-49.524117
p_1	812.467947	1677.293026	1573.560883	1349.126127
p_0	-7865.659127	-13926.696980	-12952.431721	-12191.481641
q_1	-66.824233	-49.207920	-49.067752	-55.238595
q_0	1128.073586	634.306982	630.330465	779.205941
$\hat{\sigma}_0$ [mm]	0.5	0.9	0.9	0.7

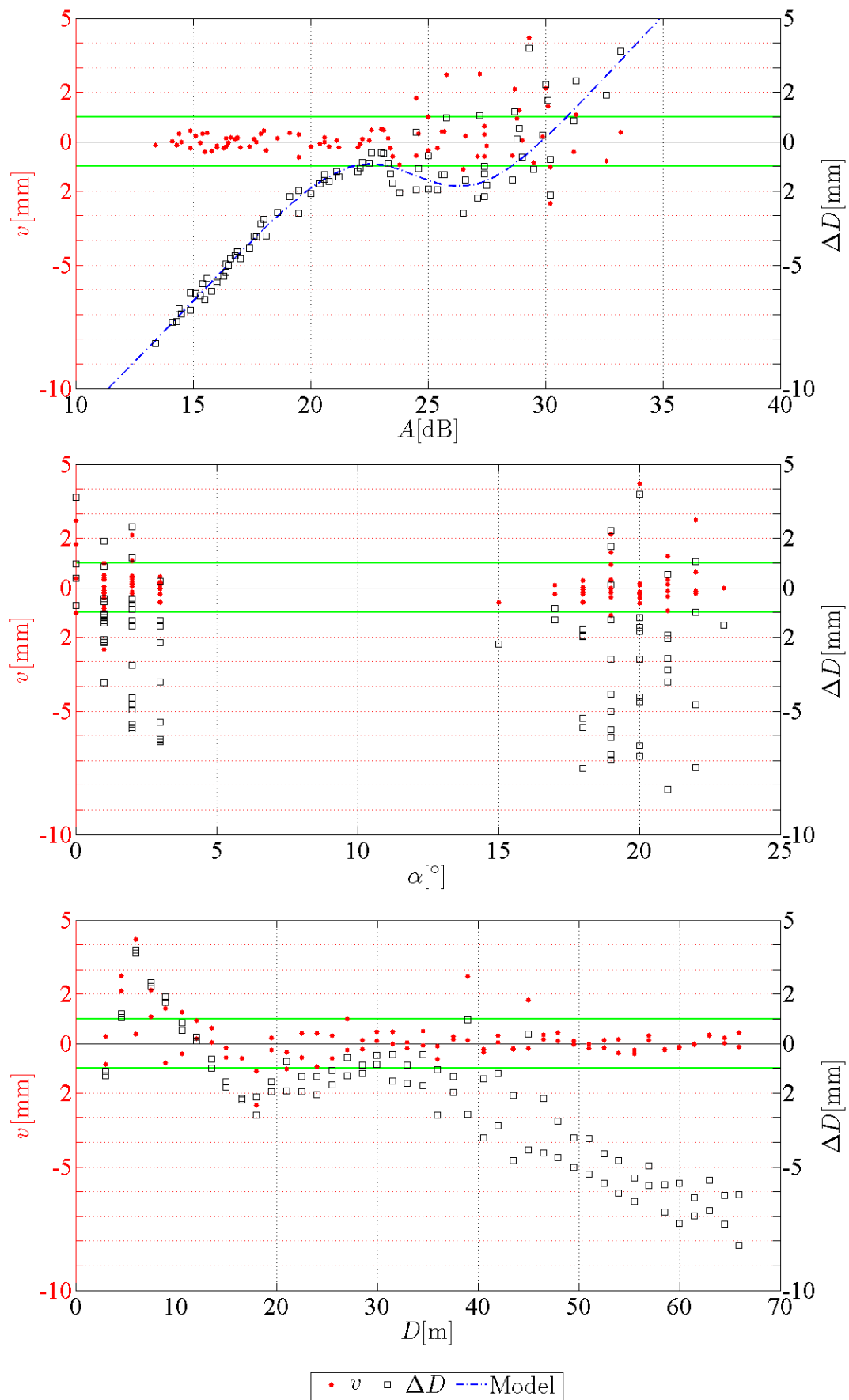
kot izpuščen, saj njegova odsotnost praktično ni imela vpliva na rezultate izravnave. Vrednosti aposteriori standardnih deviacij, ki predstavljajo eno od meril učinkovitosti modeliranja, so pod mejo 1 mm. Vrednosti vektorjev popravkov, prikazane na slikah 20, 21, 22, 23 na straneh 160, 161, 162 in 163, potrjujejo ugotovitev, da postavitev tarč bližje od 20 m ni priporočljiva, predvsem zaradi na splošno večjih vrednosti popravkov, ki nakazujejo neučinkovitost modeliranja znotraj tega območja. Vprašanje je, ali se znotraj tega območja vseeno pojavlja določen trend, ki bi ga bilo moč opaziti le z gostejšim vzorčenjem dolžin, oziroma se spremembe pogreška dolžine enostavno ne da opisati z nobenim posebnim trendom. Po drugi strani so popravki nad mejo 20 m pretežno precej pod vrednostjo 1 mm. Na podlagi ocenjenih vrednosti modelnih parametrov (glej preglednico 3) lahko izluščimo nekaj zaključkov glede razlogov za neuspešnost izbranega niza dodatnih parametrov, vključenih v začetni pristop modeliranja. Razlike v vrednostih parametrov najverjetneje ne bi bilo možno premostiti izključno s pomočjo merila in translacije jedrne funkcije. Kljub vsemu se je v okviru tega testa o vplivu skenerja pridobilo vsaj nekaj ugotovitev, ki razkrivajo njegovo obnašanje. Ne nazadnje niso pogreški tisti, ki vzbujajo nekaj skrbi, ampak nihanje njihovih vrednosti, saj jih v procesu modeliranja ni mogoče obvladovati, kar lahko vidimo na spodnjih slikah, ki na grafičen način prikazujejo rezultate končne oblike ločenih izravnnav.



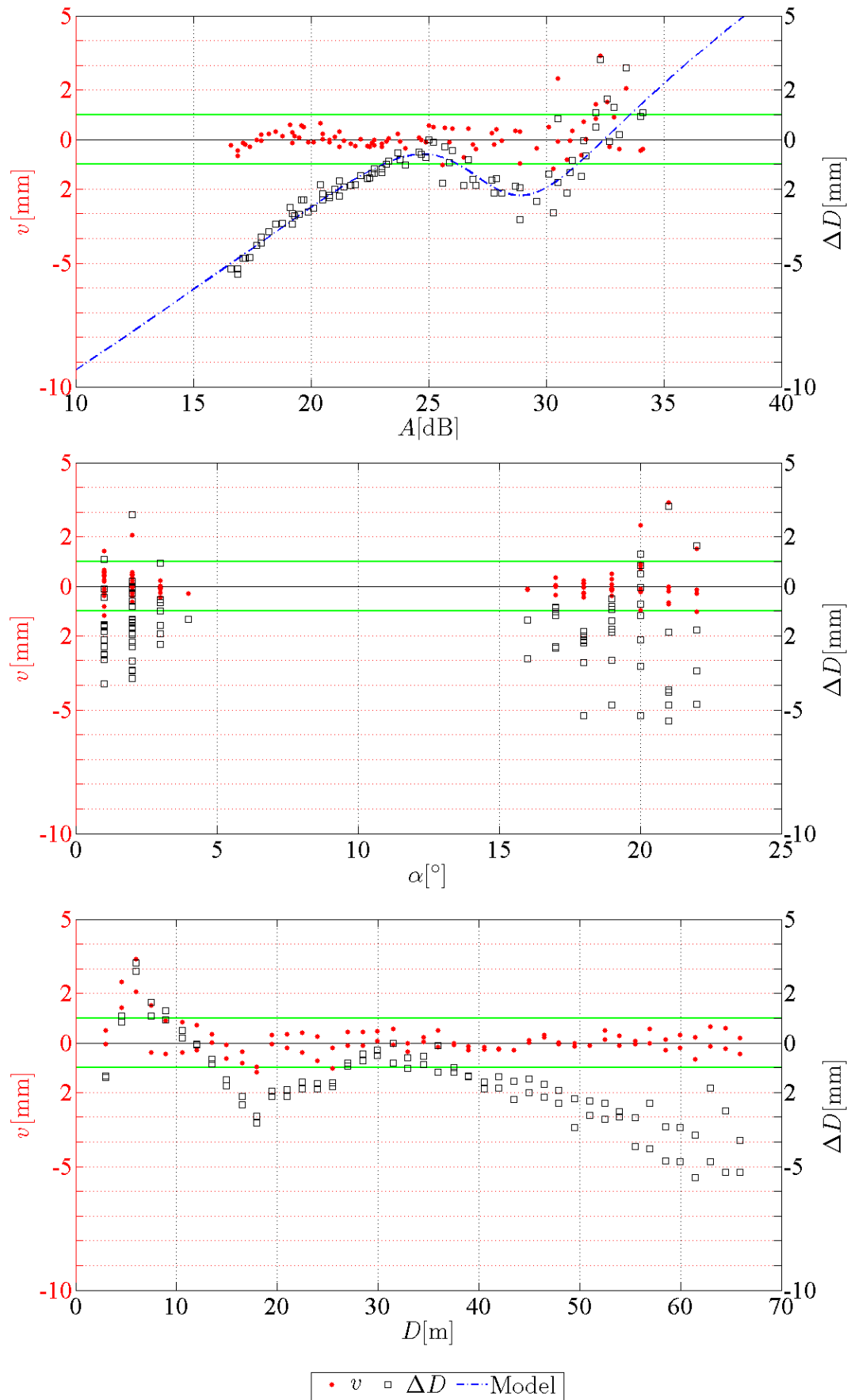
Slika 20: Vektor popravkov za T1.



Slika 21: Vektor popravkov za T2.



Slika 22: Vektor popravkov za T3.

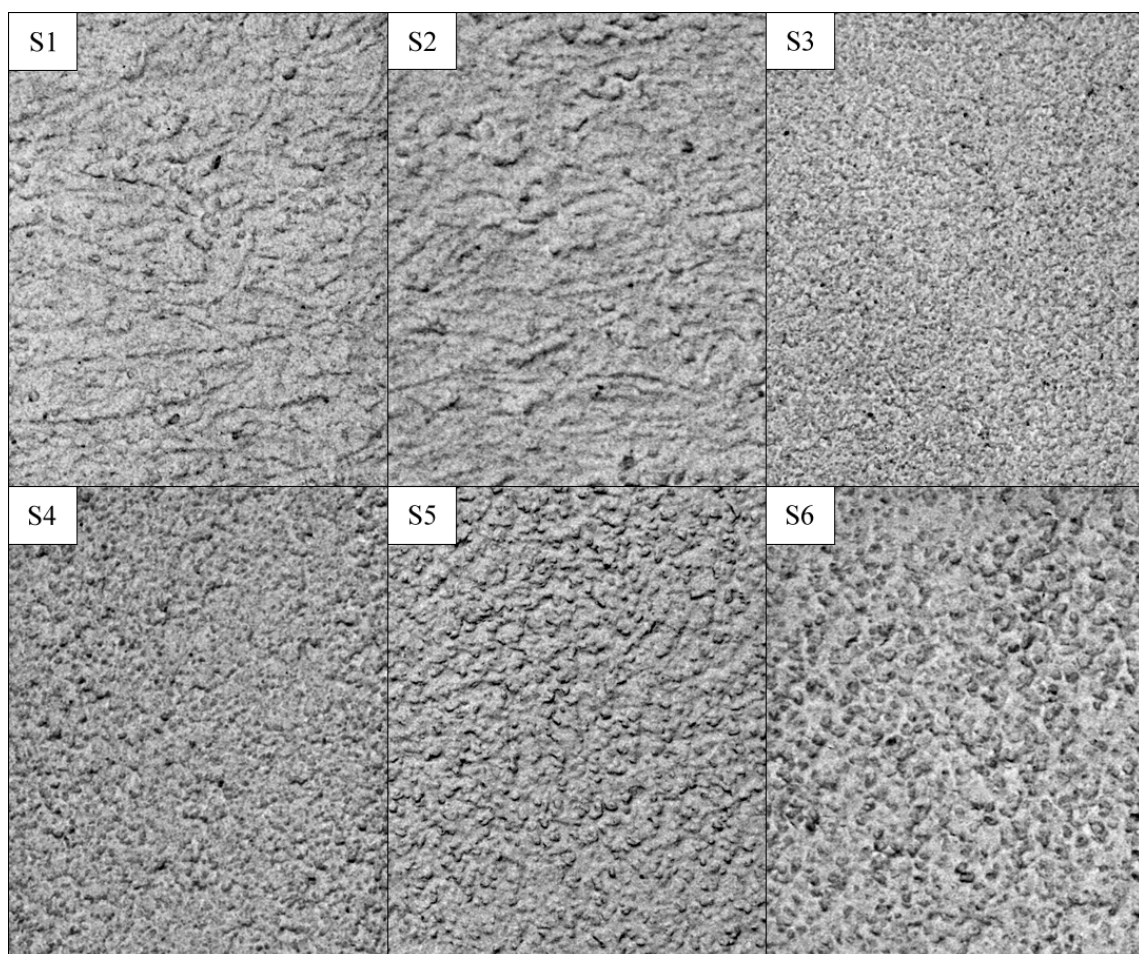


Slika 23: Vektor popravkov za T4.

3.2 Odzivnost površinskega materiala

Glede na izkušnje iz predhodnega testa je bilo hkrati pomembno preveriti tudi odziv skenerja na spremembe površinskih lastnosti objekta. Ti rezultati so ključnega pomena za izvedbo testa 2, kjer raziskovalni cilji in narava problema narekujejo testiranje natančnosti izmere dolžin in posledično stopnje občutljivosti instrumenta glede na površino objekta.

Za analiziranje vplivov na natančnost brezkontaktne izmere dolžin v testu 2 je bilo v okviru tega eksperimenta obravnavanih šest različnih vzorcev, označenih z S1 do S6. Vzorci so bili skrbno pripravljeni z namenom čim boljšega posnemanja najpogostejših površinskih pogojev na terenu. Na sliki 24 so prikazane povečane slike vzorcev za poudarek njihovih posebnosti. Vzorci pred-



Slika 24: Povečane slike testnih vzorcev, vsaka zajema $\approx 5\%$ originalne velikosti vzorcev.
 Dimenziije slik so 12 cm x 9 cm.

stavljajo ne samo različne stopnje zrnatosti, ampak se razlikujejo tudi po načinu razporeditve zrn. Vzorca zgoraj levo, S1 in S2, sta predstavnika nehomogene razporeditve, dosežene na podlagi zribanja obeh površin. Za razliko od teh dveh so vsi ostali vzorci narejeni z glajenjem površine, kar posledično vodi do bolj homogene razporeditve. Glede na velikosti zrn so bile uporabljene štiri stopnje, in sicer 1.0 mm, 1.5 mm, 2.0 mm in 2.5 mm (glej preglednico 4). Zrna so bila umešana

v omet in nanešena na kvadratne plošče površine $\frac{1}{4} \text{ m}^2$, kar lahko vidimo na sliki 26 na strani 166. Očitno je, da velikost zrn in hrapavost površine⁶ (σ_h) po končani pripravi plošč nista enaki, na eni strani zaradi ometa, na drugi pa tudi zato, ker je bil omet na plošče nanešen ročno.

Za oceno dejanske hrapavosti površine je bila vsaka izmed plošč skenirana z mersko roko Metris D50 (Nikon, 2010), ki za opis geometrije objekta uporablja princip triangulacije in katere natančnost določitve položaja je pod mejo $50 \mu\text{m}$, zato je bila primerna za to nalogu. Rezultate skeniranja so predstavljeni skenogrami visoke gostote, pri čemer je vsak od njih vseboval več kot milijon točk. Zaradi izredno majhne stopnje šuma tega instrumenta v primerjavi z velikostjo zrn je bila iz podatkov jasno razvidna večina površinskih detajlov na ploščah. V naslednjem koraku se je skenogram plošč razdelilo na površinske zaplate velikosti $2 \text{ cm} \times 2 \text{ cm}$, da bi hkrati lahko določili lokalne spremembe hrapavosti površine po celotnem vzorcu. V povprečju je posamezna zaplata (oziroma segment) vsebovala okoli 3000 točk, s pomočjo katerih so se v postopku MNK ocenile referenčne ravnine. Te ravnine predstavljajo povprečen nivo površine v posameznem segmentu. Z ocenjevanjem lokalnih referenčnih ravnin, namesto ene same za celoten vzorec, se praktično izognemo vplivu upogibanja površine plošč. V preglednici 4 so podane končne informacije o lastnostih posameznih vzorcev. Očitno so razlike v $\bar{\sigma}_h$ majhne, kar postavi vprašanje, ali bodo

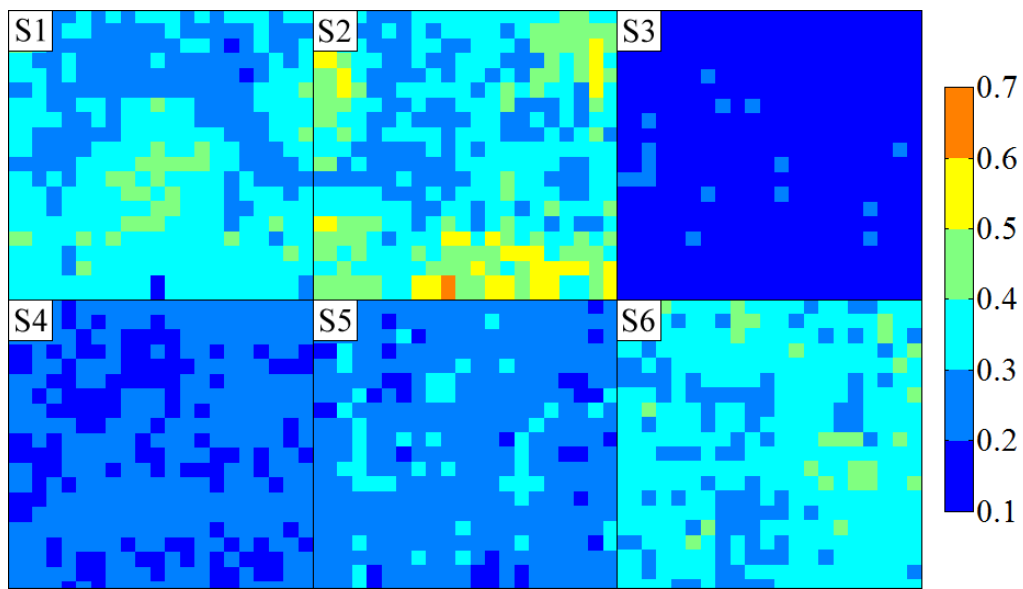
Preglednica 4: Lastnosti vzorcev. $\bar{\sigma}_h$ je povprečna hrapavost površine, izračunana na podlagi 400 zaplat na vsakem vzorcu. V splošnem predstavlja povprečna hrapavost 15 % velikosti zrn.

Vzorec	Velikost zrna [mm]	$\bar{\sigma}_h$ [mm]	Opomba
S1	2.0	0.32	zaribani
S2	2.5	0.36	zaribani
S3	1.0	0.17	glajeni
S4	1.5	0.21	glajeni
S5	2.0	0.25	glajeni
S6	2.5	0.35	glajeni

te razlike povzročile različno obnašanje posameznih vzorcev pri sipanju svetlobe, kar bi lahko v nadaljevanju vplivalo tudi na natančnost dolžin. Glede na Rayleighov kriterij (Rees, 2001) lahko namreč površine vseh vzorcev, z vidika običajnih valovnih dolžin impulzov, opredelimo kot grobe, čeprav lahko pričakujemo manjša odstopanja od idealnega Lambertovega modela odboja. Za razliko od povprečne hrapavosti so na sliki 25 prikazane spremembe v σ_h glede na posamezno zaplato, kar odraža dejstvo, da je bil omet na plošče nanešen ročno. Če naj bi vzorci posnemali dejanske površinske pogoje na terenu, kjer so takšna odstopanja vedno prisotna, potem ni odveč, če so prisotna tudi v vzorcih.

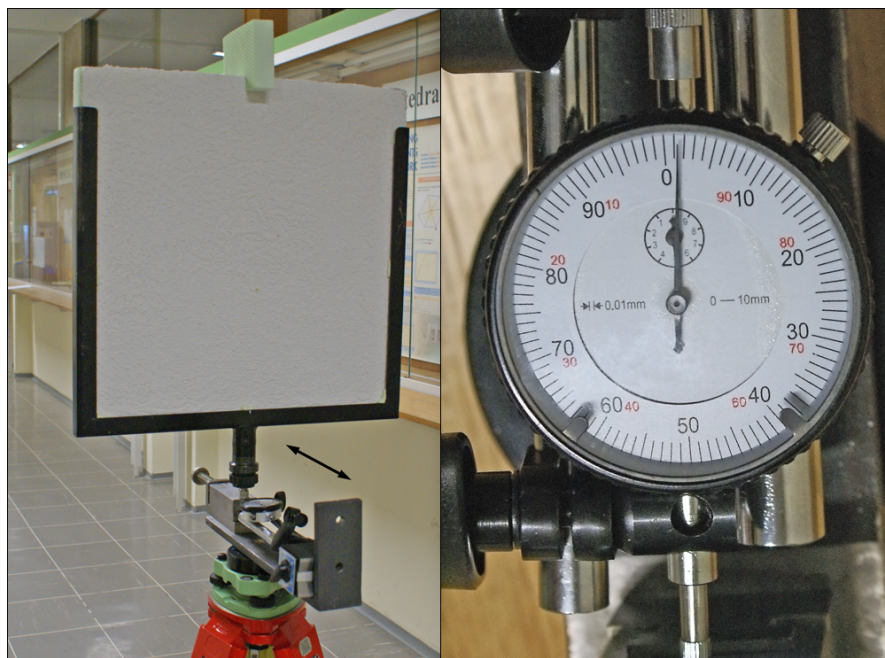
Po zaključku analize hrapavosti površin je bila pozornost preusmerjena v izvedbo testa, ki je bil izveden v istem, 70 m dolgem hodniku, kjer je bil opravljen test kalibracije tarč. Tokrat so bili

⁶Tukaj je hrapavost površine enostavno opredeljena kot standardna deviacija dejanskih odstopanj od povprečnega nivoja površine.



Slika 25: Razlike hrapavosti površine v [mm] – frontalni pogled.

uporabljeni trije stativi, postavljeni približno na razdaljah 20 m, 40 m in 65 m od enega konca hodnika, kjer je bil postavljen dodaten stativ za pritrpitev merskega instrumenta. Ponovno so bili vsi stativi horizontirani s pomočjo preciznih cevnih libel. Na vsakem od treh stativov so se plošče vpele v *vilično* držalo, ki se je nato pritrtilo na gibljivo vodilo posebej za ta namen narejene kovinske platforme (glej sliko 26). Z vrtenjem vijaka na eni strani platforme je mogoče vodilo premikati



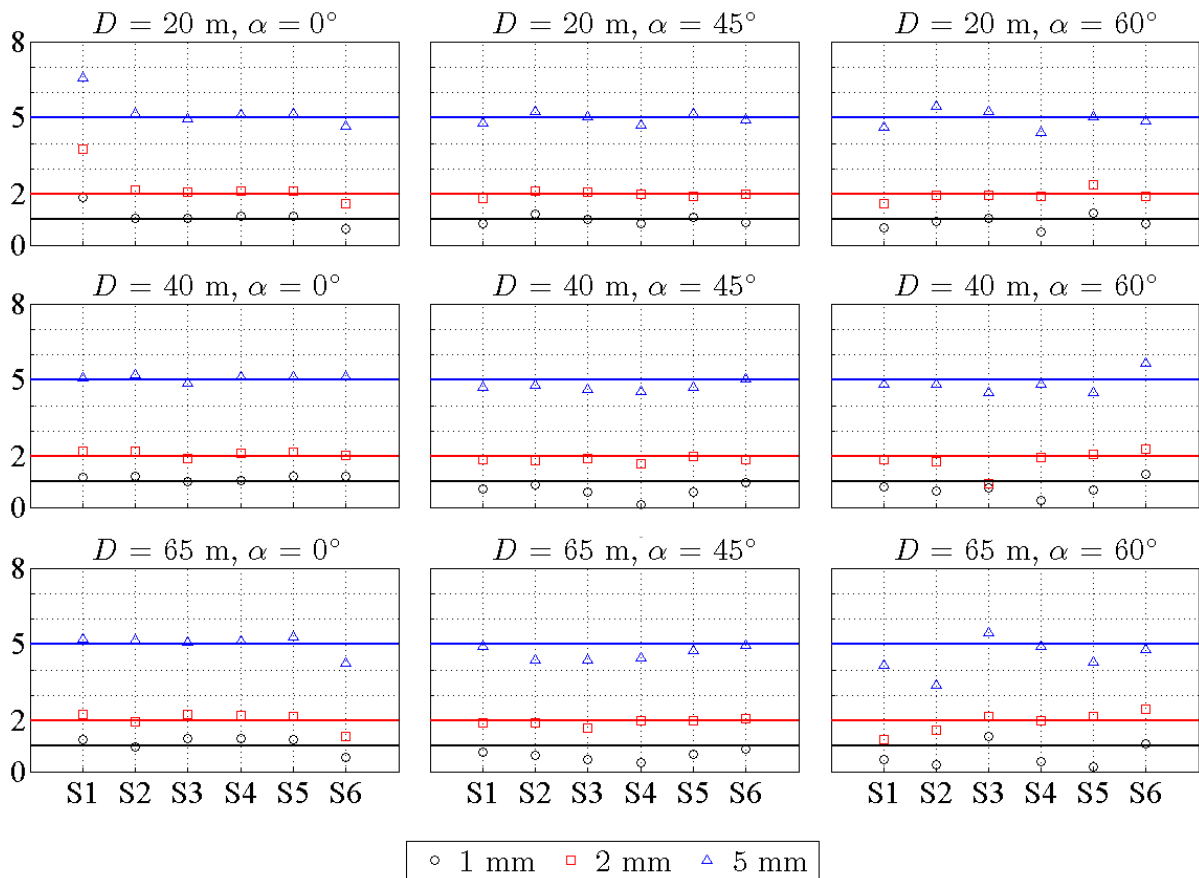
Slika 26: Držalo za plošče in merska ura.

vzdolž ene same smeri, ki je na sliki 26 označena s puščico. Zadnjo komponento predstavlja merska ura, vpeta med vodilo in krajišče platforme, ki je upognjeno navzgor. En polni obrat na merski uri predstavlja premik za 1 mm, kar je razvidno iz slike 26. Ker je držalo mogoče obračati okoli

vertikalne osi, so bile plošče na vsakem stativu skenirane pri treh različnih vpadnih kotih (20° , 45° in 60°). S tem je bilo možno ugotoviti, na kakšen način bo vpad energije vplival na natančnost dolžin, in sicer ne samo glede na razdaljo, ampak tudi glede na vpadni kot. Na vsakem stojišču in pri vseh vpadnih kotih so bile nato plošče skenirane v štirih položajih vodila, tj. v začetnem (referenčnem) položaju in po premiku za 1 mm, 2 mm in 5 mm. To simulirano zaporedje premikov je bilo izvedeno vzdolž smeri proti skenerju, kar pomeni, da je platformo bilo treba ustrezno usmeriti. Odstopanja med obema smerema, tj. smerjo premika in smerjo proti skenerju, je bilo treba minimizirati, čeprav imajo pri teh velikostih premikov zelo majhen vpliv. Na primer, premik za 5 mm na merski uri vzdolž za 10° odklonjene smeri drsenja je manj kot 0.1 mm krajsi kot premik vzdolž smeri proti skenerju. Posledično torej s pazljivim ročnim usmerjanjem platforme bistveno ne vplivamo na rezultate. Pri vpadnih kotih 45° in 60° so bile v vseh položajih vodila plošče skenirane samo enkrat, medtem ko so bile pri vpadnem kotu 0° v vseh položajih vodila skenirane v petih ponovitvah, da bi s tem lahko analizirali ponovljivost in stabilnost skenerja. Na podlagi predstavljene merske sheme je celotna izvedba meritev trajala okoli šest ur, in sicer ponovno z uporabo instrumenta Riegl VZ-400. Po zaključku skeniranja je bilo delovanje merske ure preverjeno tudi s pomočjo klasične terestrične izmere dolžin, pri čemer je bil na vodilo pritrjen reflektor GPH1P. Na vsakem stativu je bila s tahimetrom Leica TS30 v vseh položajih vodila dolžina izmerjena petkrat. Razlike med povprečnimi vrednostmi dolžin in odčitki na merski uri so znašale manj kot 0.2 mm. Predstavljena merska shema omogoča obravnavo premikov relativno glede na začetni položaj vodila, medtem ko meritev TLS in klasične terestrične metode na nivoju milimetrov ni mogoče primerjati. Vse plošče so bile skenirane z ločljivostjo 5 mm, kar predstavlja približno 6000 (kot 0°), 4500 (kot 45°) in 3000 (kot 60°) točk na skenogram, če tiste, ki ležijo blizu robovom, izvzamemo iz analize. V nadaljevanju so bile preostale točke uporabljene za oceno izravnalnih ravnin. Tudi če plošče niso povsem ravne, to pri izračunu premikov ne igra nobene vloge, če se njihova integriteta ne spremeni. Ocenjene vrednosti modelnih parametrov (težišča in normalni vektorji) predstavljajo vhodne podatke za izračun premikov po modelu 1, predstavljenem v podoglavlju 2.8.1. Z uporabo tega modela je možno določiti izključno premike vzdolž ene izbrane smeri, v tem primeru je to smer začetne normale. Zato je pomembno, da ta smer sovpada s smerjo drsenja vodila, če hočemo izračunane premike uskladiti z odčitki na merski uri. To ne velja pri vpadnih kotih 5° in 60° , kjer je normalne vektorje treba deliti s $\cos(\alpha)$.

Rezultati testa pokažejo, da so bili vpadni koti realizirani znotraj $\pm 2^\circ$. Poleg tega razmerja $\frac{A_{45^\circ}}{A_{0^\circ}}$ in $\frac{A_{60^\circ}}{A_{0^\circ}}$ nakazujejo, da se v povprečju 10 do 20 % več energije vrne do sprejemnika kot v primeru, če bi bili vzorci idealne Lambertove površine. Kljub tem odstopanjem je pri vseh vzorcih možno opaziti podobne odbojne lastnosti, kar pomeni, da imajo razlike v hrapavosti površin majhen vpliv. Posledično lahko podobnosti opazimo tudi v odvisnosti amplituda od razdalje, pri čemer amplituda upada z $1/D^2$. Na osnovi takšnega rezultata lahko sklepamo, da se vzorci z vidika šuma v ravnini plošče in v nadaljevanju tudi stopnje ujemanja med izračunanimi premiki ter odčitki na merski uri ne bodo bistveno razlikovali. Zares, analiza je potrdila, da je pri vseh vzorcih v postopku ocene ravnin $\hat{\sigma}_0$ ostala skoraj nespremenjena. Šum se do razdalje 70 m pri vpadnem kotu 0° ni veliko

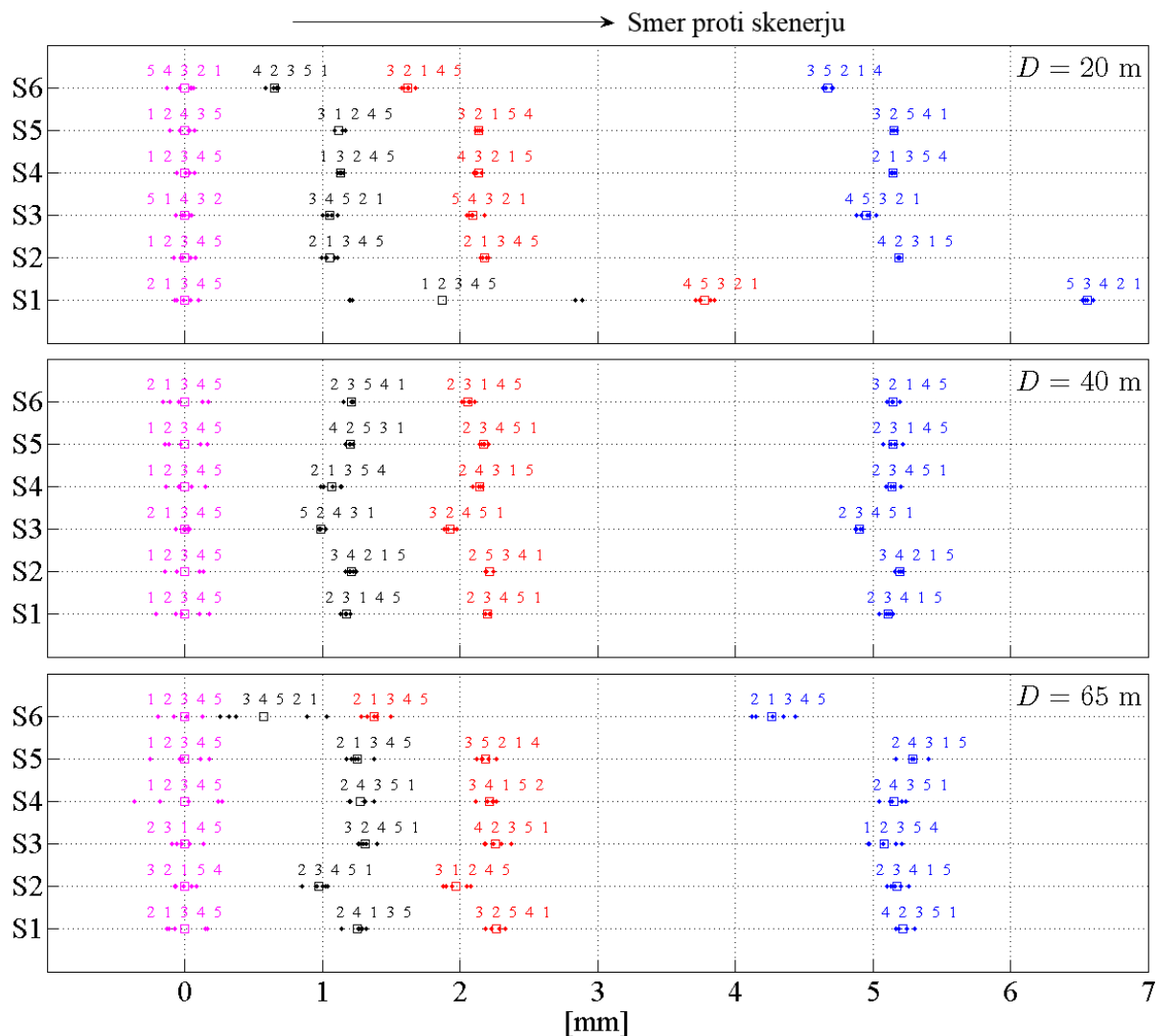
spremenil, ampak šele pri zasuku za kot 45° ali 60° , saj je bila v tem primeru količina odbite energije odvisna od obeh vplivov. Če povzamemo, je povprečna vrednost $\hat{\sigma}_0$ za vse vzorce znašala okoli 1.6 mm, vendar je na razdalji 65 m in pri vpadnem kotu 60° doseгла 2.2 mm. Stopnja ujemanja med izračunanimi premiki in odčitki na merski uri je prikazana na sliki 27. Analiza skenogramov



Slika 27: Rezultati premikov v [mm]. Pri $\alpha = 0^\circ$ so premiki rezultat povprečenja petih zaporednih skenogramov v vsakem položaju vodila.

v odvisnosti od časa zajema hkrati nakazuje, da so nekatera odstopanja od odčitkov na merski uri najverjetneje rezultat nihanj napetosti pri napajanju skenerja s pomočjo baterij. To je najbolj očitno pri S1 na razdalji 20 m in $\alpha = 0^\circ$ ali pri S6 na razdalji 65 m in $\alpha = 0^\circ$, ko so bile baterije po nekaj urah skeniranja že zelo prazne. Posledično se je takšnim intervalom pomanjkanja energije kot tudi zagonskemu času instrumenta treba izogniti. Na podlagi rezultatov na sliki 27 lahko ugotovimo, da začnejo izračunani premiki nihati pri vpadnem kotu 60° , še posebno na razdalji 65 m. Po drugi strani je premike velikosti 2 mm in 5 mm možno razločiti do vpadnega kota 45° ne glede na razdaljo. Po predvidevanjih je kakovost ocenjenih vrednosti premikov bolj ali manj enaka za vse vzorce, pri čemer odstopanja od odčitkov na merski uri odražajo napake razdaljemera na tem majhnem velikostnem nivoju.

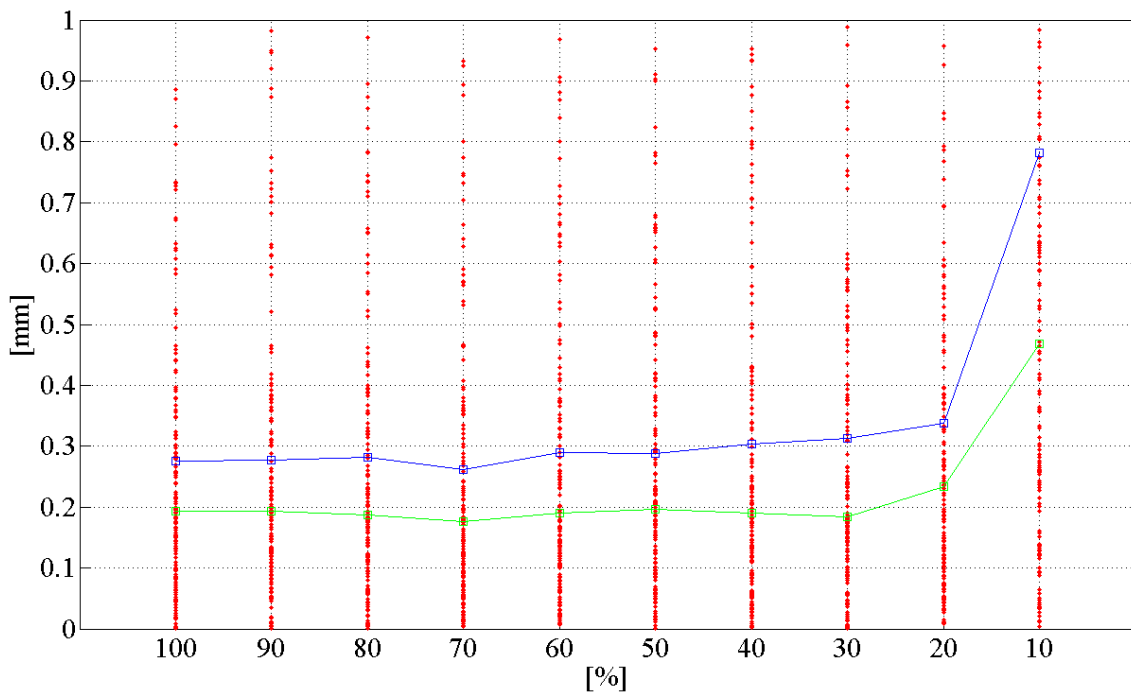
V nadaljevanju so na sliki 28 prikazani rezultati analize večkratnih skenogramov pri vpadnem kotu 0° , ki omogočajo obravnavo ponovljivosti skenerja. Očitno ponovljivost nekoliko nazaduje z naraščanjem razdalje. Poleg tega je na osnovi številk, ki označujejo časovno zaporedje skenogramov,



Slika 28: Večkratni skenogrami pri vpadnem kotu 0° . Številke poleg točk predstavljajo zaporedje skeniranja pri določenem položaju vodila. Položaji povprečnih ravnin so tukaj označeni s kvadratki.

mogoče opaziti prisotnost sistematičnih vzorcev v začetnem položaju vodila, tj. v začetni fazi postopka izmere (glej npr. S1 na razdalji 40 m). V teh primerih so izravnalne ravnine na začetku najdlje od skenerja, nato pa se mu začnejo približevati. Sčasoma se ob premikanju plošč ti vzorci izgubijo. To velja tudi za odstopanja od povprečnih ravnin, ki so majhna celo na razdalji 65 m. Na podlagi rezultatov lahko zaključimo, da povprečenje skenogramov ni imelo bistvenega vpliva na izračunane premike.

Splošen vtis, ki ga dobimo po pregledu rezultatov je, da je povprečna točnost premikov precej pod mejo 1 mm, če izključimo rezultate na razdalji 60 m in pri vpadnem kotu 60° . Za pridobitev ocene stabilnosti odstopanj od odčitkov na merski uri glede na velikost skenirane površine (in posledično glede na število točk), je bila celotna površina zmanjšana do velikosti 10 % originala. Povprečno odstopanje ostane do velikosti 20 % originalnega okna skoraj nespremenjeno, kot je razvidno iz slike 29. Če skeniramo površino z ločljivostjo 5 mm, potem znaša dimenzija okna pri 20 % ve-



Slika 29: Odstopanja od odčitkov na merski uri pri različnih nivojih redukcije točk. Rdeče točke predstavljajo absolutne vrednosti vseh odstopanj, tj. vseh vzorcev pri vseh vpadnih kotih. Modra črta nakazuje povrečno, zelena pa mediano odstopanj.

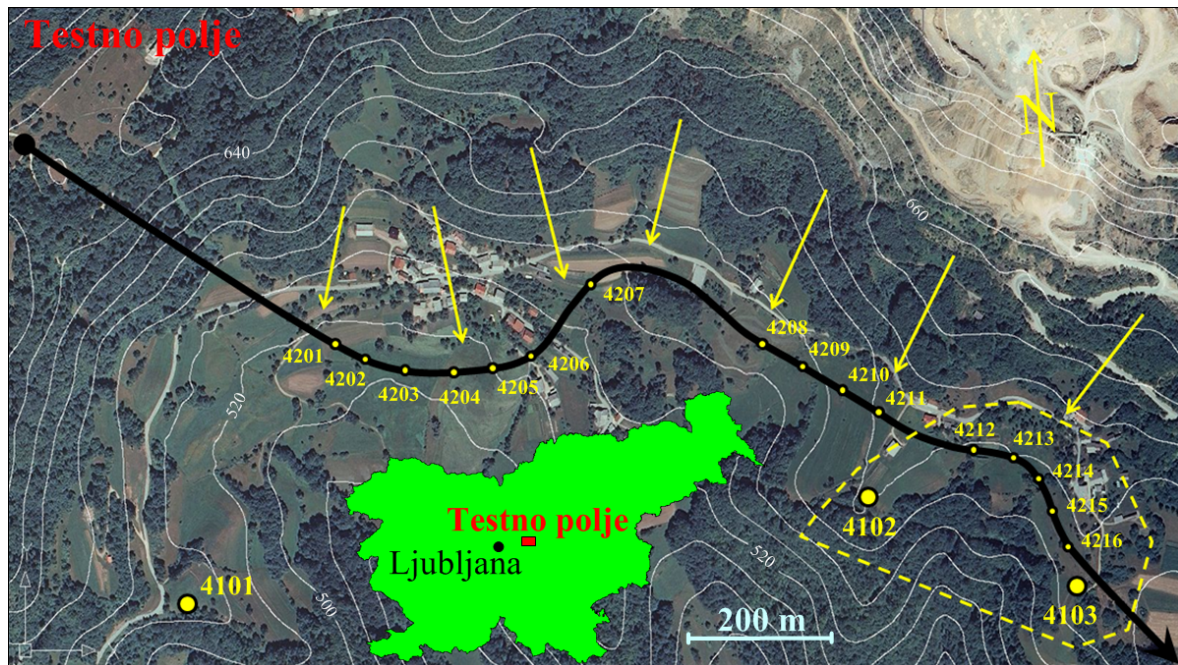
likosti originala manj kot 10×10 cm in vsebuje okoli 250 točk pri vpadnem kotu 0° , 180 točk pri kotu 45° in 100 točk pri kotu 60° . Te informacije so pomembne pri odločanju o gostoti skeniranja objektov testa v naravi 2, kjer je bil uporabljen isti skener. Z njihovo pomočjo je mogoče ugotoviti, koliko točk mora vsebovati tako majhna površinska zaplata, če hočemo premike oceniti z natančnostjo pod mejo 1 mm. Hkrati bo skener treba postaviti v bližino obravnavanega objekta (npr. $D < 50$ m) in iz končne analize deformacij izključiti točke, katerih vpadni kot presega mejo 45° . Na ta način bo stopnja občutljivosti skenerja najmanj podvržena pomanjkljivostim razdaljmera ter tako vsaj zaznava premikov velikosti 2 mm in 5 mm, če se seveda pojavijo, znotraj njegovih zmožnosti.

3.3 Test v naravi 1: Plinovod

3.3.1 Testno polje in njegove posebnosti

Plinovod, ki je bil v okviru tega raziskovalnega testa uporabljen za analizo deformacij, je del slovenske mreže za dobavo zemeljskega plina, ki ga upravlja podjetje Geoplín, največji dobavitelj zemeljskega plina v Sloveniji. Ta mreža je bila vzpostavljena z namenom oskrbe izključno industrijskih objektov s plinom, zato je pritisk v cevovodu precej visok (5000 hPa). Zaradi visokega pritiska in geomorfoloških sprememb terena je nekatere dele mreže treba kontinuirano spremljati

(enkrat letno) za morebitne premike in deformacije. Spremljanje se zdi še bolj upravičeno, saj poteka plinovod na večih od teh kritičnih lokacij blizu objektov trajne naselitve. Za testno polje je bila izmed vseh izbrana najbolj problematična lokacija, ki se nahaja okoli 30 km vzhodno od Ljubljane (slika 30). Na sliki 30 lahko vidimo, da poteka plinovod približno vzporedno s plastnicami,



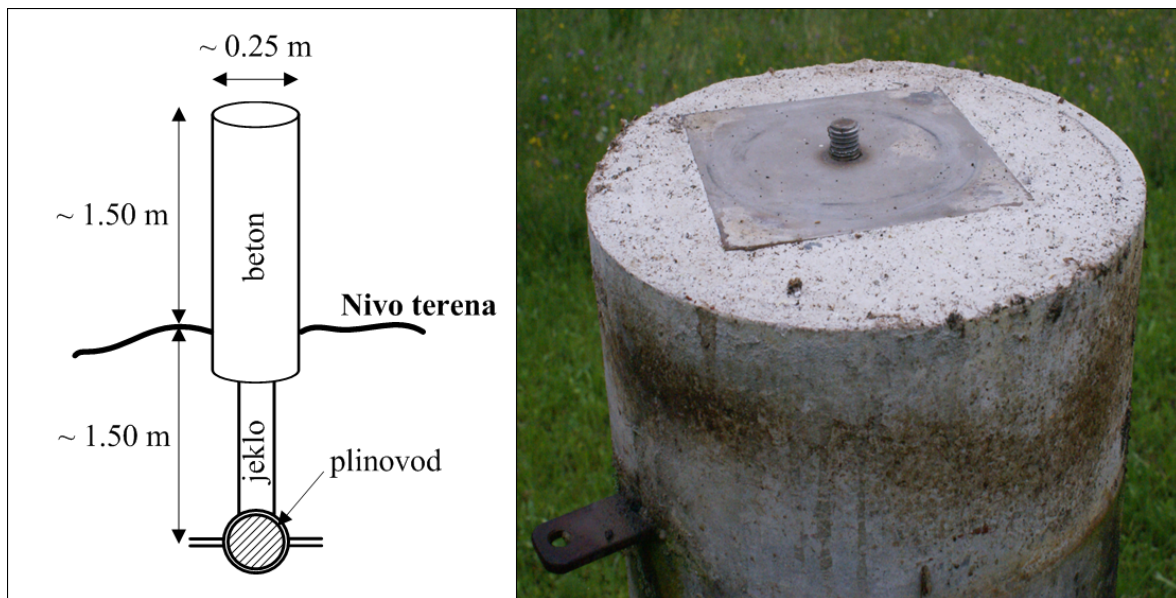
Slika 30: Ortofoto posnetek testnega polja. Zaradi velikosti testnega polja in raziskovalne narave tega raziskovalnega projekta je bilo pod drobnogled postavljen samo območje označeno s črtkano črto.

kar razkriva njegovo izredno ranljivost na pravokotne sile, ki jih povzročajo zemeljske mase nad nivojem plinovoda (označeno s puščicami). Višina terena pada od severa proti jugu, s povprečno nadmorsko višino okoli 600 m. Drsenje različnih slojev terena postane še bolj intenzivno v obdobjih močnih padavin, predvsem spomladini in v jeseni. Iz tega razloga je upravnik plinovoda v nekaterih delih že zgradil sistem drenaž za odvajanje odvečne vode.

V času njegove izgradnje konec 1970-ih, ko se je plinovod položil pod zemljo, so se hkrati za izvajanje geodetskih opazovanj vgradili posebni betonski stebri, ki so s plinovodom neposredno povezani. Na sliki 30 so ti opazovalni stebri označeni s krogci, oštreljeni od 4201 do 4216. Podrobnejši prikaz zasnove opazovalnih stebrov je mogoče videti na sliki 31. Poleg teh stebrov so bili na treh lokacijah, upoštevajoč predhodno izvedeno geološko analizo terena, postavljeni referenčni stebri 4101, 4102 in 4103 (slika 30). Ti stebri so bili stabilizirani na predvidoma stabilnih tleh, da bi lahko služili kot referenčne točke za primerjavo premikov opazovalnih stebrov, in niso povezani s plinovodom. Do izvedbe te raziskave se stabilnost referenčnih stebrov ni nikoli preverjala.

Kot je prikazano na sliki 31, je vrh tako referenčnih kot opazovalnih stebrov opremljen z vijakom in kovinsko ploščo (pri čemer vijak ni poravnан z osjo stebra), ki služita za pritrditev merskega instrumenta (npr. elektronskega tahimetra ali antene GNSS) ali reflektorja. Jekleni drog, ki opazovalni steber povezuje s plinovodom, je širok okoli 8 cm in zato domnevno dovolj tog, da se

posledično os stebra ob premikanju slojev terena ne upogiba. Tudi cev plinovoda, premera 15 cm, je iz jekla, ki mora biti dovolj prožna, da absorbira sile iz okolice. Stabilnost referenčnih stebrov se



Slika 31: Stebri za spremjanje premikov podzemnega cevovoda.

je dosedaj obravnavala s pomočjo enostavnega tahiometričnega pristopa. Položaji opazovanih točk so bili določeni iz referenčnih stebrov 4101, 4102 ali 4103, za katere se je predvidevalo, da so stabilni. Opazovane točke se nahajajo v presečišču vijakov in vrhnih ravnin opazovalnih stebrov, približno 1.5 m nad nivojem terena (slika 31). V primeru, da so stebri izpostavljeni nagibanju, ki ga povzroča drsenje zgornjih slojev terena, potem premike opazovanih točk ne moremo obravnavati kot zanesljivo merilo dejanskih premikov plinovoda pod zemljo. Nezmožnost neposrednega dostopa do plinovoda je tako prispevala k ugotovitvi, da je reprezentativne točke za analizo premikov (poglavlje 2.8.2) možno določiti izključno na osnovi modeliranja oblike nadzemnega dela opazovalnih stebrov (slika 31, levo).

3.3.2 Terenska izmera

Glede na metodologijo, predstavljeno v poglavju 2, sta bili izvedeni dve terminski izmeri, prva na začetku junija in druga na začetku novembra 2008, ki skupaj odražata šestmesečno obdobje morebitnih pojavov deformacij. Zaradi odprtosti terena in pomanjkanja zanesljivih orientacijskih točk so bila za realizacijo referenčnega sestava primernejša opazovanja GNSS. Kratko časovno obdobje med obema izmerama je narekovalo pojav predvsem manjših deformacij (v območju milimetrov). Zato se je predvidevalo, da bo ta test primeren za ovrednotenje delovne hipoteze.

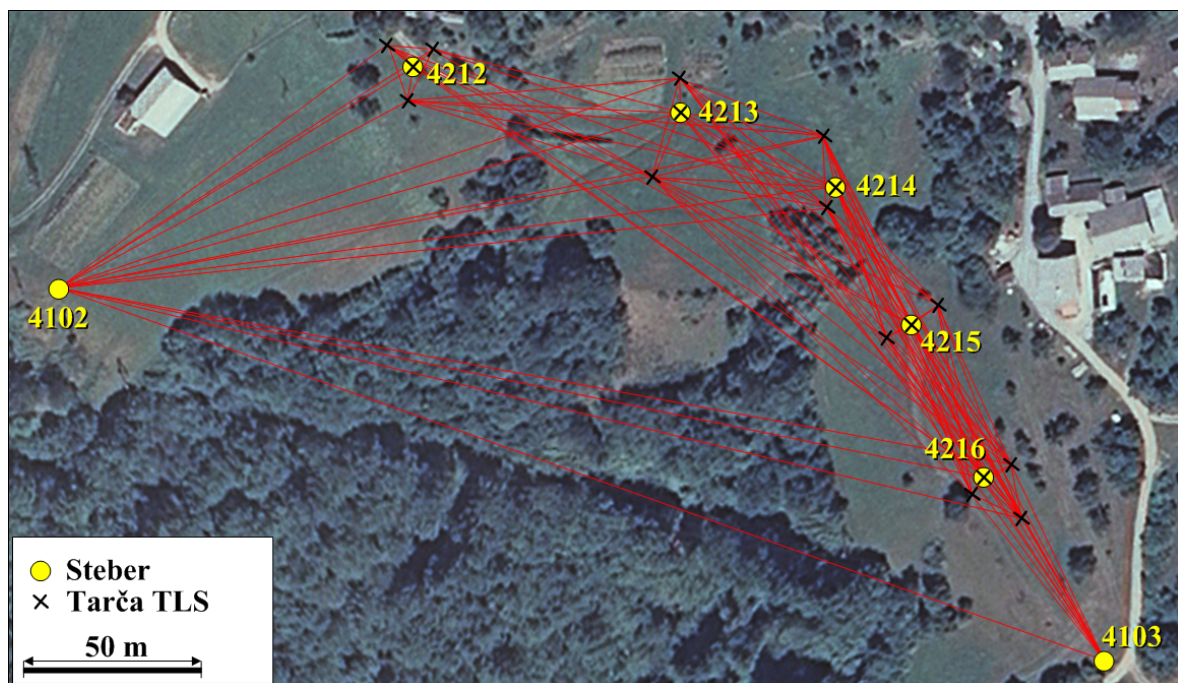
Pred izvedbo druge terminske izmere se je zaradi številnih močnih padavin v septembru in oktobru 2008 dodatno povečala verjetnost nastanka plazov na obravnavanem območju. Tudi meteorološki pogoji so bili v obeh izmerah precej različni, predvsem temperatura zraka, zato je bilo merjenje fizikalnih lastnosti atmosfere za določitev meteoroloških popravkov dolžin neizogibno.

Vrednosti izmerjenih meteoroloških parametrov iz obeh terminskih izmer so povzete v preglednici 5. Za izmero temperature zraka in psihrometrične diference je bil uporabljen precisen Assmanov psihrometer (z ločljivostjo termometra 0.1°C). Zračni tlak pa je bil izmerjen s pomočjo digitalnega barometra Paroscientific, št. modela 760-16B, z ločljivostjo 0.01 mbar in relativno natančnostjo 0.01 %. Pri prenosu metodologije na teren je postalo jasno, da bo za dosego velike natančnosti

Preglednica 5: Test v naravi 1: atmosferski parametri dveh terminskih izmer, povprečne vrednosti. Vsi atmosferski parametri so bili izmerjeni samo na strani instrumenta.

Datum izmere	Temperatura [$^{\circ}\text{C}$]	Vlažnost [%]	Zračni tlak [mbar]
Junij 2008	23.4	92.0	948.9
November 2008	-1.2	87.8	953.9

reprezentativnih točk vseh opazovalnih stebrov na sliki 30 izmera v vsakem terminu trajala več kot en dan. Ker je bil glavni namen te raziskave analizirati možnosti predlagane metodologije za potrebe spremeljanja deformacij, je bil pod drobnogled postavljen samo najvzhodnejši del testnega polja (območje, ki je na sliki 30 označeno s črtkano črto). Iz tega razloga je bilo v analizo morebitnih premikov vključenih samo pet opazovalnih stebrov (stebri 4212, 4213, 4214, 4215 in 4216). Po drugi strani so bila opazovanja GNSS izvedena na vseh treh referenčnih stebrih 4101, 4102 in 4103, saj je bila na ta način zagotovljena boljša geometrija in zanesljivejša ocena premikov. Geodetska mreža, razvita z namenom povezave oblakov točk z referenčnim sestavom in določitve položajev opazovanih točk na vrhu vsakega stebra, je prikazana na sliki 32. Za izključitev možnih pogreškov z izvorom v spremembah geometrije mreže so bile tarče TLS v obeh izmerah postavljene na skoraj enaka mesta. Z izjemo opazovalnih stebrov (slika 32) so bile tarče TLS postavljene na stative. V

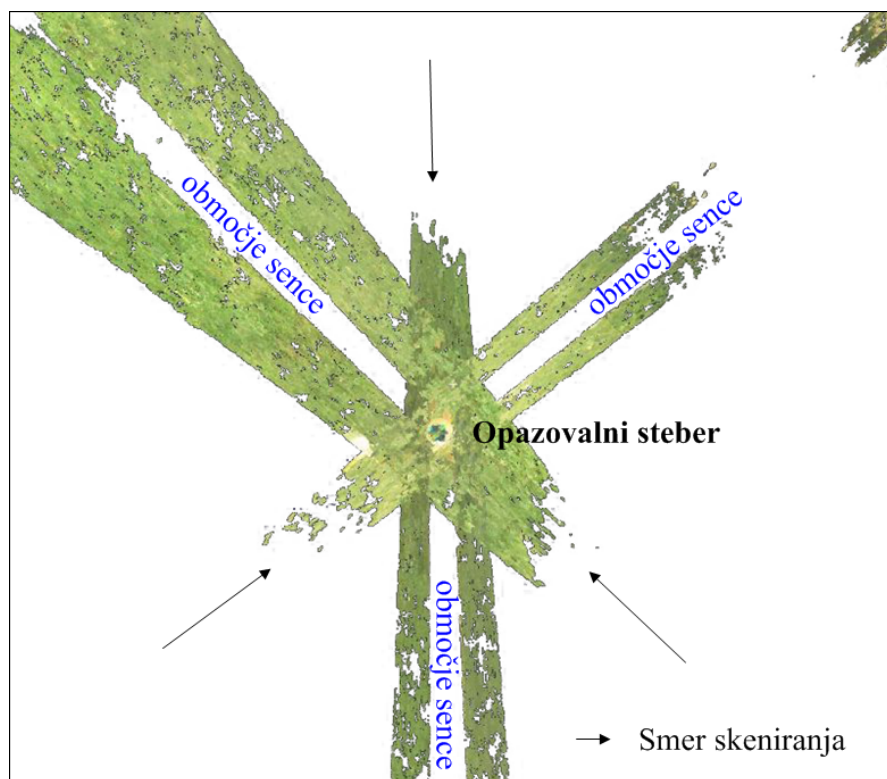


Slika 32: Geodetska mreža razvita v bližini obravnavanega objekta.

okviru klasičnih terestričnih meritev sta bila v izmeru vključena tudi referenčna steba 4102 in 4103, kar je omogočalo primerjavo izravnane dolžine 4102–4103 z rezultati opazovanj GNSS.

V geodetski mreži so bili opazovani vsi možni koti in dolžine, s skupno devetnajstimi stojišči instrumenta in v petih girusih na vsakem stojišču, kar je zagotavljalo veliko redundanco v postopku izravnave, ki bo predstavljena v poglavju 3.3.3.2. Opazovanja so bila izvedena z elektronskim tahimetrom Leica TCRP 1201, ki je opremljen s sistemom APT. Modulacijska frekvenca, adicijska konstanta, indeksni in kolimacijski pogrešek so bili predhodno preizkušeni s strani uradnega zastopnika, zato je instrument deloval po zahtevah proizvajalca. Za signalizacijo točk v mreži so bili uporabljeni reflektorji Leica GPH1P, GPR121 in GMP101. Adicijske konstante vseh reflektorjev so bile prav tako določene pred vsako terminsko izmero. Horizontiranje instrumenta in reflektorjev je bilo izvedeno s preciznimi cevnimi libelami. Po horizontiraju podnožij se le-teh ni več premikalo, da bi se s tem izognili morebitnim pogreškom centriranja.

Skeniranje je potekalo s treh različnih zornih kotov za vsak opazovalni steber (slika 33), in sicer s pomočjo skenerja Leica Scanstation 2, pri čemer so bila stojišča enakomerno razporejena okoli vseh stebrov. Na vsakem stojišču je instrument hkrati poskeniral tudi 4 do 5 ploskih Leica tarč iz slike 2 (skrajno leva). Povprečna razdalja od skenerja do stebra je bila okoli 10 m. Skeniranje je



Slika 33: Položaji skenerja glede na opazovalni steber. Sosednji oblaki točk so imeli približno 30 % preklopa.

bilo izvedeno z ločljivostjo 2 mm v obeh smereh, kar je zagotovilo izredno gosto vzorčenje površine vseh obravnavanih stebrov. V primerjavi s tahimetrom skener pred posamezno terminsko izmero ni bil kalibriran. Eden glavnih razlogov je, da je bil dobavljen s strani uradnega predstavnika podjetja

Leica v Sloveniji in je zato domnevno deloval po zahtevah proizvajalca. Koraki obdelave meritev TLS bodo predstavljeni v poglavju 3.3.3.3. V celoti je izvedba klasičnih terestričnih meritev in meritev TLS na terenu trajala ves dan.

V vsaki terminski izmeri je bila kmalu po izvedbi klasične terestrične metode in skeniranja na referenčne stebre nameščena merska oprema GNSS. Opazovanja GNSS so se nato nepretrgoma nadaljevala še naslednja 2 do 3 dni s pomočjo dvofrekvenčnih sprejemnikov Trimble 4000 SSE/SSI z antenami z antensko ploščo Trimble Compact L1/L2 oziroma Trimble Geodetic L1/L2. Minimalni višinski kot je bil izbran na podlagi priporočil za zelo natančno obdelavo (ki jih najdemo v IGS, 2009 in EPN, 2009) in lastnosti programske opreme (Dach in sod., 2007). Med izmero je bil višinski kot nastavljen na 0° , in sicer zaradi ocene parametrov troposfere in višin z visoko zanesljivostjo (Even-Tzur in sod., 2004). Interval registracije je bil nastavljen na 15 s. V preglednici 6 so povzete vse lastnosti obeh terminskih izmer. Podnožja na stebrih 4102 in 4103, ki so bila

Preglednica 6: Lastnosti terminskih izmer GNSS.

Datum izmere	Min. višinski kot/Interval registracije	Trajanje
Junij 2008	$0^\circ/15$ s	48 ur
November 2008	$0^\circ/15$ s	72 ur

predhodno uporabljena za klasične terestrične meritve, so bila odstranjena šele po zaključku opazovanj GNSS, ponovno zaradi preprečitve vnosa pogreškov centriranja pri menjavi instrumentov. V obeh izmerah je bilo zbranih dovolj opazovanj GNSS za določitev položaja z veliko natančnostjo.

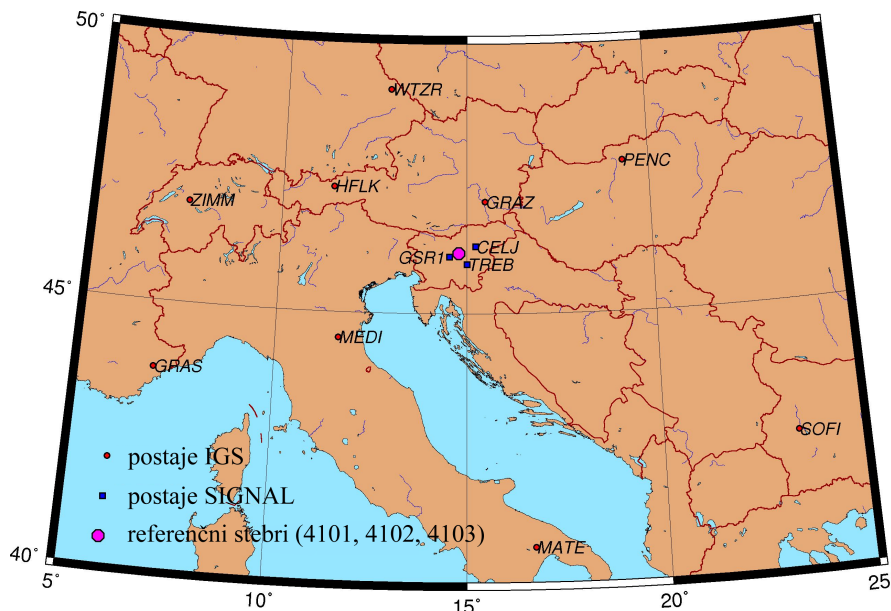
3.3.3 Rezultati

Po zaključku terenskih izmer je bilo v naslednjem koraku treba surove meritve obdelati, da bi na ta način dobili vhodne podatke za deformacijski model 2 (reprezentativne točke, poglavje 2.8.2). Alternativni model (model z omejeno smerjo iz poglavja 2.8.1) v primeru tega testa ni bil uporabljen. Meritve vsake merske tehnologije so bile obdelane ločeno. Najprej je bilo na podlagi opazovanj GNSS treba dolotočiti koordinate referenčnih stebrov. Slednje so bile nato vključene v izravnavo klasičnih terestričnih meritev, katere rezultat so bili položaji tarč TLS za izvedbo absolutne orientacije oblakov točk ter opazovanih točk na vrhu stebrov. V zadnjem koraku je bila v okviru izravnave modelirana še oblika stebrov. V naslednjih podpoglavljih bodo posebnosti obdelave posamezne, v izmero vključene tehnologije bolj podrobno opisane.

3.3.3.1 Opazovanja GNSS

Upoštevajoč priporočila iz poglavja 2.2, je bila realizacija referenčnega sestava na homogen način zagotovljena z vklopom referenčnih točk (korak 1 splošnega pristopa, poglavje 2.1) v globalno mrežo IGS permanentnih postaj GNSS. Za širšo lokalno stabilnost referenčnega sestava so bile v

obdelavo opazovanj vključene tudi bližnje postaje GNSS, ki pripadajo slovenski mreži permanentnih postaj, imenovani SIGNAL (2009). V naslednjem koraku se je bilo treba odločiti, katere od teh postaj bodo obravnavane kot referenčne in katere kot kontrolne. Kriterij izbora je temeljal na datumu vzpostavitve postaje, njeni lokaciji in kakovosti, kot so predlagali Bergeot in sod. (2009). Permanentne postaje GRAS, MATE, PENC, SOFI, WTZR in ZIMM so bile izbrane za referenčne, medtem ko so bile ostale obravnavane kot kontrolne postaje. ITRF2005 (Altamimi in sod., 2007) je bil izbran za referenčni koordinatni sestav (ITRF, 2009). Lokacije vseh permanentnih postaj, ki so bile vključene v obdelavo opazovanj GNSS, so prikazane na sliki 34. V vsaki terminski izmerti



Slika 34: Lokacije permanentnih postaj GNSS.

so bili podatki obdelani v enem koraku, in sicer na osnovi linearne kombinacije z odstranjениm vplivom ionosfere ter neznanim številom celih valov, določenim v območju celih števil. Za obdelavo podatkov je bil uporabljen program Bernese GPS Software, verzija 5.0 (Dach in sod., 2007). Plimovanje čvrste zemlje in vodnih mas oceanov je bilo vključeno po priporočilih McCarthyja in Pettita (2009), s koeficienti plimovanja vodnih mas pridobljenimi od Onsala Space Observatory (2009) in obdelanimi po modelu GOT00.2. Sledilo je modeliranje odstopanj faznih centrov anten na osnovi relativnih kalibracijskih parametrov, ki jih zagotavlja IGS. Vpliv troposfere je bil za vsako uro ocenjen po apriori modelu Saastamoinena in Niellovi projekcijski komponenti troposferske refrakcije (Niell, 1996). Končna rešitev, ki je temeljila na prosti izravnavi, je vključevala tudi modeliranje azimutno anizotropnega vpliva troposfere s pomočjo gradientne metode (Dach in sod., 2007).

Neznano število celih valov, določeno v območju celih števil, je bilo ocenjeno na osnovi dveh postopkov. Pri kratkih baznih vektorjih (do 150 km) je bil uporabljen postopek SIGMA (Dach in sod., 2007), in sicer v dveh korakih; najprej na linearni kombinaciji širokega pasu (L5), nato pa še na obeh nosilnih valovanjih, tj. L1 in L2, glede na neznano število celih valov linearne kombinacije širokega pasu. Daljši bazni vektorji so bili obravnavani v okviru postopka QIF (Mervat, 1995).

Kot rečeno, so bile končne koordinate v obeh izmerah ocenjene v referenčnem sestavu ITRF2005. Zaradi tektonskih premikov evrazijske plošče so bile ocenjene vrednosti koordinat transformirane v ETRF89 (Boucher in Altamimi, 2008). V zadnjem koraku so bile 3-razsežne geocentrične koordinate ETRF89 transformirane še v državne ravninske koordinate (npr. v transverzalno Mercatorjevo projekcijo), kjer jih je bilo mogoče v nadaljevanju uporabiti za klasično terestrično izmero (korak 2 splošnega metodološkega pristopa). Za zagotovitev idenčnih koordinat v obeh izmerah, ki bi se nato lahko uporabile za obdelavo klasičnih terestričnih meritev in meritev TLS, so bile novembrske vrednosti položajev točk 4102 in 4103 togo premaknjene na junijске. V preglednici 7 so za obe terminski izmeri podane ocenjene vrednosti koordinat referenčnih stebrov, in njim pripadajoče standardne deviacije, v državni kartografski projekciji. Višine točk v mreži so bile določene v

Preglednica 7: Ocenjene vrednosti koordinat referenčnih stebrov.

Steber	E [m]	σ_E [mm]	N [m]	σ_N [mm]	Datum izmere
4101	482 459.5975	1.0	108 430.2116	2.0	jun 2008
	482 459.6140	1.0	108 430.1959	1.0	nov 2008
4102	483 370.3219	1.0	108 571.3014	2.0	jun 2008
	483 370.3219	1.0	108 571.3017	1.0	nov 2008
4103	483 681.1483	1.0	108 464.2422	2.0	jun 2008
	483 681.1483	1.0	108 464.2419	1.0	nov 2008

okviru trigonometričnega višinomerstva (poglavlje 3.3.3.2), zato v preglednici 7 niso podane. Standardne deviacije v preglednici 7 so rezultat množenja natančnosti koordinat iz programa Bernese GPS Software (verzija 5) s faktorjem 10, kot predlagajo Mao in sod. (1999).

3.3.3.2 Klasična terestrična izmera

Z izvedbo klasičnih terestričnih meritev v petih girusih je bilo v prvem koraku obdelave treba izračunati srednje vrednosti posameznih opazovanj. Za ustrezno redukcijo poševnih dolžin so se na osnovi, s psihrometrom in barometrom izmerjene temperature, zračnega tlaka in delnega tlaka vodne pare, izračunali meteorološki popravki dolžin. Za izračun delnega tlaka vodne pare je bila uporabljena Sprungova enačba za Assmanov aspiracijski psihrometer. Nasičeni tlak vodne pare je bil določen glede na Magnus-Tetenovo enačbo. Referenčni in dejanski lomni količnik atmosfere pa sta bila izračunana po Ciddor (1996) ter Ciddor in Hill (1999). V postopku redukcije dolžin za meteorološke popravke je bil upoštevan samo prvi popravek hitrosti. Drugi popravek hitrosti se je zanemaril, saj njegova vrednost na razdalji 400 m znaša približno 10^{-5} mm.

Poleg tega se je iz postopka redukcije dolžin izpustil tudi popravek zaradi ukrivljenosti merskega žarka, ki na razdalji 400 m (kar je več od najdaljše izmerjene dolžine) znaša okoli 10^{-6} mm. Popravljene vrednosti dolžin so se nato s pomočjo izmerjenih višin instrumenta in reflektroja reducirale na nivo stebrov. Za razliko od stebrov se pri pritrditvi merske opreme na stativ višina instrumenta oz. reflektorja ni izmerila. V zadnjem koraku so bile dolžine reducirane na ploskev

referenčnega elipsoida (ničelni nivo) in nato še v ravnino državne kartografske projekcije. Prvo od teh redukcij je bilo možno izvesti šele po predhodni določitvi višinskih razlik med točkami mreže. Vrednosti višinskih razlik so bile določene v okviru trigonometričnega višinomerstva. Izračunane višinske razlike so se v postopku MNK izravnale, pri čemer je bila točka 4102 izbrana za referenčno. Na ta način so se pridobile nadmorske višine točk v mreži in njim pripadajoči parametri natančnosti. Glede na rezultate lahko ugotovimo, da je povprečna standardna deviacija višin v prvi izmeri znašala 0.5 mm, v drugi pa 0.4 mm. Za določitev pravilnih višin tarč TLS, ki služijo za absolutno umestitev oblakov točk, je bilo treba upoštevati še vertikalno ekscentriteto med reflektorjem.

Končna faza obdelave klasičnih terestričnih meritev je vključevala izravnavo (po MNK) vseh izmerjenih in ustrezno reduciranih merskih količin za oceno položajnih koordinat točk v mreži. Vsem kotom so bile pripisane enake uteži, saj se pogoji znotraj posamezne terminske izmere niso bistveno spremenjali. Enake uteži so bile dodeljene tudi dolzinam v mreži, predvsem zato, ker so bile relativno kratke in izmerjene s skoraj enako natančnostjo. Opazovanja so bila najprej izravnana v obliki proste mreže z minimalno sledjo matrike kofaktorjev koordinatnih neznank. Samo na ta način je mogoče določiti natančnosti izmerjenih količin neodvisno od datuma mreže. Hkrati je bil za ugotavljanje prisotnosti grobih pogreškov uporabljen Baardov Data Snooping, ki zagotavlja informacije o notranji in zunanji zanesljivosti mreže (Caspary, 1988). V drugem koraku je bila izravnava ponovljena, tokrat s točko 4102 privzeto kot dano ter orientacijskim kotom iz 4102 na 4103. Ti dve referenčni točki glede na ugotovitve obdelave opazovanj GNSS med obema izmerama nista bili izpostavljeni premikom (glej poglavje 4.1.1). Rezultati končne izravnave so podani v preglednici 8.

Preglednica 8: Rezultati izravnave z minimalnim številom datumskih parametrov: aposteriori standardne deviacije, natančnosti izravnanih vrednosti opazovanj in položajne natančnosti točk v mreži.

Datum	$\hat{\sigma}_0$	$\hat{\sigma}_{Hz} ["]$	$\hat{\sigma}_D [\text{mm}]$	$\hat{\sigma}_{\text{pos,max}} [\text{mm}]$	$\hat{\sigma}_{\text{pos,min}} [\text{mm}]$	$\hat{\sigma}_{\text{pos,avg}} [\text{mm}]$
Jun 2008	0.99994	1.4	0.5	0.3	0.2	0.2
Nov 2008	1.00002	1.3	0.4	0.2	0.1	0.2

3.3.3.3 Terestrično lasersko skeniranje

Začetna faza obdelave podatkov TLS je zajemala umeščanje oblakov točk (poglavlje 2.5). Povprečna natančnost absolutne orientacije v obeh izmerah je znašala $\sigma_{AO} = 1 \text{ mm}$. Spomnimo, da je bilo v tem testu ocenjevanje centrov tarč izvedeno na osnovi amplitudno uteženega povprečja, in sicer s pomočjo tarčam prilagojenega načina skeniranja, ki proizvede gost vzorec točk izključno osrednjega dela tarče. Z uporabo tega načina skeniranja se sočasno upošteva tudi pogrešek izmerjene dolžine na podlagi v skener vgrajenih korekcijskih faktorjev, ki jih določi proizvajalec. Zaradi tega predhodno

ni bilo treba izvesti dodatnih testov za oceno in modeliranje dolžinskih napak, kot npr. v primeru Rieglovega skenerja. Odsotnost kakršnih koli večjih sistematičnih pogreškov v postopku absolutne orientacije je bila potrjena z obsežno vizualno analizo v območjih preklopa med sosednjimi oblaki točk. Po umestitvi oblakov so se točke, ki niso pripadale površini stebra, ročno odstranile iz skenogramov. Oblaki točk za posamezen steber so tako vsebovali okoli 250 000 točk, ki so se uporabile za modeliranje oblike stebrov.

Glede na korak 6 splošnega metodološkega pristopa so se stebri v okviru metode najmanjših kvadratov modelirali na podlagi modela valja, ki je opisan v Luhmann in sod. (2006). Za določitev parametrov valja potrebujemo najmanj 5 točk, pri čemer se minimizirajo pravokotne razdalje točk $P_i(x_i, y_i, z_i)$ od pripadajoče izravnalne ploskve (glej sliko 35):

$$d_i = r_i - r \quad (23)$$

kjer je:

$$r_i = \frac{\sqrt{u_i^2 + v_i^2 + w_i^2}}{\sqrt{a^2 + b^2 + c^2}} \quad (24)$$

in:

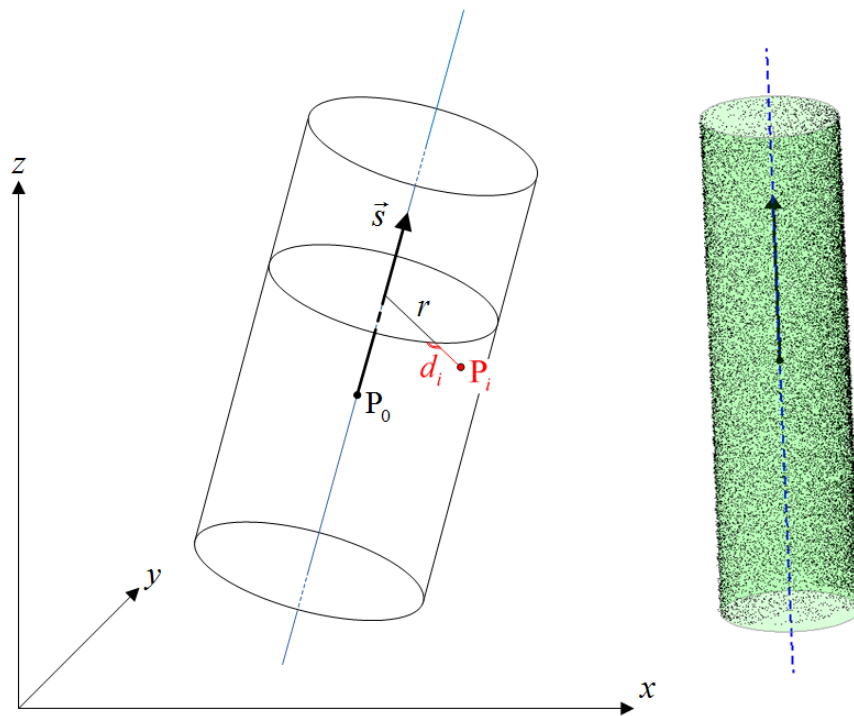
$$\begin{aligned} u_i &= c \cdot (y_i - y_0) - b \cdot (z_i - z_0) \\ v_i &= a \cdot (z_i - z_0) - c \cdot (x_i - x_0) \\ w_i &= b \cdot (x_i - x_0) - a \cdot (y_i - y_0) \end{aligned} \quad (25)$$

Kljub temu, da je valj določen s:

- točko na osi: $P_0(x_0, y_0, z_0)$,
- smernim vektorjem: $\vec{s}(a, b, c)$,
- polmerom: r ,

je samo pet od teh parametrov linearne neodvisnih (x_0, y_0, a, b, r) . Ker je minimizacijska funkcija d nelinearna, se neznani parametri ocenijo na iterativen način. Iz rezultatov izravnave je razvidno, da je povprečna aposteriori ocena za vse stebre v obeh terminskih izmerah znašala 1.3 mm ($\hat{\sigma}_{0,\min} > 1.1$ mm, $\hat{\sigma}_{0,\max} < 1.5$ mm). Vse te vrednosti so precej pod nivojem šuma, ki ga za ta skener podaja njegov proizvajalec (2 mm). Na podlagi histogramov popravkov d_i je hkrati možno ugotoviti, da v obdelavo podatkov niso bili vključeni grobi pogreški, kar je bilo potrjeno z Gaussovo porazdelitvijo popravkov obravnavanih točk. Prostorska razporeditev vektorja popravkov nakazuje, da je izbira stojišč skenerja (kot je prikazano na sliki 33) dejansko ublažila vpliv največjih pogreškov posameznega skenograma v smeri skeniranja, kar je ena od slabosti impulznih skenerjev. Na ta način so imeli vplivi pogreškov dolžin bolj ali manj homogen učinek na izračunane parametre valja. Ta učinek je na primeru stebra 4212 prikazan na sliki 36, ki prikazuje prostorsko razporeditev vektorja popravkov in njegovo shematično razlago. Enak rezultat je bil opažen tudi na drugih opazovalnih stebrih. Analiza prostorske razporeditve vektorja popravkov v območjih preklopa je zagotovila dodatno potrditev kakovosti absolutne orientacije, kar pomeni, da je bilo umeščanje izvedeno brez prisotnosti sistematičnih pogreškov.

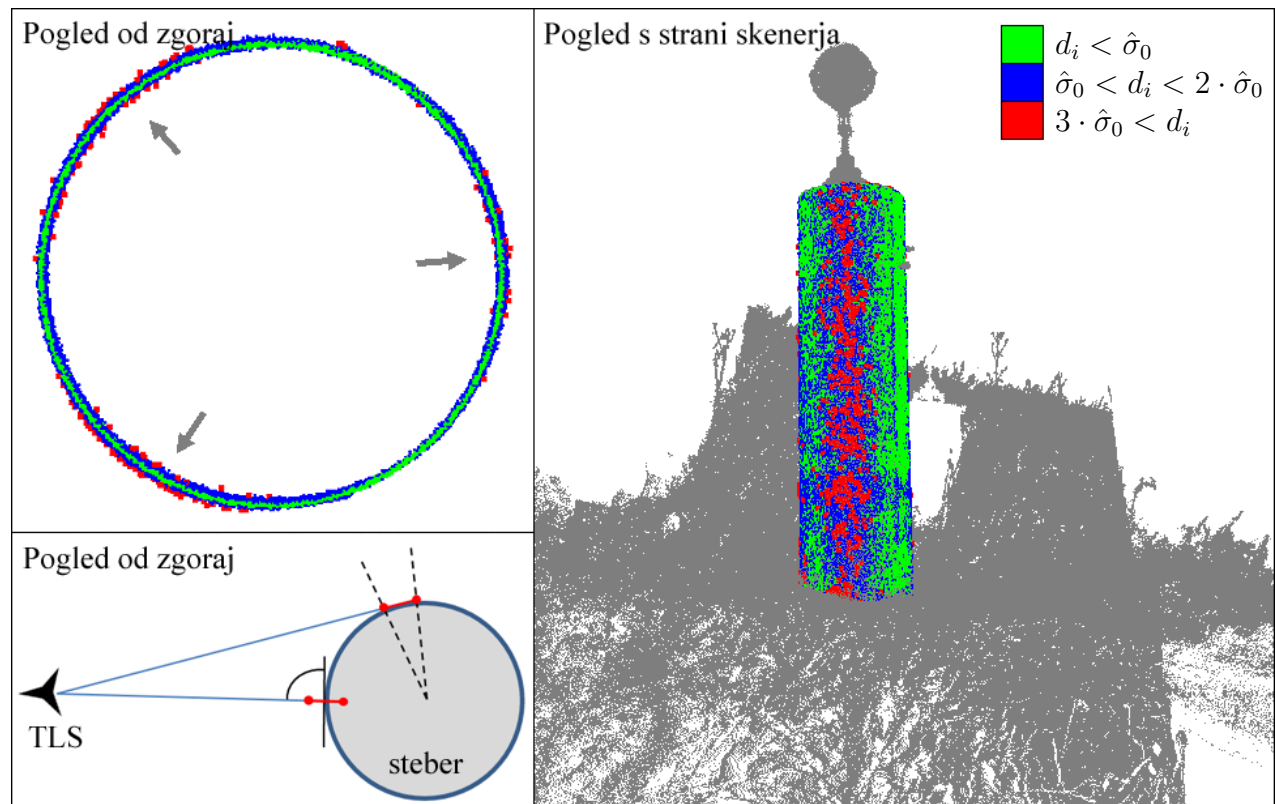
V naslednjem koraku je bila raziskana pravilnost modela. Pri pregledu merit kakovosti izravnave



Slika 35: Parametri valja, določeni v postopku izravnave (levo) in primer rezultata iz programa MATLAB, ki prikazuje ocenjeno os valja (desno; samo vsaka 100-ta točka je izrisana).

(vektorjev popravkov) lahko glede tega povzamemo, da oblika stebrov ni povsem valjasta, ampak so prisotne majhne sistematične napake, ki ne presegajo ± 1.5 mm. Kljub majhnim velikostim so te napake postale očitnejše pri prehodu v cilindrični koordinatni sistem (Θ, z, d_i) , kjer je bilo lažje ugotoviti, da so stebri nekoliko (ne povsem) eliptični, in sicer v azimutalni smeri. Po višini se nekateri stebri od vrha navzdol razširijo, medtem ko so drugi bolj konveksne oblike. Na tako majhnem velikostnem nivoju odstopanj nobenega od prostorskih vzorcev popravkov ni možno opisati z enostavnim matematičnim modelom. Na splošno je bilo pri stebru 4212 opaziti največja, medtem ko pri stebrih 4215 in 4216 najmanjša odstopanja. Steber 4212 je hkrati imel tudi najbolj očiten eliptičen vzorec v azimutalni smeri.

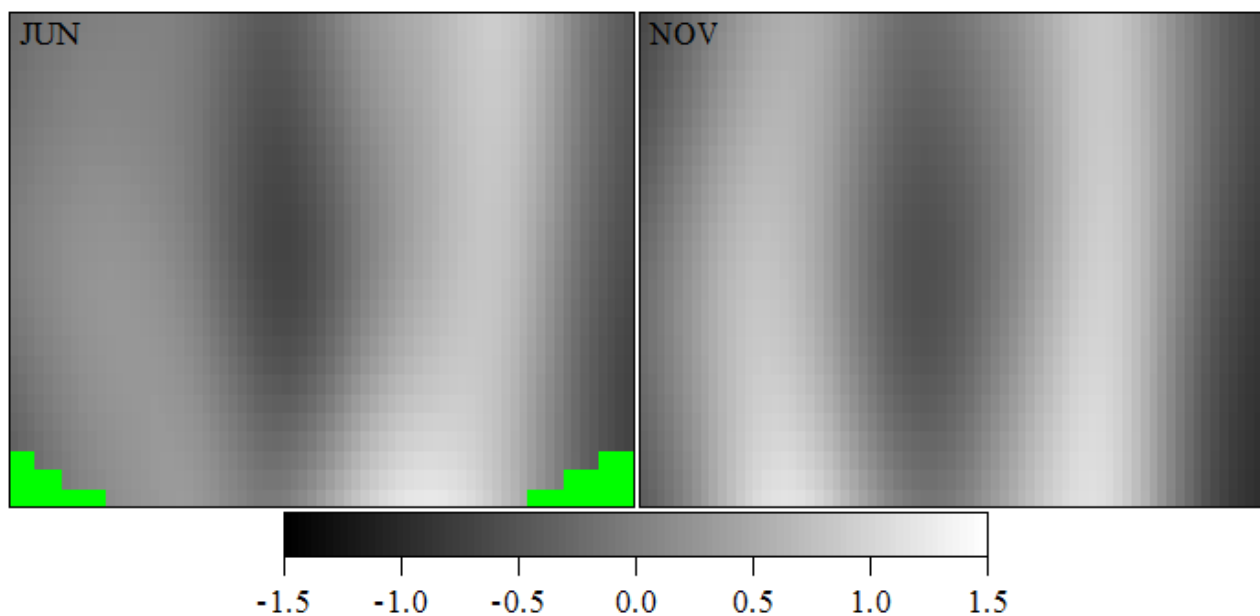
Z vidika časovne stabilnosti so bili vzorci popravkov posameznih stebrov v obeh izmerah skladni, zato so na parametre valja vplivali na enak način. Posledično lahko povzamemo, da se dejanska oblika nadzemnega dela opazovalnih stebrov ni deformirala zaradi kakršnih koli zunanjih vplivov. Skladnost posameznih vzorcev ni bila testirana samo vizualno, ampak tudi z odštevanjem parov mrežnih modelov (novembrskega in junijskoga), ki so bili izdelani na osnovi cilindričnih koordinat ustreznih oblakov točk. Slika 37 prikazuje tašna dva mrežna modela za steber 4212 z velikostjo celice 5 cm. Pred odštevanjem so bili posamezni mrežni modeli zglajeni z Gaussovim filtrom, saj je bilo na ta način možno ohraniti dejanski trend (odstopanja od valja) in se hkrati izogniti lokalnim nepravilnostim, ki izvirajo iz merskih pogreškov. Modela na sliki 37 sta rezultat uporabe tega filtra in razkrivata skoraj eliptično površino stebra 4212. Po odštetju mrežnih modelov so bile preostale razlike globoko v območju pod mejo enega milimetra, s čimer lahko zaključimo, da se oblika ni spremenila. Ostalo pa je vprašanje, ali so ocenjene vrednosti parametrov valja odvisne od določene



Slika 36: Primer prostorske razporeditve vektorja popravkov (desna slika). Največje vrednosti popravkov so v smereh skeniranja, ki so nakazane s puščicami na sliki levo zgoraj. Kljub podobni (ne)natančnosti dolžin je minimizacija pravokotnih razdalj r_i vodila do manjših vrednosti popravkov proti robovom stebrov (slika levo spodaj).

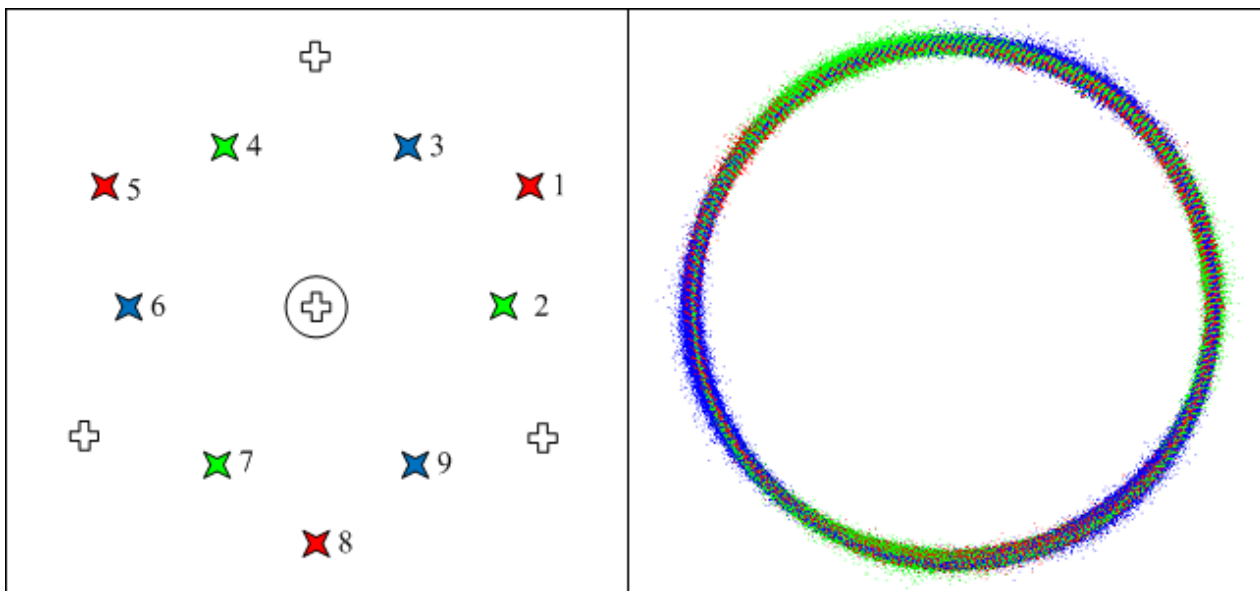
smeri skeniranja. V obeh izmerah so bile lokacije stojišč skenerja skoraj, a ne povsem enake. Da bi dobili odgovor na to vprašanje, je bila na mestu stebra 4212, ki je od modela valja najbolj odstopal, izvedena dodatna izmera. Če ima smer skeniranja kakršen koli vpliv, potem se ga bo opazilo pri stebri 4212.

Rezultat dodatne izmere so predstavljali oblaki točk, zajeti z devetih ločenih stojišč, enakomerno razporejenih okoli stebra. Površina stebra je bila skenirana z enako ločljivostjo (2 mm) kot v obeh predhodnih izmerah. Z vidika obdelave podatkov je bila tokrat edina razlika v tem, da je bilo treba koordinatni sistem enega od stojišč izbrati za referenčnega. Pri dodatni izmeri namreč analiza ne zahteva absolutnega položaja oblakov točk. Po drugi strani je bila relativna orientacija izvedena v dveh zaporednih korakih. Najprej so se transformacijski parametri ocenili s pomočjo enačb, predstavljenih v poglavju 2.5, in sicer ob uporabi štirih tarč, ki so bile skenirane na vsakem stojišču. Nato so se vsi oblaki točk in vsi ocenjeni centri tarč transformirali v referenčni sistem, da bi jih lahko uporabili kot vhodne podatke za drugi korak. V drugem koraku se je relativna orientacija ponovno izvedla ob pomoči postopka ICP (Besl in McKay, 1992), v okviru katerega se je ocenilo skupno 60 neznank. Poleg transformacijskih parametrov (48 neznank za 8 stojišč) so se v tej končni izravnavi, ki je sočasno vključevala meritve vseh stojišč, ocenile tudi koordinate tarč (dodatnih 12 parametrov).



Slika 37: Mrežni model vektorja popravkov za 4212. Zelena barva predstavlja manjkajoče podatke zaradi visoke vegetacije v junijski terminski izmeri.

Uporaba postopka ICP je bila koristna, saj je MNK sedaj minimizirala ne samo koordinatne razlike tarč, ampak tudi odstopanja med pari točk (na strani objekta) vzdolž smeri normalnih vektorjev. Iz tega razloga je bilo treba predhodno v vsaki točki oceniti normalni vektor. Izravnava se je zaključila po dvajsetih iteracijah z aposteriori standardno deviacijo $\hat{\sigma}_0 = \sigma_{\text{RO}} = 0.5$, ocenjeno na osnovi zelo visoke redundance zaradi velike količine točk na površini stebra. Rezultati algoritma ICP in razporeditev stojišč dodatne izmere so prikazani na sliki 38. Po zaključku relativne orientacije so bili



Slika 38: Razporeditev stojišč (pogled od zgoraj s stebrom v sredini) in rezultati ICP. Zvezde označujejo položaje stojišč, medtem ko križi predstavljajo položaje tarč.

po enačbah 23–25 za štiri razporeditve stojišč izračunani parametri valja. Rezultati teh izravnava so podani v preglednici 9. Prve tri razporeditve so bile izbrane zato, ker simulirajo podobne merske

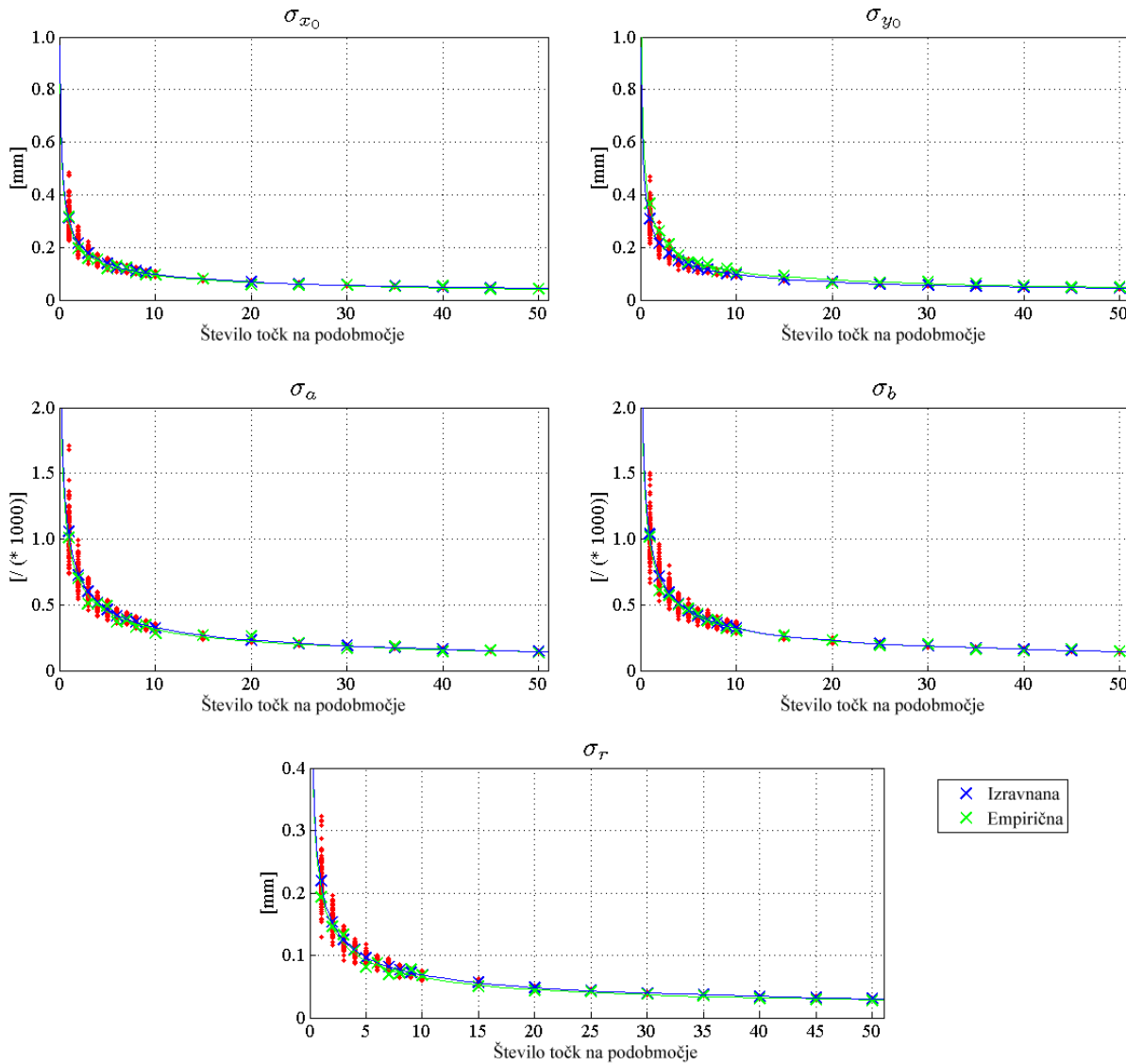
Preglednica 9: Rezultati izravnave ocenjeni na osnovi štirih razporeditev stojišč. Koordinate P_0 med sabo niso primerljive, saj so odvisne od razporeditve točk. D je razdalja od stojišča do stebra.

Razporeditev	D [m]	a	b	c	r [m]	$\hat{\sigma}_0$ [mm]
1,5,8	12	-0.08368	0.03192	0.99598	0.1254	1.4
2,4,7	8	-0.08377	0.03193	0.99597	0.1255	1.5
3,6,9	8	-0.08376	0.03196	0.99597	0.1257	1.6
1-9	/	-0.08373	0.03193	0.99598	0.1256	1.5

pogoje kot v junijski in novembrski izmeri (tj. tri stojišča na steber s preklopom $\approx 30\%$, glej sliko 33). Zadnjo razporeditev lahko obravnavamo kot kontrolno, saj pokaže, da uporaba vseh oblakov točk v postopku izravnave valja, ne vpliva na izravnane vrednosti. Glede na rezultate v preglednici 9 lahko izpeljemo pomemben zaključek te analize, ki potrjuje, da v obeh terminskih izmerah os valja (katerega koli opazovalnega stebra) najverjetnejše ni bila podvržena vplivom sprememb geometrije skeniranja. V primerjavi s tem testom so bile razlike v geometriji skeniranja v junijski in novembrski izmeri veliko manjše, saj je bila vzpostavitev enakih snemalnih pogojev upoštevana kot del priporočil splošnega metodološkega pristopa (poglavlje 2.1). Komponente smernega vektorja a , b in c , ki igrajo ključno vlogo v končni analizi premikov, se od prve do zadnje razporeditve zelo malo razlikujejo. Posledično velja, da tudi v primeru, če bi bile spremembe parametrov osi v junijski in novembrski izmeri tako velike kot tiste iz preglednice 9, te spremembe ne bi imele nobenega vpliva na izračun reprezentativnih točk, ki bo predstavljen v poglavju 4.1.2.

V zadnjem delu obdelave podatkov TLS je bilo treba oceniti zanesljive mere natančnosti parametrov valja na podlagi velike redundance točk, kar je bilo nakazano v poglavju 2.7.2. Ob uporabi vseh točk v izravnavi dobimo preko zakona o prenosu pogreškov zelo očitno preoptimistično oceno za Σ_{xx} . Vse tako določene standardne deviacije so namreč pod mejo $10 \mu\text{m}$, s smernimi kosinusi, ki so brez enot, ocenjenimi najbolj natančno. V naslednjem koraku se je postopek izravnave ponovil, tokrat le z osmimi točkami na steber (štirimi na vrhu in štirimi pri dnu vsakega oblaka točk z enakomerno radialno razporeditvijo), da bi tako pridobili prvi vtis o velikosti faktorja precenjenosti. Glede na postopek, opisan v poglavju 2.7.2, so bili nato oblaki točk posameznega stebra razdeljeni na manjša podobmočja, izravnava pa ponovljena v osemnajstih zaporednih korakih. V vsakem koraku so bili modelni parametri ocenjeni iz stotih vzorcev, sestavljenih na osnovi naključnega izbora enakega števila točk iz vsakega podobmočja. Število točk na podobmočje in na korak je bilo $n_{i,i=1\dots 18} = 1, 2, 3 \dots 10, 15, 20 \dots 50$. Glede na dimenzijske podobmočje je bila izravnava izvedena z dvema različnima velikostima. Najprej so bili oblaki točk razdeljeni na večja, nato pa še na manjša podobmočja, da bi lahko ugotovili, ali ima to kakršen koli vpliv na rezultate. Izkazalo se je, da oba pristopa izravnave (8 točk, naključno vzorčenje) kažeta v smeri redukcije parametrov natančnosti valja za faktor 100. Na ta način sta bili določeni zgornja in spodnja meja, kar uokvirja

kakovost izravnanih količin in ponuja bolj trdno in zanesljivo osnovo za analizo deformacij. Analiza je hkrati pokazala, da povečevanje števila točk preko meje 35 točk na podobmočje ne prinaša bistvenih sprememb, saj postane korelacija med točkami tako močna, da se posamezne ocene parametrov ne spreminja več. Ne nazadnje postane po uporabi faktorja precenjenosti jasno, da so mere natančnosti parametrov valja precej primerljive z rezultati klasične terestrične metode, kljub očitni razliki v zmogljivosti instrumentov. Na sliki 39 so prikazani rezultati opisanega postopka na primeru stebra 4216. Enaki rezultati so bili pridobljeni tudi pri ostalih stebrih. Nazadnje so bile



Slika 39: Standardne deviacije parametrov valja po vzorčenju. Rdeče točke predstavljajo rezultate stotih naključno izbranih vzorcev v vsakem koraku. Modri križci označujejo povprečne vrednosti standardnih deviacij iz izravnav stotih naključno izbranih vzorcev. Zeleni križci pa predstavljajo standardne deviacije ocenjenih vrednosti parametrov valja, tj. empirične standardne deviacije. Izmed parametrov valja polmer ne bo vključen v deformacijski model, predstavljen v zadnjem poglavju.

v izravnavo vključene še uteži. Te so bile določene z upoštevanjem zgolj vpadnega kota α , ki se

je neprimerno bolj spremenjal od dolžin, za katere se je predvidevalo, da so bile izmerjene z bolj ali manj enako natančnostjo. Po vključitvi uteži $p_i = \cos(\alpha)$ se rezultati analize vzorčenja niso spremenili, kar velja tudi za parametre valja. Smerni vektorji osi ostajajo daleč najbolj natančno določeni parametri. S tega vidika je bila v testu 1 uporaba metode TLS smiselna, zlasti če analiziramo samo trende nagibanja stebrov, kar omogoča boljše razumevanje vplivov drsenja terena na opazovalne stebre. Na podlagi izračunanih nagibov je hkrati mogoče ugotoviti, ali premiki opazovanih točk na vrhu stebrov odražajo dejansko premikanje plinovoda.

3.4 Test v naravi 2: Podporni zid

3.4.1 Testno polje in njegove posebnosti

V primerjavi s testom 1 so bile posebnosti tega testa v mnogih pogledih različne, kar je bilo omenjeno že na začetku tega poglavja. Glede na to dejstvo bo tudi sposobnost metode TLS za odkrivanje majhnih premikov in deformacij testirana še en korak naprej.

Na začetku leta 2010 se je na slovenski obali pričela gradnja predora z namenom vzpostavitev manjkajoče povezave med dvema že zgrajenima deloma avtocesto, ki bo povezala osrednjo Slovenijo s hrvaško obalo. Ker je območje nad izkopom gosto poseljeno, je bila sprejeta odločitev o spremeljanju vplivov izkopa ne samo v notranjosti predora, ampak tudi na površju. Spremljanje na površini vključuje vse umetne objekte s čvrsto in dobro opredeljeno geometrijo, tj. stavbe, podporne zidove, ceste itd., za zagotovitev popolnega nadzora nad morebitnimi poškodbami, povzročenimi s podzemnimi gradbenimi deli. Kljub vrtanju v stabilno kamnino višinska razlika med stropom predora in površjem v nekaterih delih ni zelo velika (minimalna višina nadkritja znaša 15 m), kar je bil odločilen dejavnik za uvedbo geodetske spremeljave. Slika 40 prikazuje posamezne sektorje celotnega območja, kjer se bo izvajala spremeljava. V teh sektorjih namreč predor poteka najbližje površju. Na podlagi geološke študije območja je bilo ugotovljeno, da je kamnina dovolj trdna, vprašanje



Slika 40: Sektorji izbrani za spremeljanje posledic gradnje. Do sedaj je bil izkopan samo sektor 1, zato bo analiza deformacij v nalogi omejena zgolj na to območje.

pa je, ali so v tej trdni kamnini mogoče prisotne kakršne koli manjše vrzeli, ki bi se med izkopavanjem lahko porušile, kar ne bi poškodovalo samo infrastrukture, ampak bi lahko ogrožalo tudi življenja. Izven teh vrzeli naj bi vplive izkopa absorbirala stabilna kamnina, zato se pričakuje, da bodo morebitni premiki in deformacije na površju po velikosti majhni. Takšna napoved je ponovno predstavljala osnovo za preizkus delovne hipoteze.

Z osredotočenjem na sektor 1 v preostanku naloge (pod tem sektorjem je bil predor dosedaj izkopan) so bili v analizo vključeni trije objekti, in sicer podporni zid, stavba in cesta, prikazani na sliki 41. Analiza v nalogi bo postavila poseben poudarek na zid, saj le-ta vsebuje največ površinskih detajlov za uporabo obeh deformacijskih modelov, predstavljenih v poglavju 2.8. Z vidika delovne hipoteze in njenega ovrednotenja v okviru tega raziskovalnega projekta, kjer so bili v spremljavo vključeni večji objekti, bi rezultati lahko zatrili več odgovora ozziroma informacij o učinkovitosti predlaganega metodološkega pristopa. Pred začetkom izkopa so se v bližini vhoda v predor stabilizirali



Slika 41: Obravnavani objekti in stabilizirani stebri v sektorju 1. Samo okoli 25 % celotnega podpornega zidu je vidnega na sliki, ki sicer v dolžino meri okoli 130 m, v višino pa 10 m. Črni črti na desni sliki označujeta zorno polje leve slike.

trije betonski stebri (1000, 479 in 474 na sliki 41), ki bodo omogočali usmerjanje napredovanja podzemnih aktivnosti in določitev premikov predorske cevi med gradnjo. Hkrati je bil točno nad osjo predora stabiliziran dodaten steber 481 za spremljanje premikov med začetno fazo vrtanja in pozneje za spremljanje premikov vhoda v predor (portala). Ti stebri so bili zasnovani za prisilno centriranje merske opreme.

Po obsežni analizi v fazi planiranja geodetske mreže je bil steber 1000, ki je lociran najdlje od obravnavanega sektorja (tik ob obali), izbran za referenčno točko. Ta steber je bil hkrati izbran tudi zato, ker je edini stabiliziran stran od območja predorskoga vhoda, kjer so tla izpostavljena

morebitnim premikom, ki jih povzročajo različni delovni stroji. V primerjavi s stebroma ob vhodu v predor (479 in 474) je bil steber 1000 vgrajen v bolj trdno kamnito podlago umetno postavljenega obalnega pasu. Zaradi dejstva, da sta stebra 479 in 474 tako izpostavljena, je bila sprejeta odločitev, da bo orientacija geodetske mreže realizirana z opazovanjem oddaljene točke (v tem primeru vrha cerkve, oddaljenega okoli 10 km), ki je bil viden s stebrov 1000 in 474. Razen stebra 1000 so bili vsi ostali stebri obravnavani kot kontrolne točke, ki so se v mrežo vključile zgolj za izboljšavo njene geometrije. Vidnosti med vsemi točkami v mreži (stebri in stojišči tarč TLS) ni bilo mogoče zagotoviti zaradi vegetacijskega pasu, ki je ločeval obravnavane objekte od obale (glej sliko 41, desno). Zaščitne ograje, postavljene okoli vhoda v predor, so dodatno onemogočile vidnost med stebri 1000, 479 in 474 in preprečevale vzpostavitev optimalnih merskih pogojev med točkami v mreži. Dodatni kompromisi so morali biti sprejeti tudi pri izboru lokacij skenerja in tarč TLS v neposredni bližini obravnavanih objektov, saj je bilo do hiše možno dostopati samo z ene strani. Po drugi strani je bila cesta, ki gre skozi sektor 1, med obema terminskima izmerama odprta za promet. Posledično je to pomenilo, da je bilo treba za zapolnitev senc v oblakih točk zidu, kot tudi ceste, skeniranje na nekaterih stojiščih izvesti s pomočjo večkratnih skenogramov. Če povzamemo, prenos predlagane metodologije na teren je bil že zaradi vseh teh ovir precejšen izziv, čeprav se je lahko ravno zato pridobilo več praktičnih izkušenj, ki so bile koristne med končnim ovrednotenje hipoteze.

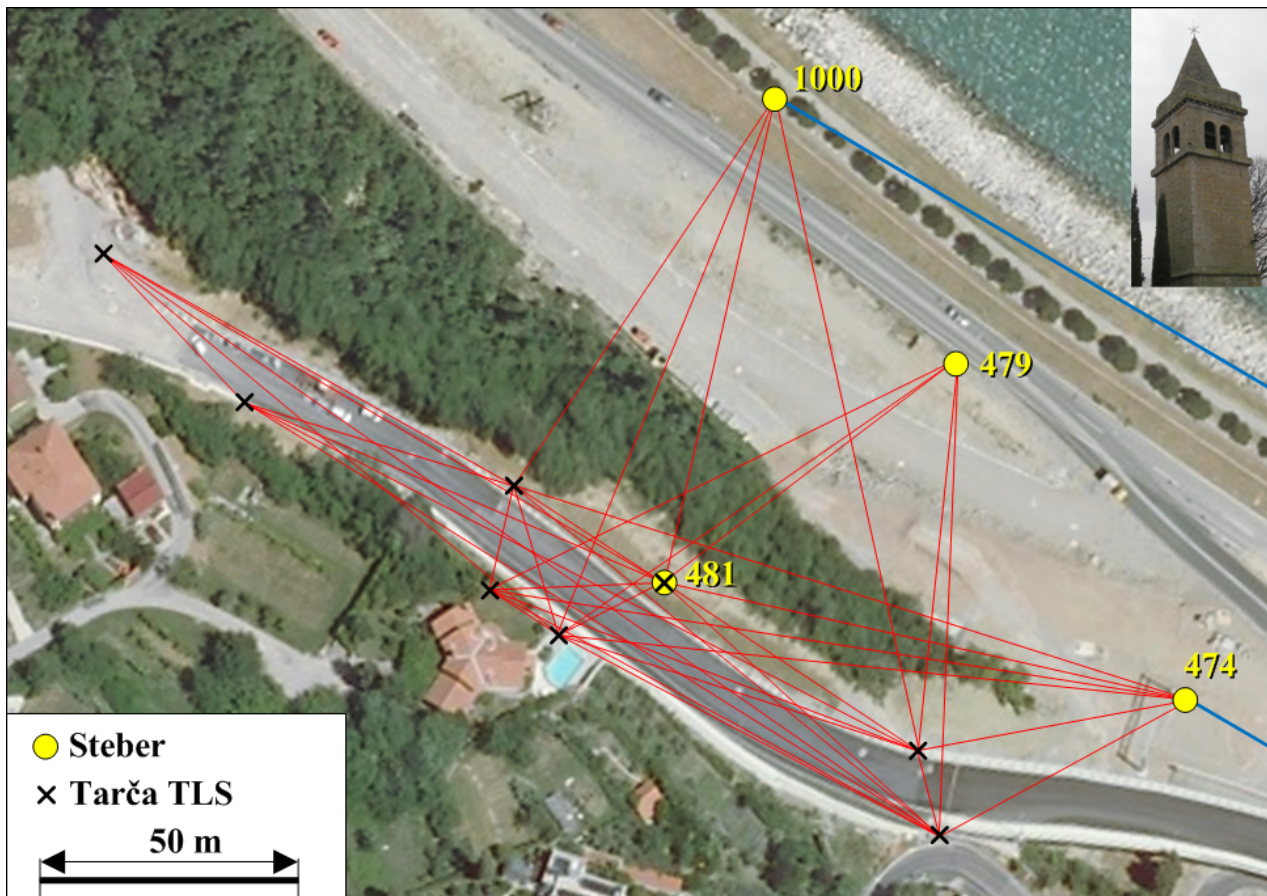
3.4.2 Terenska izmera

Ob uporabi istih metodoloških korakov iz poglavja 2 kot pri testu 1 sta bili izvedeni dve terminski izmeri, prva maja 2010, preden se je začelo izkopavanje predora v prvem sektorju, in druga februarja 2011, malo po izkopu tega sektorja. Vsaka od izmer je bila zaključena v enem dnevu, vključno s klasično terestrično izmero in izmero TLS. Za razliko od testa 1 se tokrat stabilnosti referenčnega sestava ni posebej analiziralo z nobeno od geodetskih merskih tehnologij. Glede na lokacijo in stabilnost tal okoli referenčne točke mreže kot tudi orientacijske točke se je v tem primeru domnevalo, da so med obema izmerama datumski parametri ostali nespremenjeni.

Ker so bila opazovanja obeh terminskih izmer izvedena v različnih delih leta, je bilo merjenje atmosferskih pogojev ponovno neizogibno, da bi lahko opazovane dolžine popravili za vse sistematične pogreške. V preglednici 10 so povzeti izmerjeni meteorološki parametri iz obeh terminskih izmer. Za merjenje temperature zraka in psihrometrične diference je bil uporabljen isti precizni Assmannov psihrometer kot v testu 1 (z ločljivostjo termometra $0.1\text{ }^{\circ}\text{C}$). Tudi zračni tlak je bil tokrat izmerjen s pomočjo digitalnega barometra Paroscientific, št. modela 760-16B, z ločljivostjo 0.01 mbar in relativno natančnostjo 0.01 %. Geodetsko mrežo, razvito za navezavo oblakov točk na referenčni sestav, je sestavljalo 12 točk, vključno s štirimi stebri (1000, 479, 474 in 481), točko orientacije ter sedmimi stojišči tarč. Z izjemo stebra 481 so bile tarče postavljene na stative, pri čemer so ostale lokacije stativov približno enake v obeh izmerah. Na sliki 42 je prikazana geodetska mreža z dodanimi črtami, ki nakazujejo vizure med točkami. V geodetski mreži so bili vzdolž rdečih črt (glej sliko 42)

Preglednica 10: Test v naravi 2: atmosferski parametri dveh terminskih izmer, povprečne vrednosti. Vsi atmosferski parametri so bili izmerjeni samo na strani instrumenta.

Datum	Temperatura [°C]	Vlažnost [%]	Zračni tlak [mbar]
Maj 2010	19.0	79.8	1003.0
Februar 2011	9.8	66.2	1024.1



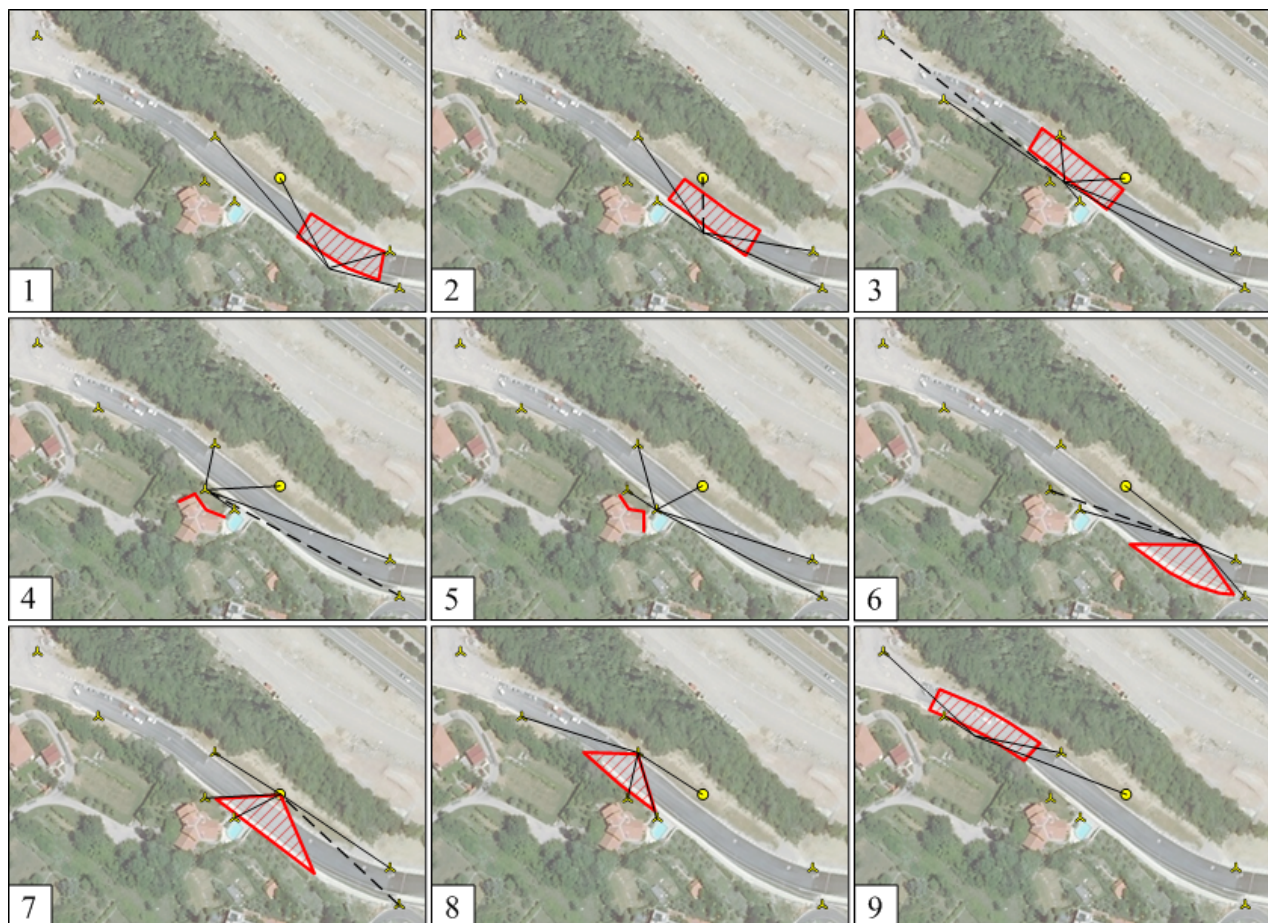
Slika 42: Geodetska mreža razvita v bližini obravnavanih objektov. Modri črti označujeta smer proti orientacijski točki oz. vrhu cerkve, oddaljenem okoli 10 km (slika desno zgoraj).

opazovani koti in dolžine v obeh terminskih izmerah. Na točko orientacije so bila iz stebrov 1000 in 474 izvedena samo kotna opazovanja. Tudi tokrat je bila zagotovljena velika redundanca meritov, in sicer z opazovanji v sedmih girusih na vsakem stojišču. V tem testu so bile meritve izvedene z elektronskim tahimetrom Leica TS30, pri čemer je bil njegov sistem APT uporabljen na vseh stojiščih, razen seveda pri opazovanju orientacijske točke, proti kateri je bilo viziranje opravljeno na ročen način. Modulacijska frekvenca, adicijska konstanta, indeksni in kolimacijski pogrešek so bili predhodno preizkušeni s strani uradnega zastopnika, zato je instrument deloval po zahtevah proizvajalca. Za signalizacijo točk v mreži so bili uporabljeni isti reflektorji kot v testu 1, tj. GPH1P in GPR121 z adicijskimi konstantami določenimi pred vsako izmero. Tudi horizontiranje instrumenta in reflektorjev je bilo v tem testu izvedeno z istimi preciznimi cevnimi libelami kot v primeru testa

v naravi 1. Zaradi združljivosti vse merske opreme, vključno s skenerjem (Riegl VZ-400), na čigar glavo je bil pritrjen poseben adapter, po horizontiranju podnožij le-teh ni bilo treba več premikati. Na ta način so se pogreški centriranja ponovno minimizirali.

Ker je bil v tem testu uporabljen Rieglov skener, je to pomenilo, da je bilo treba vsako od štirih ploskih Leicinh tarč predhodno označiti, saj je le tako bilo mogoče v postopku obdelave meritev odpraviti pogreške dolžin na osnovi ustreznih parametrov korekcijskih funkcij (podanih v preglednici 3). Posledično je bilo treba v testu 2 zaradi uporabe teh korekcijskih funkcij pri obdelavi meritev (poglavlje 3.4.3.2) koordinate centrov tarč oceniti na podlagi predlaganega dvokoračnega postopka, opisanega v poglavju 2.4.1. Določitev centrov tarč s postopkom amplitudno uteženega povprečja ni bilo mogoče, saj so bile dolžine skener – tarča prevelike.

Skeniranje objektov je bilo izvedeno z devetih stojišč, ki so prikazana na sliki 43. Cesta je bila skeni-



Slika 43: Položaji skenerja v obeh terminskih izmerah. Rdeče črte označujejo skenirano površino, medtem ko so črne črte usmerjene proti skeniranim tarčam. Črtkane črne črte pa predstavljajo dodatne tarče, ki so bile skenirane samo v drugi terminski izmeri.

rana s stojišč 1, 2, 3 in 9. Prva tri stojišča so bila postavljena na vrhu podpornega zidu, medtem ko se je zadnje nahajalo na pločniku poleg ceste. S stojišč 4 in 5 je potekalo skeniranje dostopnega dela hiše, in sicer s pritrditvijo skenerja v podnožji obeh stativov ob hiši, ki sta sicer služila za sto-

jišča tarč TLS. Podporni zid pa je bil skeniran s stojišč 6, 7 in 8, pri čemer sta dve stojišči ponovno služili za pritrdiritev skenerja (tj. stojišči 7 in 8 – steber 481). Obravnavani objekti so bili skenirani z ločljivostjo 5 mm (v obeh smereh), kar je vodilo do oblakov točk velike gostote, ki so vsebovali do 10 milijonov točk. Položaji stojišč skenerja so bili izbrani tako, da se razdalja do objektov in posledično gostota točk ni veliko spremenjala. Razen na stojiščih, ki so se uporabila za skeniranje hiše, se je na vseh ostalih površina objektov skenirala v največ petih ponovitvah, predvsem zaradi stalnega prometa, ki je povzočal sence v skenogramih.

Na vsakem stojišču je bilo skeniranih 4 do 7 tarč, z ločljivostjo 1 mm na površini tarče, torej enako kot v testu za analizo pogreška dolžine, opisanem v poglavju 3.1.2. Za zagotovitev identičnih sne malnih pogojev z vidika razporeditve tarč je bilo pomembno vsako od njih (z njeno unikatno označbo) postaviti na isti stativ v obeh izmerah. Na ta način bi morali imeti preostali sistematični pogreški (tisti, ki jih v postopku modeliranja ni bilo mogoče v celoti odpraviti) podoben vpliv na končne rezultate. Na stojiščih 3, 4, 6 in 7 je bila v okviru druge terminske izmere skenirana ena dodatna tarča (črtkane črne črte na sliki 43), saj je bila vegetacija takrat nizka. Glede na stojišča skenerja je bila razporeditev stojišč tarč daleč od idealne in omejena zaradi številnih fizičnih ovir. Hkrati se tudi ni bilo vedno mogoče izogniti skeniranju tarč z razdalje manjše od 20 m, kljub dejству da je bilo modeliranje pogreška dolžin v tem območju manj učinkovito (glej slike 20–23 na straneh 160–163).

Kalibracija skenerja je bila izvedena s strani proizvajalca, ki je ugotovil, da instrument deluje glede na njegove zahteve. Med kalibracijo se je preizkušalo razdaljemer, enoto za usmerjanje žarka (zrcalo) in sistem za odčitavanje kotov. Poleg te ni bila dodatno izvedena nobena posebna podrobna kalibracija.

3.4.3 Rezultati

Po zaključku obeh terminskih izmer bosta naslednji dve podpoglavlji ponovno posvečeni opisu korakov obdelave meritev, katerih namen je izračun vhodnih parametrov za končno analizo premikov in deformacij, ki bo sicer predstavljena v poglavju 4. Za razliko od testa 1 sta bila v tem testu za analizo zidu uporabljeni oba deformacijska modela, opisana v poglavju 2.8, medtem ko je bilo hišo in cesto možno obravnavati samo v okviru modela z omejeno smerjo (poglavje 2.8.1). Prvo podpoglavlje se bo osredotočilo na določitev položajev tarč TLS iz meritev klasične terestrične izmere. V drugem podpoglavlju pa bo predstavljena analiza absolutne orientacije in vseh nadaljnjih korakov obdelave meritev TLS.

3.4.3.1 Klasična terestrična izmera

Po izračunu srednjih vrednosti posameznih opazovanj iz sedmih girusov so bili v tem testu položaji točk v mreži (tarč TLS in stebrov) ocenjeni z obravnavo mreže kot trirazsežne. Ravno zato ocen-

jevanje koordinat ni potekalo ločeno za položajne koordinate in višinske razlike kot pri testu 1. Namesto tega je metoda najmanjših kvadratov sočasno vključevala vse merske količine, tj. horizontalne kote, zenitne distance in poševne dolžine. Isti koraki obdelave, ki so opisani spodaj, so bili izvedeni v obeh terminskih izmerah.

Pred izvedbo izravnave je bilo poševne dolžine najprej treba popraviti za meteorološke popravke, da bi jih lahko obravnavali ne kot refrakcijske krivulje, ampak njim pripadajoče prostorske tetive (ravne linije). Ti popravki so bili po istih korakih kot v testu 1 izračunani na podlagi meritev temperature, zračnega tlaka in delnega tlaka vodne pare, izmerjenih s pomočjo psihrometra in barometra. Tako je bil delni tlak vodne pare določen po Sprungovi enačbi za Assmanov aspiracijski psihrometer. Nasičeni tlak vodne pare je bil izračunan na osnovi Magnus-Tetensove enačbe, pri čemer sta bila referenčni in dejanski lomni količnik ponovno določena glede na Ciddor (1996) in Ciddor in Hill (1999). Ker maksimalna dolžina v mreži ni presegla 200 m, je to pomenilo, da je bil od vseh popravkov dolžin samo prvi popravek hitrosti nezanemarljiv. Drugi popravek hitrosti in popravek zaradi ukrivljenosti merskega žarka sta se tudi v tem testu lahko izpustila iz redukcije dolžin.

Poleg poševnih dolžin je bilo treba popraviti tudi zenitne razdalje z_m , pri čemer sta bili za ta namen upoštevani ukrivljenost Zemlje in refrakcija ($z_{corr} = z_m - D \cdot \frac{1-k}{2R}$, kjer je R polmer Zemlje, k pa koeficient refrakcije). Ta korekcijski faktor neposredno vpliva na višinske razlike in lahko na razdalji 200 m doseže vrednost 3 mm.

V zadnjem koraku so bile po Kuangu (1996) izpeljane enačbe popravkov za vsako izmerjeno in ustrezno popravljeno vrsto opazovanj (horizontalni koti, zenitne razdalje in poševne dolžine) z namenom pridobitve ocenjenih 3R položajev točk v mreži. Apriori standardna deviacija σ_0 je bila izračunana kot povprečje standardnih deviacij vseh opazovanj. V obeh terminskih izmerah so se znotraj posameznega tipa vsem opazovanjem pripisale enake uteži, saj so bila določena s skoraj enako natančnostjo. Opazovanja so bila ponovno najprej izravnana v obliki proste mreže z minimalno sledjo matrike kofaktorjev koordinatnih neznank. Na koncu se je izravnava ponovila, tokrat s stebrom 1000, privzetim kot dano točko, ter smernim kotom iz stebra 1000 na točko orientacije kot dano smerjo. Rezultati izravnave klasičnih terestričnih meritev so podani v preglednici 11.

Po izvedbi izravnave so se višine točk v mreži preračunale s pomočjo znane vertikalne ekscen-

Preglednica 11: Rezultati izravnave z minimalnim številom datumskih parametrov: globalni test modela, natančnosti izravnanih vrednosti opazovanj in položajne natančnosti točk v mreži in [mm].

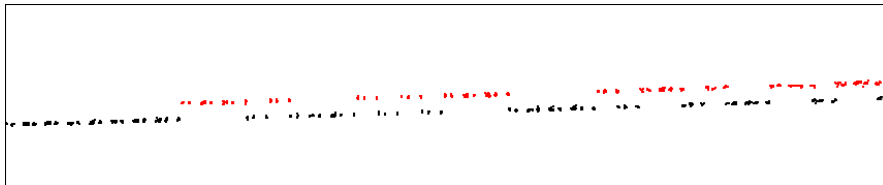
Datum	$\hat{\sigma}_0^2 / \sigma_0^2$	$\hat{\sigma}_{Hz}$ ["]	$\hat{\sigma}_z$ ["]	$\hat{\sigma}_D$ [mm]	$\hat{\sigma}_{pos,max}$	$\hat{\sigma}_{pos,min}$	$\hat{\sigma}_{pos,avg}$
Maj 2010	1.00	0.6	1.0	0.1	0.9	0.5	0.7
Feb 2011	1.04	0.6	1.0	0.1	0.8	0.6	0.7

tricitete med tarčami TLS in reflektorji. V primeru stebrov (razen pri stebru 481, ki je bil uporabljen za stojišče tarč) so se izravnane vrednosti višin, ob upoštevanju izmerjenih višin instrumenta oz. reflektorja, reducirale na nivo vrhov stebrov.

3.4.3.2 Terestrično lasersko skeniranje

Iz zelo gostih oblakov točk je bilo v prvem koraku treba odstraniti vse tiste, ki ne pripadajo obravnavanim objektom. Te točke so se odstranile na ročen način. V naslednjem koraku so se večkratni skenogrami združili, da bi se nastale sence, ki jih je povročil promet, zapolnile. Nato so se iz skenogramov odstranile tudi vse točke, oddaljene za več kot 30 m od skenerja. Ta meja je bila izbrana glede na rezultate testa odzivnosti površinskega materiala (poglavlje 3.2). Po določitvi normalnih vektorjev v vseh preostalih točkah so se v skenogramih nazadnje ohranile samo tiste, katerih vpadni kot je bil manjši od 45° . Prag za vpadni kot je bil ponovno izbran glede na zmogljivosti skenerja, ki je bila testirana na šestih vzorcih S1–S6 (slika 24). Jasno je, da bi se morala analiza premikov in deformacij omejiti na objekte, ki posnemajo površinske latnosti vzorcev. Takšne površine je bilo možno najti na delih hiš kot tudi na celotnem podpornem zidu. Po drugi strani pa cesta predstavlja izjemo, saj asfalt s svojim majhnim albedom ni bil zajet med vzorce. Kljub tej opazki je bil najzanimivejši del ceste, neposredno nad predorskima osema, analiziran ob predpostavki, da zmogljivost razdaljemera pri skeniranju te vrste površine ne bo bistveno nazadovala, če bosta pred tem uporabljeni omenjena pragova za vpadni kot in dolžino.

Pri pregledu oblakov točk med to začetno fazo obdelave je bila opažena prisotnost nepravilnosti, ki so povzročile, da so bili nekateri profili premaknjeni iz pravilnih položajev. Posledico tega vpliva je mogoče videti na sliki 44. Izkaže se, da te nepravilnosti niso rezultat skeniranja neke določene



Slika 44: Nepravilnosti profilov. Profili obarvani z rdečo so napačni.

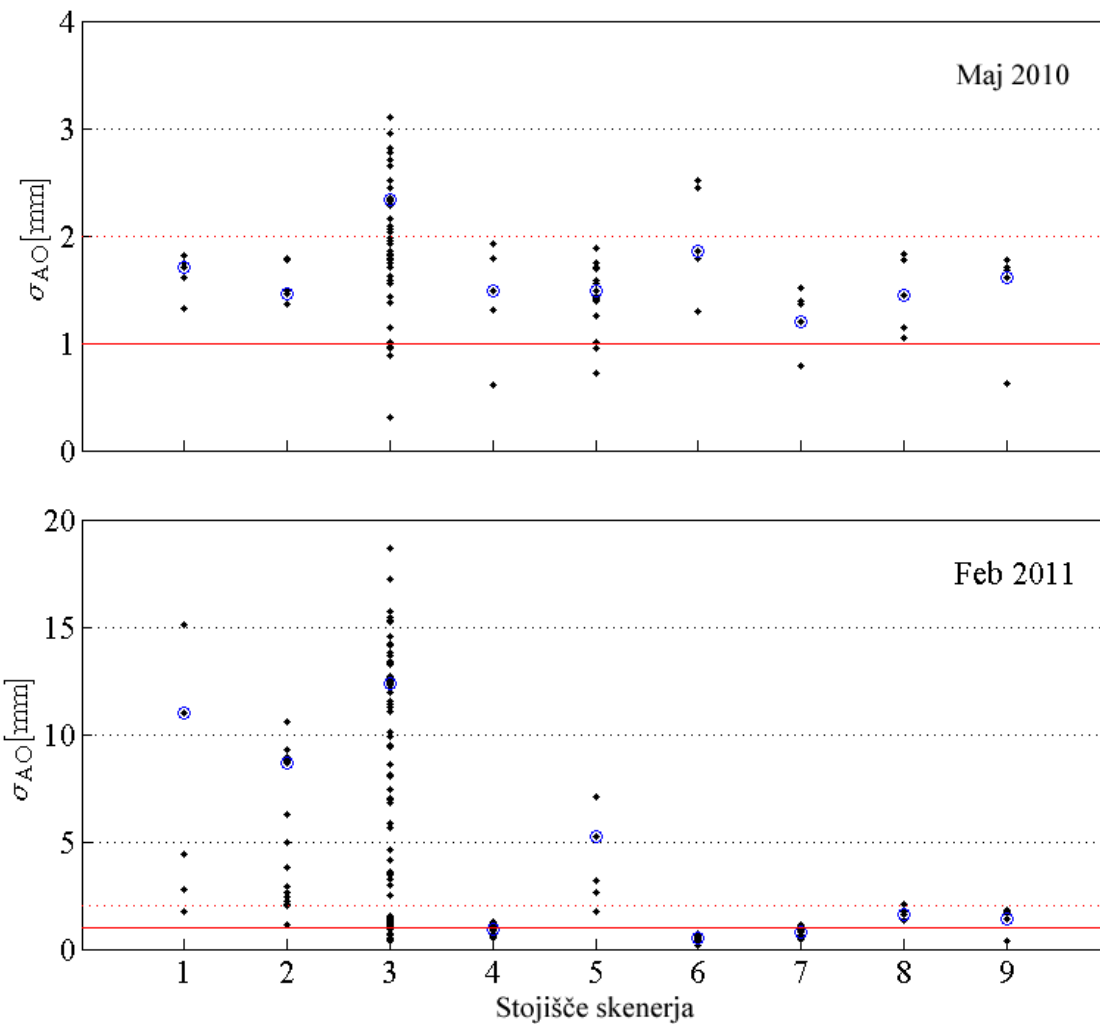
površine, ampak jih povzroča instrument. Poleg tega je ta premik profilov mogoče opaziti celo znotraj enega obrata tristranega zrcala, ki usmerja žarek vzdolž vertikalne smeri in s tem ustvarja značilne trojice profilov, ki jih vidimo na sliki 44. Velikost premika je odvisna od vpadnega kota (večji kot je vpadni kot, bolj očiten postane premik). Na sliki 44 napačni profili od ostalih odstopajo za približno 1 cm, pri čemer je ta velikost premika konstanta, saj se vpadni kot bistveno ne spremeni. Ena izmed možnih razlag opaženega sistematičnega pogreška je, da je bila kotna hitrost zrcala podvržena nihanju, ki se je pojavilo samo takrat, ko se je med skeniranjem zrcalo vrtelo (nihanja se niso pojavila, kadar je zrcalo osciliralo). Posledično so bili impulzi oddani pri napačnih vertikalnih kotih, kar je povzročalo podaljševanje oziroma krašanje dolžin. Kakor koli že, za odkritje pravega vzroka teh pogreškov bi bilo treba s tem instrumentom izvesti več testov, na podlagi katerih bi se pokazalo, ali so vzorci premikov po naravi sistematični ali naključni. Prisotnost teh napak je nakazovala nestabilnost skenerja, kljub dejству, da ga je proizvajalec predhodno preizkusil. Pred izvedbo vseh nadaljnjih korakov obdelave podatkov, kot tudi končne analize deformacij, je bilo napačne profile

treba odstraniti. Dolžine do vseh preostalih točk so se nato popravile še za meteorološke popravke, za katere se je izkazalo, da so manjši od 0.5 mm na maksimalni razdalji 30 m.

Po pripravi oblakov točk v okviru začetne faze je bila pozornost preusmerjena v analizo kakovosti absolutne orientacije, s pomočjo katere se je meritve posamezne izmere povezano s skupnim referenčnim sestavom. V ta namen je bilo treba oceniti položaje tarč za vsako stojišče skenerja glede na predlagani dvokoračni postopek. Nadalje je bilo treba dolžine do tarč popraviti za vse sistematične pogreške (tj. najprej za meteorološke popravke in nato še za dolžinske pogreške obravnavane v poglavju 3.1.2, ki so rezultat skeniranja retroreflektivnega dela tarče s tem skenerjem). Brez uporabe, predvsem parametrov funkcij pogreška dolžine iz preglednice 3, bi bile lahko ocenjene vrednosti dolžin do tarč pogrešene do 1 cm, torej nivoja, ki ga je bilo treba reducirati pred oceno transformacije v naslednjem koraku.

Zaradi omejenih pogojev na terenu z vidika geometrije skener – tarča in dolžinami do tarč⁷ (slika 43) je bilo treba opraviti podrobno analizo kakovosti in stabilnosti transformacije. Hkrati se je takšna analiza zdela smiselna, da bi se lahko izognili morebitnim časovnim nihanjem amplitude, opaženim med kalibracijskim testom tarč, ki bi lahko v veliki meri poslabšala kakovost transformacije. V ta namen so bili za vsako stojišče transformacijski parametri (rotacijska matrika R in vektor translacije t ; merilo se ni ocenjevalo) izračunani iz vseh možnih kombinacij tarč. Na primer, stojišče z n tarčami zagotovi skupno $\sum_{k=3}^n \binom{n}{k} = \sum_{k=3}^n \frac{n!}{k!(n-k)!}$ nizov transformacijskih parametrov (R_i, t_i), vključno z nizom, pridobljenim na podlagi vseh tarč. Ker za test 2 velja, da $n_{\max} = 7$, je bilo maksimalno število nizov 99. Po oceni transformacijskih parametrov in pripadajočih σ_{AO} za vsak niz, je bilo možno v območjih preklopov preveriti skladnost sosednjih oblakov točk, ki so bili predhodno transformirani z različnimi nizi (R_i, t_i). Tako je bila kakovost transformacije kontrolirana na podoben način kot v testu 1 (na strani tarč in objekta), s to razliko, da tokrat kontrole na strani objekta zaradi obsežnosti dela ni bilo možno izvesti izključno vizualno, ampak šele ob uporabi numeričnega pristopa. Odstopanja med sosednjimi oblaki točk v območjih preklopa so se določila z razdelitvijo območij na segmente velikosti 20 x 20 cm, oceno lokalnih ravnin za vsak segment ter izračunom dolžin vzdolž smeri normal, torej podobno kot pri deformacijskem modelu 1. Edina razlika je bila, da so v tem primeru vsi oblaki točk pripadali isti terminski izmeri. Na sliki 45 so za obe izmeri prikazane vrednosti σ_{AO} za vsak niz tarč in za vsako posamezno stojišče skenerja. Rezultati na sliki 45 povedo, da je bila natančnost absolutne orientacije na stojiščih 1 do 5 močno pod vplivom geometrije skener – tarča, še posebej v drugi terminski izmeri. Velika odstopanja v σ_{AO} na teh stojiščih so bila pokazatelj nestabilnosti transformacije. Na podlagi skupne primerjave vrednosti za σ_{AO} in vrednosti odstopanj na strani objekta je bila nestabilnost transformacije za stojišča 1 do 5 dodatno potrjena. Odstopanja med prekrivajočimi se oblaki točk so, od enega do drugega niza transformacijskih parametrov, znašala tudi do 1 cm. Posledično meritev na teh stojiščih ni bilo možno umestiti v referenčni sestav z zahtevano natančnostjo. Zato jih je bilo

⁷Najbližja tarča je bila oddaljena precej manj kot 20 m, do koder je bila učinkovitost modeliranja dolžinskega pogreška omejena. Po drugi strani je bilo nekaj dolžin do tarč daljših od 70 m, kar pomeni, da je bil pogrešek dolžin ocenjen z ekstrapolacijo.



Slika 45: Pregled natančnosti absolutne orientacije. Modri krogi predstavljajo kombinacijo, pri kateri so bile v oceno transformacijskih parametrov vključene vse tarče na posameznem stojišču. Pazi na različen interval vrednosti za σ_{AO} na y osi.

treba izključiti iz vseh nadalnjih analiz. Na stojiščih 4 in 5, ki sta služili za skeniranje hiše, je bilo odstopanja na strani objekta v posamezni izmeri sicer možno zmanjšati pod mejo 1 mm. Kljub temu je bil rezultat primerjave oblakov točk prve in druge izmere nesmiseln. Meritve prve izmere so se namreč nahajale nad tistimi iz druge izmere. Očitno je bil problem v transformaciji, saj so bile vse tarče na eni, objekt pa na drugi strani horizonta. V takšnih primerih lahko, že ob zelo majhnih odstopanjih na strani tarč, ta odstopanja postanejo precej očitnejša na strani objekta.

Za razliko od stojišč 1 do 5, je analiza pokazala, da je kakovost in posebno stabilnost transformacije na stojiščih 6 do 9 mnogo večja. Meritve teh štirih stojišč, ki so omogočala rekonstrukcijo celotnega zidu in zanimivega dela ceste neposredno nad predorskima osema, je bilo možno uporabiti v analizi premikov in deformacij. Izmed vseh nizov transformacijskih parametrov (R_i, t_i), ocenjenih na stojiščih 6 do 9 za obe izmeri, so bile izbrane optimalne razporeditve tarč, in sicer glede na oba kakovostna kriterija, tj. natančnost orientacije ter povprečnega odstopanja segmentov v območjih preklopov. V preglednici 12 so podane vrednosti obeh kriterijev ter hkrati tudi povprečna odstopanja

med koordinatami točk v mreži in tarčami, katerih položaji so bili transformirani z izbranim nizom transformacijskih parametrov. Izbrani optimalni nizi transformacijskih parametrov (katerih mere

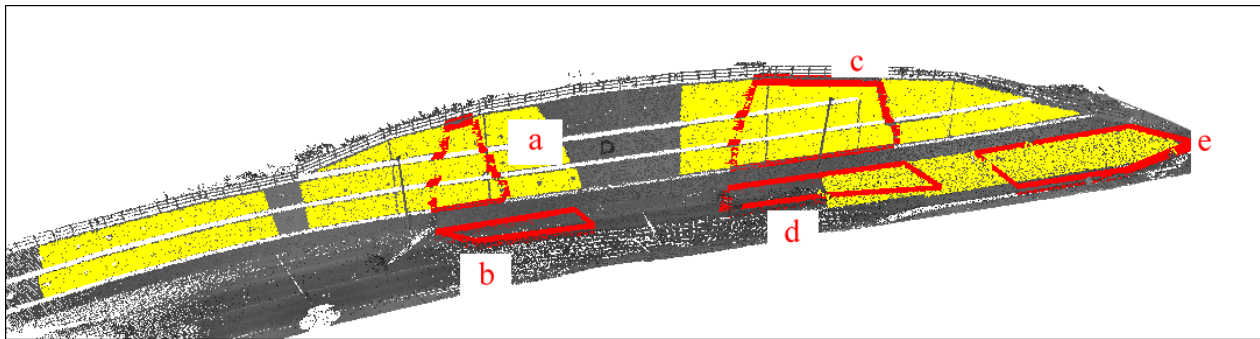
Preglednica 12: Kakovost postopka absolutne orientacije za stojišča 6 do 9 v [mm]. Δ označuje povprečno odstopanje segmentov v območjih preklopov, ki so prikazana na sliki 46. Nadpisane črke a do e ob vrednostih Δ so dodane za povezavo med vrednostmi iz preglednice in njim pripadajočimi območji na sliki.

Datum	Stojišče	σ_{AO}	dx	dy	dz	$dxyz$	Δ		
Maj 2010	6	1.3	0.4	1.1	0.2	1.2	0.9 ^a	-	-
	7	0.8	0.5	0.3	0.3	0.8	1.5 ^b	0.5 ^c	-
	8	1.0	0.7	0.6	0.1	0.9	-	0.6 ^d	0.3 ^e
	9	0.6	0.5	0.2	0.1	0.5	-	-	0.3 ^e
Feb 2011	6	0.6	0.3	0.4	0.2	0.6	0.6 ^a	-	-
	7	1.0	0.7	0.5	0.2	1.0	0.3 ^b	1.6 ^c	-
	8	1.8	1.4	0.7	0.2	1.6	-	0.8 ^d	0.3 ^e
	9	1.4	1.2	0.6	0.7	1.6	-	-	0.3 ^e

kakovosti so predstavljene v preglednici 12) so bili izračunani na osnovi 3 do 4 tarč na stojišče v obeh terminskih izmerah. Dolžine do tarč na posameznem stojišču so merile od 20 do 70 m, kar predstavlja območje, znotraj katerega je bila učinkovitost modeliranja pričakovano največja (pod nivojem 1 mm). Z vidika vrednosti Δ so se oblaki točk s stojišč 6 in 7 ter 7 in 8 prekrivali v dveh območjih, enem na cesti in drugem na podpornem zidu (zato dve vrednosti). Po drugi strani so se oblaki točk s stojišč 8 in 9 prekrivali samo na cesti. Te vrednosti so bile pridobljene na osnovi velikega števila segmentov velikosti 20 x 20 cm, pri čemer so bili vsi segmenti, ki so vsebovali manj kot 100 točk kot tudi tisti, katerih šum je bil nad vrednostjo 5 mm (tj. robovi na zidu), izključeni iz izračuna. Da bi vrednosti Δ lahko obravnavali kot reprezentativne, so se odstopnja segmentov za vsako območje preklopov ponovno izračunala, tokrat z velikostjo segmenta 10 x 10 cm, minimalnim številom točk 50 ter stopnjo šuma 3 mm. Vrednosti Δ se niso bistveno spremenile.

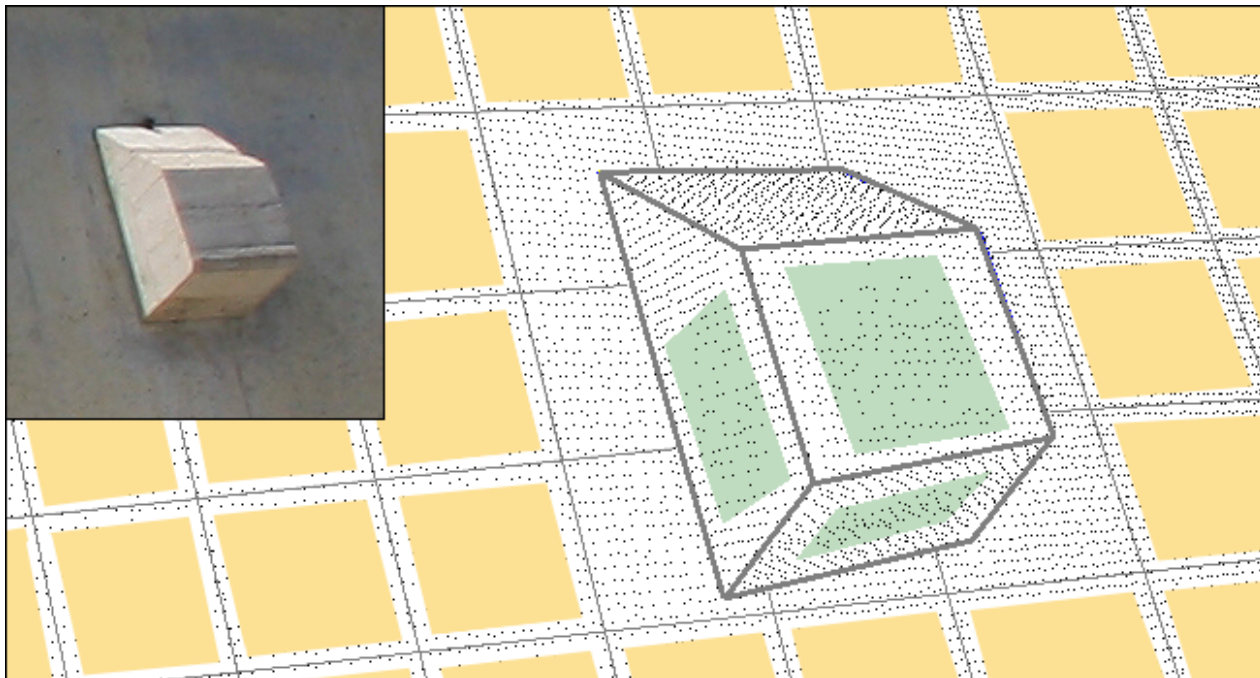
Po izboru optimalnih nizov transformacijskih parametrov so se območja preklopov preverila tudi vizualno, da bi se prepričali o medsebojni skladnosti med oblaki točk ter jih tako lahko obravnavali kot eno združeno entiteto. Slika 46 prikazuje območja preklopov, ki so bila med analizo kakovosti absolutne orientacije obeh izmer vzeta pod drobnogled. Na sliki 46 manjkajoča dva dela podpornega zidu (vrzeli v rumenih točkah) ni bilo možno obravnavati v okviru nadaljnjih korakov, saj so bile v teh delih odkrite nepravilnosti profilov, in sicer v meritvah druge terminske izmere.

V zadnjem delu tega poglavja so bile rumene točke, prikazane na sliki 46, uporabljene za modeliranje oblike obravnavanih objektov (korak 6 splošnega metodološkega pristopa). Šele tako je bilo ploskovne modele mogoče analizirati v okviru deformacijskih modelov, opisanih v poglavju 2.8. Oba objekta je bilo možno modelirati na enak način, tj. z razdelitvijo oblakov točk na manjše površinske segmente (zaplate) glede na koordinatne osi ter lokalnim aproksimiranjem površine z ravninskim modelom (glej poglavje 2.7.1). Poleg tega so bili na površini zidu odkriti detajli (značilke), ki so omogočali izvedbo modeliranja preko postopka segmentacije. Te značilke so



Slika 46: Območja preklopov na zidu (a in c) in na površini ceste (b, d in e) za stojišča 6 do 9. Rumene točke na zidu in na cesti pripadajo področjem, ki bodo v obravnavana v preostalem delu naloge. Sive točke so bile dodane zgolj za izboljšavo vizualnega dojemanja.

prikazane na sliki 47. Na gladkem delu zidu (oranžne ravnine, slika 47) je bilo modeliranje izve-



Slika 47: Modeliranje zidu s pomočjo ravninskega modela. Oranžne ravnine so bile določene z razdelitvijo oblaka točk na segmente, zelene ravnine pa so rezultat uporabe postopka segmentacije, ki je bil predstavljen v poglavju 2.7.1).

deno s pomočjo segmentov velikosti 20 x 20 cm. Velikost segmenta je bila izbrana po predhodni analizi vzorcev vektorjev popravkov, pridobljenih v okviru postopka izravnave oziroma določitve najbolje prilegajočih ravnin. V okviru te analize je bila za izbrano velikost segmenta uporaba linearnega modela potrjena. Izmed vseh segmentov so bili modelirani samo tisti, ki so vsebovali več kot 400 točk. Ta prag je bil uporabljen tudi v postopku segmentacije, katere rezultati so prikazani na sliki 47 (zelene ravnine, odkrite na površini značilk na zidu). Poleg praga za število točk je bil v

postopek modeliranja vključen tudi prag ravninskega šuma (3 mm), da bi se na ta način izključilo tiste segmente, ki vsebujejo grobo pogrešene točke.

Pridobljeni modeli so bili sedaj pripravljeni za ugotavljanje površinskih sprememb, predstavljenih v zadnjem poglavju naloge (poglavlje 4.2). Poleg površinskih značilk, prikazanih na sliki 47, ki so omogočale določitev reprezentativnih točk (deformacijski model 2, poglavje 2.8.2), je bilo preostali del zidu, zaradi odsotnosti kakršnih koli posebnih detajlov, možno obravnavati samo v okviru modela z omejeno smerjo (deformacijski model 1, poglavje 2.8.1). Iz istega razloga je ta model predstavljal tudi edino možnost za analizo površine ceste, ki se jo je modeliralo z uporabo enake velikosti segmentov in enakih pravgov kot v primeru zidu.

4 ANALIZA IN DISKUSIJA

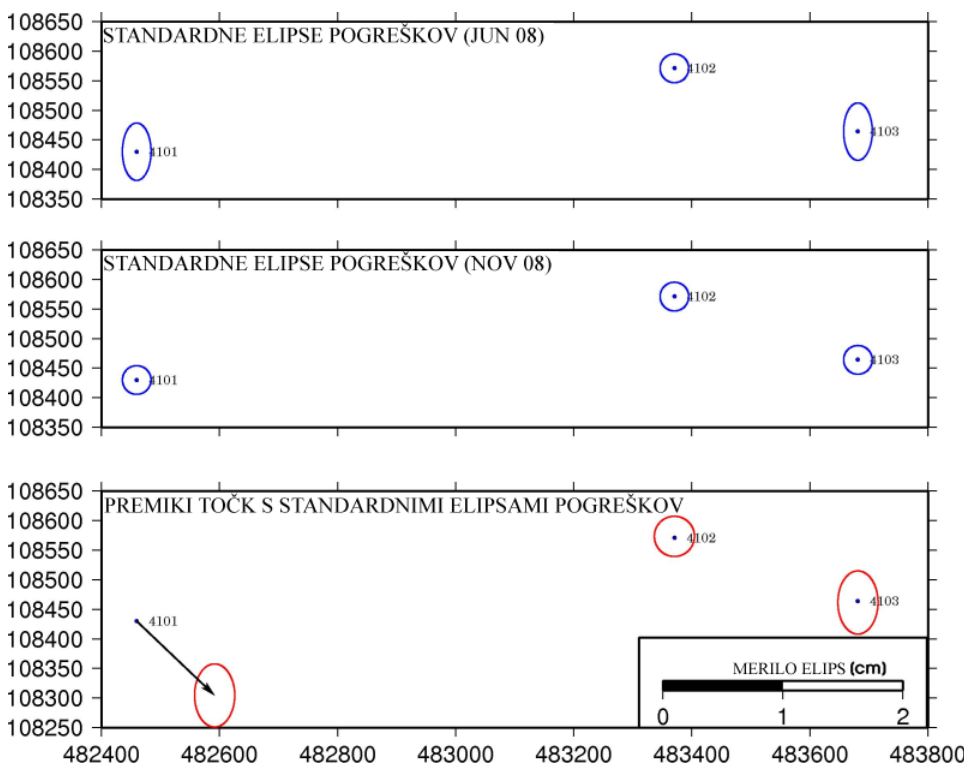
Zadnje poglavje povzema rezultate zadnjega koraka splošnega metodološkega pristopa, tj. analizo premikov in deformacij ploskovnih modelov obeh testov v naravi glede na oba predlagana modela, predstavljena v poglavju 2.8. V prvem delu poglavja bo v okviru deformacijskega modela 2 opisana analiza stebrov testa v naravi 1. V drugem delu poglavja pa bo v okviru obeh deformacijskih modelov (model z omejeno smerjo in model, ki temelji na reprezentativnih točkah) sledila obravnava zidu in ceste.

4.1 Test v naravi 1

Zaradi posebnosti testnega polja tega preizkusa v naravi je bila kakovost in stabilnost referenčnih stebrov kontrolirana s pomočjo opazovanj GNSS. Rezultati stabilnosti datuma mreže so predstavljeni v naslednjem podpoglavlju. V drugem in tretjem podpoglavlju pa so opisani rezultati premikov stebrov.

4.1.1 Stabilnost datuma

Na podlagi rezultatov terminskih izmer GNSS, predstavljenih v preglednici 7, so bile za referenčna steba 4102 in 4103 pridobljene statistično identične koordinate. Po drugi strani se je referenčni steber 4101 med obema izmerama GNSS premaknil za več kot 1 cm. Glede na te rezultate je bilo mogoče zaključiti, da se oba referenčna steba 4102 in 4103, ki sta bila v tej raziskavi uporabljeni za nadaljnja terestrična opazovanja in meritve TLS, lahko obravnavata kot stabilna. Na sliki 48 je v grafični obliki prikazana analiza stabilnosti referenčnih stebrov. Ker je bila dolžina med stabilnima referenčnima stebroma 4102 in 4103 (glej sliko 32) opazovana v okviru geodetske mreže s precizno klasično terestrično metodo, je to zagotovljalo dodatno informacijo glede stabilnosti teh dveh referenčnih točk. Razlika med izravnanimi dolžinama 4102–4103 iz obeh terminskih izmer, ocenjenima na osnovi klasičnih terestričnih opazovanj, je znašala manj kot 1 mm. Takšen nivo (ne)skladnosti imamo lahko za rezultat merskih napak in ne premika katerega koli od obeh referenčnih stebrov. Ta razlika je bila enaka tako v primeru izravnave geodetske mreže v obliki proste mreže kot tudi v primeru izravnave z minimalnim številom datumskih parametrov.



Slika 48: Grafična predstavitev rezultatov premikov referenčnih stebrov.

4.1.2 Določitev reprezentativnih točk

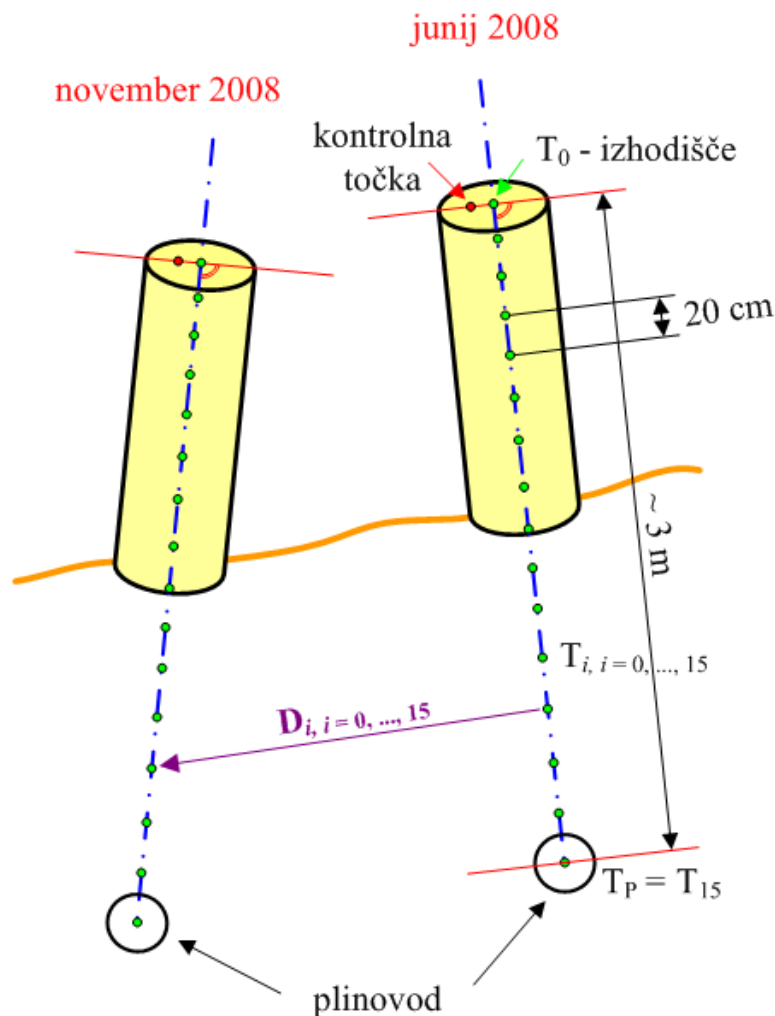
Glede na obliko stebrov so vhodne količine za določitev identičnih reprezentativnih točk sestavljeni:

- položaji opazovanih točk, ki so se obravnavale kot kontrolne točke in so bile vključene v izračun reprezentativnih točk, kar bo opisano spodaj. Položaji teh točk so se ocenili izključno na osnovi klasičnih terestričnih meritev;
- osi stebrov (parametrizirane s točko na osi in smernim vektorjem), ocenjene na osnovi rezultatov izravnave meritev TLS.

Če želimo zagotoviti, da bodo pri izračunu premikov uporabljene točke, ki so dejansko identične v obeh izmerah, potem je bilo treba kontrolne točke opazovalnih stebrov najprej projicirati na njihove osi, in sicer s pomočjo kriterija najkrajše razdalje (vzdolž pravokotnic). Kot je bilo že omenjeno, te kontrolne točke ne ležijo točno na oseh stebrov. Pravokotne razdalje od osi znašajo od 2 do 16 mm, odvisno od izbranega opazovalnega stebra.

V naslednjem koraku so bile vse reprezentativne točke določene z ekstrapolacijo navzdol do centra plinovoda ob pomoči smernih vektorjev osi. Dodatna analiza je potrdila, da se razdalje kontrolnih točk od osi niso spremenile (integrirtega stebra je torej ostala nespremenjena). Zato je na osi projicirane točke bilo možno uporabiti kot izhodišča ekstrapolacije. Če bi uporabili zgolj parametre osi stebrov, ocenjene iz oblakov točk, enakost ekstrapoliranih točk ne bi bila zagotovljena, saj točke na osi (P_0 v enačbah 23–25) niso primerljive. Na sliki 49 je prikazan izračun reprezentativnih točk, ob

izbranem koraku ekstrapolacije 20 cm in maksimalno dolžino 3 m od izhodišča, kar ustreza približni razdalji centrov plinovoda od vrhov stebrov.

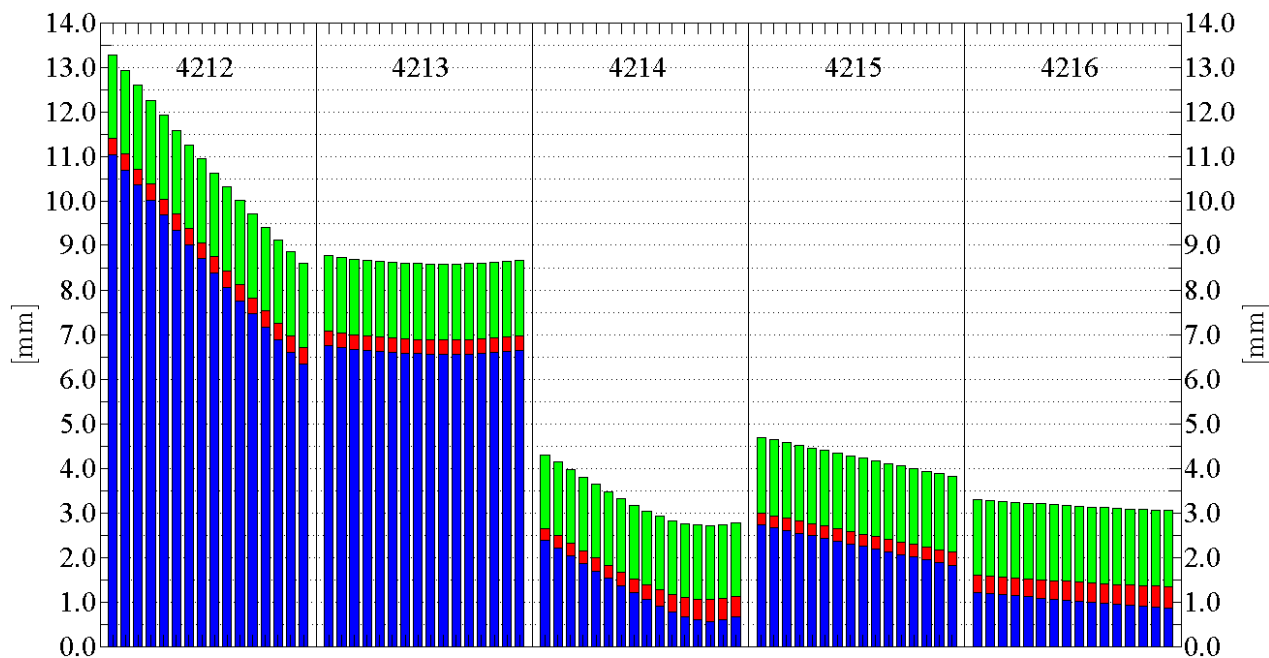


Slika 49: Identične točke za določitev premikov D_i vključno z izhodiščno točko T_0 in točko v centru cevovoda T_P .

4.1.3 Analiza premikov

Rezultati uporabe pristopa, opisanega v prejšnjem podpoglavlju, so pokazali, da so se stebri 4212, 4213, 4214 in 4215 premaknili, medtem ko se steber 4216 ni. Velikosti premikov so prikazane na sliki 50. Premik reprezentativnih točk na oseh valjev ni linearne funkcija razdalje od pripadajočega izhodišča. V primeru stebrov, kjer se oblika v obdobju med obema terminskima izmerama ni spremenila, bi lahko za prikaz rezultatov na sliki 50 uporabili tudi analitično funkcijo premikov. Vendar pa ob upoštevanju predlagane metodologije iz poglavja 2.8.2 velja omeniti, da bi bilo v primeru bolj kompleksnih objektov, katerih oblika se je deformirala (zato je treba reprezentativne točke določiti

na sami površini), analitično funkcijo težko oziroma nemogoče poiskati. Na sliki 50 je bil pri vseh



Slika 50: 3R vektorji premikov stebrov (modri stolpci), standardne deviacije premikov (rdeči stolpci) in položajne standardne deviacije reprezentativnih točk T_i , ki so bile uporabljene za izračun vektorjev premikov (zeleni stolpci, prikazane so maksimalne vrednosti standardnih deviacij med $T_{i,\text{JUN}}$ in $T_{i,\text{NOV}}$).

položajnih standardnih deviacijah reprezentativnih točk $T_{i,i=0\dots 15}$ uporabljen faktor 3, s čimer se je območje zaupanja povečalo na 99.73 %. Na ta način je postal razvidno, da sta bila steba 4212 in 4213 izpostavljena največjim premikom, ki so znašali več kot 1 cm do 6.4 mm za steber 4212 in okoli 6.5 mm za steber 4213. Ob pregledu trendov premikov je bilo mogoče ugotoviti, da se je steber 4212 nagnil, saj namreč vrednosti premikov od vrha navzdol padajo. Premik plinovoda pod 4212 je posledično samo 57 % premika izhodišča na vrhu, kar pomeni, da imajo nagibi lahko precej velik vpliv na vrednosti premikov. Zato z opazovanjem izključno vrhov stebrov ne moremo pridobiti natančne in zanesljive informacije o premikih plinovoda. To dejstvo je zelo pomembno, saj lahko prepreči lažno alarmiranje s strani upravnika plinovoda. Enak vzorec nagibanja ni bil opažen pri stebru 4213. Pri tem stebru premiki nakazujejo, da se je vseh šestnajst točk vzdolž osi stebra premaknilo za skoraj enako vrednost in zato ni prisotnih očitnih vplivov nagibanja.

Druga dva steba 4214 in 4215 sta bila izpostavljena manjšim vplivom premikanja tal, še posebej steber 4214, kjer so se značilno premaknile samo zgornje tri točke T_0 do T_3 , medtem ko se ostale niso. Premiki nižje ležečih točk so pod nivojem njim pripadajočih natančnosti krajnih točk. Tudi pri stebru 4214 je nagibanje stebra povzročilo redukcijo premikov za okoli 21 %, če primerjamo T_0 in T_3 , vendar pa na nivoju centra plinovoda T_P ni bilo zaznati premikov.

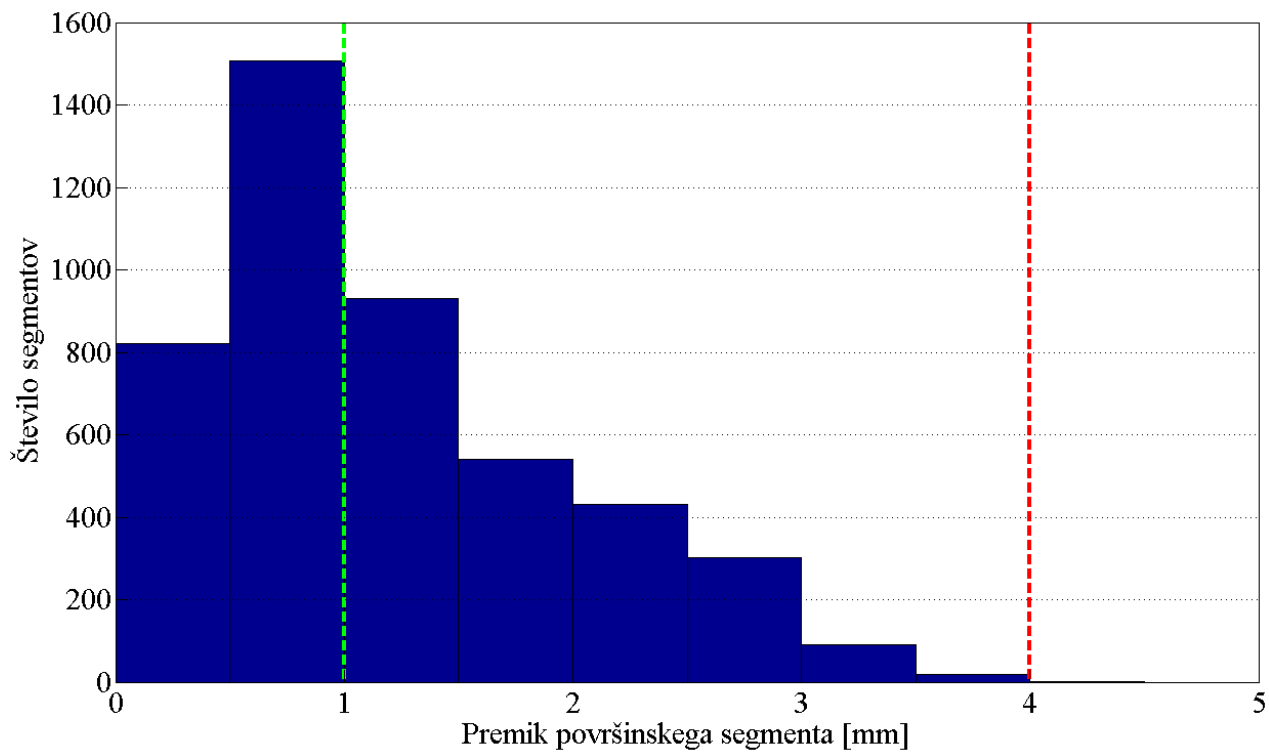
Premiki steba 4215 so znašali med 2.7 in 1.8 mm in so padali od vrha navzdol. Tudi tukaj rezultati kažejo, da je nagibanje stebra imelo nekoliko manjši vpliv na nivoju plinovoda kot na vrhu, z

redukcijo premikov za 33 %. Vendar pa na mestu stebra 4216 premikov ni bilo zaznati, saj nobeden od vektorjev premikov ni bil večji od pripadajočih območij zaupanja krajnih točk.

Predstavljeni rezultati so bili pridobljeni z vključitvijo vseh točk TLS in standardnimi deviacijami parametrov valjev, določenimi na osnovi pristopa vzorčenja, opisanega na koncu poglavja 3.3.3.3. Z zmanjševanjem točk do 50 % je bilo pri analizi premikov mogoče priti do enakih zaključkov. Zato predstavljeni rezultati odražajo visoko stopnjo zanesljivosti s povprečno standardno deviacijo premikov okoli 0.4 mm. Vendar pa v primeru redukcije točk TLS pod mejo 50 % postanejo rezultati nestabilni do te mere, da vzorec premikov ni več možno ohranjati. Hkrati so se rezultati, predstavljeni na sliki 50, primerjali tudi z analizo smernih vektorjev osi, da bi na način potrdili lastnosti nagibanj stebrov. V zadnjem koraku je bila preverjena še smer premikov, tj. na kakšen način sovpadajo s smerjo terena. Oba testa sta glede kakovosti rezultatov in trendov potrdila, da so nesporni.

4.2 Test v naravi 2

Analiza ugotavljanja sprememb se bo najprej osredotočila na zid, saj je bila njegova obravnava izvedena v okviru obeh deformacijskih modelov. Če začnemo z modelom z omejeno smerjo, je bil le-ta sposoben zaznati premike in deformacije izključno v smeri pravokotno na površino zidu. V vsakem površinskem segmentu so bili ocenjeni parametri izravnalnih ravnin (težišča in normalni vektorji) iz obeh izmer uporabljeni za izračun premikov vzdolž referenčnih smeri, tj. normalnih vektorjev iz prve izmere. Izračunani premiki predstavljajo razdalje od težišč iz prve izmere do presečišč referenčnih smeri z ravninami iz druge izmere (glej sliko 9). Okoli 4500 površinskih segmentov (zaplat), najdenih na zidu, je bilo analiziranih v modelu, saj so vsebovali dovolj točk ter izpolnili kriterije pravilnosti modela (glede na nivo šuma ter vzorca popravkov). Na sliki 51 so rezultati modela z omejeno smerjo prikazani v obliki histograma. Glede na rezultate modela z omejeno smerjo lahko zaključimo, da večina premikov površinskih segmentov zidu statistično ni pomembnih. Velikost premikov segmentov pravokotno na zid je očitno premajhna, da bi jih lahko obravnavali kot dejanske premike. Nekaj segmentov s premikom nad mejo 4 mm, ki so sicer dovolj veliki, enostavno ne nakazuje kakršnega koli jasnega trenda, ki bi ga lahko imeli za realističnega. Rdeča in zelena črtkana črta na sliki 51 sta rezultat postopka prenosa pravih pogreškov, ki se začne s polarnimi koordinatami posameznih točk v instrumentovem koordinatnem sistemu σ_{φ_i} , σ_{θ_i} in σ_{D_i} (z vsako od teh pomnoženo s faktorjem 3) in nadaljuje vse do končnih točk, ki se uporabijo za izračun premikov, vključno s transformacijo in postopkom modeliranja. Rdeča črtkana črta označuje trikratno skupno položajno natančnost $\sigma_{P_i} = 3 \cdot \sqrt{\sigma_{C_i}^2 + \sigma_{P_{i,int}}^2}$, kjer so σ_{C_i} in $\sigma_{P_{i,int}}$ pripadajoče položajne natančnosti težišč iz prve izmere ter presečišč referenčnih smeri ter ravnin iz druge izmere. Izračuni hkrati pokažejo, da so standardne deviacije premikov (zelene črtkane črte) skoraj tako velike kot večina premikov segmentov. Če povzamemo, analiza rezultatov modela z omejeno smerjo potrjuje, da se površinski pogoji na gladkem delu zidu (v to niso vključene površinske značilke iz slike 47) niso spremenili do nivoja 4 mm, ki ga predvideva postopek prenosa pravih pogreškov. Če so se



Slika 51: Histogram premikov površinskih segmentov kot rezultat modela z omejeno smerjo. Rdeča črtkana črta predstavlja trikratno skupno položajno natančnost parov točk, iz katerih so bili izračunani premiki. Zelena črtkana črta pa predstavlja standardno deviacijo ocenjenih vrednosti premikov.

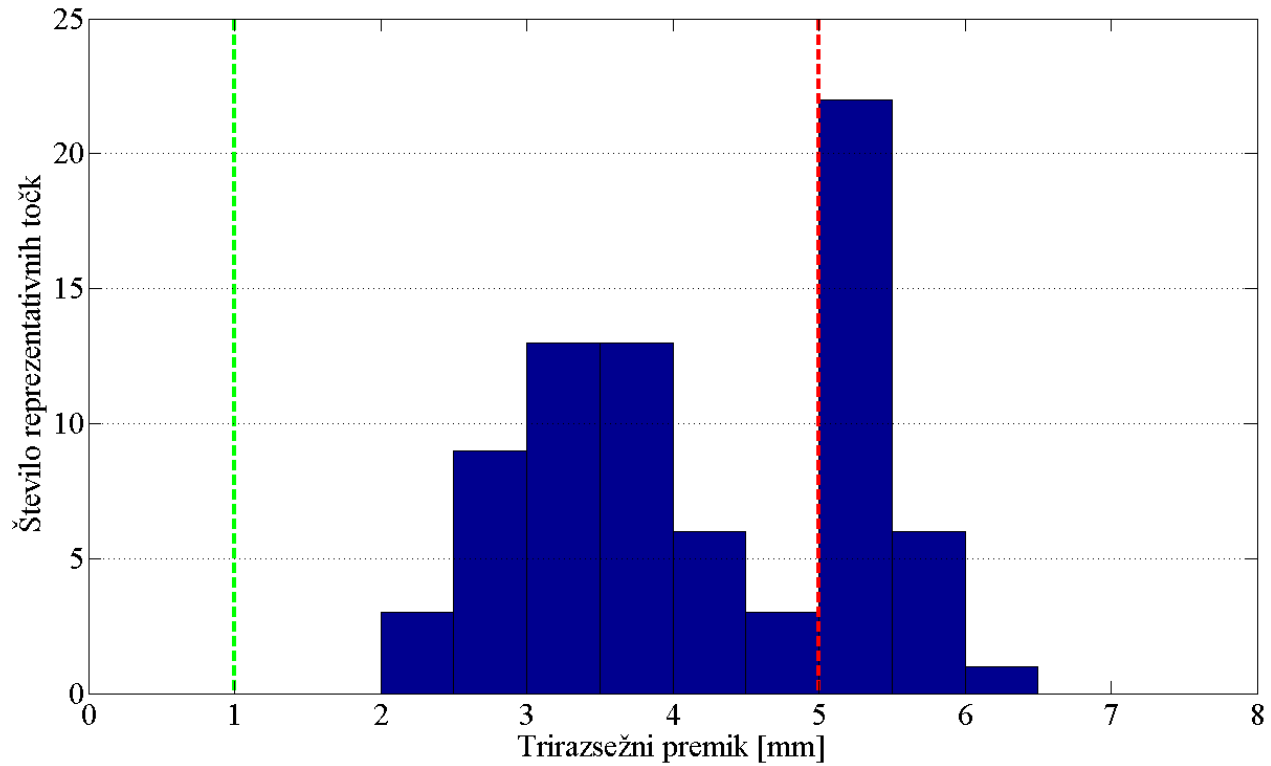
kakršne koli spremembe sicer zares zgodile, teh meritve TLS niso zaznale.

V okviru drugega deformacijskega modela je bilo na površinskih značilkah (glej sliko 47) možno določiti identične reprezentativne točke v presekih sosednjih ravnin, ki so bile s postopkom segmentacije, opisanim v poglavju 2.7.1, odkrite na različnih straneh omenjenih značilk. Te enolične reprezentativne točke so bile izračunane s presekanjem različnih trojic ravnin, pri čemer jih je na celotnem zidu bilo okoli 100. Te točke so omogočale določitev premikov na enak način kot v primeru točkovnega načina geodetske spremljave (kot trirazsežne vektorje). Izmed vseh ravnin, določenih v okviru postopka modeliranja, so se samo tiste, ki so izpolnjevale stroge pogoje segmentacije, uporabile za izračun presečnih točk. Pri tem so se grobo pogrešene točke TLS in robovi vedno izključili iz obdelav, hkrati pa se je za vsako ravno preverjala tudi prostorska razporeditev vektorjev popravkov. Nazadnje so bile presečne točke P_i za posamezno trojico ravnin izračunane po:

$$P_i = \frac{-d_1(\vec{n}_2 \times \vec{n}_3) - d_2(\vec{n}_3 \times \vec{n}_1) - d_3(\vec{n}_1 \times \vec{n}_2)}{\vec{n}_1 \cdot (\vec{n}_2 \times \vec{n}_3)} \quad (26)$$

kjer so \vec{n}_1 , \vec{n}_2 in \vec{n}_3 normalni vektorji pripadajočih ravnin v trojici. Členi d_1 , d_2 in d_3 so konstante v enačbah ravnin, ki se izračunajo na podlagi komponent normalnih vektorjev in težišč. V tem drugem deformacijskem modelu je bila uporabljena podobna strategija prenosa pravih pogreškov kot pri

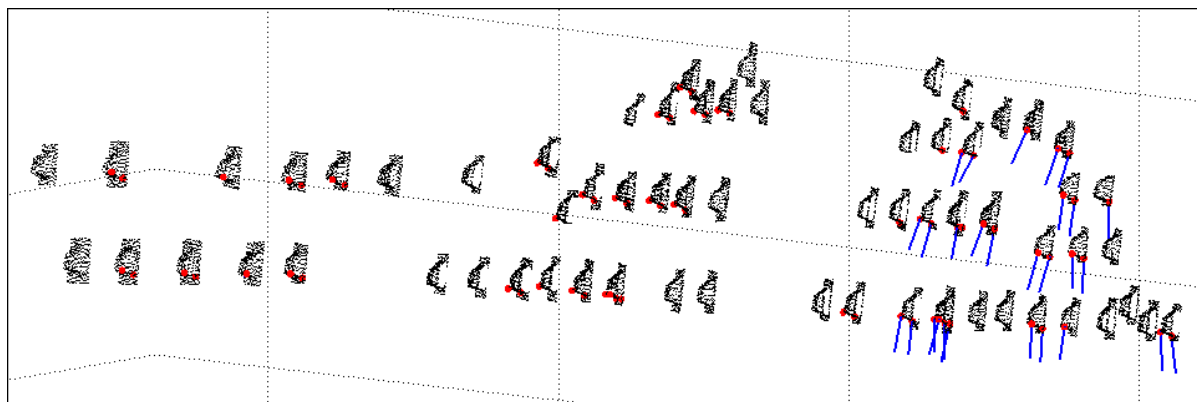
modelu z omejeno smerjo. Edina razlika v modelu 2 je nastala v zadnjem delu postopka prenosa pogreškov, kjer je enačba 26 nadomestila tiste iz modela 1. Rezultati deformacijskega modela 2 so prikazani na sliki 52. Za histogram rezultatov tega deformacijskega modela sta značilna dva vrhova,



Slika 52: Histogram premikov zidu pridobljen iz modela 2. Rdeča in zelena črtkana črta ponazarjata isti kakovostni meji kot na sliki 51, tj. trikratno skupno položajno natančnost in standardno deviacijo ocenjenih vrednosti premikov.

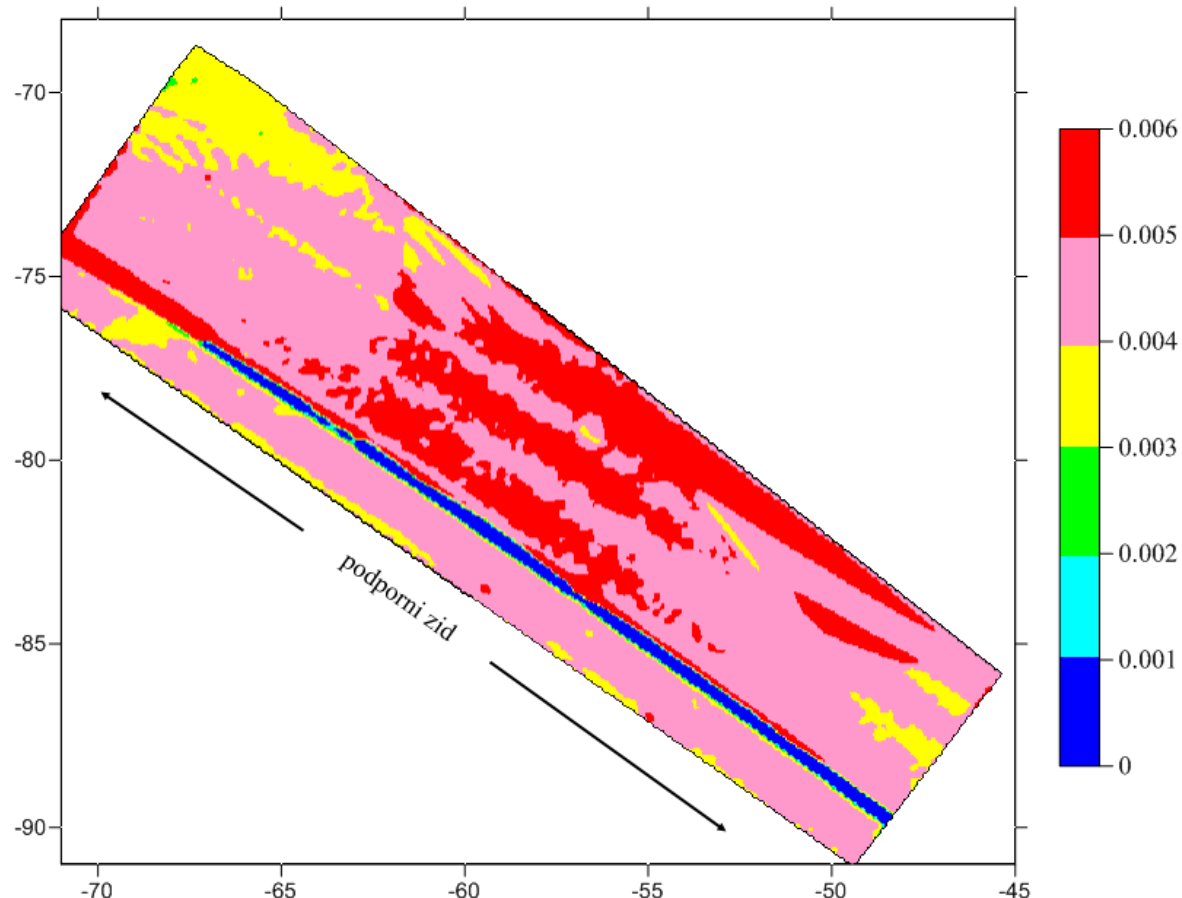
od katerih je samo eden statistično pomemben, tj. tisti nad rdečo črtkano črto. Reprezentativne točke so bile izpostavljene premikom, dovolj velikim, da bi jih lahko imeli za dejanske premike. Glede na smer premikov teh točk rezultati nakazujejo, da je vertikalna komponenta vektorjev premikov tista, ki prevladuje, kar pomeni, da so se vse točke, povezane s premiki večjimi od 5 mm, premaknile navzdol. Še bolj zanimivo je dejstvo, da so statistično pomembni premiki povezani s točkami, ki se nahajajo na delu zidu neposredno nad predorskima osema, kar lahko vidimo na sliki 53. Na sliki 53 so rdeče točke brez pripadajočih vektorjev (modre črte) tiste, ki so se premaknile za manj kot 5 mm, mejo ki ločuje značilne premike od vseh ostalih. Na podlagi rezultatov te analize obstaja velika verjetnost, da se je del zidu iz slike 53 premaknil za okoli 5 do 6 mm. Preostali majhen dvom bi lahko močno zmanjšali, če bi lahko rezultate primerjali z alternativnim merskim postopkom, npr. precizno klasično terestrično metodo.

Po drugi strani pa bi ob prevladujoči in značilni vertikalni komponenti premikov na enem delu zidu pričakovali, da se bo takšen trend pojavil tudi na cesti poleg zidu (glej sliko 46). V primeru, da se rezultati skladajo, bi to lahko dodatno potrdilo končne ugotovitve analize. Zares, kot lahko vidimo na sliki 54, ki prikazuje premike površine ceste, določene v okviru modela z omejeno smerjo,



Slika 53: Smeri vektorjev premikov reprezentativnih točk na zidu. Črne točke, ki predstavljajo oblake točk obravnavanih površinskih značilk, so prikazane zgolj za lažjo orientacijo. Rdeče pike označujejo 100 točk, ki so bile določene s preseki trojic ravnin. Od vseh stotih obravnavanih točk so samo tiste, katerih premik je značilen, prikazane s pripadajočimi smermi premika, tj. modrimi črtami, ki so bile za potrebe prikaza povečane s faktorjem 200.

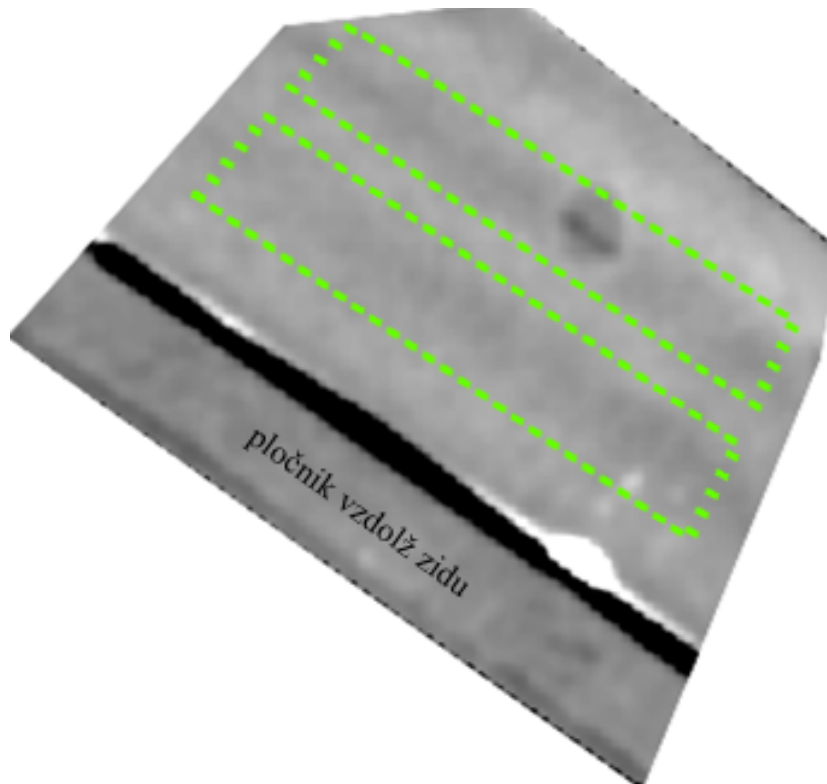
so se tudi na cesti nekateri površinski segmenti premaknili za velikost, ki bi najverjetneje morala biti obravnavana kot dejanski premik. Analiza površine ceste je bila možna le v okviru defor-



Slika 54: Velikost premikov površine ceste. Vrednosti okvirja predstavljajo koordinatni sistem, vrednosti v legendi pa so v [m]. Lokacija tega dela ceste je prikazana na sliki 46.

macijskega modela 1 zaradi gladkosti in pomanjkanja kakršnega koli površinskega detajla, ki bi omogočal določitev reprezentativnih točk. Na podlagi rezultatov iz slike 54 lahko segmente, ki so se premaknili za več kot 4 mm, obravnavamo kot značilne premike, saj so bili zaradi uporabe enakih korakov obdelave kot v primeru zidu rezultati prenosa pravih pogreškov skoraj enaki. To pomeni, da je bila položajna standardna deviacija 4 mm, standardna deviacija premikov pa okoli 1 mm. Poleg tega tudi tukaj vektorji premikov kažejo v isto smer kot tisti, določeni na površinskih značilkah zidu, tj. smer navzdol. Če že torej nimamo na razpolago alternativnega vira informacij, pa lahko vsaj ugotovimo, da so bili podobni rezultati pridobljeni ne samo na dveh različnih lokacijah, ampak tudi z uporabo dveh različnih deformacijskih modelov. Preostalo majhno vrzel do trdnega prepričanja v rezultate lahko praktično zapolnimo samo na podlagi nekih kontrolnih meritev oziroma s pomočjo ponavljanja izmer. Ta druga možnost predstavlja dodaten izhod, saj je v vsaki shemi geodetske spremljave kontinuiteta meritev pomembna in lahko sčasoma hkrati razkrije, ali so trendi premikov opazni v večih izmerah. Na tej točki kažejo zaključki analize v prid izjavi, da sta se tako del zidu kot del ceste premaknila navzdol za okoli 5 mm.

Med to obsežno analizo je bil na površini ceste opažen še en dodaten zanimiv pojav, ki je postal viden po transformaciji oblakov točk v mrežno obliko ter odštetju višin celic vzdolž vertikalne smeri. Skoraj zagotovo so se kolesnice, zaradi nenehnega prometa, na obravnavani cesti sistematično ugreznile za okoli 2 mm. Tako majhni premiki so sicer precej pod mejo statistične značilnosti, vendar pa ob vizualnem pregledu rezultata vzorec postane očiten. Na sliki 55 je ugezanje kolesnic nakazano s črnima pasovoma, ki izstopata od preostalega dela ceste. Odkritje tega vzorca



Slika 55: Vzorec ugezanja kolesnic v obliki mrežnega modela, prikazan od blizu.

je pomembno iz dveh razlogov. Najprej zato, ker ga je mogoče zaznati samo s ploskovno mersko tehnologijo, kot je TLS. Poleg tega pa takšno odkritje ponuja več zaupanja v stopnjo občutljivosti samega instrumenta, saj ta majhna sprememba površine ceste ni ostala neopažena. Posledično lahko torej vključitev metode TLS v geodetsko spremljavo na marsikateri način privede do presenetljivih rezultatov.

4.3 Ovrednotenje laboratorijskih testov

Nazadnje je treba narediti povzetek laboratorijskih testov, če želimo ovrednotiti njihovo kakovost in učinkovitost, nakazano v podpoglavljih, ki so posvečena opisom testnih rezultatov. Ti testi so morali bili izvedeni na zelo pazljiv in dosleden način, da bi se izognili pojavu morebitnih pogreškov. Na podlagi trdnega prepričanja lahko zaključimo, da rezultati laboratorijskih testov, kakršni koli že so, niso bili podvrženi napakam z izvorom v sami izvedbi. Poleg tega lahko tudi idejne zaslove teh testov, zaradi njihove preprostosti, obravnavamo kot dovolj zanesljive za zagotovitev zelo natančnih rezultatov.

Klub kakovostni izvedbi laboratorijskih testov pa bi bilo treba zaradi pojava merskih napak na tako majhnem velikostnem nivoju ponoviti predvsem prvi test, kjer so se mehanske nepopolnosti tarč preverjale na osnovi ročno izvedenih opazovanj. S ponovitvijo testa v različnih pogojih bi se zagotovila večja zanesljivost rezultatov, čeprav se s tem končne ugotovitve tega testa najverjetnejše ne bi spremenile. Dejstvo je, da so štiri v analizo vključene tarče nekoliko različne konstrukcijske kakovosti in da je pogreške, ki se pojavijo pri vrtenju tarč, težko modelirati. Pretežni del teh pogreškov je po velikosti manjši od ± 1 mm, znotraj te meje pa bi bilo treba vzorce odstopanj centrov ponovno preveriti, ne glede na kakovost instrumentarija za izvedbo opazovanj. Zaenkrat se je zaradi očitne stabilnosti upošteval izključno pogrešek vertikalne ekscentricitete za tarčo T4, velikosti 1 mm (glej sliko 11 na strani 148). Preostalega dela pogreškov ni bilo mogoče uspešno modelirati, kar pomeni, da se lahko vpliv tega dela do določene mere odpravi le v okviru ocene transformacije.

Za razliko od velikosti pogreškov v prvem testu so bili v okviru drugega testa odkriti precej večji pogreški. Ker sta bila oba testa zasnovana za analizo vplivov napak, ki neposredno vplivajo na kakovost transformacijskih parametrov v testu v naravi 2, bi bila ob nemodeliranju dolžinskih pogreškov kakovost transformacije precej slabša. Podaljšanje maksimalne razdalje od skenerja do tarče je bilo izvedljivo le s skeniranjem retroreflektivnega dela, na osnovi katerega se oceni dolžina do tarče. Zaradi izbora točk na retroreflektivnem delu površine tarče se pojavijo dolžinske napake velikosti do 1 cm, kar je skoraj desetkrat več od velikostnega reda pogreškov iz prvega laboratorijskega testa. V splošnem lahko s pomočjo korekcijskih funkcij iz preglednice 3 te pogreške zmanjšamo pod mejo enega milimetra, čeprav se lahko ob nestabilnem obnašanju pogreškov učinkovitost modeliranja zmanjša. V testu odkrito nestabilno obnašanje dolžinskih pogreškov predvidoma povzroča retroreflektivni del tarče, lahko pa ima izvor tudi v samem instrumentu. Zaradi tega bo treba za analizo nihanj pogreškov izvesti dodatne teste. Obstaja verjetnost, da je nezmožnost

učinkovitega modeliranja teh nihanj pripomogla k izključitvi meritev nekaterih stojišč v testu v naravi 2. Najverjetneje bi se nihanjem amplitudo lahko izognili le z zamenjavo retroreflektivnega traku na tarči z manj "agresivnim" trakom. V vsakem primeru ostaja iskanje primernejšega tipa tarč v okviru prihodnjih aktivnosti kot tudi izvedba pristopa modeliranja, kjer sta prispevka skenerja in tarče k celotnem dolžinskem pogrešku ločena.

Z rezultati laboratorijskega testa, kjer se je preverjala občutljivost skenerja glede na različne vzorce objektne površine, je bilo možno pridobiti pomembne informacije, ki so se uporabile pri odločitvah o razdalji od skenerja do objekta, omejitvi vpadnega kota ter gostoti točk. Glede na zaključke zadnjega laboratorijskega testa sta bili prilagojeni geometrija in parametri skeniranja v testu v naravi 2 (maksimalna razdalja od objekta 30 m, maksimalni vpadni kot 45° in gostota točk, ki odgovarja minimalno 400 točkam na ploskovni segment). Hkrati se lahko aposteriori standarde deviacije, ocenjene za vsak vzorec posebej (od 1.6 mm do 2.2 mm), uporabijo za nadgradnjo variančno kovariančnih matrik surovih meritev TLS (predvsem za dolžinsko komponento) pri izvedbi postopka prenosa pravih pogreškov. Na osnovi ocenjenih aposteriori vrednosti je bil v okviru testa v naravi 2 prirejen proces modeliranja, pri čemer so se izključili vsi ploskovni segmenti z nivojem šuma večjim od 3 mm. Rezultati zadnjega laboratorijskega testa so ne nazadnje opozorili na negativne učinke, ki so jih povzročila nihanja napetosti pri napajanju skenerja. Zaradi tega se v okviru testa v naravi 2 v intervalih pomanjkanja energije kot tudi v intervalih ponovnega zagona instrumenta skeniranje ni izvajalo, da bi se tako zmanjšal vpliv na zmogljivostne sposobnosti instrumenta. Kot rečeno, so rezultati zadnjega laboratorijskega testa nakazali, da je premike velikosti 2 mm in 5 mm možno razločevati, kar govori v prid končnim ugotovitvam deformacijske analize.

5 ZAKLJUČKI

Rezultate testov, predstavljenih v nalogi, je sedaj treba ovrednotiti z vidika delovne hipoteze, ki je bila izpostavljena v poglavju 1.2. Poleg tega rezultati ponujajo tudi možnost za oceno kakovosti metodoloških korakov, predstavljenih na začetku poglavja 2. Namen te točke je torej v opisu zaključkov celotnega dela, ki je bil izveden za potrebe naloge.

Na podlagi rezultatov naloge je možno podati jasne razloge, da je delovno hipotezo mogoče sprejeti z veliko mero zaupanja. Upoštevanje predlagane metodologije lahko vodi do zelo natančne obravnave deformacij v dolgoročnem pogledu, in sicer na celotni površini objektov in ne samo na manjšem številu signaliziranih (tj. stabiliziranih) točk. Metoda TLS je dokazala svojo sposobnost zagotavljanja zelo natančnih podatkov in jo zato lahko obravnavamo kot komplementarno mersko metodo, ki je ne samo združljiva z ostalimi, dobro uveljavljenimi merskimi tehnikami velike natančnosti, ampak lahko pomembno prispeva k celovitejšemu razumevanju deformacij. Kljub temu pa je analiza pokazala, da ima izvedba meritev TLS v območju milimetrov tudi svojo ceno, saj je tako delo na terenu kot tudi obdelavo podatkov treba opraviti zelo skrbno in preudarno. Poleg tega je znotraj območja milimetrov stopnja zaznave deformacij podvržena različnim vplivom, kot so:

- izbor merske opreme (skener, tarče),
- pogojev na terenu (lastnosti ploskev, oddaljenosti od objekta, vpadnega kota, geometrije geodetske mreže),
- učinkovitost modeliranja sistematičnih pogreškov (kalibracijski parametri),
- ustrezne in pravilnega načina prenosa pravih pogreškov, ki zajema vse korake obdelave meritev.

Ocenjevanje premikov in deformacij pod nominalnimi sposobnostmi skenerja je načeloma izvedljivo. To dejstvo je bilo dokazano v okviru testa v naravi 1, kjer je bila metoda TLS uporabljena za določitev osi stebrov. V tem testu so se rezultati TLS ujemali z rezultati precizne klasične terestrične metode do visoke stopnje. Analiza meritev testa 1, ki je bila prvič objavljena v Vezočnik in sod. (2009), je bila v nalogi izvedena še korak naprej, čeprav ostajajo objavljeni končni rezultati v članku nespremenjeni. Po drugi strani je bila vloga metode TLS v testu 2 še precej večja in je kljub nekaterim problemom z instrumentom ter absolutno orientacijo zagotovila obetajoče rezultate z vidika možnosti uporabe metode TLS za potrebe zelo natančne geodetske spremljave. V obeh testih v naravi sta bili vzpostavitev enakih snemalnih pogojev na terenu in izvedba obdelave meritev na osnovi enakih korakov obravnavani kot pomembna vidika splošnega metodološkega pristopa, da bi se tako izognili kopiranju kakršnih koli dodatnih pogreškov. Če želimo, da bo v dolgoročnem pogledu spremjanje premikov in deformacij učinkovito, potem je te pogreške treba karseda minimizirati.

Modeliranje sistematičnih pogreškov in določevanje kalibracijskih parametrov za vso mersko opremo je prav tako nujno. Brez tega koraka, vključenega v metodološki pristop, so lahko zmožnosti

analize deformacij v območju milimetrov močno omejene. Ne samo, da je modeliranje sistematičnih pogreškov treba vključiti v proces obdelave meritev, ampak bi bilo kalibracijske parametre (npr. funkcije pogreška dolžine pri tarčah, sistematične pogreške skenerja) treba določati na osnovi pogostih in rednih testov, saj bi le tako njihova ocena temeljila na veliki redundanci opazovanj (po možnosti zajetih v različnih okoljskih pogojih). Na ta način bi postalo tudi jasno, kaj se dogaja z njihovo časovno stabilnostjo. Ne nazadnje so zaželeni tudi dodatni testi o odzivnosti površinskih materialov, ki bi zagotavili informacije o stabilnosti skenerjeve zmogljivostne stopnje.

K analizi premikov in deformacij ni mogoče pristopiti brez ustreznega in pravilnega postopka prenosa pravih pogreškov. Poleg tega je med fazo modeliranja pomembna vpeljava primerenega stohastičnega modela ter realistično ocenjevanje mer natančnosti za vse vhodne podatke obeh deformacijskih modelov. S tem se izognemo preveč optimističnim standardnim deviacijam, ki so v veliko primerih samo odraz velike redundance meritev TLS. Glede na rezultate, predstavljene v poglavju 4, so takšne sheme prenosa pogreškov razkrile, da lahko TLS v določenih primerih pri odkrivanju premikov in deformacij seže pod nivo 5 mm. Kljub temu pa ostajojo premiki velikosti 1 mm nedosegljivi, vsaj po uporabi trikratnega pravila za natančnost točk. Z vidika velikosti zaznanih premikov je meja 5 mm veliko bolj realistična, še posebaj kadar obravnavamo večje objekte oziroma kadar snemalni pogoji niso idealni. Stopnjo zaznave lahko nekoliko povečamo, če skeniramo objekt z večkratnimi skenogrami in povprečimo rezultate. Večkratni skenogrami lahko hkrati prispevajo k stabilnosti zaznave deformacij, kot je bilo pokazano med testiranjem odzivnosti površinskega materiala.

Snemalni pogoji lahko ne nazadnje odločijo, ali lahko podatke uporabimo za ugotavljanje sprememb na tako majhnem velikostnem nivoju. V okviru testa v naravi 2 so neidealni pogoji, in sicer glede števila tarč TLS in geometrije mreže, prispevali v izločitvi meritev nekaterih stojišč. Če želimo premostiti takšno oviro, je priporočljivo uporabiti več tarč na stojišče ter tako povečati natančnost in stabilnost ocenjenih transformacijskih parametrov. Da ob tem s klasično terestrično izmero ne bi podaljšali celotne izmere na terenu, vseh tarč ni nujno treba vključiti v geodetsko mrežo, ampak jih lahko uporabimo izključno za namene relativne orientacije. Kakovost relativne orientacije lahko nadalje izboljšamo s pomočjo ustrezne integracije tarč in postopka ICP (Haring, 2007). Po izračunu parametrov relativne orientacije med sosednjimi stojišči skenerja lahko v naslednjem koraku celoten blok (tj. vse meritve TLS z vseh stojišč) sočasno umestimo v referenčni sestav. Za izvedbo analize o kakovosti transformacije tudi na strani objekta je potrebno upoštevati tudi velikost območij preklopov. Z današnjimi skenerji, ki jih odlikuje zelo velika hitrost skeniranja, lahko velikost območij preklopov povečamo preko 50 % brez posebne izgube časa. Več kot je teh območij in večja kot so, boljšo kontrolo na kakovostjo transformacije lahko zagotovimo.

Za okrepitev stopnje zaupanja v rezultate analize deformacij je včasih priporočljivo stabilizirati nekaj kontrolnih točk na obravnavani objekt in oceniti njihove položaje s pomočjo alternativne merske tehnologije. Takšen večsenzorski način geodetske spremljave je zagotovo eden od današnjih trendov in bo pomemben tudi v prihodnosti. Vključitev kontrolnih točk in komplementarnih geodetskih tehnik ne poslabša kakovosti predlaganega metodološkega pristopa, ampak lahko v

končnem pripomore k stopnji zaupanja v rezultate takšnih občutljivih geodetskih nalog, ne glede na tip uporabljenih tehnologij.

5.1 Smernice nadaljnega raziskovalnega dela

Kljud predstavljenemu delu v nalogi ostajajo nekatere teme predmet nadalnjih raziskav v bližnji prihodnosti. Bodoči raziskovalni cilji bodo osredotočeni na spodaj navedena področja, ki lahko ne nazadnje prispevajo k skupni kakovosti predlaganega pristopa analize deformacij iz meritev TLS:

- umeščanje oblakov točk znotraj referenčnega sestava,
- časovna stabilnost kalibracijskih parametrov (tako za skener kot tudi za tarče),
- testiranje zmogljivosti skenerja na večjem številu vzorcev različnih površinskih lastnosti,
- zmanjšanje skupnega časa izvedbe in obdelave meritev,
- realizacija *ad hoc* multisenzorskih merskih zasnov za spremljanje premikov in deformacij.

Prvi izmed ciljev se neposredno nanaša na iskanje optimalnih tarč TLS, ki bi bile z vidika sistematičnih pogreškov zelo kakovostne, hkrati pa bi jih bilo možno integrirati z ostalimi reflektorji v skupno konstrukcijsko zasnovo. Na ta način bi se lahko zmanjšale oz. nadzorovale morebitne ekscentritete, kar bi zagotovljalo, da se pri menjavi enega reflektorja z drugim ne bi pojavile nepotrebne napake. Glede na rezultate predstavljeni v nalogi lahko zaključimo, da je koordinatna ocena položajev točk v geodetski mreži lahko precej večja kot ocena položajev tarč iz meritev TLS. Največkrat glavni razlog za takšno ugotovitev ni kakovost postopka ocene centrov tarč, ampak slabša učinkovitost modeliranja sistematičnih pogreškov na strani tarč. Posledično lahko nezmožnost nadzorovanja teh sistematičnih pogreškov vpliva na kakovost transformacije. Zaradi tega bo treba v okviru nadalnjih raziskav izboljšati učinkovitost modelov za minimizacijo sistematičnih pogreškov, ki se pojavijo med oceno transformacijskih parametrov.

Na vidiku ostaja, kot eden izmed pomembnih ciljev, tudi sistematična izvedba kalibracije skenerja. Skenerja, ki sta bila uporabljena za izvedbo testnih meritev sta bila kalibrirana samo s strani proizvajalcev, kar pomeni, da bo treba poglobiti znanje o prisotnosti kakršnih koli dodatnih oz. preostalih sistematičnih pogreškov in jih poskusiti ustrezno modelirati. Poleg tega bo treba v okviru bodočih testov raziskati časovno stabilnost kalibracijskih parametrov tako na strani skenerja kot tudi stabilnost sistematičnih pogreškov na strani tarč (npr. vrednosti parametrov funkcij pogreška dolžine). Časovna stabilnost teh parametrov bo ne nazadnje podala informacijo o kakovosti izbrane merske opreme TLS in narekovala pogoje njene uporabe v nalogah geodetske spremljave (tudi z vidika stopnje zaznave premikov in deformacij). Na osnovi primerne razporeditve stojišč skenerja med izvedbo terminskih izmer lahko veliko redundanco meritev TLS uporabimo tudi za namene sprotne kalibracije (*on-the-job calibration*), opisane npr. v Dorninger in sod. (2008), Molnár in sod. (2009) ali Bae in Lichti (2010).

V okviru naslednje naloge bo treba natančnost izmere dolžin TLS testirati na večjem številu vzorcev

različnih površinskih lastnosti. Vzorci se morajo razlikovati glede na kemično sestavo, barvo, hrapavost in vsebnost vlage, da bi lahko tako vzpostavili ustreznou podatkovno bazo, ki bi pomagala ne samo pri izbiri primernih objektnih površin za skeniranje, ampak tudi pri določitvi pogojev skeniranja (npr. z vidika razdalje od objekta in vpadnega kota). Testiranje zmogljivosti skenerja na večih vzorcih bo pripomoglo k izboljšavi vpogleda v omejitve uporabe metode TLS za dolgoročno spremeljanje deformacij.

Ne nazadnje bo treba optimizirati skupen čas za zajem in obdelavo meritev do takšne mere, ki bo še vedno zagotavljala analizo deformacij v območju milimetrov. Kljub temu je vredno poudariti, da je treba za dosego milimetrskega nivoja meritve izvesti zelo pazljivo, kar seveda preprečuje zelo očitno zmanjšanje časa tako na terenu kot tudi v fazi obdelave meritev. Vendar pa bi s poskusom poenostavitev postopkov obdelave meritev metodologijo lahko približali manj usposobljenim operaterjem. Zaenkrat je skupen čas izvedbe in obdelave meritev primerljiv z ostalimi zelo natančnimi geodetskimi nalogami. Vendar pa bodo v prihodnosti smernice skoraj zagotovo usmerjene v bolj avtomatiziran način spremljave, in sicer z uporabo multisenzorskih zasnov, pri čemer bo vsaka komponenta služila za točno določeno nalogu, kar bo hkrati zagotavljalo pogostejo izvedbo opazovanj obravnavanega objekta. Takšne multisenzorske zaslove se bodo lahko izognile fazi skeniranja tarč in oceni njihovih centrov, s tem pa tudi vsem pogreškom, ki izvirajo iz teh postopkov. Ideja je namreč v trajni stabilizaciji skenerja na mersko platformo (npr. steber), ki se nahaja v bližini obravnavanega objekta, kar bi omogočalo popolno pokritost njegove površine s točkami TLS. Stabilnost merske platforme bi se lahko preverjala s pomočjo preciznih klasičnih terestričnih meritve iz oddaljenih stojišč, ki bi bila stabilizirana na stabilnih tleh. Klasične terestrične meritve ne bi služile izključno za preverjanje stabilnosti stojišča skenerja na daljavo, ampak bi bile hkrati zasnovane tako, da bi se ob izvedbi pogostih in avtomatiziranih opazovanj med temi oddaljenimi stojišči preverjala tudi stabilnost referenčnega sestava. Avtomatiziran postopek izmere bi zmanjšal količino dela na terenu in omogočal preverjanje trenutnega stanja obravnavanega objekta na osnovi bolj pogostih ploskovnih meritvev, kar bi zagotovo v veliki meri prispevalo k stopnji zanesljivosti in razumevanja končnih rezultatov analize deformacij.

6 POVZETEK

Spremljanje premikov in deformacij antropogenih prostorskih struktur in objektov predstavlja eno izmed najbolj zahtevnih področij v geodeziji. V zadnjih nekaj letih je terestrično lasersko skeniranje (TLS) postalo pospešeno vključeno v različne naloge inženirske geodezije, vključno s področjem spremeljanja premikov in deformacij. Kljub naraščajočemu številu predstavljenih rešitev pa ostaja odkrivanje milimetrskih premikov še vedno zelo aktivno področje raziskovanja, kar je eden od razlogov za poskus ovrednotenja potencialnih možnosti uporabe te zanimive merske tehnologije na tako majhnem velikostnem nivoju. V primerjavi z ostalimi senzorskimi tehnologijami in točkovnimi načini spremeljanja, kjer je ugotavljanje deformacij omejeno na nekaj diskretnih in dobro signaliziranih točk, ima metoda TLS nekatere prednosti, in sicer:

- sposobnost hitrega in ploskovnega načina izmere,
- zmožnost modeliranja oblike objektov na osnovi velike redundance meritev,
- brezkontaktna narava, ki ne zahteva neposrednega dostopa do objekta.

Glede na trenutno stanje na raziskovalnem področju je bilo smiselno pristopiti k opredelitvi delovne hipoteze, ki pravi, da je z vidika dolgoročnega spremeljanja metodo TLS možno uporabiti za ugotavljanje premikov in deformacij v območju milimetrov. Takšno ovrednotenje je zahtevalo povezavo metode TLS z ostalimi geodetskim merskimi tehnologijami (opazovanja GNSS, precizna klasična terestrična izmera), da bi lahko zagotovili kakovost in stabilnost referenčnega sestava. Naloga poskuša obravnavati te probleme v okviru predlaganega metodološkega pristopa.

Predlagani metodološki pristop je razdeljen na sedem različnih korakov, pri čemer je bilo slednje treba do podrobnosti analizirati in po potrebi prilagoditi, da bi lahko izpolnili zahteve po veliki natančnosti. Ti koraki predstavljajo neke vrste smernice, ki se lahko uporabijo pri kakršni koli nalogi spremljave z metodo TLS, ne glede na obravnavani objekt in stopnjo površinskega detajla. Prvi korak se posveča delu metodološkega pristopa, ki je z vidika dolgoročne geodetske spremljave eden izmed najbolj problematičnih, in sicer načinom kontrole kakovosti in stabilnosti referenčnega sestava. Referenčne točke morajo biti stabilizirane izven območja deformacij, kar lahko v določenih primerih pomeni daleč stran od obravnavanih objektov. Zaradi tega je za zagotavljanje dolgoročne povezave med temi referenčnimi točkami in oblaki točk objektnih površin slednje treba umestiti v izbrani referenčni sestav s pomočjo tarč TLS. V koraku 2 se predlaga, da se tarče TLS (postavljene v okolici opazovanega objekta) vključijo v geodetsko mrežo, ki zajema tudi referenčne in kontrolne točke. Položaje tarč TLS je treba hkrati oceniti na vsakem stojišču skenerja na podlagi skenogramov visoke ločljivosti. V ta namen so v okviru koraka 3 predstavljene možnosti za izvedbo tega postopka ekstrakcije in ocene centrov, pri čemer je bil za potrebe naloge predlagan alternativni pristop k oceni centrov uporabljenih tarč. V koraku 4 je treba oceniti transformacijo, na podlagi katere lahko oblaki točk objektnih površin končno umestimo v referenčni sestav. Po vzpostavitvi povezave z referenčnim sestavom se preostali koraki metodološkega pristopa najprej osredotočijo na opis načina

skeniranja obravnavanih objektnih površin z vidika zagotovitve homogene točkovne pokritosti ter omejitev procesa zajema meritev TLS. Sledijo smernice procesa modeliranja ploskev, ki predstavlja pomemben del metodološkega pristopa, če želimo v celoti izkoristiti veliko redundanco podatkov. Ploskovni modeli se nazadnje analizirajo v okviru dveh predlaganih deformacijskih modelov, ki so bili izdelani za uporabo v povsem splošnih okoliščinah. Izbera modela je odvisna izključno od količine površinskega detajla. Prvi model se lahko vedno uporabi, medtem ko je drugi omejen na ploskve z zadostno količino detajla. Ne glede na uporabljen model je v vsakem primeru treba vzporedno izvesti prenos pravih pogreškov, če želimo ločiti dejanske premike od merskih napak. Na osnovi predlaganih metodoloških korakov sta bila v naravi izvedena dva testa za analizo premikov in deformacij treh objektov (plinovoda v testu 1, podpornega zidu in ceste v testu 2). Pred izvedbo testov v naravi so bili opravljeni dodatni trije laboratorijski testi za analizo dveh ključnih komponent metodološkega pristopa:

- kakovosti tarč TLS,
- zmogljivosti razdaljemera skenerja glede na različne površinske lastnosti.

Kakovost tarč TLS je bila analizirana v okviru dveh ločenih testov, tj. testa za preverjanje mehanskih nepopolnosti in testa za analizo obnašanja sistematičnih pogreškov dolžin TLS, ki so se pojavili zaradi skeniranja retroreflektivnega dela tarč s skenerjem, ki je bil uporabljen v testu v naravi 2. Rezultati prvega od teh dveh testov so razkrili razlike med štirimi uporabljenimi tarčami kljub dejству, da so vse enakega tipa. Drugi test je bil zagotovo upravičen, saj je razkril velike sistematične pogreške dolžin TLS, ki jih je bilo treba za vsako tarčo posebej modelirati. Rezultati obeh testov so pomembno prispevali k definiranju obsega vplivov napak, katerim je ne nazadnje podvržena kakovost transformacijskih parametrov. Poleg tega je bila izključno za potrebe testa v naravi 2 analizirana tudi zmogljivost skenerja glede na vpliv različnih površinskih lastnosti na izmero dolžin TLS. Testni vzorci so zajemali najpogosteje zastopane površinske pogoje v testu v naravi 2. Rezultate tega testa je bilo možno uporabiti pri odločitvah glede razdalje od skenerja do objekta, omejitev vpadnega kota ter gostote točk. Na podlagi ugotovitev laboratorijskih testov je bilo treba terminske izmere testov v naravi ustrezno prilagoditi, da bi se vnos merskih napak karseda zmanjšal. Upoštevajoč priporočila metodološkega pristopa, so bili v okviru obeh testov v naravi vzpostavljeni enaki snemalni pogoji, in sicer v dveh terminskih izmerah za vsak test. Za razliko od testa v naravi 1, kjer je bila kakovost in stabilnost referenčnih točk analizirana z opazovanji GNSS, se ta korak zaradi predpostavke o stabilnosti tal pri testu v naravi 2 ni izvedel. V fazi obdelave meritev obeh testov v naravi so bila klasična terestrična opazovanja med točkami v mreži izravnana z veliko natančnostjo, upoštevajoč meritve trenutnih atmosferskih pogojev. Po transformaciji oblakov točk objektnih površin v referenčni sestav se je v testu 1 oblika obravnavanih ploskev modelirala s pomočjo modela valja, v testu 2 pa z ravninskim modelom. Zaradi velikosti objektov v testu 2 je bil postopek modeliranja izведен bodisi z razdelitvijo izvornih oblakov točk na ploskovne segmente bodisi na podlagi postopka segmentacije, ki je bil predlagan v koraku 6 metodološkega pristopa. Končni rezultati obeh testov v naravi, tj. ploskovni modeli in njim pripadajoče ocenjene mere natančnosti,

so predstavljali vhodne podatke za deformacijsko analizo.

Ker se oblika modelov ni deformirala, je bilo v testu v naravi 1 ploskovne modele mogoče reducirati na nivo reprezentativnih točk, ki niso ležale na površini objektov. Pri določitvi teh reprezentativnih točk so sodelovale kontrolne točke, ocenjene iz klasičnih terestričnih meritev. Tako klasične terestrične meritve kot opazovanja GNSS so potrdila stabilnost referenčnih točk v mreži med obema izmerama. Po drugi strani je analiza razkrila, da so se obravnavani objekti premaknili za okoli 2 do 10 mm. Prenos pravih pogreškov v testu 1 je razkril, da lahko premike večje od ≈ 2 mm obravnavamo kot značilne. V testu v naravi 2 je bilo podporni zid mogoče analizirati v okviru obeh deformacijskih modelov, pri čemer rezultati prvega modela niso nakazali prisotnosti kakršnih koli premikov in deformacij. Kljub temu pa so rezultati drugega modela razkrili, da se je del podpornega zida v vertikalni smeri premaknil za 5 do 6 mm. Ti rezultati so bili potrjeni pri analizi površine ceste, ki je bila izvedena v okviru prvega deformacijskega modela. Velikost in smer premikov je bila tako ocenjena na osnovi dveh različnih pristopov (deformacijskih modelov) na dveh sosednjih objektih. V testu v naravi 2 je prenos pravih pogreškov razkril, da lahko premike večje od 4 mm (za prvi deformacijski model) in 5 mm (za drugi deformacijski model) obravnavamo kot značilne. Na osnovi rezultatov laboratorijskih testov bi takšen velikostni nivo premikov moral biti znotraj zmogljivosti tako skenerja kot tarč. Ne nazadnje je bilo med analizo površine ceste ugotovljeno, da so se kolesnice v manj kot enem letu sistematično ugrenile za okoli 2 mm.

Na podlagi rezultatov naloge je možno podati jasne razloge, da je delovno hipotezo mogoče sprejeti z veliko mero zaupanja. Upoštevanje predlagane metodologije lahko vodi do zelo natančne obravnave deformacij v dolgoročnem pogledu, in sicer na celotni površini objektov in ne samo na manjšem številu signaliziranih (tj. stabiliziranih) točk. Metoda TLS je dokazala svojo sposobnost zagotavljanja zelo natančnih podatkov in jo zato lahko obravnavamo kot komplementarno mersko metodo, ki je ne samo združljiva z ostalimi, dobro uveljavljenimi merskimi tehnikami velike natančnosti, ampak lahko pomembno prispeva k celovitejšemu razumevanju deformacij. Kljub temu k analizi premikov in deformacij ni mogoče pristopiti brez ustreznegra in pravilnega postopka prenosa pravih pogreškov. Poleg tega je med fazo modeliranja pomembna vpeljava primerenega stohastičnega modela ter realistično ocenjevanje mer natančnosti za vse vhodne podatke obeh deformacijskih modelov. S tem se izognemo preveč optimističnim standardnim deviacijam, ki so v veliko primerih samo odraz velike redundance meritev TLS. Glede na rezultate so takšne sheme prenosa pogreškov razkrile, da lahko TLS v določenih primerih pri odkrivanju premikov in deformacij seže pod nivo 5 mm. Kljub temu pa ostajajo premiki velikosti 1 mm težko dosegljivi. Z vidika velikosti zaznanih premikov je meja 5 mm veliko bolj realistična, še posebaj kadar obravnavamo večje objekte oziroma snemalni pogoji niso idealni.

7 VIRI

Alba, M., Fregonese, L., Prandi, F., Scaioni, M., Valgoi, P. 2006. Structural monitoring of a large dam by terrestrial laser scanning. V: Proceedings of International Archives of Photogrammetry, Remote Sensing and Spatial Information Sciences. Dresden, Nemčija, 25.–27. september. letnik XXXVI, del 5 (CD-ROM).

Altamimi, Z., Collilieux, X., Legrand, J., Garayt, B., Boucher, C. 2007. ITRF2005: A new release of the international terrestrial reference frame based on time series of station positions and earth orientation parameters. *Journal of Geophysical Research*, letnik 112, št. B09401: 1–19.
doi: 10.1029/2007JB004949

Bae, K. H., Lichti, D. D. 2010. On-site self-calibration using planar features for terrestrial laser scanners. V: Proceedings of the ISPRS Workshop – Laser Scanning 2007 and SilviLaser 2007. Espoo, Finska, 12.–14. september. letnik XXXVI, del 3: str. 14–19.

Austin, R. L., Schultz, R. J. 2006. Guide to Retroreflection Safety Principles and Retroreflective Measurements. American Traffic Safety Services Association. Fredericksburg, Virginija.
<http://atssa.com/galleries/default-file/RetroreflectionGuide-ATSSA.pdf> (pridobljeno 7.11.2010).

Bergeot, N., Bouin, M. N., Diament, M., Pelletier, B., Régnier, M., Calmant, S., Ballu, V. 2009. Horizontal and vertical interseismic velocity fields in the Vanuatu subduction zone from GPS measurements: Evidence for a central Vanuatu locked zone. *Journal of Geophysical Research*, letnik 114, št. B06405: 1–20.

doi: 10.1029/2007JB005249

Besl, P. J., McKay, H. D. 1992. A method for registration of 3-D shapes. *Pattern Analysis and Machine Intelligence*, letnik 14, št. 2: 239–256.

Beutler, G., Rothacher, M., Schaer, S., Springer, T. A., Kouba, J., Neilan, R. E. 1999. The International GPS Service (IGS): An interdisciplinary service in support of Earth sciences. *Advances in Space Research*, letnik 23, št. 4: 631–653.

Boucher, C., Altamimi, Z. 2008. Memo: Specification for reference frame fixing in the analysis of a EUREF GPS campaign, Version 7.
<http://etrs89.ensg.ign.fr/memo-V7.pdf> (pridobljeno 24.10.2008).

Caporali, A., Aichhorn, C., Barlik, M., Becker, M., Fejes, I., Gerhatova, L., Ghitau, D., Grenerczy, G., Hefty, J., Krauss, S., Medak, D., Milev, G., Mojzes, M., Mulic, M., Nardo, A., Pesec, P., Rus, T., Simek, J., Sledzinski, J., Solaric, M., Stangl, G., Stopar, B., Vespe, F., Virag G. 2009. Surface kinematics in the Alpine-Carpathian-Dinaric and Balkan region inferred from a new multi-network GPS combination solution. *Tectonophysics*, letnik 474, št. 1-2: 295–321.

Caspary, W. F. 1988. Concepts of Network and Deformation Analysis, Monograph 11. School of Surveying. Univerza Novi Južni Wales: str. 68–96.

Chatfield, C. 1995. The Analysis of Time Series, An Introduction. Fifth Edition. Univerza v Bathu, Chapman & Hall: str. 18–25.

Chrzanowski, A. 2006. Tasks and achievements of the FIG Working Group on deformation measurements and analysis. V: Proceedings of 3rd IAG Symposium of Geodesy for Geotechnical and Structural Engineering and 12th FIG Symposium on Deformation Measurements. Baden, Avstrija, 22.–24. maj.

http://www.fig.net/commission6/baden_2006/pdf/oc/chrzanowski_fig.pdf (pridobljeno 24.10.2008).

Ciddor, P. E. 1996. Refractive index of air: new equations for the visible and near infrared. *Applied Optics*, letnik 35, št. 9: 1566–1573.

Ciddor, P. E., Hill, R. J. 1999. Refractive index of air. 2. Group Index. *Applied Optics*, letnik 38, št. 9: 1663–1667.

Dach, R., Hugentobler, U., Frizez, P., Meindl, M. 2007. Bernese GPS Software, Version 5.0. Univerza v Bernu, Astronomski inštitut.

Dorninger, P., Nothegger, C., Pfeifer, N., Molnar, G. 2008. On-the-job detection and correction of systematic cyclic distance measurement errors of terrestrial laser scanners. *Journal of Applied Geodesy*, letnik 2, št. 4: 191–204.

EUREF Permanent Network. Guidelines for EPN Analysis Centres.

http://www.epncb.oma.be/_organisation/guidelines/guidelines_analysis_centres.pdf (pridobljeno 12.3.2009).

Even-Tzur, G., Salmon, E., Kozakov, M., Rosenblum, M. 2004. Designing a geodetic-geodynamic network: A comparative study of data processing tools. *GPS Solutions*, letnik 8, št. 1: 30–35.

Gonzales-Aguilera, D., Gomez-Lahoz, J., Sanchez, J. 2008. A new approach for structural monitoring of large dams with a three-dimensional laser scanner. *Sensors*, letnik 8, št. 9: 5866–5883.

Gordon, S. J., Lichti, D. D. 2007. Modelling of terrestrial laser scanner data for precise structural deformation measurement. *Journal of Surveying Engineering*, letnik 133, št. 2: 72–80.

Haring, A. 2007. Die Orientierung von Laserscanner- und Bilddaten bei der fahrzeuggestützten Objekterfassung. Disertacija. Tehnična univerza za Dunaju, Inštitut za fotogrametrijo in daljinsko zaznavanje: 156 str.

Hoover, A., Jean-Baptiste, G., Jiang, X., Flynn, P. J., Bunke, H., Goldgof, D. B., Bowyer, K., Eggert, D. W., Fitzgibbon, A., Fisher, R. B. 1996. An Experimental Comparison of Range Image Segmentation Algorithms. *IEEE Transactions on Pattern Analysis and Machine Intelligence*, letnik 18, št. 7: 673–689.

Horn, B. K. P. 1987. Closed-form solution of absolute orientation using unit quaternions. *Journal of the Optical Society of America*, letnik 4, št. 4: 629–642.

Horn, B. K. P. 1988. Closed-form solution of absolute orientation using orthonormal matrices. *Journal of the Optical Society of America*, letnik 5, št. 7: 1127–1135.

International Terrestrial Reference Frame.

<http://itrf.ensg.ign.fr> (pridobljeno 10.9.2009).

International GNSS Service.

<http://igscb.jpl.nasa.gov/igscb/center/analysis> (pridobljeno 10.8.2009).

Jelalian, A. V. 1992. Laser Radar Systems. Boston, Artech House: 292 str.

Joeckel, R., Stober, M. 1989. Elektronische Entfernungs- und Richtungsmessung. Stuttgart, Wittwer: str. 152–176.

Kersten, T., Sternberg, H., Mechelke, K., Acevedo Prado, C. 2004. Terrestrial laserscanning system MENSI GS 100/GS 200 - accuracy tests, experiences and projects at the Hamburg University of Applied Sciences. Panoramic Photogrammetry Workshop 2004, organizirana od TU Dresden, Univerze v Stuttgartu in ISPRS WG V/1. 19.–22. februar.

http://www.commission5.isprs.org/wg1/workshop_pano/papers/PanoWS_Dresden2004_Kersten.pdf (pridobljeno 5.11.2007).

Kogoj, D. 2005. Merjenje dolžin z elektronskimi razdaljemerji. Ljubljana, Fakulteta za gradbeništvo in geodezijo: str. 111–147.

Kraus, K., Pfeifer, N. 1998. Determination of terrain models in wooded areas with airborne laser scanner data. *ISPRS Journal of Photogrammetry and Remote Sensing*, letnik 53, št 4: 193–203.

Kuang, S. 1996. Geodetic network analysis and optimal design: concepts and applications. Chelsea, Ann Arbor Press, Inc.: str. 83–92.

Laser Scanning Europe GmbH.

<http://www.laserscanning-europe.com> (pridobljeno 12.1.2011).

Leica Geosystems AG.

<http://www.leica-geosystems.com/en/index.htm> (pridobljeno 9.1.2011).

- Lichti, D. D. 2007. Error modelling, calibration and analysis of an AM-CW terrestrial laser scanner system. *ISPRS Journal of Photogrammetry and Remote Sensing*, letnik 61, št. 5: 307–324.
- Lovas, T., Berényi, A. 2009. Laser scanning in deformation measurement. *GIM International*, letnik 23, št. 3: 17–21.
- Luhmann, T., Robson, S., Kyle, S., Harley, I. 2006. Close Range Photogrammetry. Principles, Methods and Applications. Dunbeath, Whittles Publishing: str. 87–88.
- Mao, A., Harrison, C. G. A., Dixon, T. H. 1999. Noise in GPS coordinate time series. *Journal of Geophysical Research*, letnik 104, št. B2: 2797–2816.
doi:10.1029/1998JB900033
- Mervat, L. 1995. Ambiguity Resolution Techniques in Geodetic and Geodynamic Applications of Global Positioning System. Disertacija. Univerza v Bernu, Astronomski inštitut: 155 str.
- McCarthy, D. D., Petit, G. IERS Conventions (2003), IERS Technical note 32.
<http://www.iers.org/MainDisp.csl?pid=46-25776> (pridobljeno 23.1.2009).
- Molnár, G., Pfeifer, N., Ressl, C., Dorninger, P., Nothegger, C. 2009. On-the-job Range Calibration of Terrestrial Laser Scanners with Piecewise Linear Functions. *Photogrammetrie, Fernerkundung, Geoinformation*, št. 1: 9–22.
- Niell, A. E. 1996. Global mapping functions for the atmosphere delay at radio wavelengths. *Journal of Geophysical Research*, letnik 101, št. B2: 3227–3246.
doi:10.1029/95JB03048.
- Nikon.
<http://www.nikonmetrology.com> (pridobljeno 29.9.2010).
- Onsala Space Observatory.
<http://www.oso.chalmers.se/> loading (pridobljeno 9.3.2009).
- Park, H.S., Lee, H. M. 2007. A new approach for health monitoring of structures: Terrestrial laser scanning. *Computer Aided Civil and Infrastructure Engineering*, letnik 22, št. 1: 19–30.
- Pesci, A., Teza, G. 2008. Terrestrial laser scanner and retro-reflective targets: an experiment for anomalous effects investigation. *International Journal of Remote Sensing*, letnik 29, št. 19: 5749–5765.
- Rees, W. G. 2001. Physical Principles of Remote Sensing, Second Edition. Cambridge, Cambridge University Press: str. 46–61.

Reshetyuk, Y. 2009. Terrestrial laser scanning: Error sources, self-calibration and direct georeferencing. Saarbrücken, VDM Verlag Dr. Müller Aktiengesellschaft & Co. KG: str. 63, 28–29, 32–64, 41.

Riegl, J., Bernhard, M. 1974. Empfangsleistung in Abhängigkeit von der Zielentfernung bei optischen Kurzstrecken-Radargeräten. Applied Optics, letnik 13, št. 4: 931–936.

Rottensteiner, F. 2003. Automatic generation of high-quality building models from lidar data. IEEE Computer Graphics and Applications, letnik 23, št. 6: 42–50.

Savšek-Safić, S., Ambrožič, T., Stopar, B., Turk, G. 2006. Determination of point displacements in the geodetic network. Journal of Surveying Engineering, letnik 132, št. 2: 58–63.

Schenk, T. 1999. Digital photogrammetry, Volume I, Backgrounds, Fundamentals, Automatic Orientation Procedures. Ohio, The Ohio State University, Terrascience: str. 248–249.

Slovensko omrežje stalnih postaj GNSS – SIGNAL.

<http://www.gu-signal.si/index.php> (pridobljeno 12.9.2009).

Soudarissanane, S., Van Ree, J., Bucksch, A., Lindenbergh, R. 2007. Error budget of terrestrial laser scanning: Influence of the incidence angle on the scan quality. V: Proceedings of 3D-NordOst. Berlin, Nemčija, 5.–8. december: str. 73–81.

Soudarissanane, S., Lindenbergh, R., Gorte, B. 2008. Reducing the error in terrestrial laser scanning by optimizing the measurement set-up. V: The International Archives of the Photogrammetry, Remote Sensing and Spatial Information Sciences. Peking, Kitajska, 3.–11. julij. letnik XXXVII, del B5: str. 615–620.

Tsakiri, M., Lichtenegger, D., Pfeifer, N. 2006. Terrestrial laser scanning for deformation monitoring. 3rd IAG/12 FIG Symposium. Baden, Avstrija.

http://www.ipf.tuwien.ac.at/np/Publications/tsakiriLichtenegger_Pfeifer FIG.pdf (pridobljeno 15.6.2008).

Van Gosliga, R., Lindenbergh, R., Pfeifer, N. 2006. Deformation analysis of a bored tunnel by means of terrestrial laser scanning. V: Proceedings of International Archives of Photogrammetry, Remote Sensing and Spatial Information Sciences. Dresden, Nemčija, 25.–27. september. Letnik XXXVI, del 5 (CD-ROM).

Vezočnik, R., Ambrožič, T., Sterle, O., Bilban, G., Pfeifer, N., Stopar, B. 2009. Use of Terrestrial Laser Scanning Technology for Long Term High Precision Deformation Monitoring. Sensors, letnik 9, št. 12: 9873–9895.

Vosselman, G., Maas, H. G. 2010. Airborne and Terrestrial Laser Scanning. Dunbeath, Whittles Publishing: str. 109–119.

Wagner, W., Ullrich, A., Ducic, V., Melzer, T., Studnicka, N. 2006. Gaussian Decomposition and Calibration of a Novel Small-Footprint Full-Waveform Digitising Airborne Laser Scanner. ISPRS Journal of Photogrammetry and Remote Sensing, letnik 60, št. 2: 100–112.

Wagner, W. 2007. Grundzüge der Fernerkundung für Studierende des Bakkalaureatstudiums Geodäsie und Geoinformatik. Dunaj, Inštitut za fotogrametrijo in daljinsko zaznavanje, Tehnična univerza na Dunaju: str. 152–158.

Zogg, H. M., Ingensand, H. 2008. Terrestrial laser scanning for deformation monitoring - load tests on the Felsenau viaduct (CH). V: The International Archives of the Photogrammetry, Remote Sensing and Spatial Information Sciences. Peking, Kitajska, 3.–11. julij. Letnik XXXVII, del B5: str. 555–562.